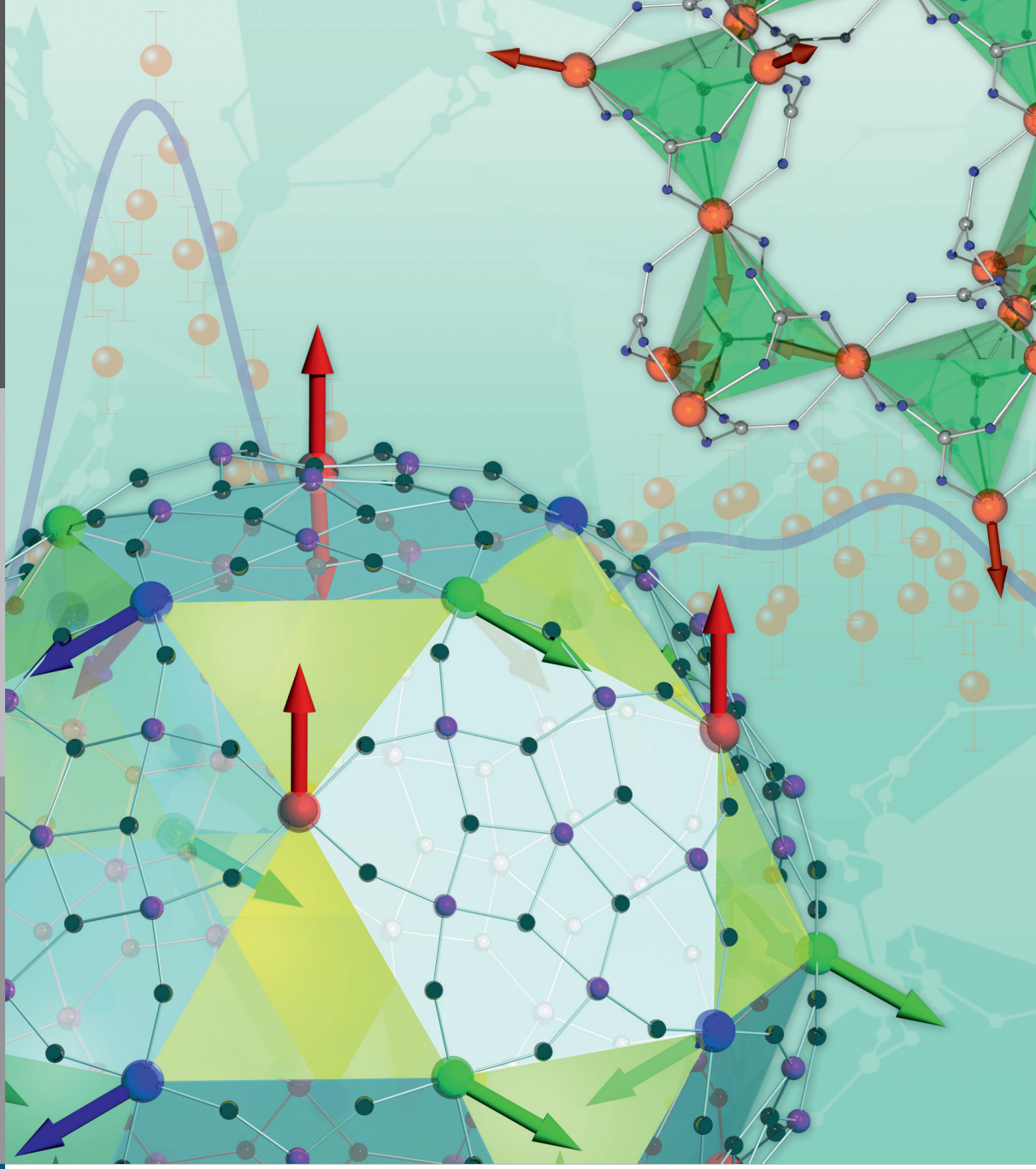

Spin Correlations and Excitations in Spin-frustrated Molecular and Molecule-based Magnets

Zhendong Fu

Mitglied der Helmholtz-Gemeinschaft

JÜLICH
FORSCHUNGSZENTRUM

Schriften des Forschungszentrums Jülich
Reihe Schlüsseltechnologien / Key Technologies Band / Volume 43

Forschungszentrum Jülich GmbH
Peter Grünberg Institute (PGI)
Scattering Methods (PGI-4 / JCNS-2)

Spin Correlations and Excitations in Spin-frustrated Molecular and Molecule-based Magnets

Zhendong Fu

Schriften des Forschungszentrums Jülich
Reihe Schlüsseltechnologien / Key Technologies Band / Volume 43

ISSN 1866-1807 ISBN 978-3-89336-797-9

Bibliographic information published by the Deutsche Nationalbibliothek.
The Deutsche Nationalbibliothek lists this publication in the Deutsche Nationalbibliografie; detailed bibliographic data are available in the Internet at http://dnb.d-nb.de.

Publisher and Distributor:	Forschungszentrum Jülich GmbH Zentralbibliothek 52425 Jülich Phone +49 (0) 24 61 61-53 68 · Fax +49 (0) 24 61 61-61 03 e-mail: zb-publikation@fz-juelich.de Internet: http://www.fz-juelich.de/zb
Cover Design:	Grafische Medien, Forschungszentrum Jülich GmbH
Printer:	Grafische Medien, Forschungszentrum Jülich GmbH
Copyright:	Forschungszentrum Jülich 2012

Schriften des Forschungszentrums Jülich
Reihe Schlüsseltechnologien / Key Technologies Band / Volume 43

D 82 (Diss., RWTH Aachen, Univ., 2011)

ISSN 1866-1807
ISBN 978-3-89336-797-9

The complete volume is freely available on the Internet on the Jülicher Open Access Server (JUWEL) at http://www.fz-juelich.de/zb/juwel

Dedicated to My Family

Acknowledgements

This thesis would not have been possible without the continuous support of many people. During the past three years, I have learned not only about physics, but also, more importantly, the rigorous attitude and the analytical and problem-solving abilities in scientific research. I am grateful that my doctoral career at Forschungszentrum Jülich has been immeasurably enriched by indispensable friends and colleagues, whom I shall always cherish.

First and foremost, I would like to express my profound appreciation to my adviser Prof. Dr. Thomas Brückel for all his invaluable guidance and support, for the many inspiring conversations, and for his great patience and encouragement throughout every process of my doctoral thesis. He showed me the way to the fascinating neutron scattering technique and molecular magnetism. His wisdom and insights leaded me to more accurate and deeper understanding to physics. It has been a really delightful experience of working in his group, where I felt a very pleasant working atmosphere and accumulated the knowledge in different aspects. I consider myself lucky to have worked in this group.

I am especially grateful to the second referee of my dissertation, Prof. Dr. Paul Kögerler, for introducing me to the fascinating area of molecular magnetism, synthesizing and offering the precious samples, and giving me valuable advices from chemical points of view. Samples are essential for an experimentalist to measure. I would also like to thank Dr. Claire Besson, Dr. Yanzhen Zheng for their great efforts in synthesizing the samples for my experiments.

I would like to thank the third referee of my dissertation, Dr. Ulrich Rücker, who is always happy to help me with different kinds of problems.

My special thanks go to Dr. Yinguo Xiao, who helped me a lot not only in scientific research but also in my life in Jülich.

I would like to thank Prof. Edmond Boschitz, a good friend who has encouraged me to seek my doctoral degree in Germany, for his great help and hospitality. He widened my view of the world with his rich experience and had been so kind as to drive me for sightseeing in Germany.

I would like to thank Dr. Subhankar Bedanta for his great help with the measurements on MPMS and the data analysis.

The neutron experiments in this dissertation have been carried out at various

institutions with the excellent expertise and support from the instrument scientists and engineers. Dr. Yixi Su, Dr. Anatoliy Senyshyn, and Dr. Giovanna Giulia Simeoni deserve special thanks for all their help in the experiments and the data analysis. Furthermore, I would like to thank: Dr. Ranjan Mittal, Dr. Wouter Borghols, Dl. Harald Schneider, Dr. Michaela Zamponi, and Dr. Tobias Unruh.

Many thanks go to Mr. Berthold Schmitz and Dr. Emmanuel Kentzinger for their help with the measurements on MPMS and PPMS.

I thank Prof. Dr. Raphael Hermann, Dr. Werner Schweika, Dr. Jörg Voigt, Prof. Dr. Manuel Angst, and Dr. Kirill Nemkovskiy, for helpful discussions.

I would also like to express gratitude to Ms. Barbara Köppchen and Ms. Roswitha Bley for their help with various nonacademic issues during my stay in Forschungszentrum Jülich.

Further acknowledgement goes to all the colleagues and friends in Jülich, whose names are not listed above, for their help in various aspects.

Finally, I give special thanks to my grand-parents, parents and parents-in-law, whose love, support, and encouragement give me strength to pursue my dreams. And most of all, my sincerest gratitude towards my beloved wife, Shu Zhang, who shows me pure unconditional love, faith, and concerns. It is so wonderful to have her love in my life. I dedicate this thesis to my loving family.

Zhendong Fu
Jülich, May 2011

Abstract

The present thesis provides extensive investigations on the effect of geometrical spin frustration in both molecular-based spin clusters and infinite pyrochlore lattice, using advanced neutron scattering, DC and AC susceptibilities, and specific heat methods.

Clear short-range spin correlations have been observed in the spin-frustrated molecular magnet $\{Mo_{72}Fe_{30}\}$ by means of polarized neutron scattering. Simulations of the spin correlations were carried out within a frustrated three-sublattice spin model. The simulations are in reasonable agreement with the differential magnetic cross section measured at 1.5 K. The specific heat of $\{Mo_{72}Fe_{30}\}$ was measured down to 60 mK. The low-lying magnetic excitations of $\{Mo_{72}Fe_{30}\}$ are identified by the Schottky anomalies in the specific heat data, consistent with the theoretical predictions of quantum rotational band model. The nature of the magnetic ground state of $\{Mo_{72}Fe_{30}\}$ can therefore be interpreted within the three-sublattice spin model, where the 30 Fe^{3+} spins are divided into three sublattices with equal and coplanar unit vectors each.

The low-lying magnetic excitations of single molecular magnet $\{As_6V_{15}\}$ were determined by means of specific heat measurements down to 60 mK. The resultant energy spectrum agrees with the theoretical predictions of the "three-spin" model and the results of inelastic neutron scattering experiments. Hence the "three-spin" model is a good approach to the magnetic ground state of $\{As_6V_{15}\}$.

Complicated magnetic behaviors have been observed in the antiferromagnetic pyrochlore $Na_3Co(CO_3)_2Cl$. The average crystal structure of $Na_3Co(CO_3)_2Cl$ was determined by means of X-ray and neutron powder diffraction measurements. Though there is no site disorder in the Co^{2+} magnetic sublattice, positional disorder may exist in Na and Cl atom sites. The DC and AC susceptibility measurements show a spin-glass-like transition at 4.5 K, and a field- and frequency- independent kink at 17 K. Temperature dependence of the specific heat exhibits a peak at 1.5 K due to a long-range magnetic order, a broad hump at 5 K associated with the spin-glass-like transition, and a very small hump at 17 K. The diffuse neutron scattering with polarization analysis reveals short-range spin correlations dominated by antiferromagnetic coupling over the range of nearest neighbors. Ferromagnetic coupling exists between next-nearest neighbors. Long-range magnetic order below

1.5 K is evidenced by magnetic Bragg peaks observed at 50 mK and can be well explained with an all-in-all-out spin configuration. Inelastic neutron scattering reveals the existence of collective magnetic excitations at 3.5 K, indicating that the transition temperature T = 4.5 K does not correspond to a complete spin-glass freezing as expected in traditional metallic spin glasses. The peak observed in magnetic susceptibility at 17 K is attributed to the onset of an intermediate partially-ordered phase transition, qualitatively consistent with the theoretical predictions for pyrochlore antiferromagnets with weak ferromagnetic next-nearestneighbor interactions. $Na_3Co(CO_3)_2Cl$ therefore exhibits exotic magnetic behavior, which has not yet been understood completely and requires more experiments in the future.

Zusammenfassung

Die vorliegende Arbeit enthält umfassende Untersuchungen über den Effekt geometrischer Spinfrustration sowohl in molekularen Spin-Clustern als auch in ausgedehnten Pyrochlor-Gittern mit den Methoden der Neutronenstreuung, Messung der DC- und AC-Suszeptibilität und der spezifischen Wärme.

Deutliche kurzreichweitige Spinkorrelationen in den Spin-frustrierten molekularen Magneten $\{Mo_{72}Fe_{30}\}$ wurden mit Hilfe von polarisierter Neutronenstreuung beobachtet. Simulationen der Spinkorrelationen auf der Basis eines frustrierten drei-Untergitter-Spinmodells erfolgten mit guter Übereinstimmung mit dem differentiellen magnetischen Streuquerschnitt bei 1.5 K. Die spezifische Wärme von $\{Mo_{72}Fe_{30}\}$ wurde bis hinab zu 60 mK gemessen. Die tief liegenden magnetischen Anregungen von $\{Mo_{72}Fe_{30}\}$ werden als Schottky-Anomalien in der spezifischen Wärme identifiziert, im Einklang mit den theoretischen Vorhersagen des „Quantum Rotational Band"-Modells. Der Ursprung des magnetischen Grundzustands von $\{Mo_{72}Fe_{30}\}$ kann daher durch das drei-Untergitter-Spinmodell beschrieben werden, bei dem die 30 Fe^{3+}-Spins in drei Untergitter mit jeweils gleichen und coplanaren Spinvektoren eingeteilt sind.

Die tiefliegenden magnetischen Anregungen des Einzelmolekülmagneten $\{As_6V_{15}\}$ wurden durch Messungen der spezifischen Wärme bis hinab zu 60 mK ermittelt. Das daraus resultierende Energiespektrum stimmt mit den theoretischen Vorhersagen des „Drei-Spin"-Modells und mit experimentellen Ergebnissen aus inelastischer Neutronenstreuung überein. Daher ist das „Drei-Spin"-Modell eine gute Beschreibung des magnetischen Grundzustands von $\{As_6V_{15}\}$.

Im antiferromagnetischen Pyrochlor $Na_3Co(CO_3)_2Cl$ wurde ein kompliziertes magnetisches Verhalten beobachtet. Die mittlere Kristallstruktur von $Na_3Co(CO_3)_2Cl$ wurde mittels Röntgen- und Neutronenpulverdiffraktometrie bestimmt. Obwohl es im magnetischen Co^{2+}-Untergitter keine Gitterplatzunordnung gibt, kann bei den Na- und Cl-Atomen Platzunordnung existieren. DC- und AC-Suszeptibilität zeigen einen spinglasartigen Übergang bei 4.5 K, und einen feld- und frequenzunabhängigen Knick bei 17 K. Die spezifische Wärme von $Na_3Co(CO_3)_2Cl$ weist einen Peak bei 1.5 K aufgrund der langreichweitigen magnetischen Ordnung und eine breite Struktur bei 5 K aufgrund des spinglasartigen Übergangs auf. Diffuse Neutronenstreuung mit Polarisationsanalyse zeigt kurzreichweitige

Spinkorrelationen, die durch antiferromagnetische Kopplungen im Bereich der nächsten Nachbarabstände dominiert wird, mindestens bis hinab zu 3.3 K. Ferromagnetische Kopplung zwischen übernächsten Nachbarn gibt es möglicherweise auch. Langreichweitige magnetische Ordnung wird durch magnetische Braggpeaks bei 50 mK belegt, im Einklang mit den Ergebnissen der spezifischen Wärme. Inelastische Neutronenstreuung zeigt die Existenz kollektiver magnetischer Anregungen bei 3.5 K, was darauf hinweist, dass die Übergangstemperatur T = 4.5 K nicht einem vollständigen Einfrieren des Spinglases entspricht wie man es von den traditionellen metallischen Spingläsern erwartet. $Na_3Co(CO_3)_2Cl$ zeigt daher ein exotisches magnetisches Verhalten, das bisher noch nicht vollständig verstanden ist und zukünftig weitere Experimente erfordert.

Table of Contents

List of Figures

List of Tables

CHAPTER 1:

Introduction

1.1 Molecular Magnetism

In the last quarter of 20th century, molecular chemistry has had great impact on the field of nanoscale magnetism by providing new magnetic clusters, which consist partially or entirely of molecular components and are commonly defined as molecular magnets [1-3]. An appealing research field, *Molecular Magnetism*, was opened accordingly. A general definition of molecular magnetism has been given by Oliver Kahn [1], who is considered as one of the founders of this area, as follows: "*Molecular magnetism deals with magnetic properties of isolated molecules and/or assemblies of molecules*". With the remarkable progress in the chemical synthesis and experimental characterization of molecular magnets, more emphasis has been given to the aspect of rational molecular design of interesting magnetic properties. Therefore, molecular magnetism becomes "*a discipline which conceives, realizes, studies, and uses new molecular materials bearing new but predictable magnetic (and other) physical property*" [4].

As the smallest well-defined quantum magnets, molecular magnets have attracted intense and ongoing attention owing to their fascinating magnetic properties and potential applications. In molecular magnets, each molecule contains a relatively small number of paramagnetic ions (i.e., spins), interacting via superexchange interactions. The magnetic molecules are well isolated by ligands, so that the bulk magnetic properties are of molecular origin because intermolecular magnetic interactions can be neglected as compared to the dominating intramolecular interactions. Beyond providing new class of magnets, molecular magnetism also offers valuable model systems of appealing physical properties, which attract much interest from the solid state physicists.

In this chapter, I will give a general introduction to the field of molecular magnetism, including the brief history, the important representatives and magnetic properties, and the neutron scattering of molecular magnets.

1.1.1 Magnetism: From Bulk to Molecules

Magnetism is one of the fundamental properties of matter and has been known to humans for millennia. From the magnetic needle compass one thousand years ago

to the magnetic digital storage nowadays, deeper understanding of magnetism accompanies the progress of human society. Traditionally, the research on magnetism in solid state physics has been focusing on inorganic elements (e.g., Fe, Co, Ni), alloys (e.g., permalloy) and simple compounds (e.g., transition metal oxides), leading to numerous technological applications [5]. An underlying assumption was built that most fundamental physics is better revealed on chemically simple materials. Yet some exciting studies in solid state physics can now be carried out on molecular magnets of chemically complicated structure [5].

The building blocks of molecular magnets are molecules rather than atoms, which distinguishes molecular magnets from the conventional magnets based on metallic and ionic lattices. Molecular magnetism originates from the magnetochemistry. In the beginning, the interest in molecular materials arose from the search for magnets from purely organic compounds. In 1991, Tamura et al. discovered the first purely organic ferromagnet based on a nitronyl nitroxide [6]. Organic molecular magnets, where spins are carried by free radicals, became the first species of molecular magnets.

Molecular magnets can also be synthesized by inorganic approach. A milestone is the discovery of Mn_{12}-acetate (Mn12ac) in 1990s, whose molecule comprises 12 manganese ions and is characterized by a ground state with S = 10 [7-10], as shown in **Figure 1-1-1**. Another interesting inorganic molecular magnet is "Fe_8", with 8 iron ions and a ground state of S = 10 per molecule [11, 12].

These molecular magnets possess high-spin ground states and at sufficiently low temperatures exhibit a pronounced hysteresis loop under magnetic fields. They show slow relaxation of the magnetization at low temperatures. Their molecules act like tiny magnets. Therefore, these molecular magnets are often called "single-molecule magnets" (SMMs) [10, 13]. In contrast to classical magnets, the magnetic properties of SMMs are of pure molecular origin, instead of cooperative effects. Besides the magnetic bistability, SMMs allow a direct observation of quantum physical properties [14], such as quantum tunneling of magnetization and quantum coherence [15-19]. SMMs have been proposed as potential candidates for some important technical applications, such as high-density magnetic storage [20], spintronics [21] and quantum computing [22].

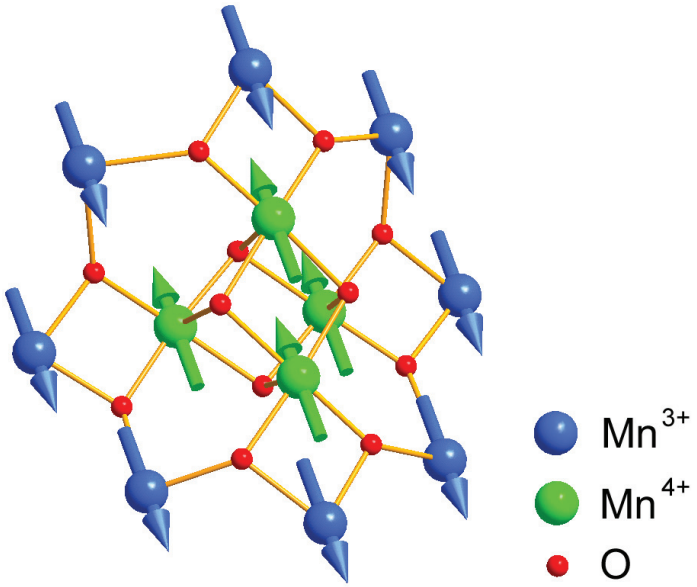

Figure 1-1-1 The ball and stick presentation of the magnetic core $Mn_{12}O_{12}$ of Mn12ac. Eight outer Mn^{3+} ions (s = 2) are parallel, and four inner Mn^{4+} ions (s = 3/2) are antiparallel to the outer spins, resulting in a ferrimagnetic spin configuration with total spin S = 10 per molecule.

The research in molecular magnetism in the past two decades has been focused on the magnetic bistability of SMMs, by pursuing high-spin ground states in conjunction with large molecular magnetic anisotropy. However, the effort to significantly increase the energy barrier stabilizing the hysteresis behavior has met a bottleneck. Consequently, the field of molecular magnetism is branching out into new areas, where new model systems of promising physical phenomena are discovered. One of these new areas is molecular polyoxometalate chemistry [23–25]. Polyoxometalates (POMs) provide the largest, structurally well-defined species of molecular magnets by now. From a bottom-up design based on well-defined building blocks, geometrical spin frustration can be realized in individual polyoxometalate molecules with highly symmetric spin structures. Combining with the metal oxide-based spin-frustrated M_3 triangles (M = e.g., Fe, Cr, V), these magnetic systems can be perfect testbeds to study how spin frustration behaves within quasi-zero dimension owing to their molecular origin. The first two materials, $\{Mo_{72}Fe_{30}\}$ and $\{V_{15}As_6\}$, presented in this thesis belong to the

spin-frustrated molecular polyoxometalate systems. The number of spin triangles per molecule is twenty and one, in $\{Mo_{72}Fe_{30}\}$ and $\{V_{15}As_6\}$, respecitvely. Detailed introductions to these two systems will be given in Chapter 3 and 4.

1.1.2 Slow Relaxation and Quantum Tunneling of Magnetization

In SMMs, ligands isolate neighboring magnetic clusters from each other. All magnetic clusters are identical and at temperatures significantly lower than the temperature equivalence of the intramolecular exchange interaction each of them can be regarded as a single magnetic unit with a total spin S, which is obtained by the sum of individual spin s within one magnetic cluster taking into account the particular magnetic exchange interactions among the spins. An essential mechanism in SMMs is an energy barrier to magnetization reorientation, which is given in the simplest case of uniaxial anisotropy by $\Delta E = |D| \cdot S_z^2$ [10]. In this expression for the energy barrier, S_z is the spin component along the easy axis of magnetization and D is the zero-field splitting parameter. The total spin of the cluster must overcome this energy barrier to switch from parallel alignment to antiparallel alignment. The anisotropy gives rise to a zero-field splitting of the S multiplets, ranging from $-M_S$ to M_S, where M_S is the magnetic quantum number of the spin operator S_z. Under no external magnetic field, the energy spectrum is plotted in **Figure 1-1-2 (a)**. All energy levels are degenerate pairs, except $M_S = 0$. At sufficiently low temperature, only the lowest two states $|\pm M_S>$ are equally populated in the ground state. Net magnetization vanishes.

As shown in **Figure 1-1-2 (b)**, if a large magnetic field is applied parallel to the z axis at sufficiently low temperatures, only the level ($M_S = -S$) corresponding to magnetization parallel to the applied magnetic field will be populated with a saturated magnetization. When the field is switched off, the system will go back to thermal equilibrium with no net magnetization, namely magnetic relaxation. As shown in **Figure 1-1-2 (c)**, half of the molecules must overcome the energy barrier to settle at $M_S = +S$ state. This relaxation progress is attributed to the coupling of the spin system to the vibrational degrees of freedom, which allows transitions from states $|M_S>$ to $|M_S \pm 1>$ [26]. This means a sequence of energy levels are involved in the reversal of molecular magnetization. The requirements for longer relaxation time are: (i) larger total spin S and (ii) larger zero-field splitting parameter D [10]. The typical relaxation time of Mn12ac is of the order of months at 2 K.

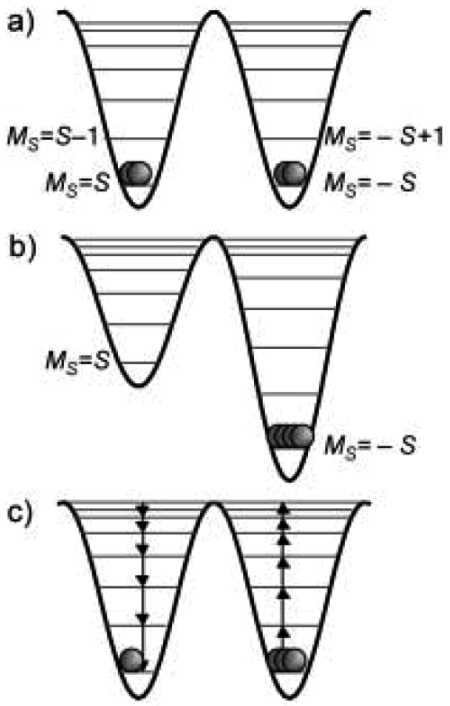

Figure 1-1-2 Energy levels for a molecule with spin state *S* and easy axis magnetic anisotropy. **(a)** In zero field the two wells are equally populated; **(b)** The right well is populated selectively after applying a magnetic field; **(c)** Equilibrium is retrieved through a series of steps after removing the field. [Picture taken from R. Sessoli and D. Gatteschi, *Angew. Chem. Int. Ed.* **42** (2003) 268]

Below the blocking temperatures, the magnetization of SMMs shows a hysteresis behavior as shown in **Figure 1-1-3** in case of Mn12ac. The clear hysteresis loops are directly associated with the slow relaxation dynamics of the system within the studied temperature range. Furthermore, some steps can be seen at the field dependence of the magnetization, where the relaxation rate is increased significantly. This phenomenon has been identified to be due to the quantum effect of the magnetic molecules, and consequently called *quantum tunneling* of the magnetization.

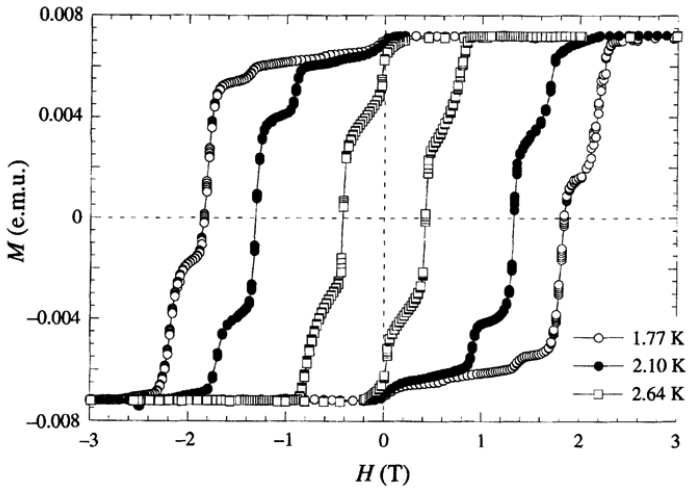

Figure 1-1-3 Magnetization hysteresis loops measured from Mn12ac with SQUID magnetometer at various temperatures. [Picture taken from L. Thomas et al., *Nature* **383** (1996) 145]

The process of quantum tunneling can be explained as follows. In zero field (top panel in **Figure 1-1-4**), the levels on both side of the barrier coincide in energy. Spin tunneling is favored under this circumstance and may compete with the thermally activated mechanism. The tunneling through the barrier causes a significant acceleration of the magnetic relaxation. If a longitudinal magnetic field is applied, the positive and negative M_S levels are no longer degenerate. Tunneling is suppressed because of the lack of coincidence between the $\pm M_S$ levels (middle panel in **Figure 1-1-4**). However, accelerations of the relaxation due to tunneling occur again when the external field fulfills the condition $H_z = n|D|/g\mu_B$. For n integer the levels on both sides of the barrier coincide. Therefore the field dependence of magnetization exhibits the step-wise hysteresis curve owing to the quantum tunneling effect at particular field values.

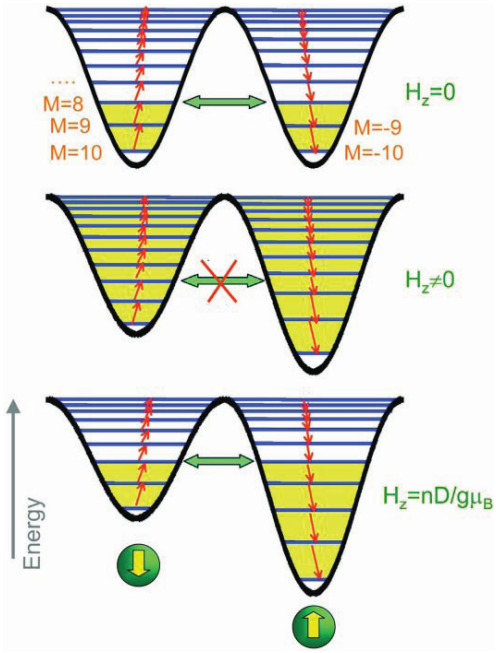

Figure 1-1-4 Energy levels of Mn12ac split by an axial anisotropy (top). In zero field, overcoming the energy barrier can occur through a thermal activation or quantum tunneling effect. If external field is applied, the levels on both sides of the barrier may not be coincident and thus tunneling is suppressed (middle), unless specific values of the field are reached (bottom). [Picture taken from R. Sessoli, *Europhys. News* **34** (2003) 41]

1.1.3 Quantum Coherence of SMMs

The key concept for quantum information processing is that a two-level system with arbitrary superpositions of its two levels can be a candidate for a quantum bit (qubit). The contribution of each of the two levels to the superposition state has a cyclic dependence on the electromagnetic radiation pulse length, leading to so-called Rabi oscillations [18, 28]. The observation of Rabi oscillations is a proof-in-principle to identify a system to be a quantum computing material or not [18]. SMMs have been regarded as candidates for quantum computing due to the magnetic bistability and the superpositions of spin eigenstates in these materials. A lot of work has been done to determine the quantum coherence time of SMMs [18, 29-32]. A long coherence time is crucial to achieve a long-lived quantum memory.

Take the Fe_4 complex (see **Figure 1-1-5**) as an example. Clear evidence for long-live quantum coherence was obtained by means of pulsed W-band electron spin resonance (ESR) spectroscopy [18].

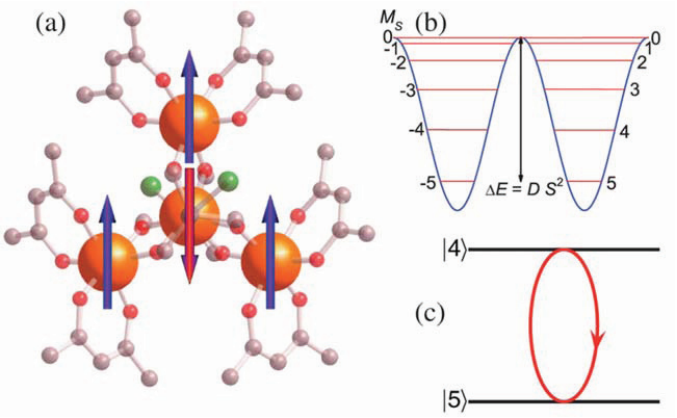

Figure 1-1-5 (a) Structure of Fe_4 molecule with relative spin orientations (S = 5). **(b)** Double-well energy diagram with anisotropic energy barrier. **(c)** Rabi cycle between magnetic sublevels. [Picture taken from C. Schlegel et al., *Phys. Rev. Lett.* **101** (2008) 147203]

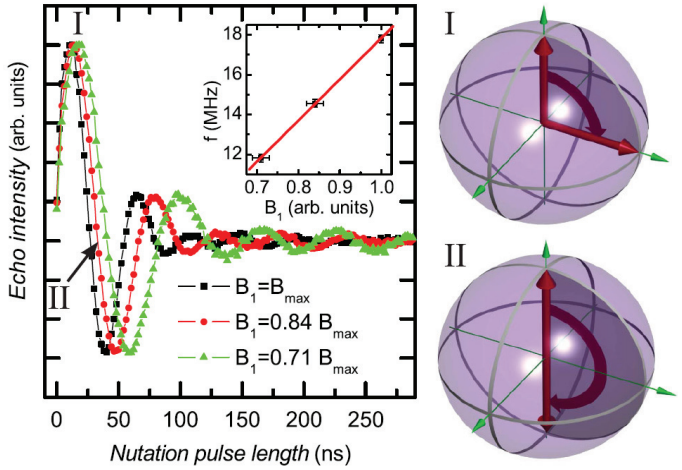

Figure 1-1-6 Rabi oscillations of Fe_4 complex as measured in pulsed ESR spectroscopy, together with corresponding path on Bloch sphere. [Picture taken from C. Schlegel et al., *Phys. Rev. Lett.* **101** (2008) 147203]

As shown in **Figure 1-1-6**, intensity oscillations can be seen clearly on the echo intensity as a function of the duration of the pulse. These oscillations are coherent spin oscillations (i.e., Rabi oscillations) in Fe_4. The observation of Rabi oscillations indicates that SMMs can be candidates for performing quantum computations [18].

1.1.4 Neutron Scattering of Molecular Magnets

Neutron scattering, has been one of the most important techniques in the study on magnetism of classical magnetic materials, including the magnetic structure, magnetic phase transitions, magnetic excitations, and so on. Neutron scattering technique is also playing an important role in the study on molecular magnets [33].

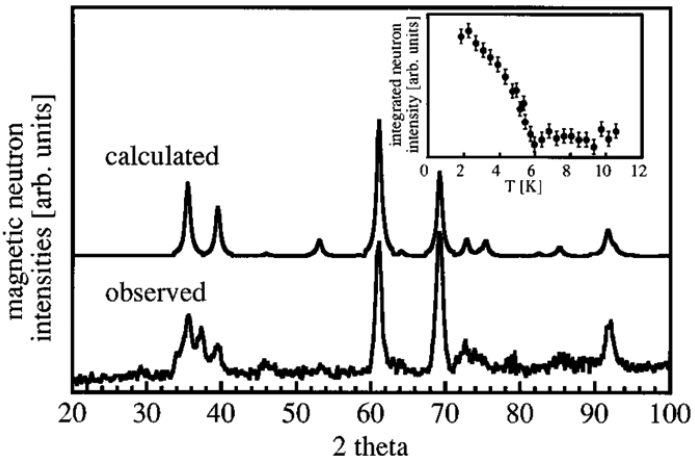

Figure 1-1-7 Observed [difference I(1.8 K) - I(12 K)] and calculated magnetic neutron diffraction patterns for $\{[P(C_6D_5)_4][Mn^{II}Cr^{III}(C_2O_4)_3]\}_n$. [Picture taken from R. Pellaux et al., *Inorg. Chem.* **36** (1997) 2301].

First, elastic neutron diffraction experiments can be used to determine the magnetic structure of molecular magnets. For example, the two-dimensional molecular complex $\{[P(C_6D_5)_4][Mn^{II}Cr^{III}(C_2O_4)_3]\}_n$ was reported to establish a long-range magnetic order at ~ 6 K [34, 35]. A neutron powder diffraction measurement was performed on this compound at 1.8 K and 12 K, and revealed several magnetic Bragg reflections by subtracting the spectrum for 12 K from the one for 1.8 K. A collinear ferromagnetic arrangement of Mn^{2+} and Cr^{3+} spins along

the c-axis was suggested to represent the magnetic ordered phase. The measured and calculated diffraction patterns are shown in **Figure 1-1-7**.

Besides the determination of long-range magnetic order, neutron diffraction can also be used to investigate the short-range spin correlations in molecular magnets. The diffuse neutron scattering with polarization analysis has proven to be a powerful tool in the study on the spin correlations of spin-frustrated molecular magnets. This will appear as an essential technique in this thesis.

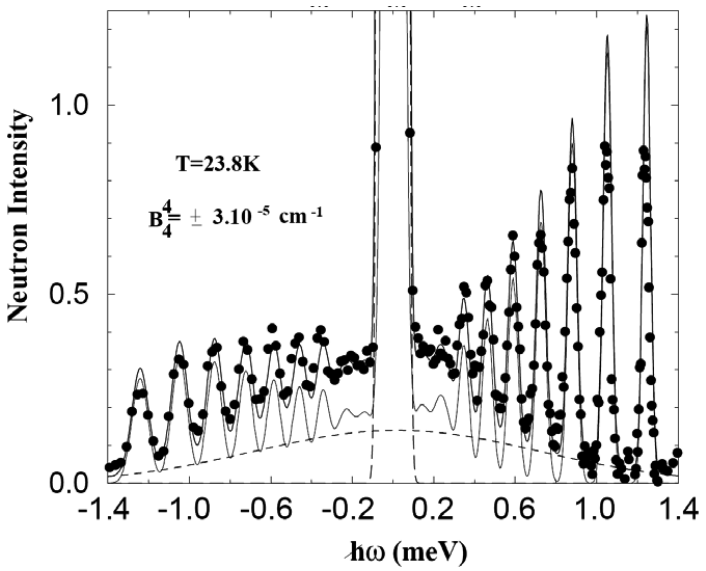

Figure 1-1-8 Energy spectrum (filled circles) of Mn12ac as measured using inelastic neutron scattering at 23.8 K. Dashed line: Lorentzian background. Long-dashed line: elastic intensity. Thin line: theoretical calculation. Thick line: the sum of all components. [Picture taken from I. Mirebeau et al., *Phys. Rev. Lett.* **83** (1999) 628]

Another important application of neutron scattering in molecular magnetism is the study on magnetic excitations using inelastic neutron scattering. As aforementioned in Section 1.1.2, some SMMs are described as a single total spin S, split by anisotropy terms into sublevels with $-S \leq M_S \leq +S$ under zero magnetic field. When neutrons interact with these spin clusters they may give rise to transitions between the M_S levels of S multiplets, according to the selection rule $\Delta M_S = 0, \pm 1$. Therefore, inelastic neutron scattering measurements of SMMs can provide detailed

information on the spectrum of the M_S energy levels. Take Mn12ac as the example [36]. The inelastic neutron scattering of Mn12ac was measured at various temperatures with incident wavelength of 5.9 Å, resulting in an energy resolution with a full width at half maximum (FWHM) about 27.5 μeV at zero energy transfer. The inelastic neutron scattering spectrum measured at 23.8 K is shown in **Figure 1-1-8**. 14 well-resolved peaks were directly observed. The positions of the inelastic peaks were independent of the temperature. The data were analyzed by considering not only the diagonal terms but also the transverse term in the spin Hamiltonian. The resultant theoretical calculation agreed excellently with the experimental spectrum, as shown in **Figure 1-1-8**. Therefore, the energy spectrum of Mn12ac has been determined precisely using inelastic neutron scattering technique [36]. The relevant anisotropy parameters could thus be determined.

1.2 Geometrical Spin Frustration

In the scope of condensed matter physics, geometrical spin frustration is an important magnetic phenomenon, which stems from the topological arrangement of the spins [37, 38]. The term "frustration" has been introduced into magnetism by Gerard Toulouse [39]. It describes the situation that "a spin (or a number of spins) in the system cannot find an orientation to fully satisfy all the interactions with its neighboring spins" [38]. Magnetic frustration has attracted long and ongoing attention and been regarded as an organizing principle that governs a wide range of physical phenomena in the collective behaviors of spins. The basic concept of frustration has been found to have practical meanings in areas from microelectronics to drug delivery. Besides the geometrical constrains, other mechanisms like competing magnetic interactions [40] or disorder [41, 42] in lattices can also cause frustration. In this section, by geometrical spin frustration I refer to the systems with no disorder or competing interactions, where the spin frustration arises only from the topology of the crystal lattice or molecular structure.

1.2.1 Geometrically Frustrated Lattices

The simplest case of geometrical frustration is the equilateral spin triangle with antiferromagnetic interactions, which has been considered by Wannier in 1950 [43]. For Ising spins with spin number *s* on the equilateral triangle in **Figure 1-2-1 (a)**, one cannot construct a ground state with all antiferromagnetic bonds fully satisfied. The ground state does not correspond to the minimum of the interaction energy of every spin pair, since one of the three spins cannot align itself antiparallel to its two neighbors simultaneously. For the sake of simplicity, the discussion in this section will be restricted to Ising spins with antiferromagnetic interactions. Naturally the real material with geometrical frustration consists of triangle-based spin structure, such as the triangular lattice (see **Figure 1-2-1 (b)**), which is built from edge-sharing triangles and has been studied theoretically by Wannier in 1950 [43]. He found in such a system, the threefold multiplicity of the lowest and degenerate energy levels results in residual entropy, even at absolute zero temperature [43].

Another two-dimensional (2D) spin-frustrated structure is constructed from corner-sharing triangles, which is named after a particular kind of Japanese basket

weave pattern, so-called "kagome" lattice (see **Figure 1-2-1 (c)**). Calculation of the residual entropy of kagome lattice shows that kagome lattice might be "more frustrated" than the triangular lattice [44]. The antiferromagnetism on kagome lattice has been studied extensively from both theoretical and experimental points of view [44-47].

What about the case of three-dimensional (3D) structures? Similar geometrical frustration as found in 2D structures can also happen in 3D structures. Corresponding to the equilateral triangle, four Ising spins with antiferromagnetic interactions at the corners of tetrahedron are frustrated. As illustrated in **Figure 1-2-1 (d)**, if two of the four spins satisfy the antiferromagnetic interaction between them, it is not possible to arrange the other two spins to fulfill all antiferromagnetic interactions between the spins simultaneously. Just like the 2D case, one can arrange the spin tetrahedra in both edge-sharing geometry and corner-sharing geometry, resulting in two frustrated 3D structures: face-centered-cubic (FCC) lattice (**Figure 1-2-1 (e)**) and pyrochlore lattice (**Figure 1-2-1 (f)**). The FCC lattice is regarded as a 3D analogue of triangular lattice, while the pyrochlore lattice as a 3D analogue of kagome lattice accordingly. The pyrochlore lattice is "more frustrated" than the FCC lattice and actually the most frustrated lattice readily realizable in three dimensions [48]. A lot of interesting physical phenomena have been observed in magnetic pyrochlores. More information about magnetic pyrochlores will be given in Chapter 5, where the investigations performed on a new compound $Na_3Co(CO_3)_2Cl$ with antiferromagnetic pyrochlore structure will be presented in detail.

A direct effect of ideal geometrical spin frustration is that it prevents the system from being long-range magnetically ordered due to the huge ground-state degeneracy, which makes the system unable to settle into any particular ground state. Even slight perturbations may introduce instabilities in spin-frustrated systems and give rise to the emergence of novel magnetic phenomena. This is actually where the attractiveness of geometrical spin frustration lies in both fundamental and applied respect [48].

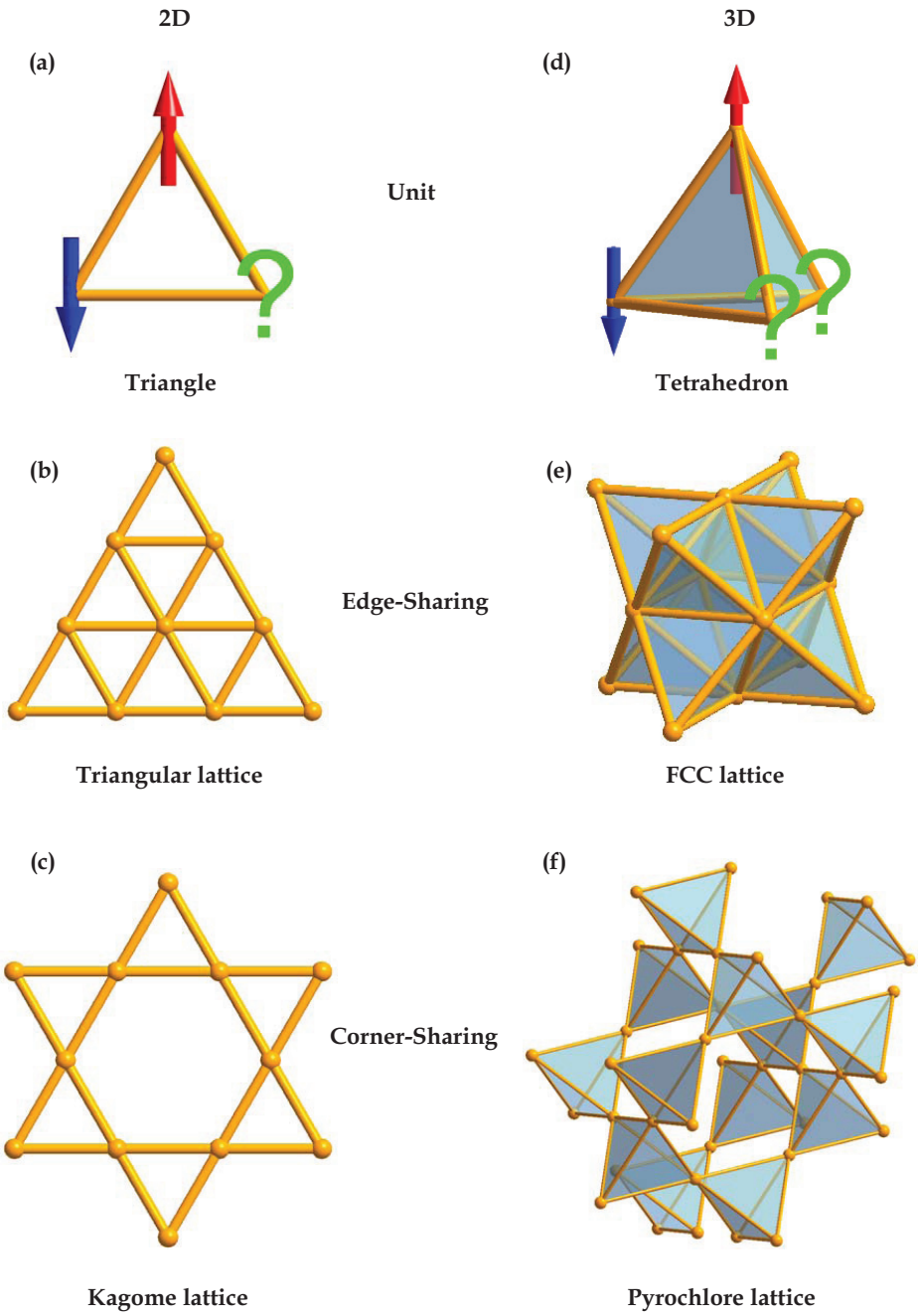

Figure 1-2-1 Examples of 2D and 3D frustrated magnetic lattices. The second and third rows correspond to the edge- and corner-sharing constructions of triangles and tetrahedra, respectively.

1.2.2 Geometrical Spin Frustration in Molecular Magnets

As discussed in the previous section, the magnetic frustration in infinite lattices has been extensively studied in condensed matter physics. Geometrical spin frustration can also happen in isolated magnetic molecules [49, 50]. A wide variety of molecular-based spin structures can be realized via bottom-up approaches of chemical synthesis. This offers the prospect for research on geometrical spin frustration at the nanoscale level.

In certain spin lattices with antiferromagnetic nearest-neighbor interactions, such as the kagome lattice and pyrochlore lattice, one expects prominent frustration effects to occur. Some molecular-based analogs of kagome lattice have been discovered. In the spin systems of these molecular magnets, corner-sharing spin triangles are arranged around square or pentagonal fragments on a spherical-like structure, resulting in spin cuboctahedron [51-53] (see **Figure 1-2-2 (a)**) and spin icosidodecahedron [53-55] (see **Figure 1-2-2 (b)**).

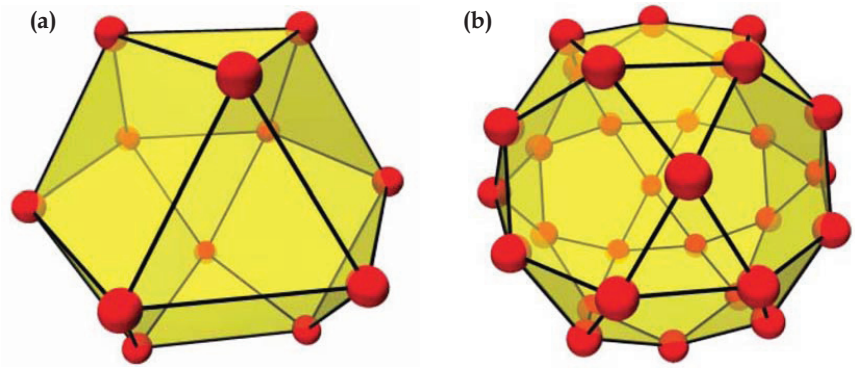

Figure 1-2-2 Structure of cuboctahedron **(a)** and icosidodecahedron **(b)**. [Picture taken from Jürgen Schnack, *Dalton Trans.*, **39** (2010) 4677].

The spin frustration leads to a non-trivial classical ground-state degeneracy in such molecules [56]. **Figure 1-2-3** is a planar projection of a spin cuboctahedron with antiferromagnetic nearest-neighbor interactions, illustrating the degenerate classical ground state. For Heisenberg spins, the nearest neighbors should have a relative angle of 120˚ between them in the classical ground states. The number of classical ground states is actually infinite since the groups of four spins (outer and inner

square) can rotate independently as long as the 120° angles between nearest neighbors are kept [56].

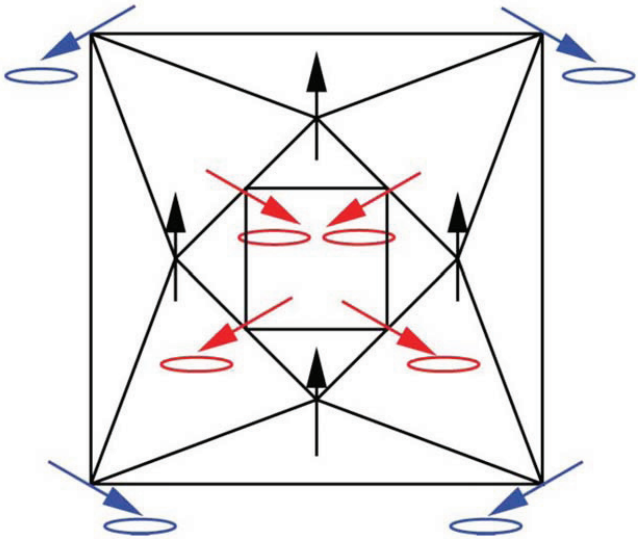

Figure 1-2-3 Planar projection of the classical ground state of spin cuboctahedron. Solid edges: antiferromagnetic interactions. Two groups of spins (out and inner square) can rotate independently in the classical ground states. [Picture taken from Jürgen Schnack, *Dalton Trans*., **39** (2010) 4677]

However, the ground state of the corresponding quantum system is non-degenerate [56, 57]. The degeneracy of the classical ground states is lifted by quantum fluctuations, which is also denoted as "order by disorder" [56, 58]. After quantum corrections, the classical ground states will appear as low-lying singlets in the quantum energy spectrum [56, 59]. **Figure 1-2-4** shows the quantum energy spectrum of antiferromagnetic cuboctahedron for spins of $s = 1/2$ and $s = 3/2$. In both cases, the ground states are non-degenerate. The case for icosidodecahedron will be discussed in Chapter 3.

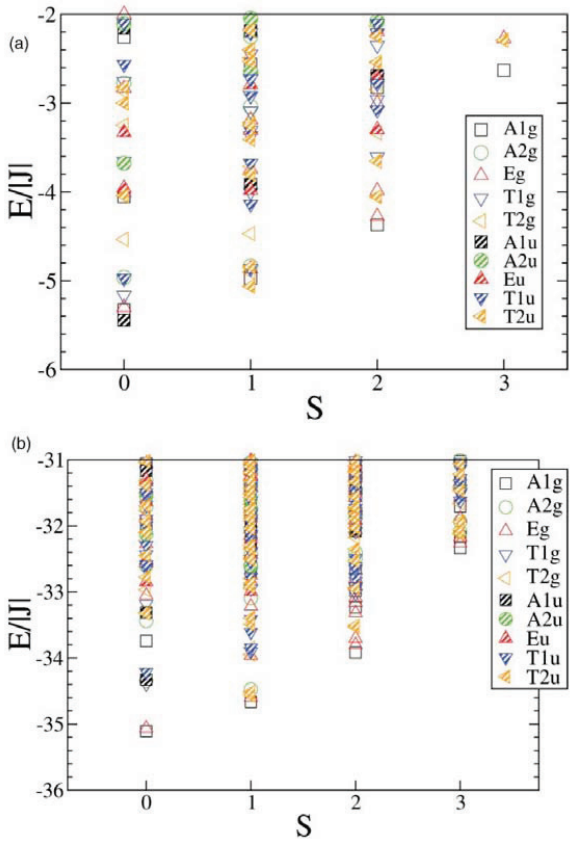

Figure 1-2-4 Low-lying energy spectrum of antiferromagnetic cuboctahedron for $s = 1/2$ **(a)** and $s = 3/2$ **(b)**. [Picture taken from Jürgen Schnack, *Dalton Trans.*, **39** (2010) 4677]

Geometrical frustration causes a variety of unusual magnetic phenomena in geometrical spin-frustrated molecular magnets, such as magnetization plateaus [60, 61] and magnetization jumps [62]. Because of the molecular origin of these systems, the frustration effect can be studied within a quasi-zero-dimensional nanoscale level, which is impossible for the traditional infinite frustrated systems. Molecular magnetism has greatly extended the understanding to geometrical spin frustration, from the synthesis of new model systems to the fundamental theoretical analysis. Some important concepts, such as localized independent magnons [56], developed in geometrical molecular magnets have proven to be universal for other frustrated systems.

1.3 Scope of this Thesis

In this thesis, I report the results of magnetization, magnetic susceptibility, heat capacity and neutron scattering measurements on two molecular magnets $\{Mo_{72}Fe_{30}\}$ and $\{As_6V_{15}\}$, and a newly-discovered antiferromagnetic pyrochlore magnet $Na_3Co(CO_3)_2Cl$. This research allows the effects of geometrical frustration and the collective behavior of interacting spins to be investigated from the quasi-zero-dimensional magnetic molecules to the infinite 3D pyrochlore lattice.

In Chapter 2, an introduction to the *xyz*-difference method with polarized neutrons is given. This method is essential for the polarized neutron scattering technique, which is the major probe used in this thesis.

Chapter 3 discusses the heat capacity and polarized neutron scattering of $\{Mo_{72}Fe_{30}\}$ in detail. The analysis of experiments is compared to the theoretical predictions within the frustrated three-sublattice spin model for this system. The calculation of the short-range spin correlations in this chapter may have general significance for the analysis on similar spin structures.

In Chapter 4, the magnetization, heat capacity and polarized neutron scattering results of $\{As_6V_{15}\}$ are presented. The low-lying magnetic excitations revealed in heat capacity are compared to the inelastic neutron scattering spectra and the theoretical prediction based on the three-spin model for $\{As_6V_{15}\}$.

Chapter 5 presents an extensive investigation of antiferromagnetic pyrochlore $Na_3Co(CO_3)_2Cl$. The crystal structure is determined using x-ray and neutron powder diffraction measurements. Static and dynamic magnetic measurements reveal novel magnetic behavior in this system. Short-range spin correlations and spin-wave-like excitations measured from neutron scattering measurements are analyzed and give an insight to the interesting spin dynamics of this system.

CHAPTER 2:

XYZ-Difference Method with Polarized Neutrons

2.1 Introduction

Neutrons are neutral particles with a nuclear spin 1/2 and a magnetic moment of μ = -1.91 μ_N, where μ_N is the nuclear magneton. The kinetic energy of neutrons is given by [63, 64]

$$\begin{aligned} E = k_B T = \frac{mv^2}{2} = \frac{\hbar^2 k^2}{2m} = \frac{h^2}{2m\lambda^2} \\ = 0.0862T = 5.227v^2 = 2.072k^2 = \frac{81.81}{\lambda^2} \end{aligned} \tag{2.1.1}$$

where E is in meV, T is in K, v is the velocity of neutrons and in km/s, k is the module of wavevector in Å^{-1}, λ is neutron wavelength in Å. Given an equivalent temperature T of ~ 300 K, the neutron wavelength λ is around 1.8 Å and the kinetic energy of neutrons is about 26 meV, which approximately match the atomic spacing and elementary excitations in most materials, respectively. These properties make neutron scattering a powerful and direct probe for studying the static and dynamic properties of materials on an atomic scale in many scientific fields [65, 66].

Neutrons for research purpose are released from nuclei through either fission or spallation nuclear reaction, as shown in **Figure 2-1-1**. In nuclear fission, a ^{235}U nucleus absorbs a thermal neutron and is thereby highly excited. The excited nucleus fissions into lighter nuclei, simultaneously releasing 2 or 3 highly energetic fast fission neutrons, which, after moderation to thermal energies by collisions with light nuclei, can cause the fission of other nuclei and start the so-called chain reaction. Another way to produce free neutrons is the spallation reaction. In spallation reaction, highly energetic protons with energies of ~ 1 GeV hit the target of heavy nuclei. The target nuclei are highly excited as a result of the so-called intranuclear cascade and "evaporate" neutrons and protons, which in turn can cause the spallation reactions of other nuclei [67, 68].

The neutrons obtained from fission reaction have typical energies of several MeV, while those from spallation reaction may have energies up to 1 GeV. They must be cooled down in moderators in order to acquire the desired energies prior to being used in scattering research. The thermal neutrons coming out from a heavy water moderator have a characteristic energy of 25 meV, and the energy of cold neutrons

from a liquid-hydrogen moderator is about 2 meV. Both thermal neutrons and cold neutrons are used in this thesis.

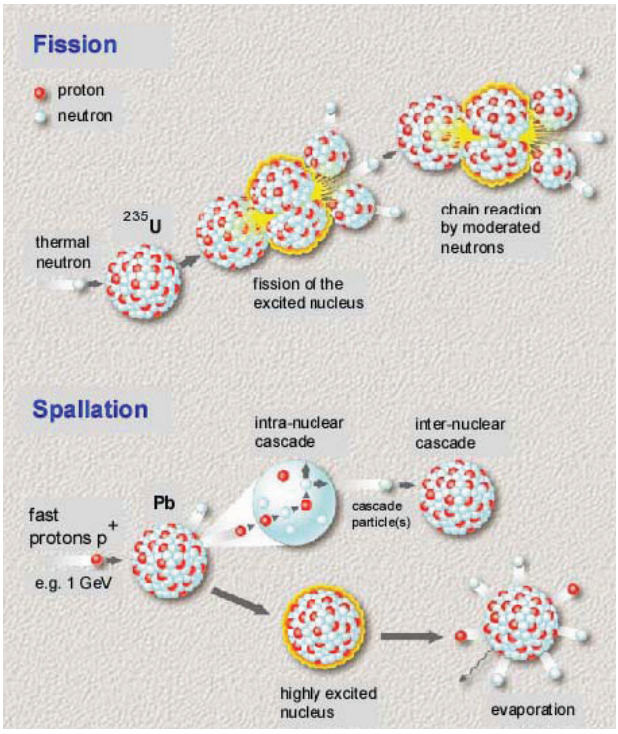

Figure 2-1-1 Schematic presentation of fission and spallation reactions. [Picture taken from D. Richter, *Scattering Techniques: Neutron Diffraction* in "*Magnetism Goes Nano: Lectures of the 36th Spring School of the Institute of Solid State Research*", S. Blügel, Th. Brückel, C. M. Schneider (eds.), (Forschungszentrum Jülich GmbH, Jülich 2005)]

In neutron scattering events, taking into account the conservation of momentum and energy, the double differetial cross section can be derived as [63, 64],

$$\frac{d^2\sigma}{d\Omega d\omega} = \left(\frac{m}{2\pi\hbar^2}\right)^2 \frac{k'}{k} \sum_{\alpha} p_\alpha \sum_{\alpha'} \left|\left\langle \boldsymbol{k}', \alpha' \middle| \hat{U} \middle| \boldsymbol{k}, \alpha \right\rangle\right|^2 \cdot \delta\left(\hbar\omega + E_\alpha - E_{\alpha'}\right). \qquad (2.1.2)$$

$\boldsymbol{k}$ and $\boldsymbol{k}'$ are the incident and outgoing wavevectors of neutrons. $|\alpha>$ and $|\alpha'>$ denote the initial and final states of the system, weighted with their thermodynamic occupation probability p_α and $p_{\alpha'}$, respectively. $\hat{U}$ is the operator for scattering potential between the neutrons and the target. The two main interaction processes of

neutrons with matter are nuclear and magnetic interaction.

The neutrons are scattered from nuclei by the strong-force interaction, whose range is very short and in the order of the nuclei diameter. Thus the scattering potential can be represented by the "Fermi Pseudopotential":

$$\hat{\boldsymbol{U}} = \frac{2\pi\hbar^2}{m}\sum_j b_j \delta\left(\boldsymbol{r} - \hat{\boldsymbol{r}}_j\right). \tag{2.1.3}$$

Here $\boldsymbol{r}_j$ is the position of the j^{th} scattering nucleus in the sample and b_j is the corresponding scattering length. Considering the plane wave function for neutrons, the double differential cross section can then be expressed by inserting Eq. (2.1.3) into Eq. (2.1.2), as

$$\begin{aligned}\frac{d^2\sigma}{d\Omega d\omega} &= \frac{k'}{k}\sum_\alpha p_\alpha \sum_{\alpha'}\left|\left\langle \alpha'\left|\sum_j b_j e^{i\boldsymbol{Q}\cdot\hat{\boldsymbol{r}}_j}\right|\alpha\right\rangle\right|^2 \cdot \delta\left(\hbar\omega + E_\alpha - E_{\alpha'}\right) \\ &= \frac{1}{2\pi\hbar}\frac{k'}{k}\sum_{jj'} b_j b_{j'}\int e^{-iwt}dt \sum_\alpha p_\alpha \left\langle \alpha\left| e^{-i\boldsymbol{Q}\cdot\hat{\boldsymbol{r}}_{j'}} e^{i\hat{H}t/h} e^{i\boldsymbol{Q}\cdot\hat{\boldsymbol{r}}_j} e^{-i\hat{H}t/h}\right|\alpha\right\rangle. \\ &= \frac{1}{2\pi\hbar}\frac{k'}{k}\sum_{jj'} b_j b_{j'}\int \left\langle e^{-i\boldsymbol{Q}\cdot\hat{\boldsymbol{r}}_{j'}(0)} e^{i\boldsymbol{Q}\cdot\hat{\boldsymbol{r}}_j(t)}\right\rangle e^{-iwt}dt\end{aligned} \tag{2.1.4}$$

H is the Hamiltonian of the scattering system. It is convenient to write Eq. (2.1.4) as

$$\frac{d^2\sigma}{d\Omega d\omega} = \frac{\sigma}{4\pi}\frac{k'}{k} NS\left(\boldsymbol{Q},\omega\right), \tag{2.1.5}$$

where $S(\boldsymbol{Q}, \omega)$ is the dynamic structure factor and is given by

$$S\left(\boldsymbol{Q},\omega\right) = \frac{1}{2\pi\hbar}\int G\left(\boldsymbol{r},t\right) e^{i(\boldsymbol{Q}\cdot\boldsymbol{r}-\omega t)} d\boldsymbol{r}dt\,. \tag{2.1.6}$$

Therefore, $S(\boldsymbol{Q}, \omega)$ is the Fourier transform of the pair correlation function

$$G\left(\boldsymbol{r},t\right) = \left(\frac{1}{2\pi}\right)^3 \frac{1}{N}\int \sum_{jj'} e^{-i\boldsymbol{Q}\cdot\boldsymbol{r}} \left\langle e^{-i\boldsymbol{Q}\cdot\hat{\boldsymbol{r}}_{j'}(0)} e^{i\boldsymbol{Q}\cdot\hat{\boldsymbol{r}}_j(t)}\right\rangle d\boldsymbol{Q} \tag{2.1.7}$$

with respect to space and time. This is the basis of the theoretical simulations of polarized neutron scattering in this thesis.

The nuclear magnetic moment associated with spin of the neutrons allows them to interact with the magnetic moment of unpaired elections in the target. The magnetic

interaction operator is given by

$$\begin{aligned}\hat{\boldsymbol{U}} &= -\hat{\boldsymbol{\mu}}\cdot\boldsymbol{B} = -\gamma\mu_N\hat{\boldsymbol{\sigma}}_{\mathrm{N}}\cdot\boldsymbol{B} \\ &= \gamma\mu_{\mathrm{N}}\left\{2\mu_{\mathrm{B}}\hat{\boldsymbol{\sigma}}_{\mathrm{N}}\cdot\nabla\times\left(\frac{\hat{\boldsymbol{s}}\times\boldsymbol{r}}{|\boldsymbol{r}|^3}\right)+\frac{e}{c}\hat{\boldsymbol{\sigma}}_{\mathrm{N}}\cdot\left(\frac{\boldsymbol{v}_e\times\boldsymbol{r}}{|\boldsymbol{r}|^3}\right)\right\},\end{aligned} \tag{2.1.8}$$

where γ = -1.913 is the gyromagnetic ratio, $\hat{\boldsymbol{\sigma}}_{\mathrm{N}}$ are the Pauli spin matrices for the neutron spin, $\hat{\boldsymbol{s}}$ is the electron spin operator, μ_{B} is the Bohr magneton and $\boldsymbol{v}_{\mathrm{e}}$ is the velocity of electron. Using Eq. (2.1.2) and Eq. (2.1.8), the double differential cross section for magnetic scattering of unpolarized neutrons by localized spins can be given as follows,

$$\left(\frac{d^2\sigma}{d\Omega d\omega}\right)_{\mathrm{mag}} = \frac{k'}{k}\left(\gamma r_0\frac{g}{2}F(\boldsymbol{Q})e^{-W}\right)^2\sum_{\alpha\beta}\left(\delta_{\alpha\beta}-\hat{Q}_\alpha\hat{Q}_\beta\right)S^{\alpha\beta}(\boldsymbol{Q},\omega), \tag{2.1.9}$$

where r_0 = 0.2818·10^{-12} cm is the classical radius of the election, g is the Landé splitting factor, $F(Q)$ is the magnetic form factor, and e^{-W} is the Debye-Waller factor due to the thermal fluctuations of the magnetic ions. The dynamic magnetic structure factor $S^{\alpha\beta}(\boldsymbol{Q}, \omega)$ is the Fourier transform of the magnetic pair correlation function and is given by

$$S^{\alpha\beta}(\boldsymbol{Q},\omega) = \frac{1}{2\pi\hbar}\sum_{jj'}\int\left\langle\hat{S}_{j'\alpha}(0)\hat{S}_{j\beta}(t)\right\rangle\left\langle e^{-i\boldsymbol{Q}\cdot\hat{\boldsymbol{r}}_{j'}(0)}e^{i\boldsymbol{Q}\cdot\hat{\boldsymbol{r}}_j(t)}\right\rangle e^{-i\omega t}dt\,. \tag{2.1.10}$$

2.2 Theory of *XYZ*-Difference Method Using Polarized Neutrons

The *xyz*-difference method using polarized neutrons is a powerful technique in the sense that various scattering contributions (i.e., nuclear coherent, spin-incoherent and magnetic scattering) can be distinguished simultaneously and unambiguously. This method is particularly important for the research in this thesis, because the magnetic neutron scattering from spin-frustrated molecular magnets are normally too weak to be extracted directly from unpolarized neutron scattering.

The early theoretical foundation for polarized neutron scattering has been set by the works of Halpen and Johnson [69], Maleyev [70], and Blume [71]. The first

neutron scattering measurements with polarization analysis were performed by Moon, Riste and Koehler in 1969 [72]. The surveys on the *xyz*-difference method with polarized neutrons have been given by Schärpf and Capellmann [73] and Brückel [74].

The discussion in this section will be restricted to the case of a multi-detector instrument like what is shown in **Figure 2-2-1** [73]. The multidetectors and the incident beam define the scattering plane (i.e., *x*-*y* plane), which makes the scattering vector $\boldsymbol{Q}$ always perpendicular to the *z* direction. The measurements are performed with the incident polarization alternately in the *x*, *y*, and *z* directions with spin-flip and non-spin-flip. The neutrons go out from the monochromator, and pass through the beryllium filter, the polarizer, the flipper, and the chopper, to the sample in the cryostat. There they are scattered by the sample and go through the guide fields and arrive at the analyzers and detectors.

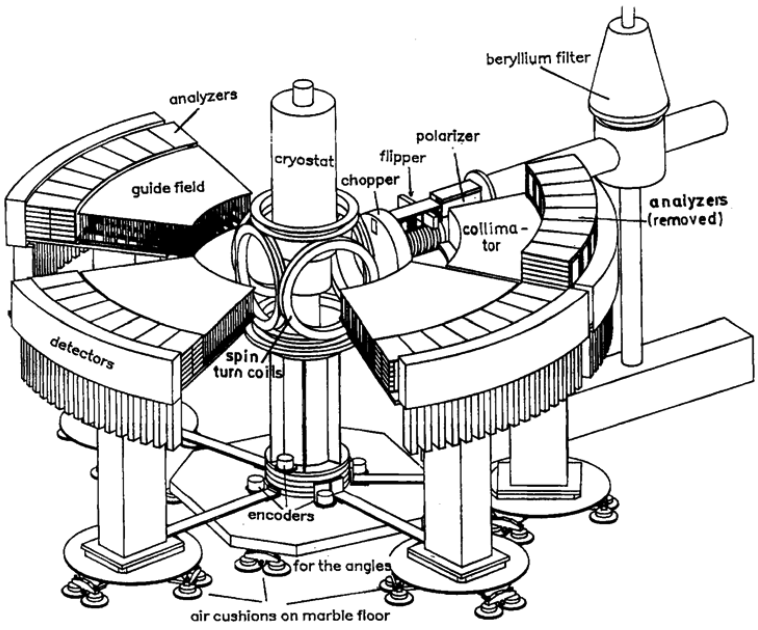

Figure 2-2-1 Schematic view of multipurpose spectrometer D7 of the Institute Laue-Langevin in Grenoble. [Picture taken from O. Schärpf and H. Capellmann, *Phys. Stat. Sol.* (a) **135** (1993) 359]

For polarized neutrons, the double differential scattering cross section is [73]

$$\left(\frac{d^2\sigma}{d\Omega d\omega}\right)_{ss'} = \left(\frac{m}{2\pi\hbar^2}\right)^2 \frac{k'}{k}\sum_{\alpha\alpha'} p_\alpha \left|\left\langle \boldsymbol{k's'},\alpha'\middle|\hat{V}\middle|\boldsymbol{ks},\alpha\right\rangle\right|^2 \cdot \delta\left(\hbar\omega + E_\alpha - E_{\alpha'}\right), \quad (2.2.1)$$

where quantum numbers without prime belong to the initial states and those with prime belong to the final states, $\boldsymbol{k}$, $\boldsymbol{s}$ are wave vector and quantum numbers of the neutron, α is the quantum number of the sample. The magnetization density of electrons $\boldsymbol{M}_e(\boldsymbol{r})$ in the sample interacts with the dipolar field $\boldsymbol{B}_n(\boldsymbol{r})$ of the neutrons, resulting in magnetic scattering. The magnetic interaction operator is $\hat{V} = \hat{\boldsymbol{M}}_e(\boldsymbol{r})\cdot\boldsymbol{B}_n(\boldsymbol{r})/4\pi\mu_B$. The matrix element $\left\langle \boldsymbol{k}'\middle|\hat{\boldsymbol{M}}_e(\boldsymbol{r})\cdot\boldsymbol{B}_n(\boldsymbol{r})\middle|\boldsymbol{k}\right\rangle$ has been given by [73]

$$\left\langle \boldsymbol{k}'\middle|\hat{\boldsymbol{M}}_e(\boldsymbol{r})\cdot\boldsymbol{B}_n(\boldsymbol{r})\middle|\boldsymbol{k}\right\rangle = \hat{\boldsymbol{M}}_e(\boldsymbol{r})\cdot\frac{\hat{\boldsymbol{Q}}}{Q}\times\left(\hat{\boldsymbol{\mu}}_n\times\frac{\hat{\boldsymbol{Q}}}{Q}\right)e^{i\boldsymbol{Q}\cdot\boldsymbol{r}} = \hat{\boldsymbol{M}}_e(\boldsymbol{r})\cdot\hat{\boldsymbol{\mu}}_{n\perp}e^{i\boldsymbol{Q}\cdot\boldsymbol{r}}. \quad (2.2.2)$$

Defining the polarization as a vector with $\boldsymbol{P} = (P_x, P_y, P_z) = P_x\boldsymbol{e}_x + P_y\boldsymbol{e}_y + P_z\boldsymbol{e}_z$, the magnitude of $\boldsymbol{P}$ is normally expressed as $|\boldsymbol{P}| = (n_\uparrow - n_\downarrow)/(n_\uparrow + n_\downarrow)$, where $n_\uparrow$ and $n_\downarrow$ are the numbers of neutrons with spin-up and spin-down.

The spin-flip and non-spin-flip magnetic cross sections for the *xyz*-polarization analysis have been given by Schärpf and Capellmann [73]. For non phase shifted part,

$$\begin{pmatrix}\Gamma^x_{\uparrow\downarrow}(\boldsymbol{r},\omega)\\ \Gamma^y_{\uparrow\downarrow}(\boldsymbol{r},\omega)\\ \Gamma^z_{\uparrow\downarrow}(\boldsymbol{r},\omega)\\ \Gamma^x_{\uparrow\uparrow}(\boldsymbol{r},\omega)\\ \Gamma^y_{\uparrow\uparrow}(\boldsymbol{r},\omega)\\ \Gamma^z_{\uparrow\uparrow}(\boldsymbol{r},\omega)\end{pmatrix} = \begin{pmatrix}\sin^2\alpha\cos^2\alpha & \cos^4\alpha & 1 & -\sin\alpha\cos^3\alpha\\ \sin^4\alpha & \sin^2\alpha\cos^2\alpha & 1 & -\sin^3\alpha\cos\alpha\\ \sin^2\alpha & \cos^2\alpha & 0 & -\sin\alpha\cos\alpha\\ \sin^4\alpha & \sin^2\alpha\cos^2\alpha & 0 & -\sin^3\alpha\cos\alpha\\ \sin^2\alpha\cos^2\alpha & \cos^4\alpha & 0 & -\sin\alpha\cos^3\alpha\\ 0 & 0 & 1 & 0\end{pmatrix}\begin{pmatrix}M_{xx}(\boldsymbol{r},\omega)\\ M_{yy}(\boldsymbol{r},\omega)\\ M_{zz}(\boldsymbol{r},\omega)\\ M_{xy}(\boldsymbol{r},\omega)+M_{yx}(\boldsymbol{r},\omega)\end{pmatrix} \quad (2.2.3)$$

and for the phase shifted part,

$$\begin{pmatrix}\Gamma^x_{\uparrow\downarrow}(\boldsymbol{r},\omega)\\ \Gamma^x_{\downarrow\uparrow}(\boldsymbol{r},\omega)\\ \Gamma^y_{\uparrow\downarrow}(\boldsymbol{r},\omega)\\ \Gamma^y_{\downarrow\uparrow}(\boldsymbol{r},\omega)\end{pmatrix} = \begin{pmatrix}-\sin\alpha\cos\alpha & -\cos^2\alpha\\ \sin\alpha\cos\alpha & \cos^2\alpha\\ \sin^2\alpha & -\cos\alpha\sin\alpha\\ -\sin^2\alpha & \cos\alpha\sin\alpha\end{pmatrix}\begin{pmatrix}M_{zx}(\boldsymbol{r},\omega)-M_{xz}(\boldsymbol{r},\omega)\\ M_{zy}(\boldsymbol{r},\omega)-M_{yz}(\boldsymbol{r},\omega)\end{pmatrix} \quad (2.2.4)$$

where $M_{\alpha\beta}(\boldsymbol{r},\omega)$ ($\alpha, \beta = x, y, z$) are the thermal and quantum mechanical average of

the corresponding correlation functions, and $\Gamma^{\alpha}_{ss'}(\boldsymbol{r}, \omega)$ ($\alpha = x, y, z$ and $s, s' = |\downarrow\rangle, |\uparrow\rangle$) is the time Fourier transform of correlation functions.

For a powder measurement, the mixed correlation functions are zero. Therefore the phase-shifted parts are all zero and only the first three columns of the non-phase-shifted parts still remain for presenting the spin-flip and non-spin-flip magnetic cross sections. Define the double differential cross section as following

$$\frac{\partial^2\sigma^{\alpha}_{ss'}}{\partial\Omega\partial\omega} = \frac{k'}{k}\left(\frac{r_0\gamma}{2}\right)^2 F^2(\boldsymbol{Q}) S^{\alpha}_{ss'}(\boldsymbol{Q},\omega) \tag{2.2.5}$$

where $S^{\alpha}_{ss'}(\boldsymbol{Q},\omega)$ is the space Fourier transform of the function $\Gamma^{\alpha}_{ss'}(\boldsymbol{Q},\omega)$. The corresponding expressions for different scattering components are

$$\frac{\partial^2\sigma_{para}}{\partial\Omega\partial\omega} = \frac{k'}{k}\frac{2}{3}\left(\frac{r_0\gamma}{2}\right)^2 F^2(\boldsymbol{Q}) M(\boldsymbol{Q},\omega), \tag{2.2.6}$$

$$\frac{\partial^2\sigma^{spin}_{incoh}}{\partial\Omega\partial\omega} = \frac{k'}{k} B^2 S_{incoh}(\boldsymbol{Q},\omega), \tag{2.2.7}$$

$$\frac{\partial^2\sigma_{coh}}{\partial\Omega\partial\omega} = \frac{k'}{k} b^2 S_{coh}(\boldsymbol{Q},\omega), \tag{2.2.8}$$

with B being the magnetic field of the electrons and b being the nuclear scalar contribution. Combining Eqs. (2.2.3) and (2.2.6-8), the six partial cross sections obtained from the measurements with polarization in x, y and z directions in both spin-flip and non-spin-flip channels are expressed as following [73]

$$\frac{\partial^2\sigma^{x}_{\uparrow\downarrow}}{\partial\Omega\partial\omega} = \frac{1}{2}\frac{\partial^2\sigma_{para}}{\partial\Omega\partial\omega}\left(\cos^2\alpha + 1\right) + \frac{2}{3}\frac{\partial^2\sigma^{spin}_{incoh}}{\partial\Omega\partial\omega} \tag{2.2.9}$$

$$\frac{\partial^2\sigma^{y}_{\uparrow\downarrow}}{\partial\Omega\partial\omega} = \frac{1}{2}\frac{\partial^2\sigma_{para}}{\partial\Omega\partial\omega}\left(\sin^2\alpha + 1\right) + \frac{2}{3}\frac{\partial^2\sigma^{spin}_{incoh}}{\partial\Omega\partial\omega} \tag{2.2.10}$$

$$\frac{\partial^2\sigma^{z}_{\uparrow\downarrow}}{\partial\Omega\partial\omega} = \frac{1}{2}\frac{\partial^2\sigma_{para}}{\partial\Omega\partial\omega} + \frac{2}{3}\frac{\partial^2\sigma^{spin}_{incoh}}{\partial\Omega\partial\omega} \tag{2.2.11}$$

$$\frac{\partial^2\sigma^{x}_{\uparrow\uparrow}}{\partial\Omega\partial\omega} = \frac{1}{2}\frac{\partial^2\sigma_{para}}{\partial\Omega\partial\omega}\sin^2\alpha + \frac{1}{3}\frac{\partial^2\sigma^{spin}_{incoh}}{\partial\Omega\partial\omega} + \frac{\partial^2\sigma_{coh}}{\partial\Omega\partial\omega} + \frac{\partial^2\sigma^{isotop}_{incoh}}{\partial\Omega\partial\omega} \tag{2.2.12}$$

$$\frac{\partial^2\sigma^{y}_{\uparrow\uparrow}}{\partial\Omega\partial\omega}=\frac{1}{2}\frac{\partial^2\sigma_{para}}{\partial\Omega\partial\omega}\cos^2\alpha+\frac{1}{3}\frac{\partial^2\sigma^{spin}_{incoh}}{\partial\Omega\partial\omega}+\frac{\partial^2\sigma_{coh}}{\partial\Omega\partial\omega}+\frac{\partial^2\sigma^{isotop}_{incoh}}{\partial\Omega\partial\omega} \tag{2.2.13}$$

$$\frac{\partial^2\sigma^{z}_{\uparrow\uparrow}}{\partial\Omega\partial\omega}=\frac{1}{2}\frac{\partial^2\sigma_{para}}{\partial\Omega\partial\omega}+\frac{1}{3}\frac{\partial^2\sigma^{spin}_{incoh}}{\partial\Omega\partial\omega}+\frac{\partial^2\sigma_{coh}}{\partial\Omega\partial\omega}+\frac{\partial^2\sigma^{isotop}_{incoh}}{\partial\Omega\partial\omega}. \tag{2.2.14}$$

From the above expressions for the measured cross sections, one can separate the nuclear coherent, spin-incoherent and magnetic cross sections simultaneously. The magnetic cross section can be extracted from measurements in either spin-flip channels by

$$\frac{\partial^2\sigma_{para}}{\partial\Omega\partial\omega}=2\left(\frac{\partial^2\sigma^{x}_{\uparrow\downarrow}}{\partial\Omega\partial\omega}+\frac{\partial^2\sigma^{y}_{\uparrow\downarrow}}{\partial\Omega\partial\omega}-2\frac{\partial^2\sigma^{z}_{\uparrow\downarrow}}{\partial\Omega\partial\omega}\right), \tag{2.2.15}$$

or non-spin-flip channels by

$$\frac{\partial^2\sigma_{para}}{\partial\Omega\partial\omega}=2\left(2\frac{\partial^2\sigma^{z}_{\uparrow\uparrow}}{\partial\Omega\partial\omega}-\frac{\partial^2\sigma^{x}_{\uparrow\uparrow}}{\partial\Omega\partial\omega}-\frac{\partial^2\sigma^{y}_{\uparrow\uparrow}}{\partial\Omega\partial\omega}\right). \tag{2.2.16}$$

The magnetic differential cross section is often taken as the average of Eq. (2.2.15) and (2.2.16) to account for the systematic errors in actual measurements.

The spin-incoherent and nuclear coherent scattering cross sections can be obtained by the following expressions:

$$\frac{\partial^2\sigma^{spin}_{incoh}}{\partial\Omega\partial\omega}=\frac{3}{2}\left(3\frac{\partial^2\sigma^{z}_{\uparrow\downarrow}}{\partial\Omega\partial\omega}-\frac{\partial^2\sigma^{x}_{\uparrow\downarrow}}{\partial\Omega\partial\omega}-\frac{\partial^2\sigma^{y}_{\uparrow\downarrow}}{\partial\Omega\partial\omega}\right), \tag{2.2.17}$$

$$\frac{\partial^2\sigma_{coh}}{\partial\Omega\partial\omega}+\frac{\partial^2\sigma^{isotop}_{incoh}}{\partial\Omega\partial\omega}=\frac{\partial^2\sigma^{z}_{\uparrow\uparrow}}{\partial\Omega\partial\omega}-\frac{1}{2}\frac{\partial^2\sigma_{para}}{\partial\Omega\partial\omega}-\frac{1}{3}\frac{\partial^2\sigma^{spin}_{incoh}}{\partial\Omega\partial\omega}. \tag{2.2.18}$$

With the help of polarization analysis, the magnetic contribution can be identified and distinguished from other contributions. Polarization analysis is particularly useful in improving the magnetic signal to background ratio if the moments and magnetic scattering are weak. Furthermore, the polarization analysis can be used to study the so-called q = 0 antiferromagnetic structure, whose magnetic peak positions coincide with the nuclear Bragg peaks and are difficult to be identified with unpolarized neutron scattering [75, 76].

CHAPTER 3:

Geometrical Spin-frustrated Molecular Magnet $\{Mo_{72}Fe_{30}\}$

3.1 Introduction

Since the discovery of Mn_{12}-acetate in the beginning of the 1990's, most efforts in the field of molecular magnetism have been dedicated to synthesize molecular magnets with high-spin ground states and high molecular magnetic anisotropy which result in the magnetic hysteresis effect in some single-molecule magnets [2, 10]. Because of the difficulty in increasing the effective energy barrier significantly, the field of molecular magnetism is branching out into new areas to explore promising molecular-based systems of attractive physical properties. These systems provide valuable test beds for nano science from both experimental and theoretical points of view [23]. Polyoxometalate molecular magnets are the largest known structurally well-defined molecular cluster species, frequently comprising highly symmetric spin arrays. Via bottom-up construction strategies, impressive polyoxometalate nanostructures can be synthesized on the basis of well-defined pentagonal building blocks [23, 27]. Spherical Keplerate molecule of the type $\{(Mo)Mo_5\}_{12}M_{30}$ (M = Fe, Cr, V) localises 30 transition metal M spins and is well isolated from neighboring molecules by ligands. The geometrical arrangement of the 30 spins in such a molecule consists of a regular arrangement of corner sharing spin triangles and spin pentagons, and can be described as a molecular analogue of a kagome lattice on the surface of a sphere. When the nearest neighbors are antiferromagnetically coupled, spin frustration occurs. This family of polyoxometalates is thus an ideal test bed for the geometrical spin frustration in finite-sized systems.

3.1.1 Introduction to Molecular Magnet {$Mo_{72}Fe_{30}$}

As one of the largest polyoxomolybdate molecular magnets synthesized to date, $[Mo_{72}Fe_{30}O_{252}(CH_3COO)_{12}\{Mo_2O_7(H_2O)\}_2\{H_2Mo_2O_8(H_2O)\}(H_2O)_{91}]\cdot 150H_2O$, {$Mo_{72}Fe_{30}$} for short, represents a highly frustrated spin system and provides us with a molecular analogue of the planar Kagome lattice [23]. The ball-and-stick representation of one {$Mo_{72}Fe_{30}$} molecule is shown in **Figure 3-1-1**.

30 Fe^{3+} (s = 5/2, L = 0) ions serve as magnetic centers and occupy the vertices of an icosidodecahedron. –O–Mo–O– fragments act as effective superexchange pathways between Fe^{3+} ions [23, 54, 55]. The 30 spins form 20 corner-sharing triangles

(highlighted in **Figure 3-1-1**) grouped around the 12 regular pentagonal {(Mo)Mo_5} building blocks. Low-field magnetic susceptibility shows dominant antiferromagnetic coupling between the nearest neighbors (see Ref. [55] and also Section 3.2), indicating spin frustration should arise.

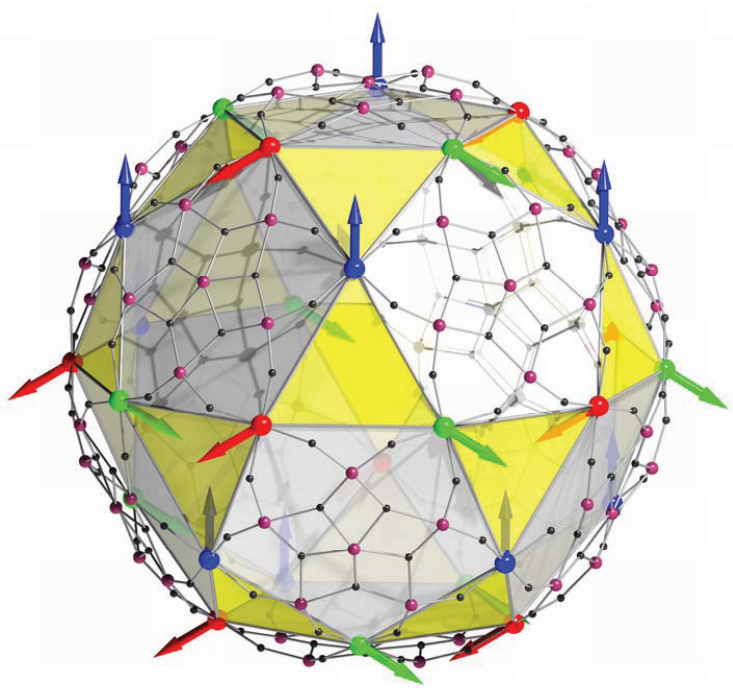

Figure 3-1-1 Ball-and-stick representation of one {$Mo_{72}Fe_{30}$} molecule (Fe: red, green, blue spheres; Mo: purple spheres; O: black spheres; C, H: not shown). The arrows (red, green, blue) denote the classical spin vectors within the frustrated three-sublattice spin model (see Section 3.1.2 for details). Twenty Fe^{3+} triangles are highlighted in yellow. [Picture taken from P. Kögerler, B. Tsukerblat and Achim Müller, *Dalton Trans.* **39** (2010) 21]

3.1.2 Three-sublattice Spin Model and Quantum Rotational Band Theory

The iron ions are located in regular octahedral $Fe^{3+}O_6$ coordination environments, leading to negligible local spin anisotropy. The Fe^{3+} ions are linked by nearly planar pentagonal fragments {(Mo)Mo_5} [55]. As shown in **Figure 3-1-2**, the magnetic exchange interactions between nearest-neighboring Fe^{3+} ions are transmitted via -O-Mo-O- bridges, whereas the next-nearest-neighbor superexchange interactions go

through -O-Mo-O-Mo-O- bridges and are estimated to be at least two orders of magnitude smaller by means of density functional theory calculation and thus negligible [23, 78]. Therefore I can safely assume the intramolecular exchange interactions are restricted among the nearest neighbors. The magnetic properties of {$Mo_{72}Fe_{30}$} can then be described by the isotropic Heisenberg model with a single exchange constant *J*, neglecting the anisotropy term [55],

$$\hat{\boldsymbol{H}} = J \sum_{<i,j>} \hat{\boldsymbol{S}}_i \cdot \hat{\boldsymbol{S}}_j + g\mu_B \boldsymbol{B} \cdot \sum_i \hat{\boldsymbol{S}}_i \,, \tag{3.1.1}$$

where $\hat{\boldsymbol{S}}_i$ and $\hat{\boldsymbol{S}}_j$ are spin operators in units of $\hbar$, $\boldsymbol{B}$ is the external field, g is the spectroscopic splitting factor, μ_B is the Bohr magneton, J is the exchange constant for nearest-neighbor coupling and found to be about 0.134 meV through a mean-field simulation approach, indicating antiferromagnetic exchange interaction [55].

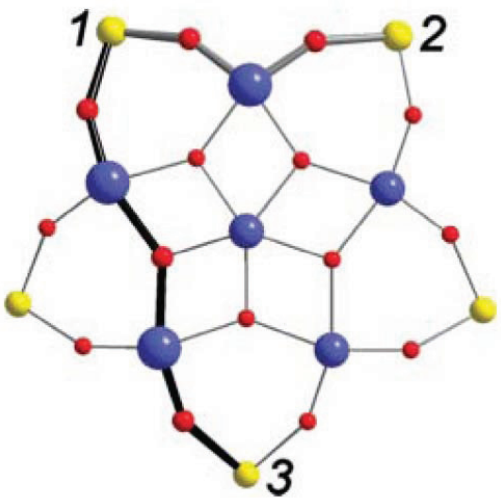

Figure 3-1-2 Five Fe^{3+} ions (yellow) connected by a pentagonal {(Mo)Mo5} group (blue: Mo; red: O). The superexchange pathways, -O-Mo-O- between nearest neighbors *1-2* and -O-Mo-O-Mo-O- between next-nearest neighbors *1-3*, are emphasized. [Picture taken from P. Kögerler, B. Tsukerblat and Achim Müller, *Dalton Trans.* **39** (2010) 21]

Approximate approaches must be taken to establish a spin model describing the way how spins arrange on the surface of this highly symmetric structure, because the

total dimension of Hilbert space of this spin system is $(2S+1)^{30} = 6^{30}$, which is astronomically large so that the complete matrix diagonalization of Hamiltonian (3.1.1) is not feasible for now. Despite this difficulty, an approximate, diagonalizable effective Hamiltonian was adopted to explain the major low-temperature properties of $\{Mo_{72}Fe_{30}\}$ [79]. The classical version of this effective Hamiltonian represents a frustrated ground state spin configuration called the "three-sublattice model", where the 30 spins can be grouped into three sublattices of 10 spins each. All the 10 spins in each sublattice are parallel and the unit vectors of the three sublattices are co-planar with 120˚ angular difference in the zero-field limit. Here the word "co-planar" means one can always find a plane parallel to all the unit vectors of the three sublattices. The sketch map of this model is shown in **Figure 3-1-1**, where the vectors of the three sublattices are indicated by red, yellow and green colors. Obviously, there are no nearest neighbors carrying the same color.

Corresponding to this classical three-sublattice configuration, the approximate quantum model was established to account for the quantum mechanical effects. The resulting effective Hamiltonian is reduced to interactions between the three sublattices with spin operators $\hat{\boldsymbol{S}}_{\mathbf{A}}$, $\hat{\boldsymbol{S}}_{\mathbf{B}}$ and $\hat{\boldsymbol{S}}_{\mathbf{C}}$, and adopted with the absence of an external magnetic field and the spin anisotropy term [23, 79, 80], which is written as

$$\hat{\boldsymbol{H}}_{\text{eff}} = \frac{J}{5}(\hat{\boldsymbol{S}}_{\text{A}} \cdot \hat{\boldsymbol{S}}_{\text{B}} + \hat{\boldsymbol{S}}_{\text{B}} \cdot \hat{\boldsymbol{S}}_{\text{C}} + \hat{\boldsymbol{S}}_{\text{C}} \cdot \hat{\boldsymbol{S}}_{\text{A}}) . \tag{3.1.2}$$

Accordingly, the energy eigenvalues of Hamiltonian (3.1.2) are given in Ref. [79]

$$E(S) = \frac{J}{10}[S(S+1) - S_{\text{A}}(S_{\text{A}}+1) - S_{\text{B}}(S_{\text{B}}+1) - S_{\text{C}}(S_{\text{C}}+1)], \tag{3.1.3}$$

where S_A, S_B, S_C are the spin quantum numbers of the three sublattices ($0 \le S_{A,B,C} \le 25$), S is the total spin quantum number ($0 \le S \le 75$), the exchange constant J is ~ 0.134 meV determined from the magnetization measurements on $\{Mo_{72}Fe_{30}\}$ [55, 79]. The degeneracies of the ground state ($S_A = S_B = S_C = 25$) and the first excited state ($S_A = 24$, $S_B = S_C = 25$ and the permutations) are $(2S+1)^2$ and $27(2S+1)^2$, respectively [81].

The resultant low-lying energy spectrum is shown in **Figure 3-1-3**, where S is the total spin quantum number. From the expression of Eq. (3.1.3), it is known that the resultant S states form a parabola for one set of S_A , S_B and S_C. The effect of an external field appears as a Zeeman term in the Hamiltonian, which lifts the degeneracies of the individual M_S = -S, …, +S substates belonging to an S state.

Spin-level-crossing will happen upon increasing the external field gradually from zero. Its positions are shown as the arrows in **Figure 3-1-4**. Eventually the system will saturate in S = 75, M_S = 75 state at $B_{sat} = 30|J|/(g\mu_B)$ = 17.7 Tesla [23, 79, 80]. This saturation field was confirmed by the high-field magnetization at 0.46 K [55].

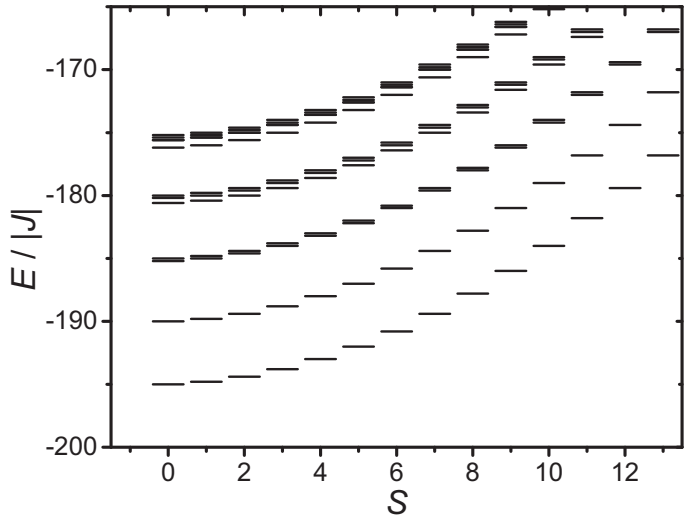

Figure 3-1-3 Low-lying section of the magnetic excitation spectrum as calculated from the quantum rotational band model.

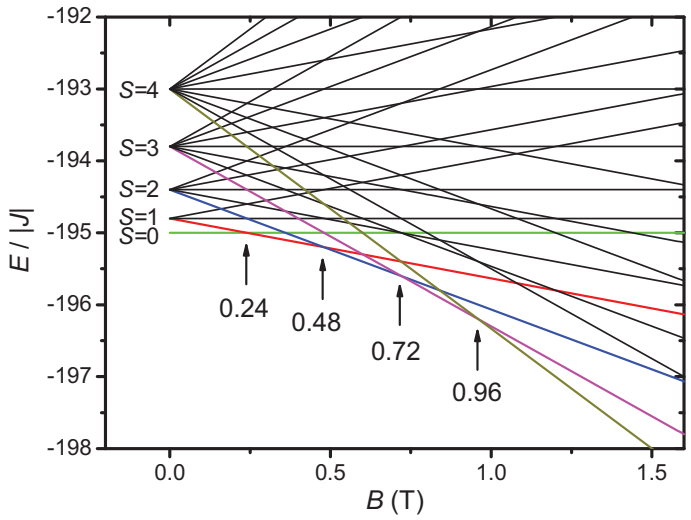

Figure 3-1-4 Splitting of the ground-state M_S sublevels under external magnetic field. Arrows mark where the spin-level-crossing happens.

Besides the high-field magnetization measurements, other techniques were also utilized to proof the validity of the three-sublattice model for {$Mo_{72}Fe_{30}$}. According to the quantum rotational band theory, the energy difference between the two lowest ground-state levels is only $|J|/5 \approx 0.03$ meV, which is very difficult to be observed experimentally. But the energy gaps between the ground state and the first excited state were directly confirmed to be ~ 0.6 meV by means of inelastic neutron scattering measurements [81]. The muon spin relaxation and ^1H nuclear magnetic resonance measurements provide further experimental determination of this first interband gap [82]. The differential susceptibility dM/dB of {$Mo_{72}Fe_{30}$} exhibits a local minimum at approximately one-third of B_{sat}, which is attributed to the thermal population of competing three-sublattice spin phases [61].

3.1.3 Motivation

{$Mo_{72}Fe_{30}$} possesses a complex, yet aesthetically beautiful molecular structure. The 30 spins with antiferromagnetic coupling between nearest neighbors provide a 3D and finite analog with periodic boundary conditions of the 2D kagome lattice, which makes {$Mo_{72}Fe_{30}$} a good model to investigate the phenomenon known as geometrical spin frustration. The three-sublattice model was developed not only for icosidodecahedron but also for some other types of polyhedral spin structures. The validity of the three-sublattice spin model for {$Mo_{72}Fe_{30}$} could be of more general significance for the studies on spin frustration in a variety of spin polyhedra. However, the aforementioned experimental support to the three-sublattice model remains indirect, since there have been no direct observations of the microscopic spin correlations resulting from the ground-state spin structure of the {$Mo_{72}Fe_{30}$} molecule.

In this chapter, an approach to the magnetic ground state of {$Mo_{72}Fe_{30}$} is attempted by a direct observation of the spin correlation function by means of polarized neutron scattering. The low-lying magnetic excitation spectrum predicted by the quantum rotational band theory is revealed using the low-temperature specific heat. The three-sublattice spin model for {$Mo_{72}Fe_{30}$} is thus strongly supported.

3.2 Magnetic Properties of {$Mo_{72}Fe_{30}$}

The magnetic susceptibility of {$Mo_{72}Fe_{30}$} was measured using a Superconducting Quantum Interference Device (SQUID) magnetometer (Quantum Design, San Diego). In this chapter, M/H is defined as the magnetic susceptibility, where M stands for the magnetization measured with the probing field H. **Figure 3-2-1** shows the magnetic susceptibility and the inverse susceptibility of {$Mo_{72}Fe_{30}$} measured from 2 K to 300 K under a probing field of 500 Oe. As seen in **Figure 3-2-1 (a)**, there is no sign of any magnetic phase transition. The molar magnetic susceptibility χ of a paramagnetic substance can be approximately described by [83]

$$\chi = \frac{N_A \mu_{eff}^{\ 2}}{3k_B T}, \tag{3.2.1}$$

where N_A is the Avogadro constant, k_B is the Boltzmann constant, μ_{eff} is the effective magnetic moment, the unit of χ is emu/mol/Oe, T is temperature in Kelvin. From Eq. (3.2.1), μ_{eff} can be determined by

$$\mu_{eff} = 2.828\sqrt{\chi T}\ . \tag{3.2.2}$$

The unit of the effective moment calculated from Eq. (3.2.2) is Bohr magneton μ_B. The temperature dependence of the product of magnetic susceptibility and temperature (χT) is shown in **Figure 3-2-1 (a)**. Obviously χT deceases continuously upon cooling, indicative of antiferromagnetic interactions between Fe^{3+} ions. At room temperature, the effective moment μ_{eff} is determined as 5.61 μ_B per Fe^{3+} ion in terms of Eq. (3.2.2), slightly smaller than the spin only value 5.92 μ_B for S = 5/2.

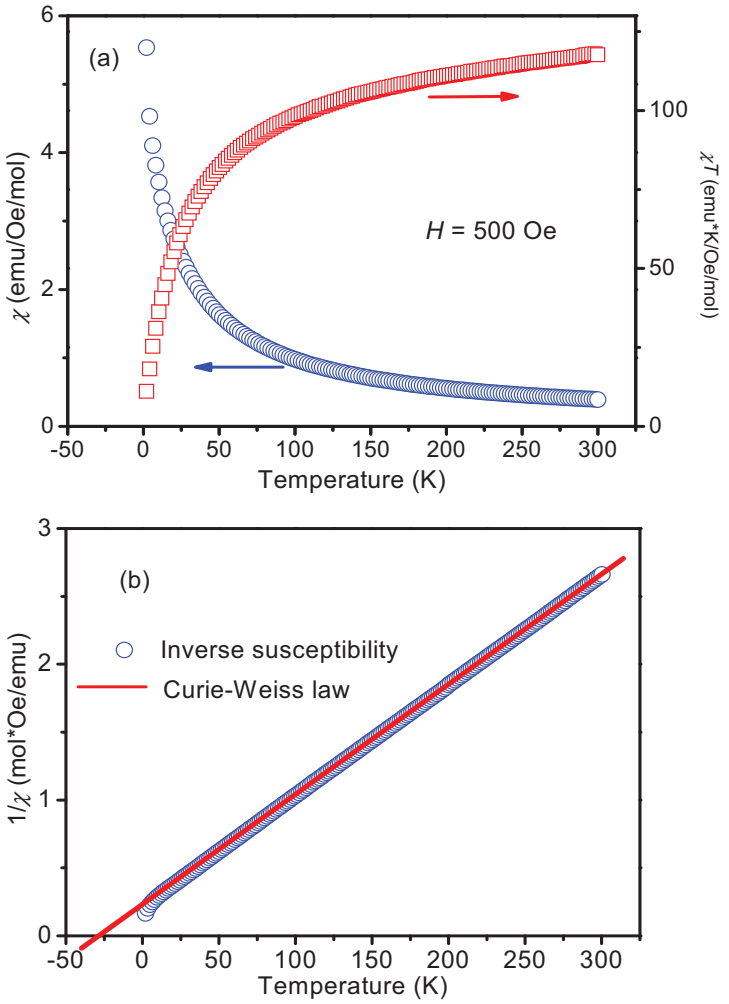

Figure 3-2-1 Magnetic susceptibility χ and inverse susceptibility of {$Mo_{72}Fe_{30}$} as a function of temperature. **(a)** χ and χT with a probing field of 500 Oe. **(b)** Inverse susceptibility with the refinement representing a Curie-Weiss law (red line).

The inverse magnetic susceptibility *vs.* temperature is plotted in **Figure 3-2-1 (b)**. A Curie-Weiss function given by Eq. (3.2.3) was fit to the inverse susceptibility over the temperature range of 30 K ≤ T ≤ 300 K. The Curie-Weiss function is known as

$$\frac{1}{\chi} = \frac{1}{C}\left(T + \Theta_{CW}\right), \tag{3.2.3}$$

where C is the Curie constant, Θ_{CW} is the Curie-Weiss temperature.

The best fit with a Curie-Weiss function is shown as the red line in **Figure 3-2-1 (b)** and gives a Curie-Weiss temperature of Θ_{CW} = -28.05 ± 0.05 K. The negative value of the Curie-Weiss temperature confirms that the nearest Fe^{3+} ions are antiferromagnetically coupled. In the mean field approximation it is assumed that every magnetic atom experiences a field proportional to the macroscopic magnetization. If only the nearest-neighbor interactions are taken into account, the effective exchange constant J_{eff} is related to the Curie-Weiss temperature via [84]

$$\left|J_{\text{eff}}\right| \Big/ k_{\text{B}} = \frac{3}{2} \cdot \frac{\left|\Theta_{\text{CW}}\right|}{S(S+1)z}, \tag{3.2.4}$$

where S = 5/2 is the spin quantum number of the Fe^{3+} ion, z = 4 is the number of nearest neighbors. $|J_{eff}|/k_B$ is then determined to be around 1.26 ± 0.01 K (~ 0.11 meV), close to the reported value of 0.134 meV [55]. The molar Curie constant obtained from the best fit is 122.60 ± 0.30 emu·K/Oe/mol. The Curie constant can be expressed as

$$C = \frac{N_{\text{A}} N \mu_{\text{B}}^2 S(S+1)}{3k_{\text{B}}} g^2, \tag{3.2.5}$$

where N = 30 is the number of Fe^{3+} ions in one {$Mo_{72}Fe_{30}$} molecule. The Landé factor g in Eq. (3.2.5) can then be determined as ~ 1.93, in reasonable agreement with the value of 1.974 reported by A. Müller et al. [55].

The magnetization as a function of the applied field was measured at 2, 10, 30, and 100 K, as shown in **Figure 3-2-2**. At 2 K, the field dependence of magnetization was measured first from 0 to 7 T, then from 7 T to -7 T, and finally from -7 T to 7 T. The measurements at other temperatures were taken from 0 to 7 T. No saturation has been reached up to 7.0 Tesla. No hysteresis behavior is found, consistent with the antiferromagnetic nature of this finite spin system.

In this section, the static magnetic properties of {$Mo_{72}Fe_{30}$} have been studied. No magnetic phase transition has been detected. The Curie-Weiss temperature was determined to be Θ_{CW} = -28.05 ± 0.05 K, indicating that the nearest-neighbor Fe^{3+} ions are antiferromagnetically coupled. The mean-field effective exchange constant is obtained as J_{eff} = 0.110 ± 0.002 meV.

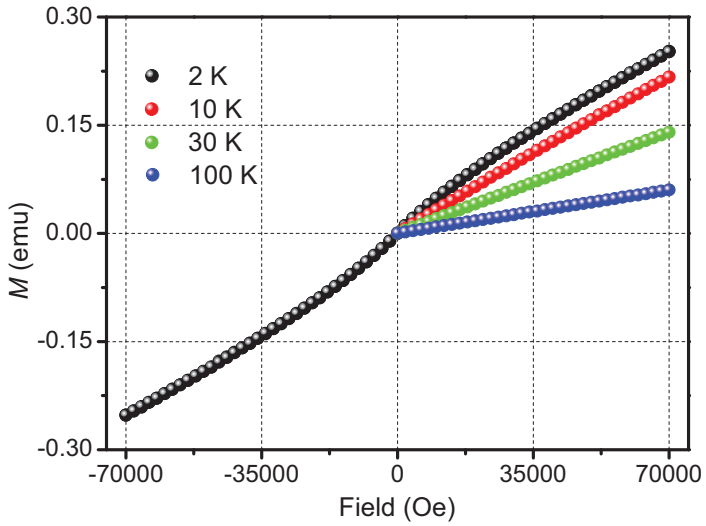

Figure 3-2-2 Field-dependent magnetization of {$Mo_{72}Fe_{30}$} at 2, 10, 30, and 100 K.

3.3 Specific Heat of {$Mo_{72}Fe_{30}$}

The specific heat of {$Mo_{72}Fe_{30}$} has been measured using a commercial Quantum Design Physical Property Measurement System (PPMS) equipped with a liquid-helium (LHe) cryostat and a dilution insert. The heat capacity values are extracted using the relaxation method [85, 86]. The background heat capacity of the microcalorimeter and the Apiezon N grease was measured carefully in a separate run and subtracted from the raw data to acquire the absolute heat capacity of the sample. In the measurements using the LHe cryostat, a rhombohedral single crystal of nondeuterated {$Mo_{72}Fe_{30}$}, with dimensions of about 2×2×1 mm^3 and mass of about 5 mg, has been used. In the measurements using the dilution insert, a thin, plate-like crystal with a flat surface and a mass of about 1 mg was used to achieve better thermal conductivity.

Figure 3-3-1 shows the temperature dependence of the specific heat measured under 0 and 5 Tesla external magnetic fields within a temperature range from 1.8 K to 300 K on nondeuterated {$Mo_{72}Fe_{30}$} crystal. There is no sign of long-range magnetic phase transition within this temperature range, which is reasonable for {$Mo_{72}Fe_{30}$} as

a molecular magnet with highly frustrated spin structure. Lacking of a non-magnetic reference of {$Mo_{72}Fe_{30}$}, the determination of the lattice contribution is rather difficult. The attempt to fit the data with a simple Debye model shows that a Debye model is inadequate to reproduce the specific heat of {$Mo_{72}Fe_{30}$}. As shown in **Figure 3-1-4**, significant splitting of the magnetic levels can already be introduced by small fields below 1 T. Therefore the change of magnetic specific heat should be seen by comparing the data for 0 T and 5 T. In **Figure 3-3-1**, the specific heat data measured under 0 and 5 T basically coincide with each other above 30 K, indicative of nonmagnetic origin within this temperature range. This agrees with the magnetic susceptibility measurements, which show that the system is basically paramagnetic within this temperature. Thus I actually do not expect any anomaly of magnetic origin above 30 K. The later discussion will focus on the low-T (< 18 K) part of the specific heat where the lattice contribution could be simplified and the magnetic nature of the system is studied in terms of the magnetic specific heat.

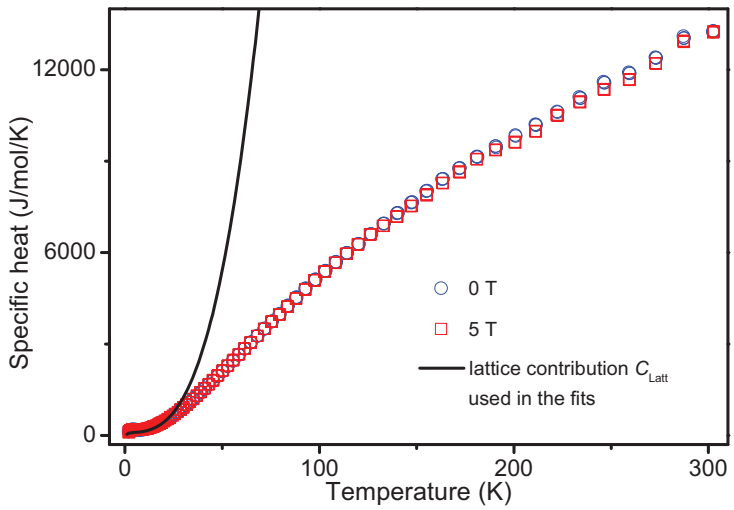

Figure 3-3-1 Specific heat data of {$Mo_{72}Fe_{30}$} from 1.8 K to 300 K under zero external magnetic field (blue circles) and 5 Tesla external field (red squares). The black line shows the lattice specific heat as used in the fits for the very low temperature data. Apparently this fit has no significance at higher temperatures.

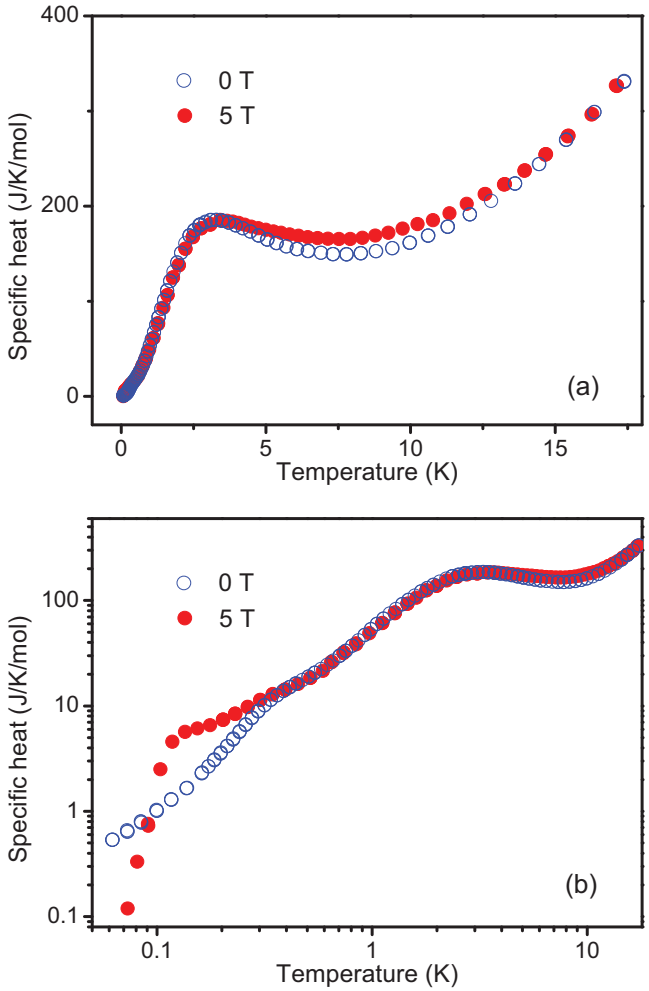

Figure 3-3-2 Specific heat data of {$Mo_{72}Fe_{30}$} from 60 mK to 18 K under 0 (blue circles) and 5 (red circles) Tesla external fields in linear-linear **(a)** and log-log **(b)** scale.

Figure 3-3-2 shows the low-*T* specific heat data of {$Mo_{72}Fe_{30}$} from 60 mK to 18 K under 0 and 5 Tesla external magnetic field. **Figure 3-3-2 (a)** is in linear-linear scale and **(b)** is in log-log scale. Firstly the data obtained under zero external field was analyzed because the absence of an external field avoids the Zeeman effect that disturbs the sequence of the energy levels (see **Figure 3-1-4**). The lattice contribution to the total specific heat was fitted with a combination of the Debye and Einstein models. As seen in **Figure 3-3-2**, there is an obvious anomaly at ~ 3 K and a small hump at ~ 0.3 K in the zero-field data. These two Schottky-like anomalies were fitted

with conventional two-level Schottky models to account for the magnetic specific heat, which are deduced as follows [87]. Imagine a two-level system, e.g., a particle with two possible energy levels, ε_1 and ε_2 ($\varepsilon_1 < \varepsilon_2$), separated by $\Delta = (\varepsilon_2 - \varepsilon_1) / k_B$. The partition function of this system is:

$$Z = \sum_{i=1}^{2} \exp(-\varepsilon_i / k_B T), \tag{3.3.1}$$

and thus the average thermal energy at temperature T is:

$$E = \frac{\partial \ln Z}{\partial\left(-\frac{1}{k_B T}\right)} = k_B T^2 \left(\frac{\partial \ln Z}{\partial T}\right). \tag{3.3.2}$$

The Schottky specific heat is then obtained by differentiating Eq. (3.3.2) with respect to temperature and multiplying it by the Avogadro number,

$$C_{Sch} = R\left(\frac{\Delta}{T}\right)^2 \frac{e^{(\Delta/T)}}{\left[1+e^{(\Delta/T)}\right]^2}, \tag{3.3.3}$$

where $R = k_B N_A = 8.3145$ J K^{-1} mol^{-1} is the ideal gas constant. The low and high temperature limits of Eq. (3.3.3) are:

$$C_{Sch} \sim R\left(\frac{\Delta}{T}\right)^2 e^{(-\Delta/T)}, \qquad T << \Delta \tag{3.3.4}$$

$$C_{Sch} \sim R\left(\frac{\Delta}{2T}\right)^2. \qquad T >> \Delta \tag{3.3.5}$$

Obviously, at low temperatures ($T << \Delta$) there is very little probability of a transition to the upper energy level and hence the upper level will be unpopulated. Consequently C_{Sch} approaches zero. As the temperature T is comparable to Δ, the transition from the lower level to the upper level can take place to an appreciable degree and result in a Schottky specific heat which is characterized by a broad peak around the temperature Δ and corresponds to a large change in entropy for a small change in temperature. At high enough temperature ($T >> \Delta$), both levels are almost equally populated and the transition probability between the levels can be neglected and thus C_{Sch} approaches zero again. The above derivation of Schottky specific heat for the two-level system can be extended to a multi-level system [87]. Suppose an

independent particle with m energy levels. Assume all the energy levels to be non-degenerate and have energies of ε_1, ε_2,…, ε_m. The average thermal energy of one such particle at a temperature T is

$$E = \frac{\sum_i \varepsilon_i \exp(-\varepsilon_i / k_B T)}{\sum_i \exp(-\varepsilon_i / k_B T)}. \quad (3.3.6)$$

For one mole of this substance, the Schottky specific heat can be calculated by differentiating the total energy with respect to T. It is described by the following expression:

$$C_{Sch} = \frac{R}{k_B^2 T^2} \frac{\sum_i \varepsilon_i^2 \exp(-\varepsilon_i / k_B T) \sum_i \exp(-\varepsilon_i / k_B T) - \left[\sum_i \varepsilon_i \exp(-\varepsilon_i / k_B T)\right]^2}{\left[\sum_i \exp(-\varepsilon_i / k_B T)\right]^2}. \quad (3.3.7)$$

After deriving the expressions for Schottky specific heat, the total specific heat from 60 mK to 18 K under zero external field was fitted with the sum of one Debye term, one Einstein term and two Schottky terms, as expressed below. The Debye term could be simplified to be proportional to T^3 at low temperatures. The total fit to the experimental data was satisfying, as shown by the red line in **Figure 3-3-3**. The data and the total fit were also plotted in log-log scale in the inset of **Figure 3-3-3**, where it could be seen that the sample still possesses significant heat capacity even at 60 mK. After analyzing the raw data, I thought it could be attributed to the residual entropy because of the highly frustrated and degenerate magnetic ground state of {$Mo_{72}Fe_{30}$}. This might explain the small divergence of the fitting curve and the specific heat data below 0.2 K. The green line in **Figure 3-3-3** represents the vibrational contribution to the total specific heat, described by the combination of the Debye and the Einstein terms [87-89],

$$C_{Latt} = C_{Ein} + C_{Debye}, \quad (3.3.8)$$

with the Einstein term C_{Ein},

$$C_{Ein} = 3Rr_E \left(\frac{T_E}{T}\right)^2 \exp\left(\frac{T_E}{T}\right)\left[\exp\left(\frac{T_E}{T}\right) - 1\right]^{-2}, \quad (3.3.9)$$

and the Debye term C_{Debye},

$$C_{\mathrm{Debye}} = R\frac{234 r_{\mathrm{D}} T^3}{\Theta_{\mathrm{D}}{}^3}. \tag{3.3.10}$$

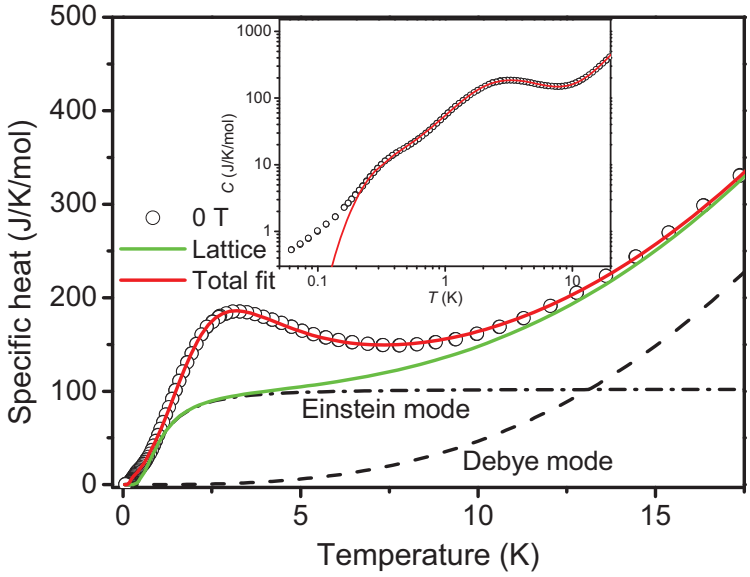

Figure 3-3-3 Low-temperature zero-field specific heat data (black circles) at 0 T and the best fit (red line) in terms of the combination of the vibrational contribution (green line) and the Schottky contributions (see **Figure 3-3-4**). The vibrational contribution is the sum of contributions from an Einstein mode (dash-dot line) and a Debye model (dashed line). Inset: data with the total fit in log-log scale.

In Eqs. (3.3.9) and (3.3.10), r_{E} is the number of Einstein oscillators per molecule, $T_{\mathrm{E}} = E_{\mathrm{Ein}}/k_{\mathrm{B}}$ is the temperature equivalent of the energy of the Einstein mode, Θ_{D} is the Debye temperature, r_{D} is the number of atoms per molecule and is estimated as 1100 in {$Mo_{72}Fe_{30}$}, taking account of the loss of crystal water molecules after the crystal was kept at room temperature. The best fit yields a Debye temperature of Θ_{D} = 349.7 ± 12.1 K. The temperature of the Einstein mode, T_{E}, is found to be 3.1 ± 0.3 K and the oscillator strength corresponds to r_{E} = 3.3 ± 0.3. The Einstein term is usually associated to the existence of flat portions of the optical phonon dispersions. The present fitting parameters suggest that very few low-frequency oscillators are active at low temperatures. However, from the plots of the Einstein mode and the Debye

mode in **Figure 3-3-3**, the Einstein-like contribution dominates the lattice specific heat below 10 K. A possible origin for this Einstein mode can be given as follows. In the polarized neutron scattering measurements on $\{Mo_{72}Fe_{30}\}$ polycrystals, a broad nuclear coherent scattering maxima at Q ~ 1.80 Å^{-1} was observed (see Section 3.5). I interpret this contribution as the scattering from the amorphous crystal water in the sample. It is known that localized harmonic vibration modes may exist in amorphous materials [90-92]. The Einstein-like contribution in the lattice specific heat may be due to the localized vibrations in the amorphous crystal water. The lattice specific heat obtained from the above fit is also plotted in **Figure 3-3-1** within larger temperature range. Above 30 K, this lattice contribution increases sharply and diverges from the experimental data since a simplified ~T^3 dependence of the Debye term, which only holds at low temperatures, is used.

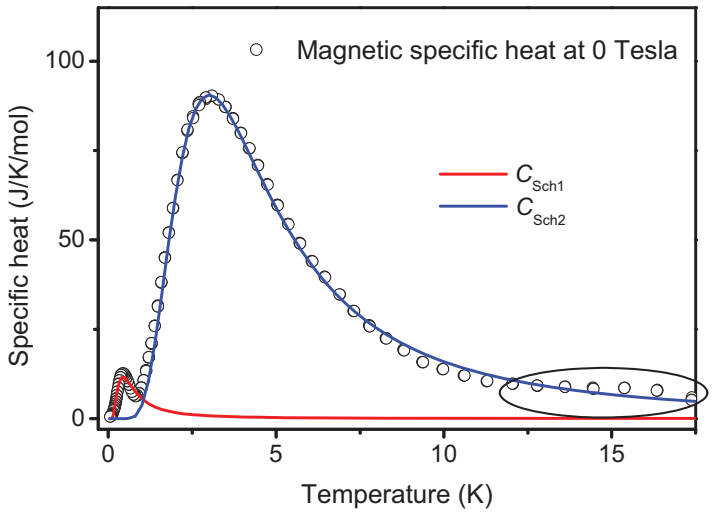

Figure 3-3-4 The magnetic specific heat contribution (black circles) at 0 T obtained by subtracting the lattice contribution from the zero-field specific heat data. The best fit using two Schottky terms is represented by the red line and the blue line, respectively.

However, I shall mention here that the determination of the vibrational contribution to the total specific heat under zero external field is not unique. Good fit to the data was also achieved by replacing the Einstein term with a linear term,

which could, e.g., be attributed to the conducting electrons localized on the surfaces of {$Mo_{72}Fe_{30}$} molecules, or some other kind of excitation leading to linear contribution to the specific heat. But the analysis of the specific heat data under 5 Tesla precluded the existence of the linear term, which will be discussed later in this section.

The magnetic contribution at zero external field is then obtained by subtracting the lattice contribution from the total specific heat, shown as the circles in **Figure 3-3-4**. Two Schottky-type anomalies are evident in **Figure 3-3-4**, which can be well fitted with the two-level Schottky model given by Eq. (3.3.3). The fitting results of the two anomalies are plotted as the red and the blue line in **Figure 3-3-4** and labeled C_{Sch1} and C_{Sch2}, respectively. The corresponding energy gaps of C_{Sch1} and C_{Sch2} are then determined as $\Delta_1 = 0.09 \pm 0.01$ meV and $\Delta_2 = 0.64 \pm 0.01$ meV. There is a small and broad hump in the data as indicated by the ellipse in **Figure 3-3-4**, which possibly originates from the thermal population of higher rotational bands. But it is too small to give confident evidence through a satisfying fit.

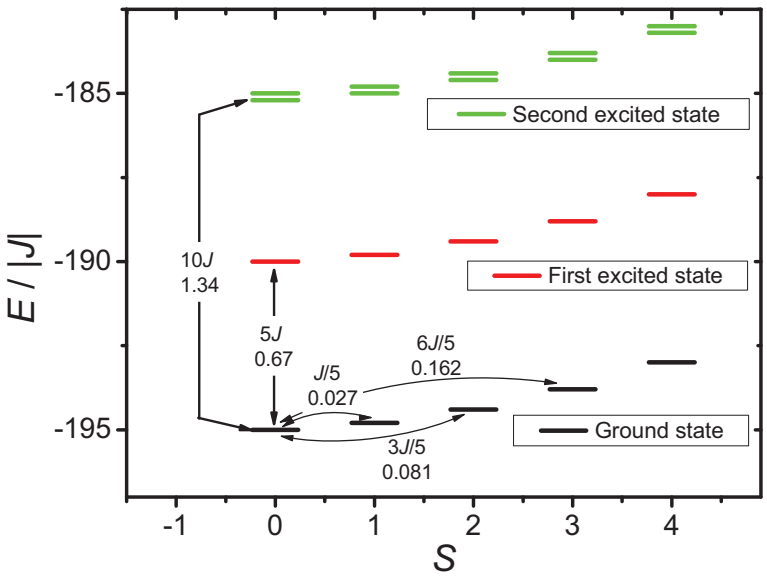

Figure 3-3-5 Low-lying rotational bands calculated from the quantum rotational band model, with the ground state levels (black short lines), the first (red) and second (green) excited state levels. The corresponding energy splitting values are in unit of meV.

These low-lying magnetic excitations revealed from the zero-field specific heat were investigated in the light of the quantum rotational band (QRB) theory of {$Mo_{72}Fe_{30}$} [79]. The resultant low-lying energy spectrum derived from the QRB theory [79, 81] is plotted in **Figure 3-3-5**.

The arrows in **Figure 3-3-5** indicate the interband energy splitting between the excited states and the ground state, as well as the intraband splitting in the ground-state levels. The Schottky anomaly C_{Sch1} (see **Figure 3-3-4**) is located at very low temperatures around 0.5 K. Very likely the ground-state levels are most populated at this temperature. The energy gap $\Delta_1 = 0.09(1)$ meV obtained from the fit can be understood as an averaged gap of the intraband splitting among the ground-state levels. As the temperature increases, the first excited state starts to be populated. The energy gap $\Delta_2 = 0.64(1)$ meV obtained from the Schottky term C_{Sch2} is close to but a little smaller than the characteristic gap 0.67 meV between the $S = 0$ ground state and $S = 0$ first excited state. Within this temperature range (around 3 K), some higher levels of the ground state should be populated. The energy gaps between these levels and the $S = 0$ first excited state are smaller than 0.67 meV. For example, the gap between $S = 2$ ground state and $S = 0$ first excited state is 0.589 meV. In the mean time, some $S > 0$ levels of the first excited state could also be populated. The gaps between them and the $S = 0$ ground state are higher than 0.67 meV. I adopt $\Delta_2 = 0.64(1)$ meV as an averaged gap for the various gaps between the ground-state levels and the first excited state levels. The second excited state is located ~ 1.34 meV above the ground state, which is possibly responsible for the small hump at around 15 K in **Figure 3-3-4**.

From the above discussion, it can be seen that the specific picture of the thermal population of the energy levels in this system could be very complicated, and a reliable many-level Schottky fit to the magnetic specific heat is almost impossible. The fit using a simple two-level Schottky model could be a good approximation to the real case. As seen in **Figure 3-3-4**, the fit yields a satisfactory match with the experimental data. The two energy gaps obtained from the fit should actually account for a number of gaps with two sets of similar energies. In an inelastic neutron scattering measurement on deuterated {$Mo_{72}Fe_{30}$} [81], the energy gap between the ground state and the first excited state is determined as ~ 0.6 meV, which is close to what was found in the zero-field specific heat data. However, the intraband transitions within ground states could not be measured due to the high

background in the inelastic neutron scattering data at small energy transfer.

Therefore based on the above analysis, the anomaly at 0.3 K in the zero-field specific heat data of {$Mo_{72}Fe_{30}$} is considered to be due to the Schottky effect arising from the thermal population of discrete ground state energy levels, while the one at 3 K originates from the Schottky effect between the ground states and the first excited states. The energy gaps that were found in the specific heat data basically reflect the low-lying magnetic excitations in {$Mo_{72}Fe_{30}$}.

The above fitting procedures were also carried out to fit the specific heat data measured with 5 T external field. As shown in **Figure 3-3-2**, the peak at ~ 3 K, which corresponds to the Schottky effect between the ground state and the first excited state levels, shifts a little towards higher temperature in the 5 T data as compared to the zero-field data. There are two anomalies at ~ 0.1 and ~ 0.3 K in the 5 T data with log-log scale (inset of **Figure 3-3-2**). The one at ~ 0.3 K can be seen more clearly in **Figure 3-3-7**. The anomaly at ~ 0.3 K should correspond to the intraband Schottky effect within the ground state levels, while the one at ~ 0.1 K is quite small in absolute specific heat value and may not be regarded as a Schottky effect. As already mentioned in the analysis of zero-field specific heat data, the sample possesses residual entropy at very low temperatures under zero external fields, owing to the highly degenerate ground state. Upon applying a 5 T external field, the ground state degeneracy is lifted, which causes a fast decrease in the 5 T specific heat as compared to the zero-field data below 0.1 K. The specific heat values of the anomaly at ~ 0.1 K is actually very small, as shown in **Figure 3-3-7** with linear-linear scale. Thus I can safely analyze the 5 T specific heat data while neglecting the anomaly at ~ 0.1 K.

Figure 3-3-6 shows the low-temperature part (T < 18 K) of the 5 T specific heat data from non-deuterated {$Mo_{72}Fe_{30}$} crystal. The total specific heat was fitted with one Einstein term (Eq. 3.3.9), one Debye term (Eq. 3.3.10) and two Schottky terms (Eq. 3.3.3). The total fit is shown as the red line in **Figure 3-3-6**. The vibrational contribution (Einstein + Debye) in this fit remains the same as the one used in the fit of zero-field data, which is reasonable because the lattice specific heat is not affected by an external magnetic field.

The magnetic contribution under 5 Tesla was then obtained by subtracting the vibrational contribution from the total specific heat, shown as the circles in **Figure 3-3-7**. Two Schottky-type anomalies were fitted with the two-level Schottky model (Eq. 3.3.3), giving two energy gaps Δ_1 = 0.08 ± 0.02 meV and Δ_2 = 0.70 ± 0.02 meV.

Taking into account the error of the fit, the intraband gap within the ground state levels and the interband gap between the ground state and first excited state did not change significantly. The reason may be as follows. A 5 T external field might have disturbed the rotational bands of the system as shown in **Figure 3-1-4**, which made the field-dependence of the energy gaps complicated and unable to be described by a simple enlargement under such a high field. For the sake of clarity, the energy gaps obtained in the fit of 0 and 5 T specific heat data are summarized in **Table 3-3-1**.

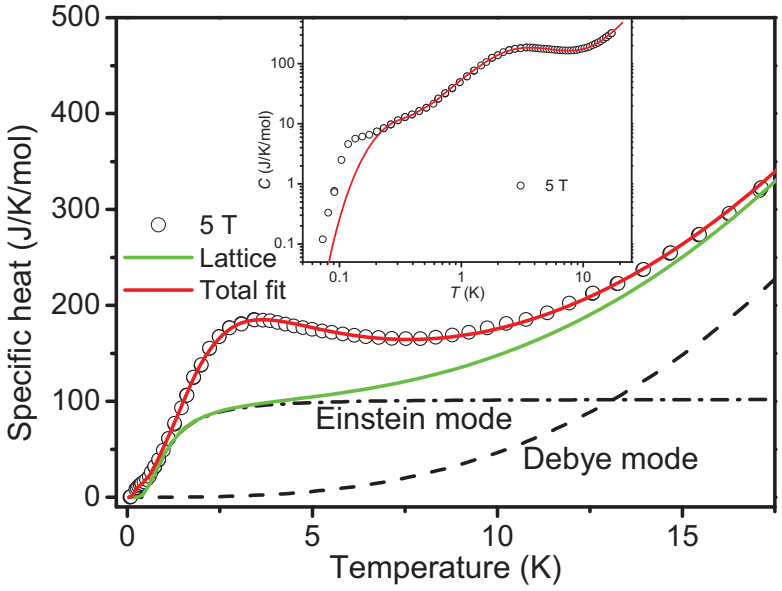

Figure 3-3-6 Low-temperature part of the 5 T specific heat data (black circles) and the best fit (red line) in terms of the combination of the vibrational contribution (green line) and the Schottky contributions (see **Figure 3-3-7**). The vibrational contribution is the sum of contributions from one Einstein mode (dash-dot line) and a Debye model (dashed line). Inset: data and total fit in log-log scale.

When fitting the specific heat data at zero field, another possibility was to use a linear term instead of the Einstein term and the fitting result was also satisfying. But as shown in **Figure 3-3-2**, the 5 T specific heat data really approach zero at the lowest temperatures as compared to the zero-field specific heat, which made the linear term used in the fit of the zero-field data unfeasible in the fit of the 5 T specific heat data. Of course, there is the possibility that the external magnetic field removed the linear

term. Such a removal should result in noticeable decrease in the specific heat at high temperatures. But as shown in **Figure 3-3-2**, the 0 and 5 T specific heat data are almost identical at high temperatures. Therefore the linear contribution should not exist in the fit of specific heat data of {$Mo_{72}Fe_{30}$}.

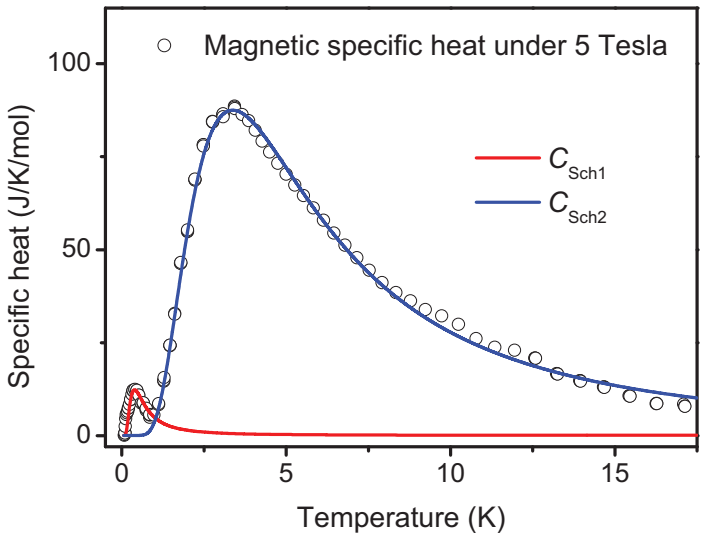

Figure 3-3-7 The magnetic specific heat contribution (black circles) obtained by subtracting the lattice contribution from the 5-Tesla specific heat data. The best fit using the Schottky terms is represented by the red line and the blue line, respectively.

Table 3-3-1 Fitting parameters for 0 and 5 T specific heat of {$Mo_{72}Fe_{30}$}. The evidence of the energy gap between the ground state and the first excited state from the inelastic neutron scattering (INS) study in Ref. [81] is given. Based on the QRB theory, some intraband energy gaps within the ground state and the gap between the S = 0 ground state and S = 0 first excited state are also given for comparison.

Parameters	Θ_E (K)	Θ_D (K)	Δ_1 (meV)	Δ_2 (meV)
0 Tesla	3.1 ± 0.3	349.7 ± 12.1	0.09 ± 0.01	0.64 ± 0.01
5 Tesla	3.1 ± 0.3	349.7 ± 12.1	0.08 ± 0.02	0.70 ± 0.02
INS [81]				~ 0.6
QRB theory [79]			0.027, 0.081, 0.162	0.67

Hence, the analysis of the specific heat data under 0 and 5 T external fields revealed two low-lying magnetic excitations at ~ 0.09 meV and ~ 0.64 meV. The former one originates from the intraband transitions within the ground states levels, while the latter one from the interband transitions between the ground state and the first excited state levels. These energy gaps are in reasonable agreement with the theoretical prediction of the quantum rotational band model and the result of inelastic neutron scattering. These results give additional strong experimental support to the quantum rotational band theory and the three-sublattice spin configuration model of {$Mo_{72}Fe_{30}$}. It is suggested that the quantum rotational band model is still practicable in explaining the low-lying magnetic excitations of {$Mo_{72}Fe_{30}$} up to about 10 K. But the study on magnetic excitations by means of specific heat method is indirect, especially for a system like {$Mo_{72}Fe_{30}$} which possesses a complex energy spectrum. In the next section, a direct observation of the magnetic excitations in {$Mo_{72}Fe_{30}$} will be attempted using high-resolution inelastic neutron scattering.

3.4 Inelastic Neutron Scattering of {$Mo_{72}Fe_{30}$}

In Section 3.3, the low-lying magnetic excitations of {$Mo_{72}Fe_{30}$} were determined by analyzing the Schottky-type anomalies in specific heat data. But no direct observations of the magnetic excitation spectrum could be given by the specific heat measurements. In this regard, the inelastic neutron scattering technique has been proven to be most effective. As discussed in Section 3.3, an inelastic neutron scattering measurement on deuterated {$Mo_{72}Fe_{30}$} has been carried out by V. O. Garlea et al. [81]. They collected inelastic neutron scattering spectra at 65 mK under zero magnetic field and observed a clear peak near an energy transfer of 0.6 meV, in rough agreement with the overall energy scale of the predicted interband transition energy $26J/5 \approx 0.69$ meV between the ground state and the first excited state. Due to the high background of inelastic neutron scattering at small energy transfer, their measurements could not identify the lowest intraband magnetic excitations within the ground state levels predicted by the rotational band theory. In order to achieve a direct determination of the low-lying magnetic excitations and compare with the theoretical models, we performed inelastic neutron scattering on deuterated {$Mo_{72}Fe_{30}$} on the backscattering spectrometer BASIS at the Spallation Neutron

Source (SNS) at the Oak Ridge National Laboratory (ORNL). [93, 94] An introduction to the backscattering method and the BASIS instrument is given in **Appendix C**.

The polycrystalline {$Mo_{72}Fe_{30}$} sample used for inelastic neutron scattering was deuterated to reduce attenuation and incoherent scattering from hydrogen atoms. The deuterated sample was dried in vacuum at 400 K for 18 hours to further reduce the hydrogen content. The drying procedure also intended to increase the amorphization of the sample to depress the attenuation to the neutron flux by Bragg diffractions. Approximately 1.8 g of deuterated and dried {$Mo_{72}Fe_{30}$} sample was sealed in a copper cylinder under helium atmosphere to make sure that the sample could be cooled down to the base temperature of 1.5 K.

The backscattering spectrometer BASIS is an inverse geometry time-of-flight spectrometer that uses Si(111) analyzer crystals to select the final energy of the neutrons of 2082 μeV (corresponding to neutron wavelength λ = 6.267 Å) out of a polychromatic incident neutron beam. In my experiments, the instrument choppers were operated at 30 Hz, making an effective dynamic range from -50 μeV to +900 μeV for the data analysis. This instrument provides a high energy resolution, ~ 3.5 μeV full width at half maximum (FWHM) at the elastic position. The detector bank of the spectrometer covers the wave vector range of $0.3 \leq Q \leq 1.9$ Å^{-1}. The background spectrum from the empty Cu holder was measured separately and was subtracted from the data to acquire the inelastic neutron scattering from the sample. A vanadium standard was measured to account for the detector efficiency. In order to study the field dependence of the spectra, a cryomagnet was used with a maximum field of $\mu_0 H$ = 5 Tesla and a base temperature of T = 1.5 K.

The inelastic neutron scattering spectra were collected at 1.5 K (under 0, 0.5 and 1 Tesla) and 4 K (under 0 and 0.5 Tesla). **Figure 3-4-1** shows the intensity contour map of $S(Q, E)$ for various temperatures and fields investigated. The x- and y- axis corresponds to the wave vector transfer Q and energy transfer E, respectively.

As shown in **Figure 3-4-1**, the high intensities at the edges of the x-axis of the spectra originated from the monitor normalization. Thus the range of the energy transfer for data analysis was taken from -50 to +900 μeV. If the background measured from the empty can was subtracted fully, negative values in the elastic line region appeared. For the plots in **Figure 3-4-1**, the background was subtracted from the raw data with a factor of 0.9, assuming a transmission of 90%. At high Q (Q >1.5 Å^{-1}), the background was too high to be subtracted properly. Hence, the high Q data

were omitted for the data analysis. The signals from the sample were rather weak. No magnetic excitation could be seen.

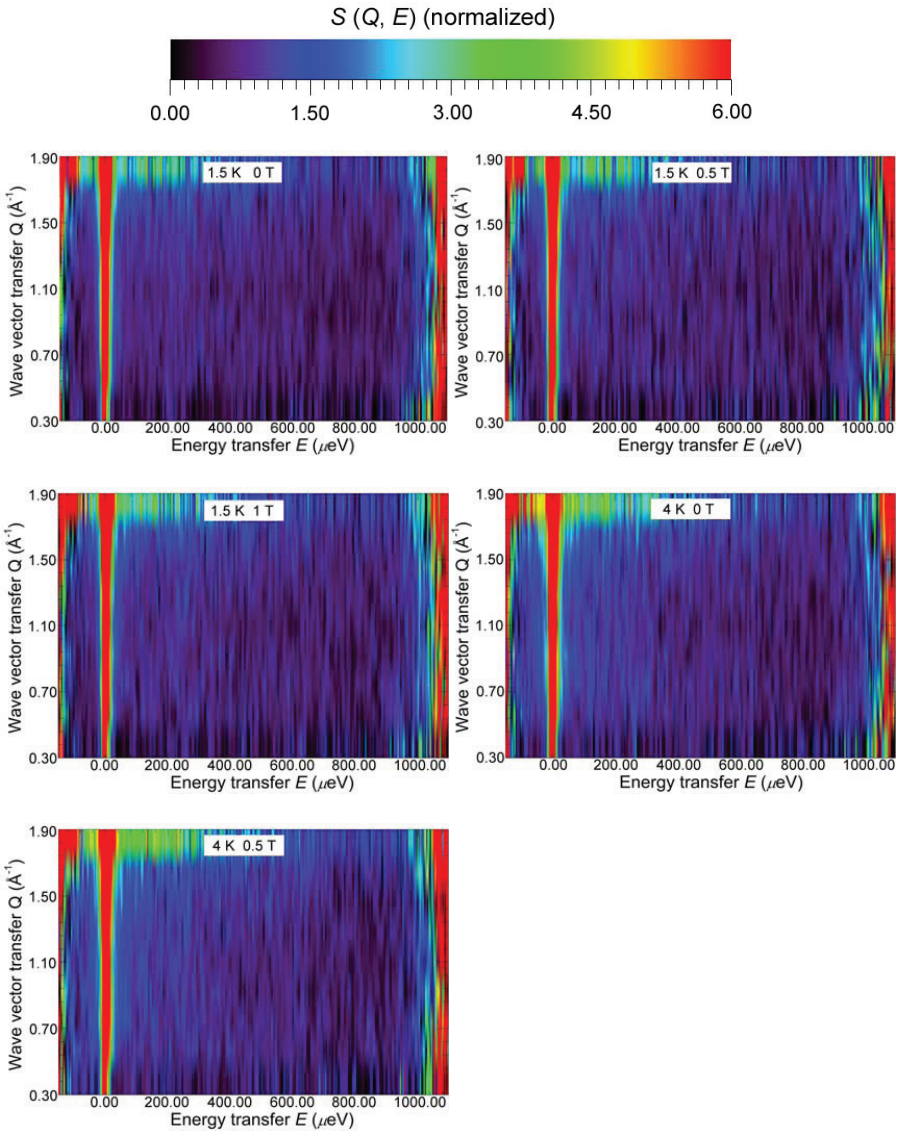

Figure 3-4-1 Intensity contour map of neutron inelastic scattering on deuterated $\{Mo_{72}Fe_{30}\}$ at 1.5 K (under 0, 0.5 and 1 T), and 4 K (under 0 and 0.5 T).

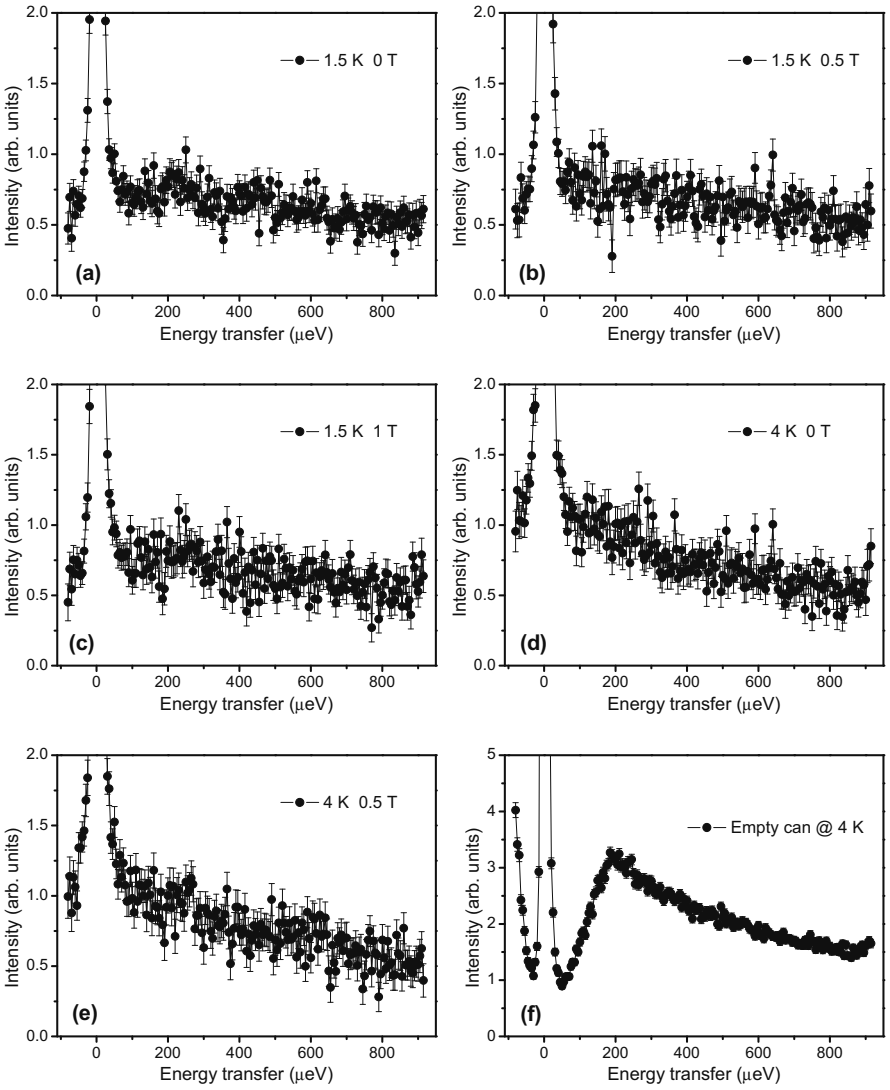

Figure 3-4-2 Neutron inelastic scattering spectra integrated over Q interval from 0.3 to 1.5 $Å^{-1}$ of deuterated {$Mo_{72}Fe_{30}$} at 1.5 K (under 0, 0.5 and 1 T) **(a) – (c)** and 4 K (under 0 and 0.5 T) **(d), (e)**; **(f)**: background spectrum measured from empty Cu can at 4 K (note the change in scale).

Figure 3-4-2 (a) – (e) shows the neutron inelastic scattering intensity, $S(E)$, representing the integration of $S(Q, E)$ within the Q range from 0.3 to 1.5 $Å^{-1}$ at the temperatures and fields investigated. The background spectrum measured from the empty Cu holder at 4 K is shown in **Figure 3-4-2 (f)**. The sharp peak at 0 μeV in all plots is the elastic-scattering component. As shown in **Figure 3-4-2**, no obvious features for magnetic excitations can be found at the energy transfer values either predicted by the rotational band theory, i.e., ~ 30 μeV and ~ 700 μeV, or suggested by the Schottky specific heat, i.e., ~ 90 μeV and ~ 640 μeV. The small peaks at ~ 200 μeV should be attributed to the imperfect subtraction of the background, because there is a large peak at this position in the background spectrum as seen in **Figure 3-4-2 (f)**. The quasielastic components in the spectra of 4 K are more prominent than those in the spectra of 1.5 K. At each temperature, nearly no field-dependence could be identified from the measurements.

As a summary of Section 3.4, unfortunately no magnetic excitations were observed from the inelastic neutron scattering measurements on deuterated $\{Mo_{72}Fe_{30}\}$ at the high-resolution backscattering spectrometer BASIS at the Spallation Neutron Source SNS, ORNL. The background was high and probably buried the weak inelastic scattering from the sample, resulting in large error bars of the data. The measurements were carried out with the cryomagnet, which might be the main source of the large background. In a successful inelastic neutron scattering measurement from deuterated $\{Mo_{72}Fe_{30}\}$ [81], about 8 g of sample was used, while the mass of the sample used in my experiment was only around 1.8 g. This could be another reason why the sample signal was weak. The magnetic scattering from this system was thus found to be quite weak. In next section, the weak magnetic scattering from $\{Mo_{72}Fe_{30}\}$ will be measured and investigated in more detail by means of polarized neutron scattering.

3.5 Diffuse Neutron Scattering with Polarization Analysis of {$Mo_{72}Fe_{30}$}

The collective phenomena of interacting magnetic moments may strongly depend on the topology of the crystal structure. As a geometrically spin-frustrated molecular magnet, {$Mo_{72}Fe_{30}$} possesses highly symmetric spin arrangements. No long-range magnetic order has been found in the specific heat measurements (see Section 3.3) even down to 60 mK, owing to the strong spin frustration and the relatively large distance between the molecules in {$Mo_{72}Fe_{30}$}. In the previous sections, some experimental results have been presented and discussed. Most of these results are consistent with the theoretical predictions made by the three-sublattice spin model and the resultant quantum rotational band theory, which have been developed to represent the frustrated ground state spin configuration of {$Mo_{72}Fe_{30}$}. However, these experimental supports of the three-sublattice spin model still remained indirect, since they were not direct observations of the spin correlations resulting from the magnetic ground state of the {$Mo_{72}Fe_{30}$} molecule. The magnetic ground state of {$Mo_{72}Fe_{30}$} is expected to be characterized by short-range spin correlations within the individual molecules, since the intermolecular magnetic interactions are negligible as compared to the intramolecular ones for this system. An intensive study on the spin correlations of {$Mo_{72}Fe_{30}$} will shed more light on the nature of the novel magnetic ground state of this complex magnetic system.

The spin correlation functions of frustrated magnetic systems containing hydrogen are difficult to measure at low temperatures because magnetic diffuse neutron scattering is often weak as compared to nuclear diffuse scattering and thermal diffuse scattering. However, diffuse neutron scattering with polarization analysis allows one to separate nuclear coherent, magnetic and nuclear spin-incoherent scattering simultaneously and unambiguously [73]. In this section, the quantitative short-range spin correlations in the large spin-frustrated molecular magnet {$Mo_{72}Fe_{30}$} are being investigated for the first time, by means of diffuse neutron scattering with polarization analysis at various temperatures.

3.5.1 Experimental Details

The {$Mo_{72}Fe_{30}$} samples were synthesized at Rheinisch-Westfälische Technische Hochschule (RWTH) Aachen University according to the method described in Ref.

[54]. $\{Mo_{72}Fe_{30}\}$ polycrystals were deuterated to minimize attenuation and incoherent scattering from hydrogen atoms. Approximately 2 g of sample was sealed in a copper holder in a helium atmosphere. Polarized neutron scattering measurements were carried out on the diffuse neutron scattering instrument DNS [95] at the FRM II research reactor (Garching, Germany), equipped with a ^{4}He closed cycle cryostat and an orange-type liquid helium cryostat. A detailed introduction to DNS is given in **Appendix C**. The energy of the incident neutron beam was 3.6 meV (corresponding to a wavelength of 4.74 Å), allowing the structure factor to be determined up to the scattering vector $\boldsymbol{Q}$ of 2.30 Å^{-1}. Within the quasistatic approximation, the nuclear coherent, spin-incoherent and magnetic scattering cross section were separated simultaneously with the *xyz*-polarization method in the spin-flip (SF) and non-spin-flip (NSF) channels [73]. In the *xyz*-polarization analysis, the multidetectors of DNS define the *x*-*y* plane, which makes the scattering vector $\boldsymbol{Q}$ always perpendicular to the *z* direction. The SF and NSF differential cross sections were then measured for the incident beam polarized in turn along *x*, *y*, and *z* direction, giving totally six partial cross sections, labeled $\mathrm{d}\sigma_{\mathrm{SF}}^{(\mathrm{x,y,z})}/\mathrm{d}\Omega$ and $\mathrm{d}\sigma_{\mathrm{NSF}}^{(\mathrm{x,y,z})}/\mathrm{d}\Omega$. The quantitative value of the differential magnetic cross section, $\mathrm{d}\sigma_{\mathrm{Mag}}/\mathrm{d}\Omega$, in units of barn (sr)$^{-1}$ per Fe atom, can be extracted from either

$$\frac{\mathrm{d}\sigma_{\mathrm{Mag}}}{\mathrm{d}\Omega} = 2\left(\frac{\mathrm{d}\sigma_{\mathrm{SF}}^{\mathrm{x}}}{\mathrm{d}\Omega} + \frac{\mathrm{d}\sigma_{\mathrm{SF}}^{\mathrm{y}}}{\mathrm{d}\Omega} - 2\frac{\mathrm{d}\sigma_{\mathrm{SF}}^{\mathrm{z}}}{\mathrm{d}\Omega}\right), \tag{3.5.1}$$

or

$$\frac{\mathrm{d}\sigma_{\mathrm{Mag}}}{\mathrm{d}\Omega} = 2\left(2\frac{\mathrm{d}\sigma_{\mathrm{NSF}}^{\mathrm{z}}}{\mathrm{d}\Omega} - \frac{\mathrm{d}\sigma_{\mathrm{NSF}}^{\mathrm{x}}}{\mathrm{d}\Omega} - \frac{\mathrm{d}\sigma_{\mathrm{NSF}}^{\mathrm{y}}}{\mathrm{d}\Omega}\right). \tag{3.5.2}$$

The two expressions correspond to independent measurements, and the magnetic differential cross section is taken as their average after verifying their equivalence to check for systematic errors. The flipping ratio correction was made using the reference measurements from an ideal isotropic incoherent scatterer, a NiCr alloy. The background was measured from an empty copper holder separatedly and subtracted from the raw data. In order to obtain the absolute scattering cross section from the sample, a vanadium standard was measured under the same experimental settings. Data was then normalized to the incoherent scattering of the vanadium

standard. The differential scattering cross section per Fe atom in absolute units was then obtained as

$$\frac{d\sigma_S}{d\Omega} = \frac{I_S N_V}{4\pi n I_V N_S}\sigma_V, \tag{3.5.3}$$

where I_S and I_V are the intensities scattered by the sample and the vanadium respectively, n is the number of Fe atoms per molecule and equals to 30, N_S and N_V are the amount of sample and vanadium atoms in the beam, σ_V is the total scattering cross section of vanadium. It should be mentioned that the determination of the absolute scattering cross section in my experiments may also be effected by the absorption (from the sample holder, the vanadium standard, the cryostat, and the sample) and the spin incoherent scattering from the sample. It is estimated that the attenuation to the primary beam in the sample measurements is around 20%, and the attenuation in the vanadium measurements is around 22%. Therefore the absolute cross section was determined using Eq. (3.5.3) without consider other factors, because they were basically canceled out.

3.5.2 Experimental Results

The polarized neutron scattering spectra of deuterated {$Mo_{72}Fe_{30}$} were recorded at various temperatures from 1.5 K to 100 K on DNS. **Figure 3-5-1** shows the nuclear coherent, spin-incoherent and paramagnetic components separated from the total scattering by means of *xyz*-polarization method. Data are plotted as a function of Q. The spin-incoherent scattering intensity is nearly constant, suggesting a successful separation of different scattering contributions. The nuclear coherent scattering shows a broad hump at high Q around 1.80 $Å^{-1}$, which can be attributed to the scattering from amorphous crystal water [96]. The high intensity of nuclear coherent scattering below 0.25 $Å^{-1}$ originates from the background of the incident neutron beam. Several nuclear Bragg peaks are located within the Q range 0.25 - 1.00 $Å^{-1}$, which are consistent with the simulation of the powder diffraction pattern (marked as the blue line at the bottom of **Figure 3-5-1**) of {$Mo_{72}Fe_{30}$}. Just like what has been indicated in the inelastic neutron scattering on BASIS, the magnetic contribution (red circles in **Figure 3-5-1**) is weak, leading to long counting time to obtain reasonable statistics. The magnetic scattering intensity is almost 40 times smaller than the total scattering intensity. Without the polarized neutron scattering method, the magnetic

component would be hardly seen. Here the magnetic scattering data were actually integrated over the energy-transfer window of DNS since no energy analysis option was installed during this experiment. The INS measurements by V. O. Garlea et al. [81] showed that the magnetic excitations of {$Mo_{72}Fe_{30}$} are lower than 3 meV. Thus the energy integration on DNS with incident neutron energy of 3.6 meV should be enough to retrieve the magnetic scattering of {$Mo_{72}Fe_{30}$}.

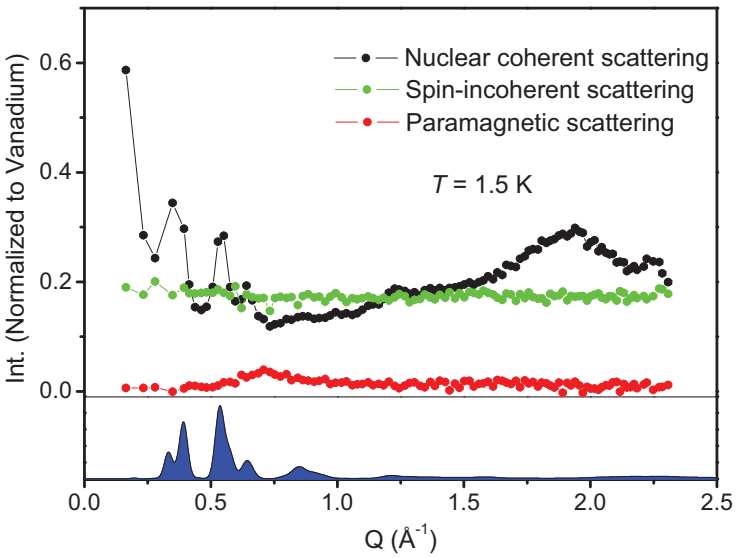

Figure 3-5-1 Nuclear coherent (black circles), spin-incoherent (green circles) and paramagnetic (red circles) contributions to the total scattering for {$Mo_{72}Fe_{30}$} at 1.5 K from *xyz*-polarization analysis at DNS. The blue area is a powder diffraction simulation convoluted with the experimental resolution.

Figure 3-5-2 presents the differential magnetic cross section, $d\sigma/d\Omega$, extracted from the total scattering cross section at 1.5, 2.5, 10, 20, 50 and 100 K from DNS measurements. The absolute magnetic cross sections were determined by calibration against the scattering of a known mass of vanadium standard. The scale of $d\sigma/d\Omega$ in **Figure 3-5-2** corresponds to the experimental curve at 100 K. The data at lower temperatures are each displaced vertically by 1.5 barn (sr^{-1}) per Fe atom for clarity.

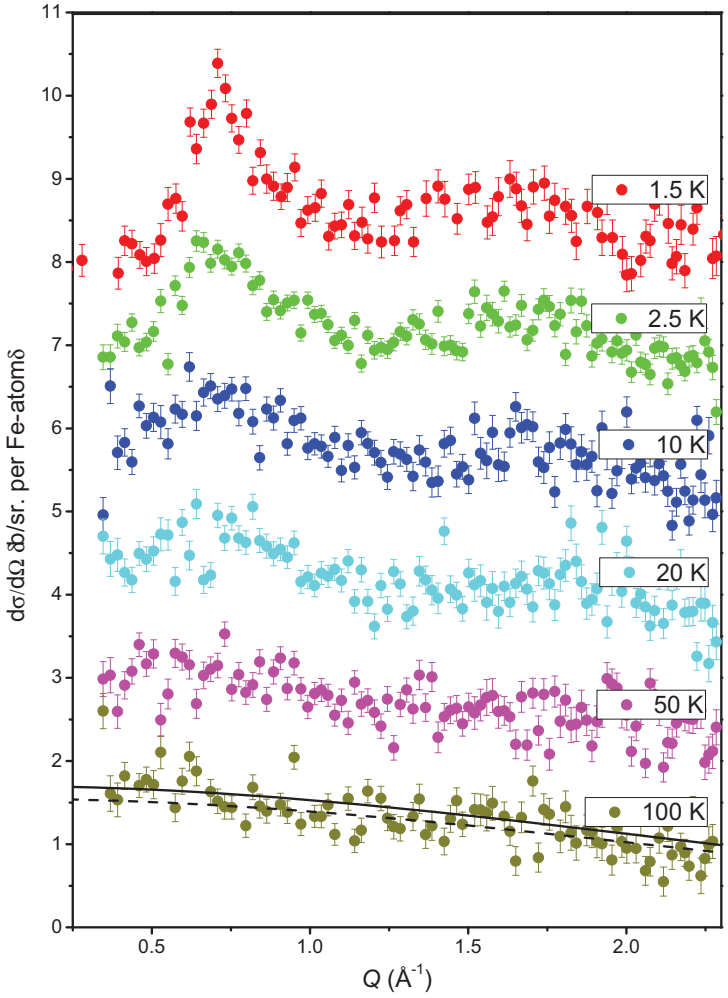

Figure 3-5-2 Temperature evaluation of the differential magnetic scattering cross section $d\sigma/d\Omega$ obtained from DNS measurements. The data at different temperatures are to scale and displaced vertically by 1.5 barn (sr^{-1}) per Fe atom each for clarity. The solid and the dashed lines indicate the pure and the 91% scaled paramagnetic form factor of Fe^{3+} ($S = 5/2$), respectively.

In the pure paramagnetic phase of {$Mo_{72}Fe_{30}$}, the Fe^{3+} moments should have no significant spin pair correlations and the Q dependence of the differential magnetic cross section should follow the paramagnetic form factor. As shown in **Figure 3-5-2**, the magnetic scattering above 50 K monotonically decreases with scattering vector Q, and agrees with the pure paramagnetic form factor of Fe^{3+} ions [97]. This result is

also consistent with the temperature dependence of the magnetic susceptibility of {$Mo_{72}Fe_{30}$} (see Section 3.2 and also Ref. [55]). Below 20 K, a diffuse peak at $Q \approx 0.70$ Å^{-1} is seen to evolve and sharpen upon cooling, indicating the presence of short-range antiferromagnetic spin correlations. No long-range magnetic order can be detected, even down to 1.5 K, owing to the strong geometrical spin frustration of the single molecules and the lack of intermolecular magnetic interactions.

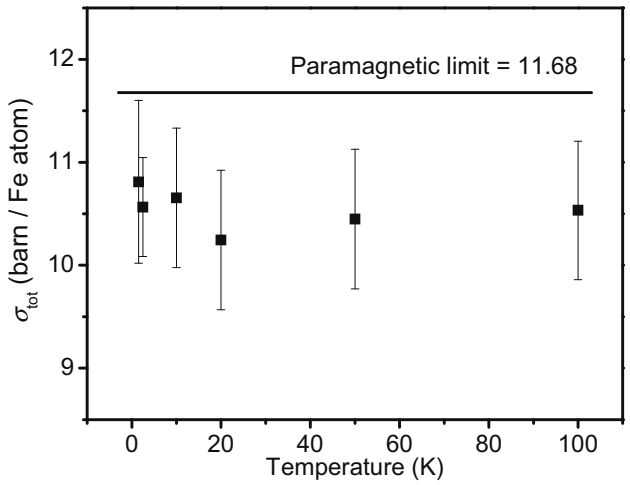

Figure 3-5-3 Temperature dependence of the total magnetic cross section (black squares) integrated over the Q range $0.39 < Q < 2.27$ Å^{-1} for {$Mo_{72}Fe_{30}$}.

The total differential magnetic cross section within the experimental energy window of DNS is determined by integration over the scattering vector Q at each temperature, shown as black squares in **Figure 3-5-3**. The integration is done over the Q range $0.39 < Q < 2.27$ Å^{-1}. The exchange interaction energy between the nearest Fe^{3+} neighbors is estimated to be ~ 1 meV (see Section 3.2 and Ref. [55]). The energy of the incident neutrons in these measurements is 3.6 meV. Therefore, the dynamic range of this spin system is well covered by the energy window of DNS. The data can be interpreted within a quasi-static approximation for the magnetic cross section. The total magnetic cross section of a pure paramagnet is given, ignoring the Debye-Waller term, by [74, 98]

$$\sigma_{\mathrm{tot}} = 8\pi \cdot \left(\frac{\lambda}{4\pi}\right)^2 \cdot \sum_i \left(\frac{\mathrm{d}\sigma}{\mathrm{d}\Omega}\right)_i Q_i \Delta Q_i$$
$$= 8\pi \cdot \left(\frac{\lambda}{4\pi}\right)^2 \cdot \sum_i \frac{2}{3}\left(\frac{\gamma e^2}{mc^2}\right)^2 S(S+1)\left\{\frac{1}{2} g F(Q_i)\right\}^2 Q_i \Delta Q_i \quad \text{barn (sr}^{-1}\text{)}, \qquad (3.5.4)$$

where $(\gamma e^2/mc^2)$ = -0.54×10^{-12} cm is the magnetic scattering length, S is the spin quantum number of the scattering ion, $F(Q)$ is the spin-only magnetic scattering form factor of Fe^{3+} (S = 5/2), and the Landé splitting factor g = 2 is taken [55]. The total magnetic cross section within the Q range from 0.39 to 2.27 Å^{-1} for the pure paramagnetic Fe^{3+} ion can be determined as 11.68 barns per Fe atom [97]. As shown in **Figure 3-5-3**, the values obtained from measurements are close to the paramagnetic limit. Thus it can be estimated that ~ 91% of the total magnetic cross section expected from the pure paramagnetic phase of {$Mo_{72}Fe_{30}$} has been observed at the investigated temperatures within the energy and Q window of DNS. The dashed line in **Figure 3-5-2** shows 91% of the paramagnetic form factor of Fe^{3+}, which agrees well with the magnetic differential cross section measured at 100 K.

3.5.3 Theoretical Simulations within Three-sublattice Spin Model

In order to determine the nature of the short-range spin correlations for the magnetic ground state of {$Mo_{72}Fe_{30}$}, I will compare the experimental data with a theoretical simulation based on the three-sublattice spin configuration model in this section. In agreement with our specific heat measurements presented in Section 3.3, the quantum rotational band theory [79] predicts that the lowest two ground-state energy levels, with total spin quantum number S = 1 and 2 respectively, locate at energies of 0.021 and 0.081 meV above the S = 0 ground state. At 1.5 K, these levels are appreciably populated. However, within the three-sublattice model, the S = 2 ground state corresponds to a rather small spin canting of 2° away from the coplanar S = 0 ground state. Within the statistical accuracy of our neutron scattering data, the resulting, minor change in spin correlations will not be detectable and thus I can safely assume that the spin correlations at 1.5 K predicted by the three-sublattice model should be very close to those of the S = 0 ground state. Experimentally, the true S = 0 ground state of {$Mo_{72}Fe_{30}$} is very difficult to reach in diffuse neutron scattering measurements, because the thermal conductivity of {$Mo_{72}Fe_{30}$} is poor and furthermore a large amount of sample is normally required in such measurements.

Therefore, the model used to reproduce the neutron scattering data is based on the S=0 ground state of $\{Mo_{72}Fe_{30}\}$. The spin correlations are calculated for a rigid configuration of classical S = 5/2 Fe^{3+} spins corresponding to the three-sublattice spin model. Only the spin correlations within individual molecules are considered in the simulation because the intermolecular magnetic correlations are negligible.

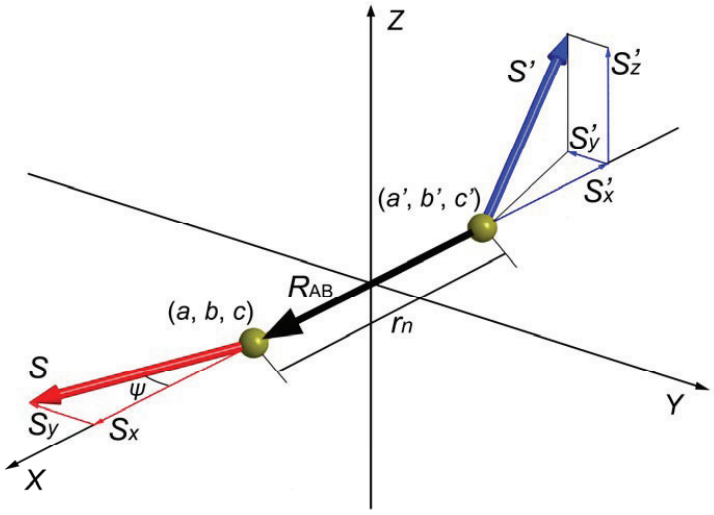

Figure 3-5-4 Two random spins ***S*** and ***S'***, and the definition of their projections on axis ***X***, ***Y*** and ***Z***.

The simulation starts with the equation given by I. A. Blech and B. L. Averbach for the differential magnetic scattering cross section of spin pairs, which, already in the powder average, can be written as [99]

$$\frac{d\sigma_{mag}}{d\Omega} = \frac{2}{3}S(S+1)\left(\frac{\gamma e^2}{mc^2}\right)^2 F^2(Q) + \left(\frac{\gamma e^2}{mc^2}\right)^2 F^2(Q) \times \sum_n \left[a_n \frac{\sin Qr_n}{Qr_n} + b_n \left(\frac{\sin Qr_n}{Q^3 r_n^3} - \frac{\cos Qr_n}{Q^2 r_n^2} \right) \right], \quad (3.5.5)$$

where $(\gamma e^2/mc^2)$ = -0.54×10^{-12} cm and $F(Q)$ have been introduced in Eq. (3.5.4), r_n is the distance from an atom at an arbitrary origin to the nth atom in the same molecule, and a_n and b_n are related to the probability of finding spin pairs with parallel components and can be expressed as

$$a_n = \left\langle \boldsymbol{S}_{\mathbf{y}} \cdot \boldsymbol{S}'_{\mathbf{y}} \right\rangle_n$$
$$b_n = 2\left\langle \boldsymbol{S}_{\mathbf{x}} \cdot \boldsymbol{S}'_{\mathbf{x}} \right\rangle_n - \left\langle \boldsymbol{S}_{\mathbf{y}} \cdot \boldsymbol{S}'_{\mathbf{y}} \right\rangle_n \quad (3.5.6)$$

where S_x, S_y and S'_x, S'_y are the projections of two spins S and S' on the X and Y directions, and are defined in **Figure 3-5-4**.

In **Figure 3-5-4**, S and S' are two random spins. Axis X is along the line going through the two spins. The X-Y plane is chosen such that S lies within this plane. Axis Z is then perpendicular to the X-Y plane. Given these definitions, the correlations of this spin pair in Z direction is zero. If the distance of the two spins is fixed as r_n, the result of Eq. (3.5.5) depends mainly on a_n and b_n, namely the scalar product of the corresponding projections of the two spins.

3.5.3.1. Spin Correlations of a Specific Ground State of {$Mo_{72}Fe_{30}$}

The first thought is to calculate the spin correlations of a specific ground state within the three-sublattice spin model. The calculation begins with the deriviation of the correlations of a random spin pair by means of Eqs. (3.5.5) and (3.5.6). As shown in **Figure 3-5-4**, assume the positions of two random spins S and S' are (a, b, c) and (a', b', c'), respectively. The vector of the bond between them is then $\boldsymbol{R}_{AB}$ = (a - a', b - b', c - c'). The X axis is defined along $\boldsymbol{R}_{AB}$ and the unit vector $\boldsymbol{e}_x$ of the X axis is given by $\boldsymbol{e}_x = \boldsymbol{R}_{AB} / |\boldsymbol{R}_{AB}|$.

The Z axis is perpendicular to S and $\boldsymbol{e}_x$. The unit vector of Z axis is given by

$$\boldsymbol{e}_z = \frac{\boldsymbol{S} \times \boldsymbol{R}_{AB}}{|\boldsymbol{S}||\boldsymbol{R}_{AB}|\sin\psi}. \quad (3.5.7)$$

Accordingly $\boldsymbol{e}_y$ is determined by performing the right-hand rule to $\boldsymbol{e}_z$ and $\boldsymbol{e}_x$.

Having determined $\boldsymbol{e}_x$, $\boldsymbol{e}_y$ and $\boldsymbol{e}_z$, the projections of S and S' in $\boldsymbol{e}_x$ and $\boldsymbol{e}_y$ directions can be expressed as following:

$$\boldsymbol{S}_x = \boldsymbol{S} \cdot \boldsymbol{e}_x \cdot \boldsymbol{e}_x \quad \text{and} \quad \boldsymbol{S}'_x = \boldsymbol{S}' \cdot \boldsymbol{e}_x \cdot \boldsymbol{e}_x$$
$$\boldsymbol{S}_y = \boldsymbol{S} \cdot \boldsymbol{e}_y \cdot \boldsymbol{e}_y \quad \text{and} \quad \boldsymbol{S}'_y = \boldsymbol{S}' \cdot \boldsymbol{e}_y \cdot \boldsymbol{e}_y \quad (3.5.8)$$

The a_n and b_n in Eqs. (3.5.5) and (3.5.6) for this spin pair can then be calculated by inserting Eq. (3.5.8) into Eq. (3.5.6). Therefore the spin correlations for a random spin

pair is determined by this method.

Select a random $\{Mo_{72}Fe_{30}\}$ molecule in the lattice (the position doesn't matter). Within the three-sublattice model, take the unit vectors of the three sublattices as (0, 0, -1), (-0.866, 0, 0.5) and (0.866, 0, 0.5). This is one of the ground states for the three-sublattice model, as shown in **Figure 3-5-5**.

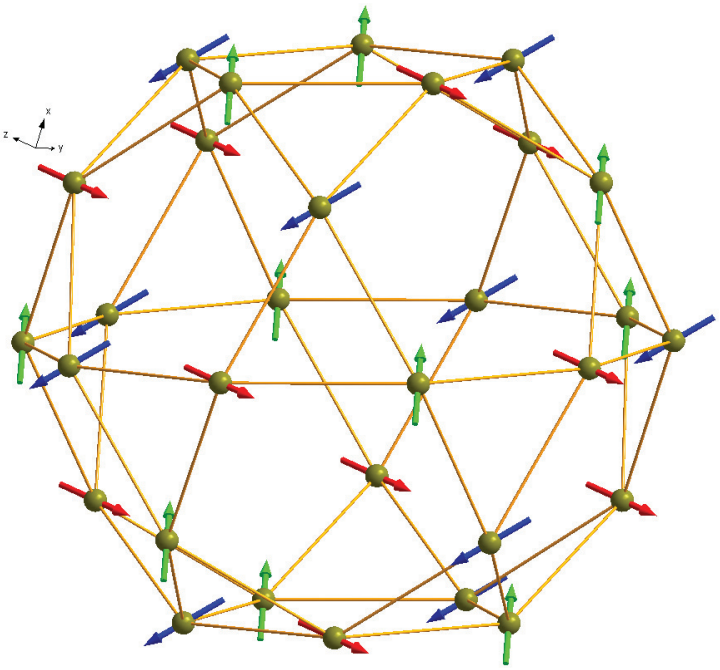

Figure 3-5-5 A specific ground state of the three-sublattice model (see text).

The spin correlations for this specific ground state can be calculated by applying the calculation for spin pair-correlation to all the spin pairs in this spin structure. The final result is plotted in **Figure 3-5-6**, along with the magnetic scattering cross section measured at 1.5 K. It can be seen that the simulation (blue line in **Figure 3-5-6**) is close to the experimental data (red circles in **Figure 3-5-6**). But clear deviations also exist. This suggests that the calculation for just one specific ground state is not enough to account for the measured magnetic scattering.

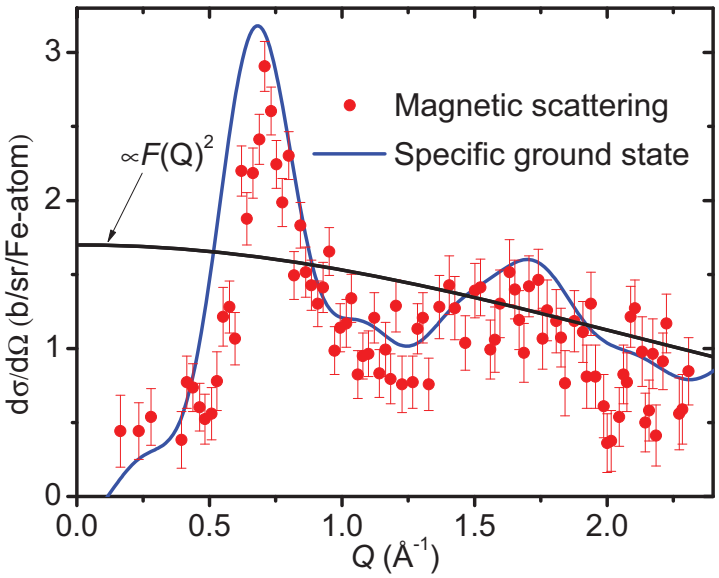

Figure 3-5-6 Calculation (blue line) for a specific ground state (see **Figure 3-5-5**) within the three-sublattice model of {$Mo_{72}Fe_{30}$}, along with the magnetic cross section (red circles) measured at 1.5 K. Black line: magnetic form factor of Fe^{3+} (S = 5/2) ions.

The specific ground state shown in **Figure 3-5-5** is of course not the only ground state for {$Mo_{72}Fe_{30}$}. When employing the three-sublattice model to {$Mo_{72}Fe_{30}$}, the spins within one molecule are no longer randomly arranged in the sense that the 30 Fe^{3+} spins are divided into three sublattices whose unit vectors are coplanar with intermediate angles of 120˚ [79, 80]. The 10 spins within each sublattice are parallel to each other. The sublattices can rotate as long as the 120˚ angular difference between them is kept. Therefore the true spin correlations for this three-sublattice spin model should be obtained by first summing the spin correlations over all versions of three-sublattice model and then averaging numerically. Setting a random Fe atom in the molecule as the origin, the simulation of the averaged spin correlations will be given in the next sections following three steps: (i) calculation of the spin correlations between the spins in the same sublattice, (ii) calculation of the spin correlations between the spins from different sublattices, and (iii) numerical average over different versions of the three-sublattice spin model.

3.5.3.2. Spin-pair Correlations between Spins in the Same Sublattice

In **Figure 3-5-7**, the spin S at the origin is shown with another spin S' from the same sublattice.

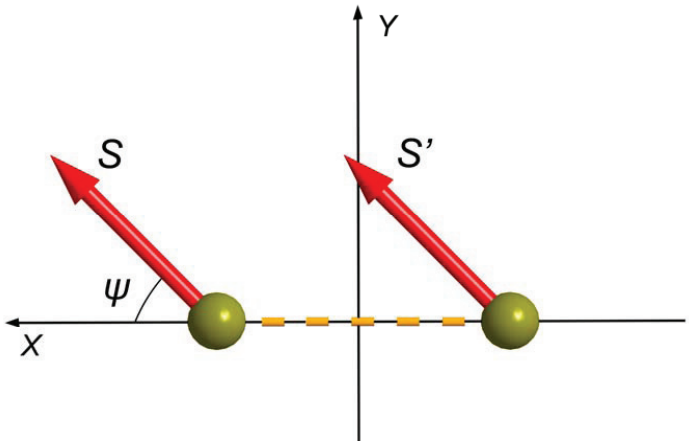

Figure 3-5-7 Two spins in the same sublattice of the three-sublattice model.

The vector of S and S' is random with an angle ψ from axis X. Since S and S' are parallel and $|S| = |S'|$,

$$S_x = S_{x'} = |S|\cdot\cos\psi\cdot e_x \quad \text{and} \quad S_y = S_{y'} = |S|\cdot\sin\psi\cdot e_y , \tag{3.5.9}$$

where e_x and e_y denote the unit vector of X and Y axis, respectively. Substitute Eq. (3.5.9) into Eq. (3.5.6),

$$\begin{aligned} a_n &= |S|^2 \sin^2\psi \\ b_n &= |S|^2 \left(2\cos^2\psi - \sin^2\psi\right) \end{aligned} . \tag{3.5.10}$$

Eq. (3.5.10) gives the coefficients a_n and b_n for spin pairs in the same sublattice, where it can be found that a_n and b_n depend only on the angle ψ. Given the spin quantum number S and the atomic distances, the spin pair-correlations between the origin spin and the other 9 spins in the same sublattice can then be determined using Eq. (3.5.5) once the vector of the origin spin is fixed.

3.5.3.3. Spin-pair Correlations between Spins from Two Different Sublattices

Before calculating the spin pair correlations between spins from two different sublattices, it should be noticed that there exist an infinite number of specific ground state configurations when employing the three-sublattice model to this icosidodecahedral spin structure, because the three spin sublattices can rotate as long as the angle remains 120˚ between their unit vectors. In any case, the analysis can start with the correlation between two spins, S and S', from two different sublattices in this model, as shown in **Figure 3-5-8**. S' can take all relative orientations, keeping the 120˚ angle with respect to the direction of S. As such, we can always obtain the spin S'' (see **Figure 3-5-8**) by a rotation of S' by 180˚ about the direction of S. Thus S and S'' belong to another configuration of the three-sublattice model. The final simulating result should be the numerical average of the spin correlations of all the spin configurations within the three-sublattice model. In the case of {$Mo_{72}Fe_{30}$}, the simulation could be greatly simplified in the sense that the relationship between spin correlation and spin direction could be neglected as long as the rigid three-sublattice model is fulfilled. The proof to this statement is given below.

Consider the total spin correlations of the two spin pairs, S-S' and S-S'', where $|S|=|S'|=|S''|$. As to the coordinate system shown in **Figure 3-5-8**, the spin correlations of both S-S' and S-S'' are zero along the Z direction because S has a zero projection on Z axis. So the discussion can be restricted to the X-Y plane. The projections of S' and S'' in X-Y plane are denoted as S'_p and S''_p, respectively. In order to show the angles between S, S', and S'' more clearly, spin S_1 is drawn at the starting point of S' and S'' and is parallel to S.

Figure 3-5-9 shows the X-Y plane, where S, S_1, S'_p and S''_p are plotted, S_1 is parallel to S, and β is the angle between S_1 and S'_p. Without loss of generality, the angle between S_1 and S' is assumed as α. α and β are also shown in **Figure 3-5-6**. $\cos\alpha$ and $\cos\beta$ are carrying the same sign.

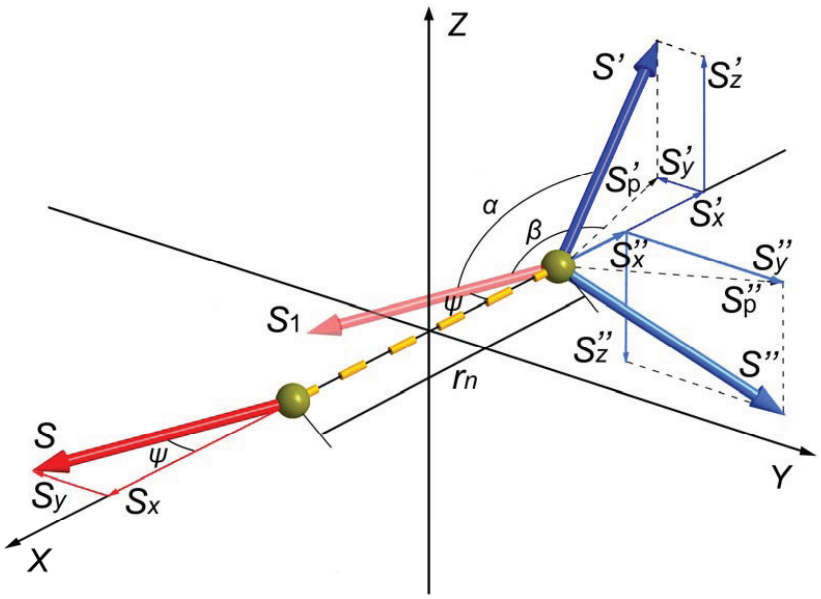

Figure 3-5-8 Spin vectors *S*, *S'*, *S''*, and their projections on axis *X*, *Y* and *Z*. The two Fe^{3+} ions belong to different sublattices. *S''* is generated by a rotation of *S'* by 180° around the direction of *S*. S_1 is parallel to *S* but not a real spin, which has been drawn to show the relation between *S*, *S'*, and *S''*.

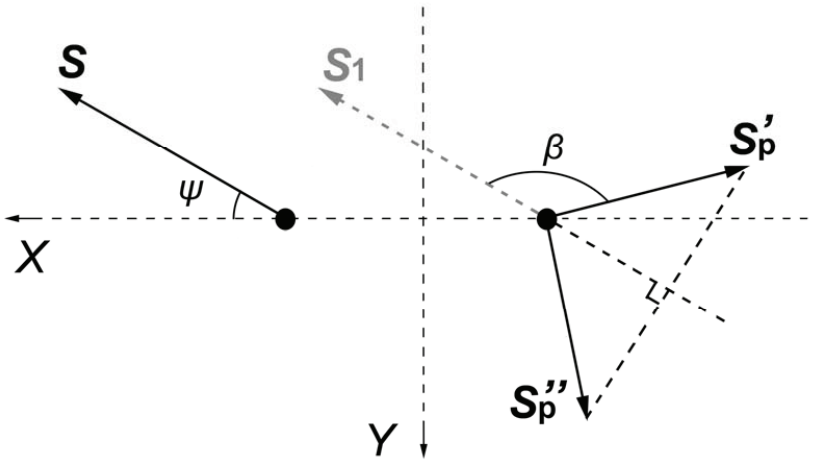

Figure 3-5-9 Spin vector *S* and the projections of *S'* and *S''* in *X*-*Y* plane, S_p' and S_p''. S_1 is parallel to *S*.

If $\cos\beta \neq 0$, $|S'_{\mathrm{p}}|$ and $|S''_{\mathrm{p}}|$ can be expressed as follows,

$$\left|\boldsymbol{S}'_{\mathrm{p}}\right| = \left|\boldsymbol{S}''_{\mathrm{p}}\right| = \frac{\left|\boldsymbol{S}'\right| \cdot \left|\cos\alpha\right|}{\left|\cos\beta\right|} = \frac{\left|\boldsymbol{S}'\right| \cdot \cos\alpha}{\cos\beta}. \tag{3.5.11}$$

The projections of $\boldsymbol{S}$, $\boldsymbol{S}'$, and $\boldsymbol{S}''$ on $\boldsymbol{X}$ and $\boldsymbol{Y}$ axis are

$$\begin{aligned} \boldsymbol{S}_{\boldsymbol{x}} &= \left|\boldsymbol{S}\right|\cos\psi \cdot \boldsymbol{e}_x & \boldsymbol{S}_{\boldsymbol{y}} &= \left|\boldsymbol{S}\right|\sin\psi \cdot \boldsymbol{e}_y \\ \boldsymbol{S}'_{\boldsymbol{x}} &= \left|\boldsymbol{S}'_{\mathrm{p}}\right|\cos(\psi+\beta) \cdot \boldsymbol{e}_x \quad \text{and} & \boldsymbol{S}'_{\boldsymbol{y}} &= \left|\boldsymbol{S}'_{\mathrm{p}}\right|\sin(\psi+\beta) \cdot \boldsymbol{e}_y . \\ \boldsymbol{S}''_{\boldsymbol{x}} &= \left|\boldsymbol{S}''_{\mathrm{p}}\right|\cos(\psi-\beta) \cdot \boldsymbol{e}_x & \boldsymbol{S}''_{\boldsymbol{y}} &= \left|\boldsymbol{S}''_{\mathrm{p}}\right|\sin(\psi-\beta) \cdot \boldsymbol{e}_y \end{aligned} \tag{3.5.12}$$

From Eq. (3.5.6), the average a_{n} and b_{n} for correlations of spin pairs $\boldsymbol{S}$-$\boldsymbol{S}'$ and $\boldsymbol{S}$-$\boldsymbol{S}''$ are

$$\begin{aligned} \overline{a_n} &= \frac{1}{2}\left\{\boldsymbol{S}_{\boldsymbol{y}} \cdot \boldsymbol{S}'_{\boldsymbol{y}} + \boldsymbol{S}_{\boldsymbol{y}} \cdot \boldsymbol{S}''_{\boldsymbol{y}}\right\} \\ &= \frac{1}{2}\left\{\left|\boldsymbol{S}\right|\sin\psi \cdot \left|\boldsymbol{S}'_{\mathrm{p}}\right|\sin\left(\psi+\beta\right) + \left|\boldsymbol{S}\right|\sin\psi \cdot \left|\boldsymbol{S}''_{\mathrm{p}}\right|\sin\left(\psi-\beta\right)\right\} \\ &= \frac{1}{2}\left|\boldsymbol{S}\right|^2 \frac{\cos\alpha}{\cos\beta}\sin\psi\left\{\sin\left(\psi+\beta\right) + \sin\left(\psi-\beta\right)\right\} \\ &= \frac{1}{2}\left|\boldsymbol{S}\right|^2 \frac{\cos\alpha}{\cos\beta}\sin\psi \cdot 2\sin\psi\cos\beta \\ &= \left|\boldsymbol{S}\right|^2 \cos\alpha\sin^2\psi \end{aligned} \tag{3.5.13}$$

and,

$$\begin{aligned} \overline{b_n} &= \frac{1}{2}\left\{\left(2\boldsymbol{S}_{\boldsymbol{x}} \cdot \boldsymbol{S}'_{\boldsymbol{x}} - \boldsymbol{S}_{\boldsymbol{y}} \cdot \boldsymbol{S}'_{\boldsymbol{y}}\right) + \left(2\boldsymbol{S}_{\boldsymbol{x}} \cdot \boldsymbol{S}''_{\boldsymbol{x}} - \boldsymbol{S}_{\boldsymbol{y}} \cdot \boldsymbol{S}''_{\boldsymbol{y}}\right)\right\} \\ &= \frac{1}{2}\left\{2\left(\left|\boldsymbol{S}\right|\cos\psi \cdot \left|\boldsymbol{S}'_{\mathrm{p}}\right|\cos\left(\psi+\beta\right) + \left|\boldsymbol{S}\right|\cos\psi \cdot \left|\boldsymbol{S}''_{\mathrm{p}}\right|\cos\left(\psi-\beta\right)\right) - 2\left|\boldsymbol{S}\right|^2\cos\alpha\sin^2\psi\right\} \\ &= \frac{1}{2}\left\{2\left|\boldsymbol{S}\right|^2 \frac{\cos\alpha}{\cos\beta}\cos\psi\left(\cos\left(\psi+\beta\right) + \cos\left(\psi-\beta\right)\right) - 2\left|\boldsymbol{S}\right|^2\cos\alpha\sin^2\psi\right\} \\ &= \frac{1}{2}\left\{2\left|\boldsymbol{S}\right|^2 \frac{\cos\alpha}{\cos\beta}\cos\psi \cdot 2\cos\psi\cos\beta - 2\left|\boldsymbol{S}\right|^2\cos\alpha\sin^2\psi\right\} \\ &= \left|\boldsymbol{S}\right|^2\cos\alpha\left\{2\cos^2\psi - \sin^2\psi\right\} \end{aligned} \tag{3.5.14}$$

In case of $\cos\beta = 0$, spin $\boldsymbol{S}$ is perpendicular to $\boldsymbol{S}'$ and $\boldsymbol{S}''$ ($\cos\alpha = 0$). The averaged a_n and b_n for spin pairs $\boldsymbol{S}$-$\boldsymbol{S}'$ and $\boldsymbol{S}$-$\boldsymbol{S}''$ are both zero. Therefore the averaged a_n and b_n can also be expressed as Eqs. (3.5.13) and (3.5.14), respectively.

Obviously, when $\alpha = 0$ (two spins are parallel), the two equations derived above become Eq. (3.5.10). It means I can unite the expressions for spin correlations of spins

within the same sublattice and spins from different sublattices. Once the angle α between S and S' is fixed, the average spin correlations of spin pairs S-S'' and S-S'' depend only on the vector of the origin, S. Of course it doesn't matter how many vectors of S' there are, as long as S'' is achievable by rotating S' by 180° with respect to the direction of S.

3.5.3.4. Numerically-averaged Spin Correlations for $\{Mo_{72}Fe_{30}\}$

Employing Eq. (3.5.13) and Eq. (3.5.14) to calculate the spin correlations of $\{Mo_{72}Fe_{30}\}$ within the three sublattice model, the mean a_n and b_n are as follows:

$$\begin{aligned} \overline{a_n} &= -\frac{1}{2}S(S+1)\sin^2\psi \\ \overline{b_n} &= -\frac{1}{2}S(S+1)\left(2\cos^2\psi - \sin^2\psi\right) \end{aligned} \quad \text{for spins from different sublattice,} \qquad (3.5.15)$$

and

$$\begin{aligned} a_n &= S(S+1)\sin^2\psi \\ b_n &= S(S+1)\left(2\cos^2\psi - \sin^2\psi\right) \end{aligned} \quad \text{for spins in the same sublattice,} \qquad (3.5.16)$$

where $S = 5/2$ is the spin quantum number of Fe^{3+} ions. Obviously, the spin pair correlations in the three-sublattice model of $\{Mo_{72}Fe_{30}\}$ depend only on ψ, namely the vector of the spin at the origin.

It should be noticed that actually every molecule in the sample could possess a specific ground state within the three-sublattice spin model. Therefore I simulated the spin correlations of $\{Mo_{72}Fe_{30}\}$ within an individual molecule and then take a numerical average over all molecules. The Fe^{3+} ion at the origin is chosen arbitrarily. The numerical simulation is performed for a number of different spin vectors randomly laid at the origin, i.e., a collection of different spin ground states of $\{Mo_{72}Fe_{30}\}$ molecule. The numbers of the random vectors of the origin spin used in the simulation are 30, 100, 250, 1 000, 10 000, 65 000, and 250 000.

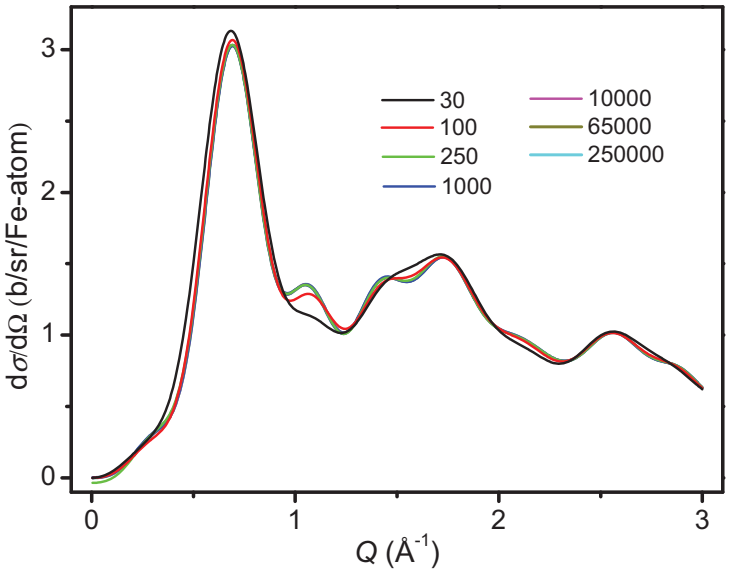

Figure 3-5-10 Simulations of spin pair correlations for {$Mo_{72}Fe_{30}$} within the three-sublattice model. The curves correspond to the simulations with different numbers (indicated by various colors) of random vectors of the origin spin.

As shown in **Figure 3-5-10**, a satisfactory degree of convergence has already been achieved for 1000 random vectors of the origin spin in my simulation. The averaged spin correlations for 250 000 random vectors of the origin spin are plotted in **Figure 3-5-11** as a blue line, which is quite close to the measured profile of the magnetic diffuse scattering (red circles in **Figure 3-5-11**). Both the pronounced peak at ~ 0.70 $Å^{-1}$ and the broad feature at ~ 1.60 $Å^{-1}$ are well reproduced in the simulation. The dashed green line in **Figure 3-5-11** represents the 91% scaled simulation curve, which agrees better with the experimental data since 91% of the magnetic scattering was observed in our measurements at DNS.

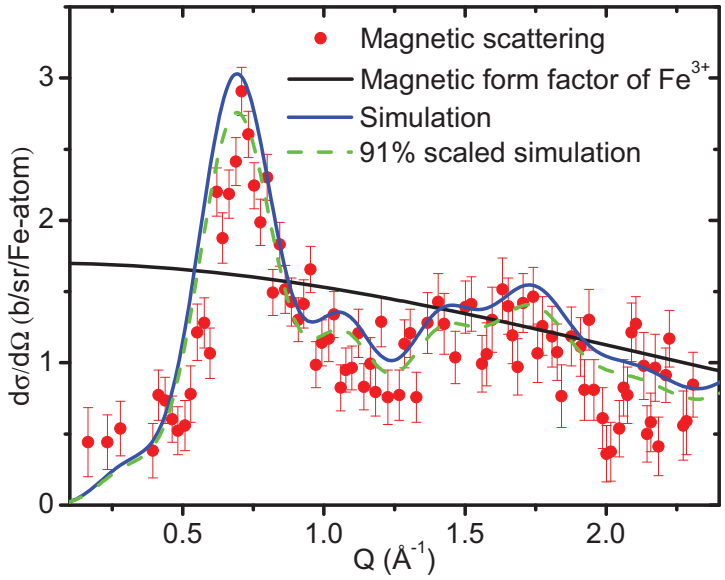

Figure 3-5-11 Magnetic diffuse scattering at 1.5 K in absolute units for {$Mo_{72}Fe_{30}$} (red circles); simulation of the averaged spin pair correlations for {$Mo_{72}Fe_{30}$} within the three-sublattice spin configuration model (blue line). Green dashed line: 91% scaled simulation curve.

3.5.3.5. Simplified Method to Simulate Spin Correlations

In the above calculation of spin-pair correlations for the three-sublattice model, one has to integrate ψ over the space. Considering Eqs. (3.5.5), (3.5.13) and (3.5.14), the angular integration of ψ omits the trigonometric functions containing ψ in the final spin correlations. *Hence, if the vectors of two spins can take any orientation whilst keeping a constant angle between them, the final result of the spin-pair correlations depends only on the distance and the relative angle of the two spins.*

From Eqs. (3.5.5) and (3.5.6), the term with b_n arises from the directional nature of the magnetic neutron scattering. But as discussed above, the spin correlations of {$Mo_{72}Fe_{30}$} within the three-sublattice model depend only on the distance and the relative angle of the spins. This means the interrelationship between spin correlation and spin direction can be neglected, so that the term with b_n can be omitted from Eq. (3.5.5) [99]. If $b_n = 0$ in Eq. (3.5.6) and consider $\langle S_z \cdot S'_z \rangle_n = 0$, then we have

$$a_n = \left\langle \boldsymbol{S}_y \cdot \boldsymbol{S}'_y \right\rangle_n = 2\left\langle \boldsymbol{S}_x \cdot \boldsymbol{S}'_x \right\rangle_n = \frac{2}{3}\left\langle \boldsymbol{S} \cdot \boldsymbol{S}' \right\rangle_n, \tag{3.5.17}$$

Thus a more simplified equation to calculate spin-pair correlations of {$Mo_{72}Fe_{30}$} molecule is given below. Taking the powder average and neglecting the possible relationship between spin correlation and spin orientation, the differential magnetic scattering cross section in the quasi-static approximation can be described in terms of the Fourier transform of the spin pair-correlation function [47],

$$\frac{\mathrm{d}\sigma_{\mathrm{mag}}}{\mathrm{d}\Omega}(Q)=\frac{2}{3}\left(\frac{\gamma e^2}{mc^2}\right)^2 F^2(Q)\sum_r\langle \boldsymbol{S}_0\cdot\boldsymbol{S}_r\rangle\frac{\sin Qr}{Qr}, \tag{3.5.18}$$

where $\boldsymbol{S}_0$ and $\boldsymbol{S}_r$ are the atomic spin vectors at the origin and the nuclear lattice position $\boldsymbol{r}$.

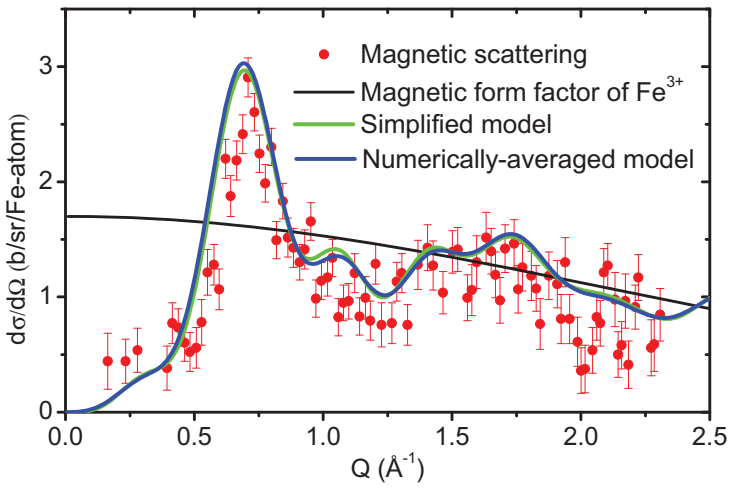

Figure 3-5-12 Comparison of the simulation results of the spin correlations for-three sublattice model using the numerically-averaged model (blue line and see Section 3.5.3.2-4) and the simplified model (green line and see Section 3.5.3.5). Red circles: Magnetic diffuse scattering at 1.5 K in absolute units for {$Mo_{72}Fe_{30}$}.

The spin pair-correlation function given by Eq. (3.5.18) depends only on the atomic distance r and the relative angle between $\boldsymbol{S}_0$ and $\boldsymbol{S}_r$. The simulation using Eq. (3.5.18) is carried out for the three-sublattice model of {$Mo_{72}Fe_{30}$}, and is compared with the simulation using the numerically-averaged model introduced in Section 3.5.3.2-4 along with the measured profile of magnetic diffuse scattering in **Figure 3-5-12**. It can be seen that the simulation using the simplified model nearly coincides with the one

using the numerically-averaged model. The tiny deviations between them are due to the approximation used in the simplified model, which omits the b_n term in Eq. (3.5.5). The result of the simplified model proves that the b_n term contributes little in the spin correlations of {$Mo_{72}Fe_{30}$}. This is a surprising result that *the spin correlations of a 3D spin structure like {$Mo_{72}Fe_{30}$} can be simulated simply by ignoring the 3D structure itself if the spins can rotate freely on their positions whilst keeping relative angles constant, owing to the fact that only the relative angles and the atomic distances matter in the simulation.* {$Mo_{72}Fe_{30}$} has been found certainly to be an ideal system to investigate this effect for three reasons: first, the magnetic ground state can be characterized by a rigid three-sublattice spin model which allows the spins to rotate with a constant relative angle of 120˚ between the spin sublattices; second, the molecular-magnet nature of {$Mo_{72}Fe_{30}$} plays an important role because it confines the spin correlations within individual molecules; third, {$Mo_{72}Fe_{30}$} molecule possesses highly symmetric, icosidodecahedral spin structure which makes a direct comparison with the measured magnetic cross section possible since no average among the different spin positions is needed.

3.5.4 Discussion

In Section 3.5, the spin correlations of {$Mo_{72}Fe_{30}$} have been investigated both experimentally and theoretically. The diffuse neutron scattering with polarization analysis on {$Mo_{72}Fe_{30}$} revealed clear short-range spin correlations below 20 K. The simulations were carried out based on the three sublattice spin model for {$Mo_{72}Fe_{30}$}. The spin correlations were first simulated by integrating all possible ground state spin configurations within the three-sublattice model, and agree well with the measured magnetic scattering cross section. A simplified spin correlation function was also used to calculate the spin correlations of {$Mo_{72}Fe_{30}$} within the three-sublattice model, which ignored the possible relationship between spin correlation and spin orientation. The simplified function nearly coincided with the result given by the numerically-averaged method. It has been found that all the simulation results are in reasonable agreement with the magnetic scattering cross section of {$Mo_{72}Fe_{30}$} obtained at 1.5 K by means of polarized neutron scattering.

A more general conclusion from the present investigation is the spin pair correlations depend only on the distance and the relative angle of the two spins in the spin pair if the vectors of the two spins can take any orientation whilst keeping a

constant angle between them. The direct consequence of employing this effect to the case of {$Mo_{72}Fe_{30}$} is that the spin correlations of this 3D spin structure can be simply calculated by considering the distances and the relative angles of the spins only, and ignoring the complex 3D structure itself. Hence, it can be concluded that the three-sublattice spin configuration can explain the magnetic diffuse neutron scattering from {$Mo_{72}Fe_{30}$} successfully. The spin correlations measured from this large, spin-frustrated magnetic system arise mainly from the individual molecules, due to the intrinsic properties of {$Mo_{72}Fe_{30}$} as a molecular magnet.

It must be noted here that all the theoretical simulations in this section are limited to a rigid three-sublattice spin configuration of classical $S = 5/2$ Fe^{3+} spins. The division of the three sublattices from 30 Fe^{3+} ions is not unique and the simulations in this section cannot distinguish the different versions because they possess the same spin correlation functions [100].

3.6 Summary

The aim of Chapter 3 is to determine the nature of the magnetic ground state of the spin-frustrated molecular magnet {$Mo_{72}Fe_{30}$}. {$Mo_{72}Fe_{30}$} is large and fascinating molecular magnet with highly symmetric icosidodecahedral spin structure. The magnetic structure of {$Mo_{72}Fe_{30}$} was investigated by means of DC magnetic susceptibility, specific heat, inelastic neutron scattering and polarized neutron scattering measurements. No long-range magnetic order has been detected at all investigated temperatures. DC magnetic susceptibility showed that the nearest-neighbor Fe^{3+} ions are antiferromagnetically coupled with an effective exchange constant $J_{eff} \approx 0.11$ meV. Two low-lying magnetic excitations at ~ 0.09 meV and ~ 0.64 meV were identified by analyzing two Schottky anomalies in the specific heat data. Based on the theoretical prediction of the quantum rotational band model, the former excitation is assigned to the intraband energy gaps within the ground state levels, while the latter one to the interband splitting between the ground state and the first excited state levels. The inelastic neutron scattering measurements on {$Mo_{72}Fe_{30}$} gave no clear evidence for magnetic excitations due to the high background. The diffuse neutron scattering with polarization analysis on {$Mo_{72}Fe_{30}$} show clear short-range spin correlations. The spin correlations collected at 1.5 K

agree well with the simulations of the Fourier transform of the spin pair-correlation function using the three-sublattice spin configuration model. The spin correlations were found to be localized within individual molecules, which is reasonable for $\{Mo_{72}Fe_{30}\}$ as a molecular magnet. A more general conclusion drawn from the present investigation is that the spin pair correlations depend only on the distance and the relative angle of the two spins in the spin pair if the vectors of the two spins can take any orientation whilst keeping a constant angle between them.

In conclusion, it is found that the three-sublattice model can explain the presented experiments well, in terms of both the magnetic excitations and spin correlations. The three-sublattice spin model is therefore a good approach to the magnetic ground state of $\{Mo_{72}Fe_{30}\}$.

CHAPTER 4:

Single-molecule Magnet $\{V_{15}As_6\}$

4.1 Introduction to $\{V_{15}As_6\}$

Single molecule magnets (SMMs) have attracted much attention because of their novel properties such as single-molecule hysteresis [8, 15] and quantum tunneling of the magnetization [12, 15, 16, 101]. Two of the best known examples are $\{Mn_{12}\}$ [102] and $\{Fe_8\}$ [12]. An important character of these systems is that they possess high spin ground state $S = 10$ and a potential energy barrier to the reorientation of the magnetic moment, which makes SMMs potential candidates for massive magnetic data storage. Besides the high-spin SMMs, the polyoxovanadate compound $K_6[V_{15}As_6O_{42}(H_2O)]\cdot 8H_2O$ [103], $\{V_{15}As_6\}$ for short, exhibits also magnetization hysteresis behavior and quantum tunneling of purely molecular origin but with an low-spin $S = 1/2$ ground state and no evident potential energy barrier to the reorientation of the magnetic moment [104]. $\{V_{15}As_6\}$ possesses interesting magnetic and electronic properties and potential use for quantum computing [23].

4.1.1 Three-spin Approximation of $\{V_{15}As_6\}$

The $\{V_{15}As_6\}$ compound crystallizes in trigonal crystal system with space group $R\bar{3}c$ and lattice parameters a = 14.029 Å, α = 79.26° and V_{cell} = 2632 Å^3 [103]. Each unit cell contains two V_{15} clusters and the magnetic interaction between the spins of near-neighbor clusters is negligible. The ball-and-stick representation of $\{V_{15}As_6\}$ is shown in **Figure 4-1-1** [23]. The 15 V^{4+} ions of spin $S = 1/2$ form a quasi-spherical structure with layers of different magnetizations: a large central V_3 equilateral spin triangle is sandwiched by two smaller V_6 nonplanar hexagons [23, 103]. The 15 spins are coupled by antiferromagnetic superexchange interaction through different pathways [23, 104, 105-108].

In principle, the discussion on this molecule should be addressed to all 15 spins (Hilbert space dimension: 2^{15}). However, considerable simplifications can be made. In a first static approximation, the couplings between the central spin triangle and the hexagons cancel each other due to the strong spin frustration in the molecule [109]. The two V_6 hexagons are rather stiff due to the large antiferromagnetic exchange interactions, which are large enough to exclude a significant contribution of the hexagons to the net magnetism even at comparably high temperature [23]. The magnetic properties of $\{V_{15}As_6\}$ are therefore governed by the central, equilateral V_3

triangle, i.e., the so-called three spin model of $\{V_{15}As_6\}$.

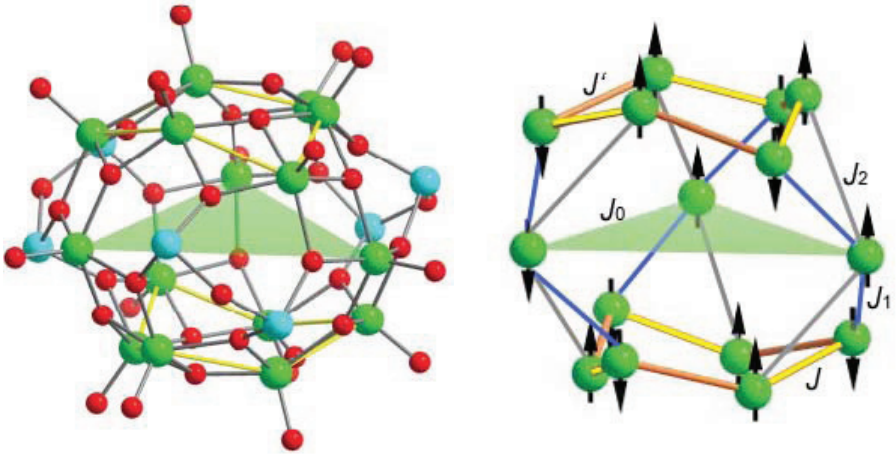

Figure 4-1-1 Left: Ball-and-stick representation of $\{V_{15}As_6\}$ (green, V; light blue, As; red, O). The central V_3 triangle is highlighted by green area. **Right**: Sketch map of the V^{4+} spin arrangement at low temperatures with various exchange constants. The strongly coupled spin pairs in hexagons are highlighted by yellow lines. [Picture taken from P. Kögerler, B. Tsukerblat and A. Müller, *Dalton Trans.* **39** (2010) 21]

In this model, each spin hexagon consists of three strongly coupled spin pairs with exchange constant $J \sim -800$ K. The spin pairs are coupled to each other with exchange constant $J' \sim -150$ K. The three spins on the central triangle are weakly and indirectly coupled to each other, in the sense that each spin of the central triangle is coupled to the two nearest spin pairs (one from the upper hexagon and the other from the lower hexagon) with exchange constants $J_1 \sim -150$ K and $J_2 \sim -300$ K. This means the 15 spins can be divided into three five-spin groups with a resultant spin $S = 1/2$ for each group. Hence in fact, the three-spin model involves all 15 spins and therefore the Hilbert space dimension remains 2^{15}, instead of 2^3 for the system with three spins. The exchange constants are shown in the right panel of **Figure 4-1-1** [110]**.**

The three-spin model was proposed to describe the low-temperature spin model of $\{V_{15}As_6\}$, and successfully predicted the low-lying magnetic excitation spectrum [110]. The ground state involves two spin doublet states ($S = 1/2$) slightly shifted from each other by slight deviations from the trigonal symmetry of the cluster [106], and a spin quartet excited state ($S = 3/2$), as shown in **Figure 4-1-2 (a)**. These low-lying states

are well isolated from the remaining quasi-continuum of spin levels above the S = 3/2 excited state, as shown in **Figure 4-1-2 (b)**.

The symmetry lowering of the cluster lifts the degeneracy of the spin doublet ground state (S = 1/2) leading to a first order zero-field splitting Δ_0 (plus small second order correction) [32, 105-108]. And the splitting in the quartet excited state (S = 3/2) belongs to a second-order effect caused by mixing S = 3/2 and S = 1/2 spin multiplets. **Figure 4-1-2 (a)** shows the Zeeman effect to these two low-lying states [23].

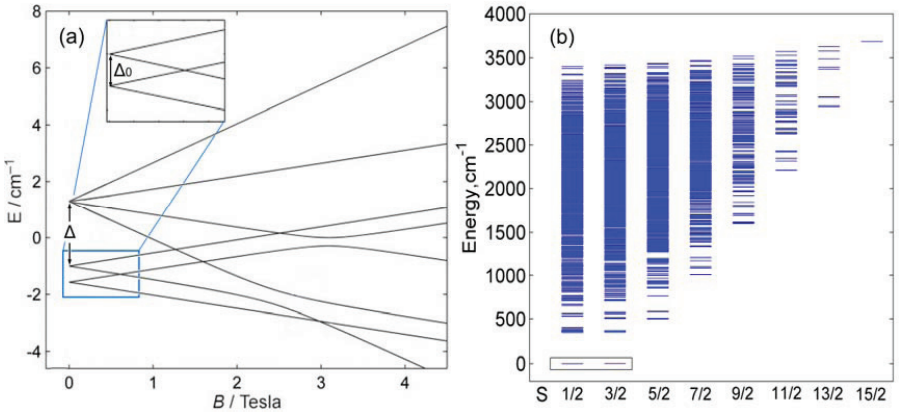

Figure 4-1-2 (a) Field dependence of the splitting of the magnetic sublevels. Δ_0 indicates the splitting of the two ground-state doublets; Δ is the energy gap between the S = 1/2 ground state and the low-lying excited state; **(b)** Zero-field energy pattern of $\{V_{15}As_6\}$ as a function of the total spin S. The ground state (S = 1/2) and the low-lying excited state (S = 3/2) are indicated in the box. [Pictures taken from P. Kögerler, B. Tsukerblat and A. Müller, *Dalton Trans.* **39** (2010) 21; B. Tsukerblat, A. Tarantul and A. Müller, *Physics Letters A* **353** (2006) 48]

The novel magnetic structure of $\{V_{15}As_6\}$ has resulted in more than 60 publications of both experimental and theoretical aspects. The staircase-like feature of the adiabatic magnetization *vs.* applied in-plane field at low temperatures has been well explained by the three-spin model of $\{V_{15}As_6\}$ [111]. Quantum oscillations have been observed from $\{V_{15}As_6\}$, suggesting that $\{V_{15}As_6\}$ could be a promising candidate to study the quantum coherence and a possible model system to investigate quantum information processing [32]. Inelastic neutron scattering measurements observed

several field-dependent transitions and provided a comprehensive understanding of the low-lying spin states, which showed that the zero-field splitting between the S = 1/2 ground state doublet is due to the symmetry lowering of the cluster [106, 112], rather than the Dzyaloshinskii-Moriya (DM) interactions [113].

4.1.2 Motivation

Besides being a promising candidate to study quantum tunneling or quantum coherence at nanoscale, {$V_{15}As_6$} also represents a quantum model for geometrical frustration at the molecular level. However, small irregularities (scalene distortion in this case) remove part of the frustration and result in a stabilized ground-state with a gap. The three-spin model has been established to approach the magnetic ground state of {$V_{15}As_6$}, and been supported by extensive experimental studies, including static magnetic susceptibility [110, 114], EPR [108, 115, 116], inelastic neutron scattering [106, 112, 117], and so on [23]. But no specific heat on {$V_{15}As_6$} has been reported. In this chapter, I present the low-temperature field-dependent specific heat measurements on nondeuterated {$V_{15}As_6$} to identify the low-lying spin states, and polarized neutron scattering measurements to study the spin correlations of deuterated {$V_{15}As_6$}.

4.2 Magnetic Properties of {$V_{15}As_6$}

The magnetic susceptibility of {$V_{15}As_6$} was measured using a Superconducting Quantum Interference Device (SQUID) magnetometer. **Figure 4-2-1** shows the molar magnetic susceptibility M/H and the inverse susceptibility of {$V_{15}As_6$} measured from 2 K to 300 K under a probing field of 500 Oe. As expected, there is no magnetic phase transition within the investigated temperature range. At high temperatures around 300 K, the inverse susceptibility doesn't follow the Curie-Weiss law, suggesting that strong spin coupling persists upon warming the sample to room temperature. This is consistent with the strong coupling ($J \approx$ -800 K) found between the spin pairs in hexagons [114, 118].

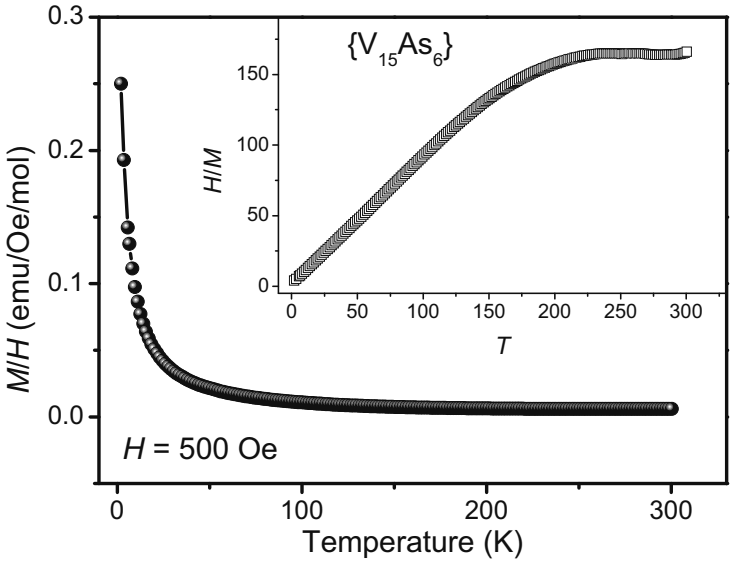

Figure 4-2-1 Magnetic susceptibility M/H and inverse susceptibility H/M of {$V_{15}As_6$} measured with a probing field of H = 500 Oe.

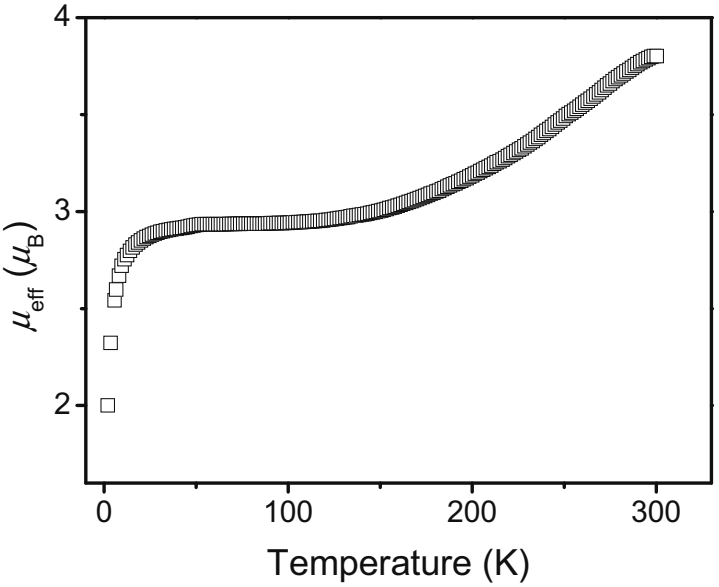

Figure 4-2-2 Temperature dependence of the effective moment of {$V_{15}As_6$}.

Figure 4-2-2 shows the temperature dependence of the effective moment of {$V_{15}As_6$}, which is calculated in terms of Eq. (3.2.2). The effective moment of {$V_{15}As_6$} keeps increasing to ~ 3.8 μ_B upon warming to 300 K, while the effective moment of 15 noninteracting V^{4+} spins ($S = 1/2$) is 6.7 μ_B. This indicates that strong antiferromagnetic coupling persists until at least room temperature. The effective moment increases sharply as temperature increases from 2 K to 20 K, and then meets a plateau at ~ 2.9 μ_B. This is consistent with the three-spin model because the three spins on the central triangle are weakly coupled (J_0 = -2.5 K [104]) at low temperature and decoupled at high temperature.

4.3 Specific Heat of {$V_{15}As_6$}

The heat capacity of {$V_{15}As_6$} has been determined by means of the method as described in Section 3.3. A small plate-like crystal with a flat surface and of about 1 mg was used in the heat capacity measurements.

The temperature dependence of the specific heat under zero external magnetic field is plotted in **Figure 4-3-1** within the temperature range 70 mK to 260 K. There is no long-range magnetic phase transition within the investigated temperature range, which is expectable for {$V_{15}As_6$} as a molecular magnet. For the sake of clarity, the data are also plotted in log-log scale in the inset of **Figure 4-3-1**. Obviously, there are two humps at ~ 0.1 K and ~ 1.5 K respectively, which are of Schottky-like shape and may reflect the low-lying magnetic excitations of {$V_{15}As_6$}.

Lacking of a non-magnetic reference, the lattice specific heat of {$V_{15}As_6$} cannot be determined precisely. The following discussion will focus on the low-temperature (T < 6 K) region, where the low-lying magnetic excitations locate and the lattice specific heat is insignificant. In order to study the magnetic specific heat, the measurements were performed at various fields of 0, 0.05, 0.5, and 8 Tesla. The field-dependent molar specific heat of {$V_{15}As_6$} is shown in **Figure 4-3-2**.

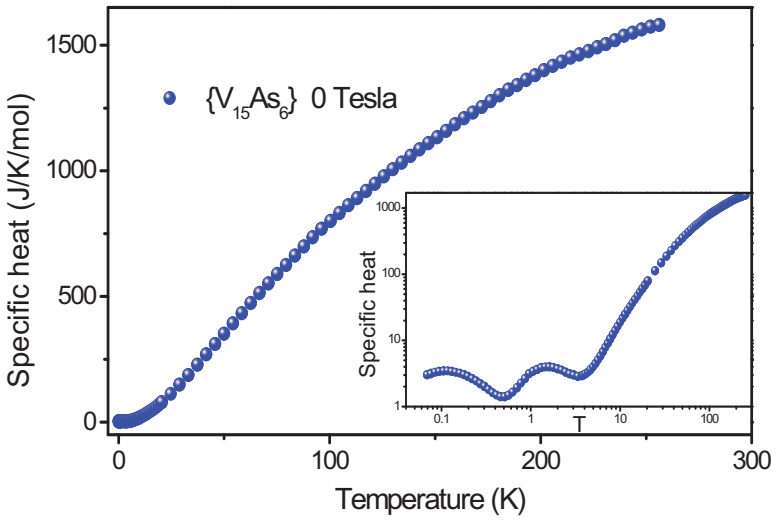

Figure 4-3-1 Temperature dependence of the specific heat of {$V_{15}As_6$} under zero external magnetic field. Inset: data in log-log scale.

As shown in **Figure 4-3-2**, there are two humps below 3 K under external fields of 0, 0.05 and 0.5 Tesla. Both humps change with the external fields, indicative of the magnetic origin of them.

The lattice contribution to the total specific heat within the temperature range 70 mK to 6 K is described by one Debye term with cubic dependence on temperature, which is

$$C_{\text{Debye}} = R\frac{234 r_{\text{D}} T^3}{\Theta_{\text{D}}{}^3}. \qquad (4.3.1)$$

In Eq. (4.3.1), R is the gas constant, Θ_{D} is the Debye temperature, r_{D} is the number of atoms per molecule and is taken as 80 for {$V_{15}As_6$}.

The two magnetic humps are fitted with the Schottky model for multi-level systems, since both the three-spin model (see **Figure 4-1-2 (a)**) [23] and the inelastic neutron scattering [106, 112] show that the magnetic excitation spectrum of {$V_{15}As_6$} is described by discrete spin levels. The multi-level Schottky term has already been derived in Chapter 3 (see Eq. 3.3.7) as the following form,

$$C_{\mathrm{Sch}} = \frac{R}{k_{\mathrm{B}}^2 T^2} \frac{\sum_i \varepsilon_i^2 \exp\left(-\varepsilon_i / k_{\mathrm{B}}T\right) \sum_i \exp\left(-\varepsilon_i / k_{\mathrm{B}}T\right) - \left[\sum_i \varepsilon_i \exp\left(-\varepsilon_i / k_{\mathrm{B}}T\right)\right]^2}{\left[\sum_i \exp\left(-\varepsilon_i / k_{\mathrm{B}}T\right)\right]^2}, \quad (4.3.2)$$

where ε_i is the energy of spin level i. Two multi-level Schottky terms are used in the fit to account for the two magnetic humps, respectively.

Based on the energy spectrum (**Figure 4-1-2 (a)**) predicted for the three-spin model, it is straight to assign the hump at ~ 0.1 K to the intraband Schottky effect of the ground state and the one at ~ 1.5 K to the interband Schottky effect between the ground state and the first excited state. A detailed description of the fitting procedure applied to the data for every field is given below:

A. Data for zero external field. The hump at ~ 1.5 K is fitted with one energy gap (Δ_4). And the hump at ~ 0.1 K is fitted with two energy gaps (Δ_0 and Δ_1), which was supposed to be fitted with one energy gap according to the energy spectrum. But as shown in **Figure 4-3-3**, the fit with two gaps to the hump at ~ 0.1 K is much better than the one with only one gap. The discussion to this result will be given latter.

B. Data for 0.05-Tesla external field. The hump at ~ 0.1 K is fitted with two gaps (Δ_0 and Δ_1). The hump at ~ 1.5 K is fitted with one gap (Δ_4), because the Zeeman splitting of the excited spin states is so small under 0.05 T that the fit is not able to separate the different gaps between the ground state and the first excited state.

C. Data for 0.5-Tesla external field. The hump at ~ 0.1 K is fitted with three gaps (Δ_0, Δ_2 and Δ_3). The hump at ~ 1.5 K is also fitted with three gaps (Δ_4, Δ_5 and Δ_6).

D. Data for 8-Tesla external field. The broad hump above 3 K is fitted with two gaps of ~ 0.61 and ~ 2.08 meV, and a small one-gap (~ 0.11 meV) Schottky term is added to account for the magnetic heat capacity at ~ 0.3 K. But the fit to the 8-Tesla data probably doesn't reflect the nature of the Schottky anomalies because the energy spectrum is significantly disturbed by this large field and it is hard to decide the levels involving in the multi-level Schottky term.

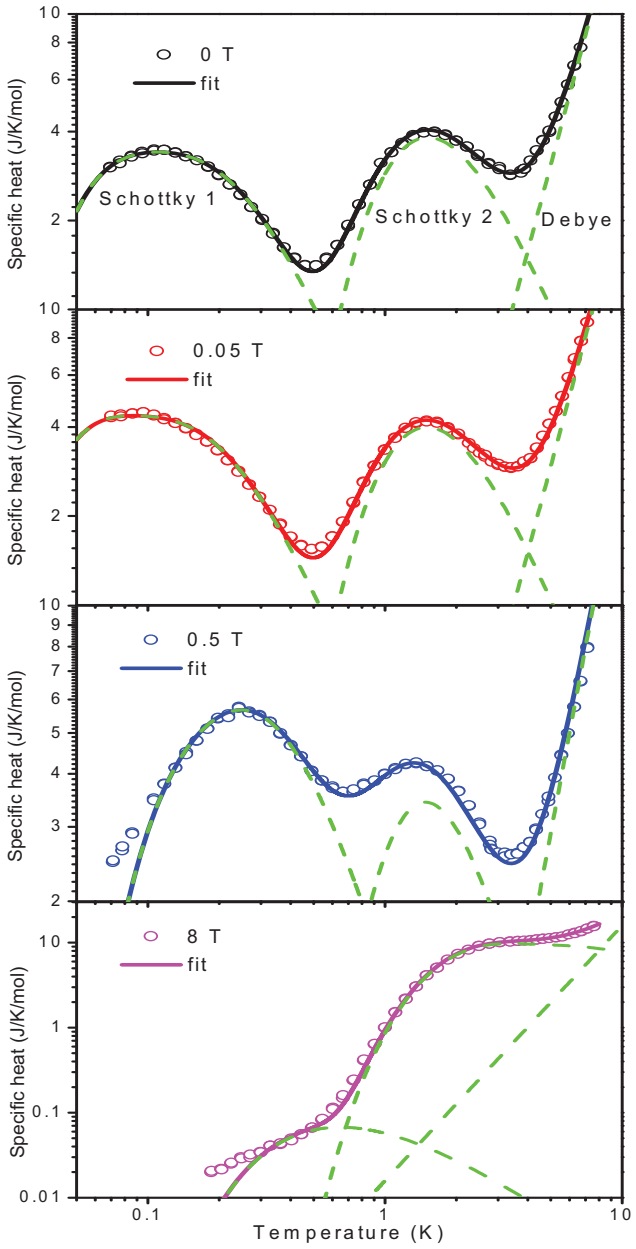

Figure 4-3-2 Temperature dependence of the specific heat of $\{V_{15}As_6\}$ under 0, 0.05, 0.5 and 8 Tesla. Lines: corresponding total fits. Data and fitting curves are plotted in log-log scale.

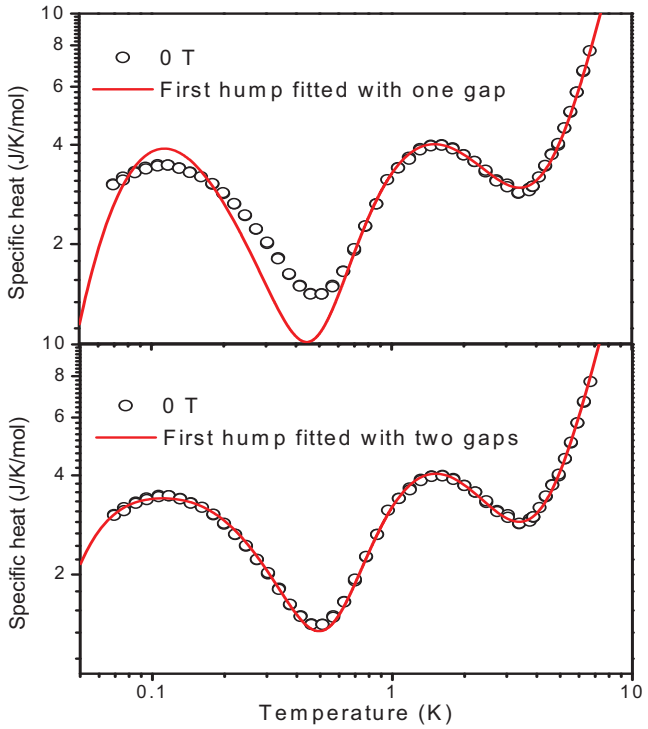

Figure 4-3-3 Comparison of the two ways to fit the Schottky anomaly ~ 0.1 K.

The best fits according to the above rules **A – D** are plotted in **Figure 4-3-2**. The Debye temperatures obtained from all fits is 186 ± 20 K, which is actually hard to be determined precisely in the fit to the low temperature specific heat only. The main purpose of the analysis here is to study the low-lying magnetic excitations, and as shown in **Figure 4-3-2**, the two Schottky components in the fitting results are dominant and affected very little by the cubic phonon term. Thus I can safely carry out the analysis on the Schottky anomalies without a precise determination of the Debye temperature. The energy gaps obtained from the fits to the data of 0, 0.05 and 0.5 Tesla are summarized in **Table 4-3-1**, along with those determined by INS measurements under the corresponding fields [106, 112]. As already discussed before, the Schottky anomalies at ~ 0.1 K in the data for 0 and 0.05 T are fitted with two energy gaps, namely Δ_0 and Δ_1 in **Table 4-3-1**. Δ_0 is in quantitative agreement with the value of the splitting (~ 0.035 meV) between the ground-state spin doublets found in INS. However, the fit with a single gap (~ 0.035 meV) is inadequate to

reproduce the Schottky anomaly at ~ 0.1 K, as shown in **Figure 4-3-3**. Another gap Δ_1 must be involved to achieve a good fit. Δ_1 is only about 0.016 meV, which is too low to be identified in the INS measurements due to the high background at small energy transfer. Actually even the gap Δ_0 ~ 0.035 meV found in INS measurements was obtained by a subtracting procedure, whose accuracy was not good enough for a quantitative analysis [112]. When applying a 0.05 T external field, the ground state doublets should split because of the Zeeman effect. But the splitting under this field is so small that the fit of specific heat data cannot tell the fine structure of the Zeeman levels. The gap Δ_0 obtained from 0.05 T data should be adopted as an average gap between the ground state doublets. As shown in **Table 4-3-1**, this gap remains almost the same up to 0.5 T within the accuracy of the fit, consistent with the energy spectrum in **Figure 4-3-4**. As to the gap Δ_1, one possibility of its origin is the splitting of the lowest ground state doublet. But this cannot explain why Δ_1 exists at zero external field. Another possibility is that the gap Δ_1 could be an artifact introduced in the fit. As shown in **Figure 4-3-2**, though the specific heat has been measured down to 70 mK, I did not retrieve the complete low-temperature part of the Schottky anomaly at ~ 0.1 K under 0 and 0.05 T external field. The limit of the data could possibly lead to the gap Δ_1 in the fit. Hence the gap Δ_0 is assigned to the splitting of the ground-state spin doublets and the origin of the gap Δ_1 remains unclear.

Table 4-3-1 Energy gaps obtained from the fits to the specific heat (SH) data of $\{V_{15}As_6\}$ under 0, 0.05 and 0.5 Tesla external magnetic field. The results of inelastic neutron scattering (INS) under the corresponding fields are listed for comparison. The details for INS results can be found in Refs. [106] and [112].

Field \ Gap		Δ_0 (meV)	Δ_1 (meV)	Δ_2 (meV)	Δ_3 (meV)	Δ_4 (meV)	Δ_5 (meV)	Δ_6 (meV)
0	SH	0.041(5)	0.015(3)	--	--	0.313(12)	--	--
(T)	INS	0.035	--	--	--	0.33	--	--
0.05	SH	0.039(4)	0.012(3)	--	--	0.310(11)	--	--
(T)	INS	--	--	--	--	--	--	--
0.5	SH	0.031(4)	--	0.070(8)	0.096(7)	0.287(13)	0.352(14)	0.480(20)
(T)	INS	--	--	0.063	0.090	0.268	0.332	0.418

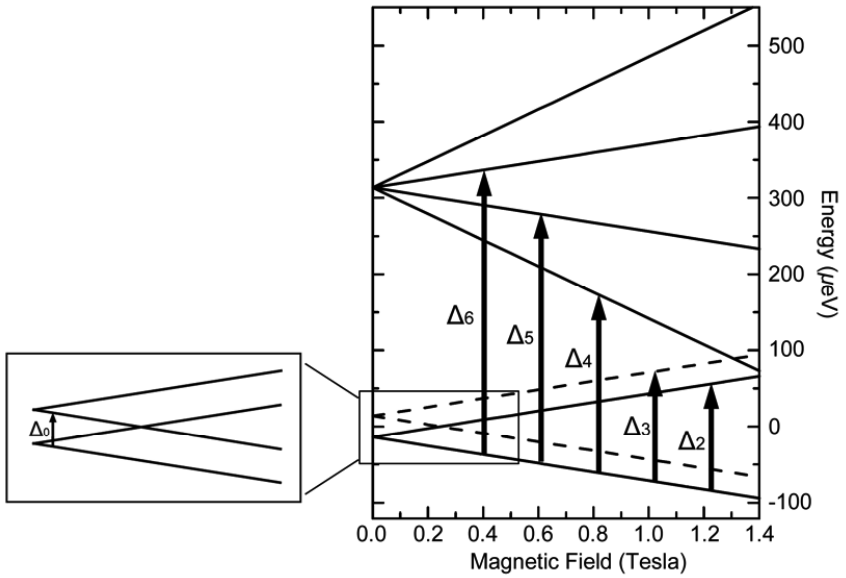

Figure 4-3-4 Low-lying energy spectrum of $\{V_{15}As_6\}$ within the three-spin model and the Zeeman splitting of the spin levels. The assignment of the energy gaps obtained by specific heat measurements is indicated by the arrows. Insets: fine structures of the ground-state spin doublets and the excited spin quadruplets.

As to the analysis on the specific heat data for 0.5 Tesla, the resultant energy gaps are basically consistent with those revealed by INS under 0.5 Tesla, except that INS did not detect the gap Δ_0 between the ground-state spin doublets. The energy gaps obtained by the specific heat measurements are drawn in **Figure 4-3-4**. The energy spectrum in **Figure 4-3-4** is based on the three-spin model [108, 119] and INS [106, 112] results. It can be seen that the energy gaps obtained in specific heat measurements are consistent with both the theoretical prediction and the direct spectroscopic observation using INS method.

As a summary of Section 4.3, the specific heat of $\{V_{15}As_6\}$ was measured down to 70 mK under 0, 0.05, 0.5 and 8 Tesla external magnetic field. By analyzing the multi-level Schottky anomalies in the specific heat data for various fields, several spin levels have been determined which are in agreement with the results of inelastic neutron scattering measurements and the three-spin model. Therefore the specific heat measurements on $\{V_{15}As_6\}$ provide strong and complimentary support to the three-spin model for $\{V_{15}As_6\}$.

4.4 Diffuse Neutron Scattering with Polarization Analysis on $\{V_{15}As_6\}$

In order to get further insight into the nature of the spin model for $\{V_{15}As_6\}$, diffuse neutron scattering with polarization analysis was performed to measure the possible spin correlations in $\{V_{15}As_6\}$. But in this case, the spin correlations are difficult to measure because each V^{4+} ion is carrying $S = 1/2$ only. And as aforementioned in Section 4.2 the spin pairs in the V_6 hexagons are strongly coupled with $J \sim 800$ K, which cause a loss of the magnetic scattering intensity even at room temperature. I cannot retrieve all the magnetic cross section by heating the sample to reach the pure paramagnetic phase, because heating $\{V_{15}As_6\}$ will drive the crystal water molecules away and then alter the crystal structure or even the magnetism. Measurements below 2 K may have a chance to observe some spin correlations.

4.4.1 Experimental Details

The $\{V_{15}As_6\}$ polycrystals were synthesized according to the method described in Ref. [103]. The sample was deuterated to minimize attenuation and incoherent scattering from hydrogen atoms. 6 grams of sample was sealed in a copper holder in a helium atmosphere. Polarized neutron scattering measurements were carried out on the diffuse neutron scattering instrument DNS [95] at the FRM II research reactor. The measurements were performed with incident wave length 4.74 Å and 2.36 Å, using an orange-type liquid helium cryostat and a dilution cryostat, respectively. The nuclear coherent, spin-incoherent and magnetic scattering components were separated simultaneously with the *xyz*-polarization method in the spin-flip and non-spin-flip channels, as already described in Chapter 2 and Chapter 3. The flipping ratio correction was made by the reference measurements on a NiCr alloy. The background was measured from an empty sample can and subtracted from the raw data. A vanadium standard was measured to obtain the absolute scattering cross section of the sample.

4.4.2 Experimental Results and Discussion

The polarized neutron scattering measurements were first performed on deuterated $\{V_{15}As_6\}$ polycrystals at 1.8 K with incident wavelength of 4.74 Å. **Figure 4-4-1** shows the Q dependence of the nuclear coherent (black circles), spin-incoherent

(green circles) and magnetic scattering (red circles) components separated by means of *xyz*-polarization method. The *Q* range was covered from 0.23 to 2.3 Å^{-1}. The nearly constant spin incoherent scattering intensity suggests a successful separation by *xyz*-polarization analysis. The magnetic scattering is rather weak, which is plotted in absolute unit in **Figure 4-4-2**.

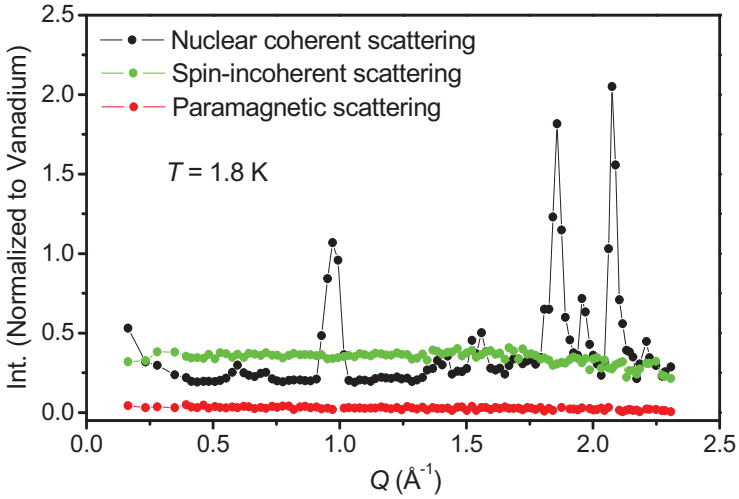

Figure 4-4-1 Nuclear coherent (black circles), spin-incoherent (green circles) and magnetic (red circles) scattering components of $\{V_{15}As_6\}$ at 1.8 K.

As shown in **Figure 4-4-2**, there is no clear sign for any long-range or short-range magnetic order in $\{V_{15}As_6\}$ at 1.8 K. The scattering profile basically reflects a paramagnetic form factor. The pure paramagnetic form factor of one free V^{4+} ion (S = 1/2) is plotted in **Figure 4-4-2** by the solid line, which is higher than the experimental scattering cross section per V^{4+} ion. The total differential magnetic cross section within the experimental energy window of DNS is determined by integration over the scattering vector *Q* range using Eq. (3.5.4). It is found that only 57% of the total magnetic cross section expected from the pure paramagnetic phase of $\{V_{15}As_6\}$ has been observed at 1.8 K within the energy and *Q* window of DNS. The dashed line in **Figure 4-4-2** represents the 57%-scaled paramagnetic form factor of V^{4+} [96], consistent with the measured magnetic differential cross section.

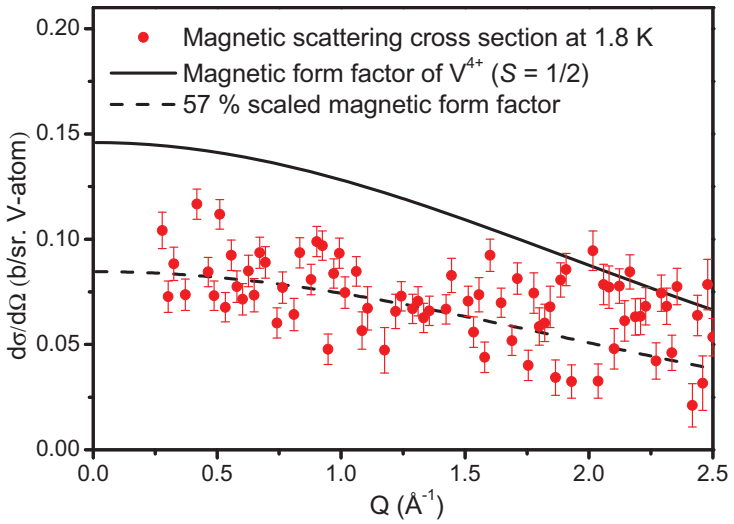

Figure 4-4-2 Magnetic scattering cross section in absolute unit at 1.8 K. Solid and dashed lines are the full and 57%-scaled pure paramagnetic form factor of V^{4+} ion, respectively.

In order to detect the spin correlations of {$V_{15}As_6$}, the polarized neutron scattering was then performed with shorter wavelength and at lower temperature using dilution cryostat. The upper panel of **Figure 4-4-3** shows the nuclear coherent, spin-incoherent and magnetic components separated from the total scattering measured at 60 mK with incident wavelength 2.36 Å. Obviously a larger *Q* range is now accessible from 0.2 to 4.3 $Å^{-1}$. The separation is not ideal probably due to the high background.

The magnetic differential cross section at 60 mK in absolute unit is plotted in the lower panel of **Figure 4-4-3**, which is too noisy to analyze quantitatively. The relatively high intensity of magnetic scattering above 1.6 $Å^{-1}$ is due to the imperfect separations caused by the strong nuclear coherent scattering at this *Q* range. But it is hard to tell whether there exist short-range spin correlations at 60 mK because of the limited quality of the data. Latter work on another sample at DNS showed that the instrument was not in good condition when working with wavelength 2.36 Å. This could be the reason for the bad quality of the data in this experiment.

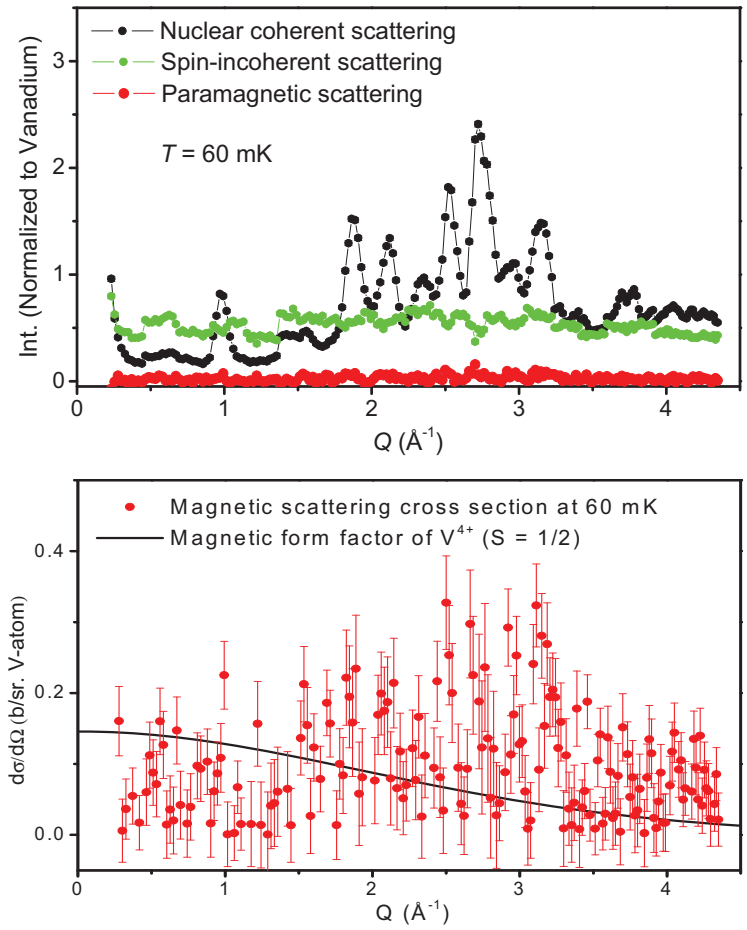

Figure 4-4-3 Upper panel: nuclear coherent, spin-incoherent and magnetic components of $\{V_{15}As_6\}$ at 60 mK. Lower panel: magnetic scattering cross section in absolute unit with pure paramagnetic form factor of V^{4+} ion.

In this section, the diffuse neutron scattering with polarization analysis on deuterated $\{V_{15}As_6\}$ has been measured with 4.74 Å at 1.8 K, and with 2.36 Å at 60 mK. No long-range or short-range magnetic order can be identified. The magnetic differential scattering cross section basically reflected the paramagnetic form factor of V^{4+}, while the loss of magnetic cross section could be explained by the strong spin-pair coupling in the V_6 hexagons in $\{V_{15}As_6\}$ molecule. Besides the intrinsic weak magnetic scattering, the imperfect working condition of the instrument might have raised the background and then covered the spin correlations that were

supposed to be observed.

4.5 Summary

The magnetic properties and structure of $\{V_{15}As_6\}$ has been investigated by magnetic susceptibility, specific heat and polarized neutron scattering. No long-range magnetic phase transition has been detected from room temperature down to 60 mK. The low-lying magnetic excitation spectrum determined by the specific heat study gave strong and complimentary support to the three-spin model of $\{V_{15}As_6\}$. No clear spin correlations have been observed in the polarized neutron scattering measurements. But the loss of magnetic scattering cross section suggested strong spin coupling in the system, consistent with the strong spin-pair couplings in V_6 hexagons predicted by the three-spin model. Therefore, the present work supports that the three-spin model could be a good approach to the magnetic structure of $\{V_{15}As_6\}$.

CHAPTER 5:

Spin-frustrated Pyrochlore Antiferromagnet $Na_3Co(CO_3)_2Cl$

5.1 Introduction

Spin frustration, as an important concept in magnetism, plays the key role in many novel and interesting magnetic phenomina [37, 48, 120, 121]. In general, spin frustration occurs when the spin system cannot minimize its total energy by minimizing all the spin-pair interactions simultaneously. Spin-frustrated magnetic structures were first discovered and investigated six decades ago [38]. Two of the well-know spin-frustrated structures are the Ising model on the antiferromagnetic triangular lattice [43] and the Heisenberg helical structure [40, 122, 123]. However, spin-frustrated magnetic systems started to attract extensive attention about two decades later in the context of spin glasses [39, 124]. Spin glass is a fundamental and universal form of magnets, whose formative ingredients are belived to be spin frustration and disorder in the system [42]. Besides the long-range ordered ferro-, ferri-, and antiferro- magnetic phase, spin glass in frozen state constitutes a new state of co-operative or collective magnetism [42]. Great efforts have been dedicated to explore the fundamental science in the spin glass systems, because of the novel experimental phenomena and new theoretical concepts discoved. In spite of the experimental and theoretical accumulations for decades, the nature of the spin-glass transition and the spin-glass state is still controversial [125, 126]. A "pass" research topic it might be, spin glass remains an intriguing and challenging field for solid state physists.

5.1.1 Brief Introduction to Spin Glasses and Pyrochlore Magnets

What is a spin glass? There is no precise and universal definition for spin glass. A working definition can be cited from Ref. [42] as follows: "A spin glass is a random, mixed-interacting, magnetic system characterized by a random, yet co-operative, freezing of spins at a well-defined temperature T_f below which a highly irreversible, metastable frozen state occurs without the usual long-range spatial magnetic order".

And how to classify any material as a spin glass? A magnetic material could probably be a spin glass if it exhibits a collection of characteristic properties listed below [125, 127]. These properties will be discussed in the later sections of this chapter.

(i) In the low-field AC susceptibility measurements, a cusp appears at a spin-glass temperature T_f, which is dependent on the measuring frequency.

(ii) In neutron scattering measurements below T_f, there is no magnetic Bragg scattering observed, demonstrating the absence of long-range magnetic order.

(iii) In the field dependent magnetization measurements below T_f, a magnetic hysteresis loop can be observed.

(iv) Irreversibility occurs. The temperature dependence of the zero-field-cooled (ZFC) and field-cooled (FC) magnetization split below T_f.

(v) Below T_f, the remanent magnetization decays very slowly with time.

(vi) The magnetization below T_f is history dependent in the sense that the sample possesses higher magnetization after a FC procedure than after a ZFC procedure, and slowly relaxes between these states upon field change.

(vii) In the magnetic specific heat, there is no sharp anomaly at T_f. A broad peak exists at around 1.3 T_f.

(viii) Aging effect and nonresonant hole-burning (NSHB) [128, 129].

In order to create a spin glass phase, two essential prerequisites must be fulfilled [42]. The first one is disorder, which can be either site disorder with a distribution of distances between the magnetic ions, or bond disorder with varying nearest-neighbor interactions. The second one is frustration, which creates a degenerate, metastable frozen ground state for a spin glass.

The first examples of spin glass were discovered in the family of dilute alloys of 3*d* transition metal impurities in a noble metal, including the well-known archetypal systems of *Cu*Mn and *Au*Fe [130, 131]. These site-random metallic spin glasses are also called canonical spin glass, where non-magnetic metal dissolves the magnetic element such as Mn, Fe, Eu, etc, introducing a random apportionment of distances between the magnetic species. Together with the oscillating Ruderman-Kittel-Kasuya-Yosida (RKKY) interaction, spin glass transition occurs, which makes positional disorder the basic and first ingredient of a potential spin glass. As to magnetic frustration, it alone is not sufficient to generate a spin glass state. Just consider an antiferromagnetic triangular lattice. It is spin frustrated, but doesn't exhibit co-operative freezing transition. Therefore frustration has to be accompanied with disorder to generate a spin glass, while disorder is believed to be the basic requirement for the spin glasses [42].

In contrast to the above conventional wisdom about spin glass, some pyrochlore

magnets seemingly exhibit spin-glass-like behaviors without obvious chemical disorder [132-136]. The so-called pyrochlore lattice is a network of corner-sharing tetrahedra, as discussed in Section 1.2. When antiferromagnetism is combined with magnetic pyrochlores, geometrical magnetic frustration is often expected from these tetrahedra-based structures and leads to unusual physical properties, attracting intensive research interest [137]. The antiferromagnetism on pyrochlore lattice was first considered by P. W. Anderson, who predicted high ground-state degeneracy and no long-range order at any temperature for Ising spins [138]. J. Villain made basically the same conclusion for the Heisenberg spin case [139].

The best-studied family of pyrochlore magnets by now is the cubic pyrochlore oxides with a general chemical formula $A_2B_2O_7$ [137], which have dominated much of the literature due to a wide variety of interesting, unusual ground states observed, such as spin glasses [132, 133, 140], spin liquids [141-143], and spin ices [144, 145]. Of particular interest is the exploration of magnetic monopole excitations in the spin-ice material $Ho_2Ti_2O_7$ [146-149]. Furthermore, it is a somewhat surprising result that spin-glass-like behavior has been observed in a few examples of pyrochlore magnets which are periodic, chemically ordered within the sensitivity of diffraction methods while the received wisdom generally assume that the formation of a spin-glass phase requires chemical disorder in addition to competing (or frustrated) interactions [42, 125, 132-136, 150]. The origin of this spin-glass-like behavior in some magnetic pyrochlores has been the subject of an intense debate and is still not completely understood [151, 152]. It was found that quantum fluctuations in the spin interactions play an important role in this glassy behavior [153-156]. On the other hand, although little evidence for site disorder among the cations or for significant vacancy concentrations on the oxygen sites was found in the spin-glass pyrochlore $Y_2Mo_2O_7$ [157, 158], a subtle nonrandom distortion of the Mo sublattice was revealed by means of X-ray-absorption fine-structure (XAFS) measurement and nuclear magnetic resonance (NMR) investigation, which could lead to the spin-glass-like behavior in this material [159, 160]. Recently, J. E. Greedan et al. reported the neutron diffraction and neutron pair distribution function (NPDF) analysis on $Y_2Mo_2O_7$ and found that the principal source of disorder is associated with the Y-O1 atom pairs rather than the Mo-Mo pairs, in disagreement with the result of XAFS measurement [161].

5.1.2 Introduction to Pyrochlore Antiferromagnet $Na_3Co(CO_3)_2Cl$

Recently, a new spin-frustrated compound $Na_3Co(CO_3)_2Cl$ was discovered whose structure features a three-dimensional anionic backbone of Co^{2+} carbonate that accommodates the sodium and chloride ions (see **Figure 5-1-1 (a)**). Magnetic Co^{2+} ions are located at the corners of a network of corner-sharing tetrahedra, i.e., pyrochlore lattice, as shown in **Figure 5-1-1 (b).** The nearest-neighboring Co^{2+} ions are antiferromagnetically coupled, which leads to a high degree of magnetic frustration (see Sections 5.3 and 5.6). In **Figure 5-1-1 (c)**, the nearest-neighboring Co^{2+} ions are drawn together by the -O-C-O- bridges between them. All the -O-C-O- bridges are identical, indicative of a single exchange constant *J* between the nearest neighboring Co^{2+} ions.

The synthesis procedures of $Na_3Co(CO_3)_2Cl$ are summarized as follows. A mixture of $CoCl_2 \cdot 6H_2O$ (5.9 g, 0.025 mol), 1,10-phenanthroline (10.0 g, 0.05 mol), Na_2CO_3 (2.5 g, 0.025 mol), ethanol (72 mL) and water (6 mL) were stirred in the air for 10 min and then transferred to a 110 mL Teflon-lined autoclave, which was heated to 160 ^oC for 96 h, followed by cooling to room temperature with a rate of 5 $^oC/h$. The resulting pink polycrystalline products were washed by large amount of ethanol/water, yielding 3.0 g (85 %). Elemental analysis showed very little contaminations by other transition metal ions (less than 0.01%).

5.1.3 Motivations

$Na_3Co(CO_3)_2Cl$ is a new pyrochlore magnetic system that has never been studied before. As its predecessors in the family of magnetic pyrochlores, $Na_3Co(CO_3)_2Cl$ is expected to possess novel magnetic properties. A thorough study on $Na_3Co(CO_3)_2Cl$ may extend the knowledge on the physics of pyrochlore magnets. In this chapter, the crystal and magnetic structure of $Na_3Co(CO_3)_2Cl$ is investigated in detail by means of various experimental techniques, including X-ray powder diffraction, neutron powder diffraction, DC and AC susceptibilities, specific heat, inelastic neutron scattering and diffuse neutron scattering with polarization analysis. Novel and interesting magnetic properties of $Na_3Co(CO_3)_2Cl$ will be presented in this chapter.

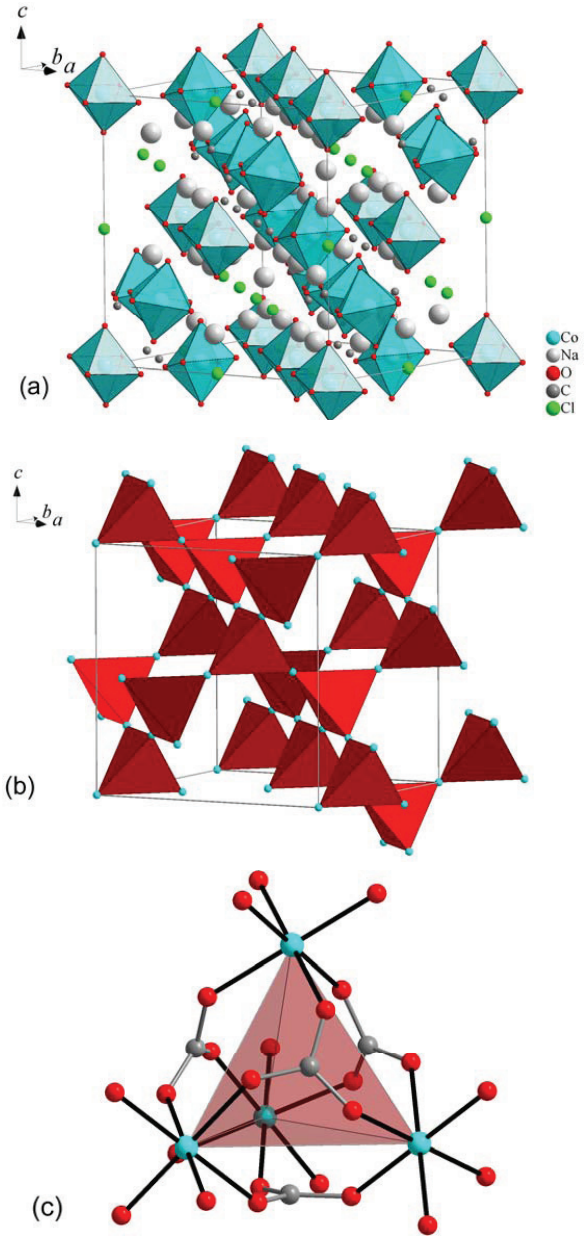

Figure 5-1-1 (a) Crystal structure of $Na_3Co(CO_3)_2Cl$ (Co: cyan spheres; Na: light gray spheres; O: red spheres; C: dark gray spheres; Cl: green spheres). (b) Pyrochlore lattice of Co^{2+} ions (cyan spheres). The corner-sharing Co^{2+} tetrahedra are highlighted by red color. (c) One Co^{2+} tetrahedron with the -O-C-O- bridges between nearest neighbors.

5.2 X-ray Powder Diffraction of $Na_3Co(CO_3)_2Cl$

X-ray single-crystal diffraction shows that $Na_3Co(CO_3)_2Cl$ crystallizes in cubic structure with space group $F\,d\,\bar{3}$ (#203) and lattice constant a = 13.9959(5) Å at 123 K. The x-ray powder diffraction (XRPD) spectrum was measured to evaluate the purity of the powder sample synthesized for other measurements. The XRPD patterns were recorded on Huber diffractometer with Cu Kα_1 radiation (30 - 40 kV, 10 - 20 mA, λ = 1.54059 Å). Data were collected in steps of 0.005˚ over the range of 23˚ ≤ 2θ ≤ 100˚ at 300 K. Structural parameters were determined from the Rietveld refinement [162] using the Fullprof suite [117]. The XRPD profiles were modeled using the Gaussian shape function. The refined parameters included scale factors, zero shifts, lattice constants, atomic positions, isotropic and anisotropic thermal parameters. Actually the refinement of the XRPD pattern with full isotropic model was as good as the present one. However when analyzing the neutron powder diffraction data (see Section 5.3), the use of anisotropic thermal parameters yielded a significantly better refinement than the one with full isotropic thermal parameters. The XRPD pattern of $Na_3Co(CO_3)_2Cl$ is shown in **Figure 5-2-1**, together with the calculated pattern and the difference between them.

In the Rietveld refinement of crystal structure, the best agreement between the XRPD data and the structural model has been found with Co occupying the (16*c*: $.\bar{3}.$) (0, 0, 0) site, Na (48*f*: 2..) (0.125, *y*, 0.125), O (96*g*: 1) (*x*, *y*, *z*), C (32*e*: .3.) (*x*+0.25, -*x*, *x*+0.25), and Cl (16*d*: $.\bar{3}.$) (0.25, 0.25, 0.5). Co and C atoms were refined with an isotropic model for the thermal movement. The Na, O and Cl sites were modeled with anisotropic model using anisotropic atomic displacement parameters as: Na (u_{11}, u_{22}, u_{33}, $u_{12} = u_{23} = 0$, u_{13}), O (u_{11}, u_{22}, u_{33}, u_{12}, u_{23}, u_{13}), and Cl ($u_{11} = u_{22} = u_{33}$, $u_{12} = -u_{23}$, $u_{12} = -u_{13}$). The refined structural parameters are summarized in **Table 5-5-1** in Section 5.5.

Rietveld refinement of the XRPD pattern confirmed that $Na_3Co(CO_3)_2Cl$ powder sample has a $F\,d\,\bar{3}$ (#203) space group with a = 14.0435(8) Å at room temperature. No additional reflections can be found, indicating a single phase of the sample. The analysis of XRPD data will be discussed in Section 5.5 in combination with the neutron powder diffraction data.

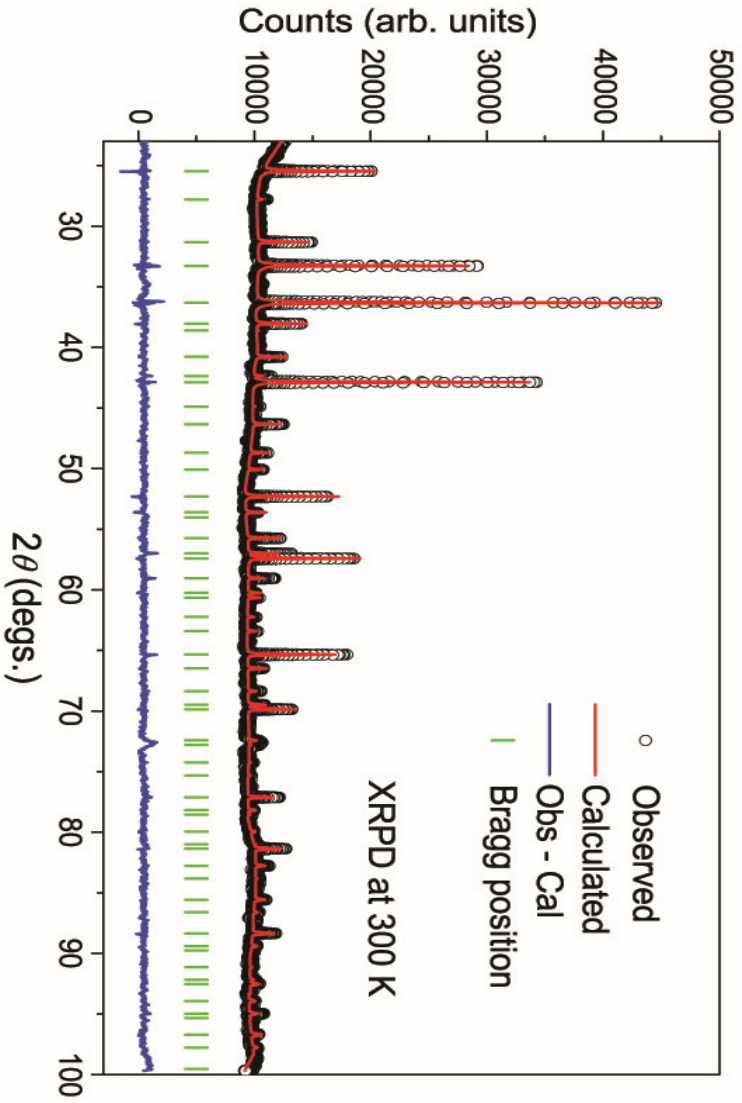

Figure 5-2-1 Experimental (Obs), calculated (Cal) and difference (Obs-Cal) X-ray powder diffraction (XRPD) patterns obtained at 300 K with the Rietveld refinement.

5.3 Magnetic Measurements of $Na_3Co(CO_3)_2Cl$

For the first step to approach the novel magnetic behavior of $Na_3Co(CO_3)_2Cl$, static and dynamic magnetic measurements were performed, as being presented in this section.

5.3.1 DC Magnetization

The DC magnetization measurements were carried out using a Superconducting Quantum Interference Device (SQUID) magnetometer. Zero-field-cooled (ZFC) and field-cooled (FC) DC magnetization curves of $Na_3Co(CO_3)_2Cl$ were measured under various probing fields. In a typical ZFC measurement, the sample was cooled down from room temperature without external magnetic field and then the magnetization was measured with a probing field. The FC magnetization data were collected while the sample was cooled down under an external field. Here M/H is defined as the DC susceptibility χ_{dc}.

Figure 5-3-1 (a) shows the temperature dependence of the ZFC susceptibility $\chi_{dc(ZFC)}$ and the FC susceptibility $\chi_{dc(FC)}$ measured from 2 K to 300 K under a probing field of 100 Oe. The temperature dependence of the inverse ZFC susceptibility $1/\chi_{dc(ZFC)}$ is shown in the inset of **Figure 5-3-1 (a)**. The data above 200 K can be well fitted by the Curie-Weiss law (red line), yielding a Curie-Weiss temperature Θ_{CW} = -33.8 ± 5.2 K and a Curie constant C = 3.5 ± 0.6 emu·K/Oe/mol. The negative value of Θ_{CW} shows dominant antiferromagnetic coupling between Co^{2+} ions. In a mean-field approximation with nearest-neighboring interactions only, the Curie constant and the Curie-Weiss temperature are given respectively [163], by

$$C = \frac{9}{8}\left[\frac{N\mu_{eff}^2}{3k_B}\right] \text{ and } \Theta_{CW} = \frac{3}{2}\left[\frac{zJS(S+1)}{3k_B}\right]. \quad (5.3.1)$$

Here μ_{eff} is the effective moment of the Co^{2+} ion, J is the exchange constant among the nearest neighbors, and z is the number of nearest neighbors and is taken as 6. It is then estimated that μ_{eff} = 5.3 ± 0.4 μ_B and J = 0.26 ± 0.05 meV.

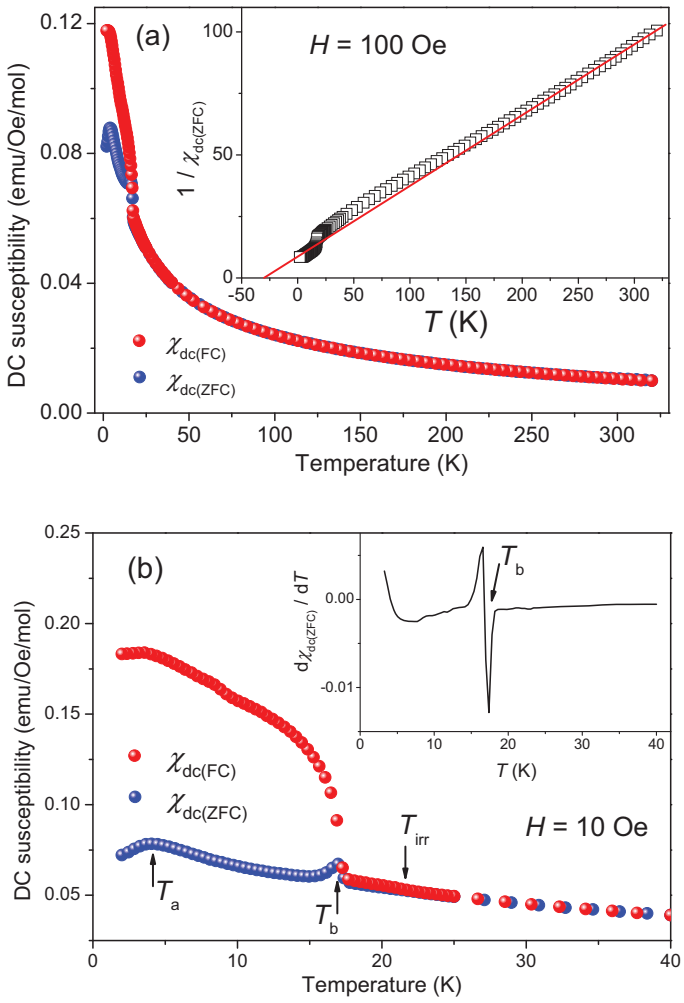

Figure 5-3-1 (a) ZFC (blue circles) and FC (red circles) DC susceptibilities of $Na_3Co(CO_3)_2Cl$ within temperature ranging from 2 K to 320 K under a probing field of 100 Oe. **(b)** Low-temperature part (2 K < T < 30 K) of the temperature dependence of the susceptibilities. T_a: temperature of the maximum of the hump in the ZFC susceptibility at around 4 K; T_b: inflection temperature; T_{irr}: irreversibility temperature of the ZFC and FC susceptibility curves. Inset of **(a)**: the temperature dependence of inverse susceptibility with the best fit of Curie-Weiss law (red line). Inset of **(b)**: temperature dependence of the differential ZFC susceptibility.

The effective moment per Co^{2+} extracted from the DC susceptibility measurement exceeds the spin-only value of 3.87 μ_B for Co^{2+} in high spin state (S = 3/2), consistent with what has been reported in the literature [164, 165]. The excess magnetic moment of Co^{2+} above the theoretical prediction of the spin-only value is due to the spin-orbital coupling contribution as often reported for Co^{2+} ions in octahedral crystal field environments [164, 165].

The temperature dependence of the ZFC and FC susceptibilities were also measured from 2 K to 40 K under 10 Oe and is plotted in **Figure 5-3-1 (b)**. As seen in **Figure 5-3-1 (b)**, the ZFC and FC susceptibilities diverge below an irreversibility temperature $T_{irr} \approx 21.4$ K. There is a hump in ZFC susceptibility at around 4 K whose peak temperature is defined as T_a. And an inflection temperature appears at $T_b \approx 17$ K, which can be seen more clearly as a sharp dip in the temperature dependence of the differential ZFC susceptibility in the inset of **Figure 5-3-1 (b)**. The origin of the kinks at T_a and T_b will be discussed later in this section.

The divergence between the ZFC and FC susceptibilities is indicative of collective spin behaviors, such as spin glass, superparamagnet, cluster glass, etc. In order to determine the nature of the magnetism of $Na_3Co(CO_3)_2Cl$, more magnetic measurements are needed.

Figure 5-3-2 shows the temperature dependence of ZFC and FC susceptibilities under various probing fields. The kink at the inflection temperature T_b (~ 17 K) decreases and finally disappears with increasing probing fields. But this inflection temperature T_b is field-independent as shown in the insets of **Figure 5-3-2**. This inflection temperature T_b may reflect the onset of some kind of long-range collective behavior of the Co^{2+} spins. The hump at T_a (~ 4 K) in the ZFC susceptibility gradually shifts to lower temperature with increasing magnetic fields. In order to identify whether the hump at T_a is a spin-glass freezing temperature, the field dependence of T_a is investigated in terms of de Almeida-Thouless (AT) line [166]. Within the mean-field approximation, de Almeida and Thouless suggested a critical line in the plane spanned by the variables temperature and magnetic field for Ising spin glasses with infinite-range random interactions. The AT line can be observed near the freezing temperature and plausibly associates the onset of irreversibility of spin glasses on macroscopic time scales [150].

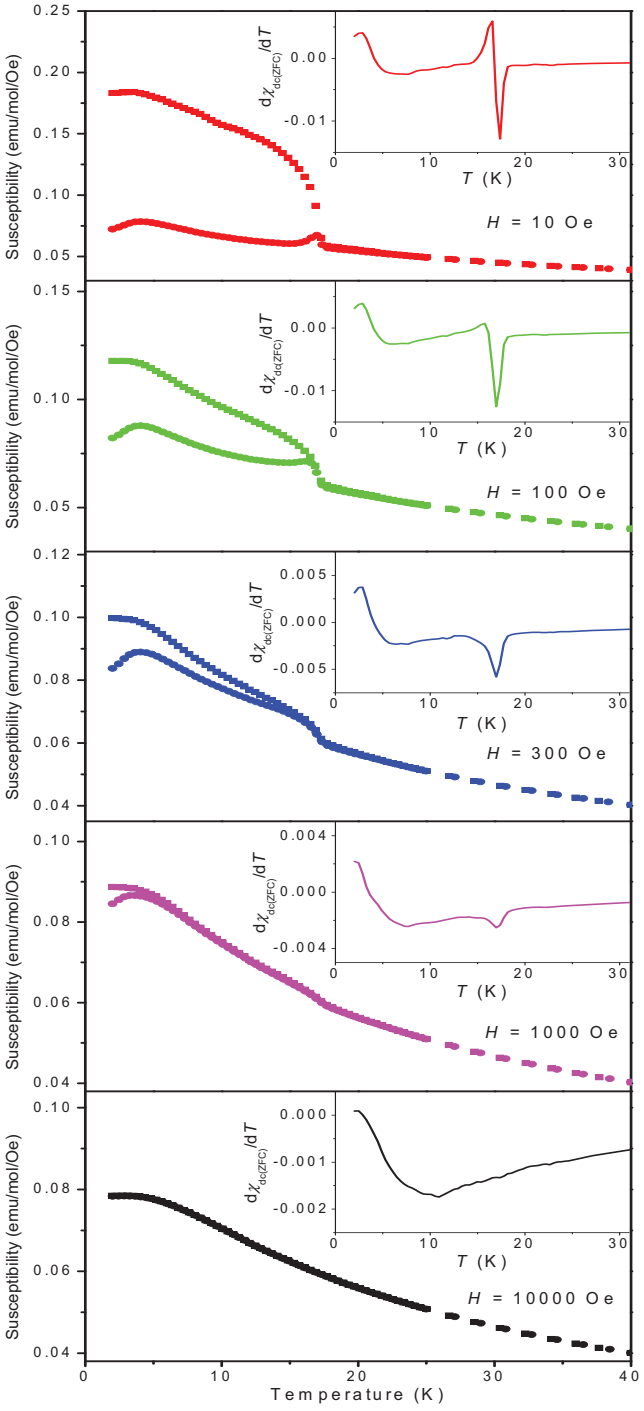

Figure 5-3-2 ZFC (circles) and FC (squares) susceptibilities for various probing fields. Insets: temperature-dependent differential ZFC susceptibilities.

The AT line can be obtained by plotting the reduced temperature $\theta_a = T_a/T_c$ versus probing field H. T_c is the Curie temperature of the material, while for a spin-glass system T_c should be replaced by the zero-field spin-glass transition temperature T_g. The reduced temperature θ_a scales with H as the following expression [166],

$$\theta_a \propto 1 - \frac{C_{AT}}{T_g} \cdot H^n . \tag{5.3.2}$$

Here C_{AT} is a constant and T_g = 4.5 K (given later in the AC susceptibility results). The field dependence of the reduced temperature θ_a is plotted in **Figure 5-3-3**. The best fit with Eq. (5.3.2) yields n = 0.59 ± 0.05. In canonical spin glass systems the mean-field theory predicts n = 2/3 [166, 167], which is close to the n value given in our results. At a large field of 10000 Oe, a deviation from the AT-line is observed in **Figure 5-3-3**, in agreement with what has been reported that deviations from the AT-line may happen in some spin glasses under large magnetic fields [168, 169].

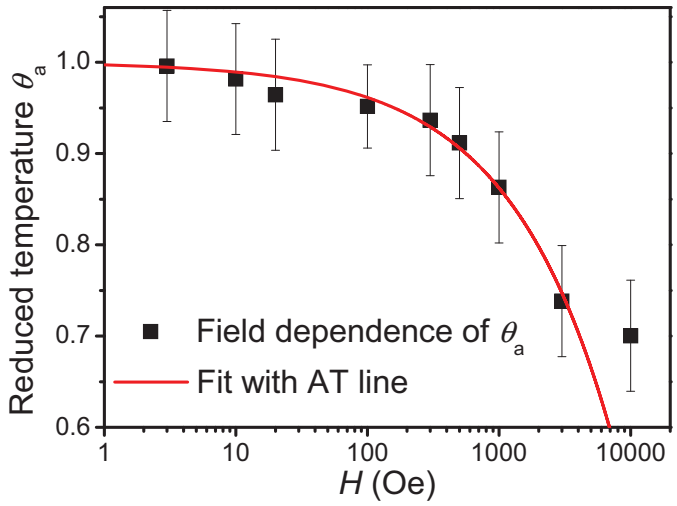

Figure 5-3-3 Field dependence (black squares) of the reduced temperature θ_a obtained in ZFC susceptibilities under various probing fields. Red line: the best fit in terms of Eq. (5.3.2) (see text).

The analysis of the field dependence of T_a shows that the hump at T_a probably stems from a spin-glass-like freezing process. Now the downshift of T_a with increasing magnetic fields makes sense because higher magnetic fields suppress the

energy barriers and thus reduce the freezing temperature. The inflection temperature T_b shows no field dependence, which seems to be associated with a long-range collective magnetic behavior.

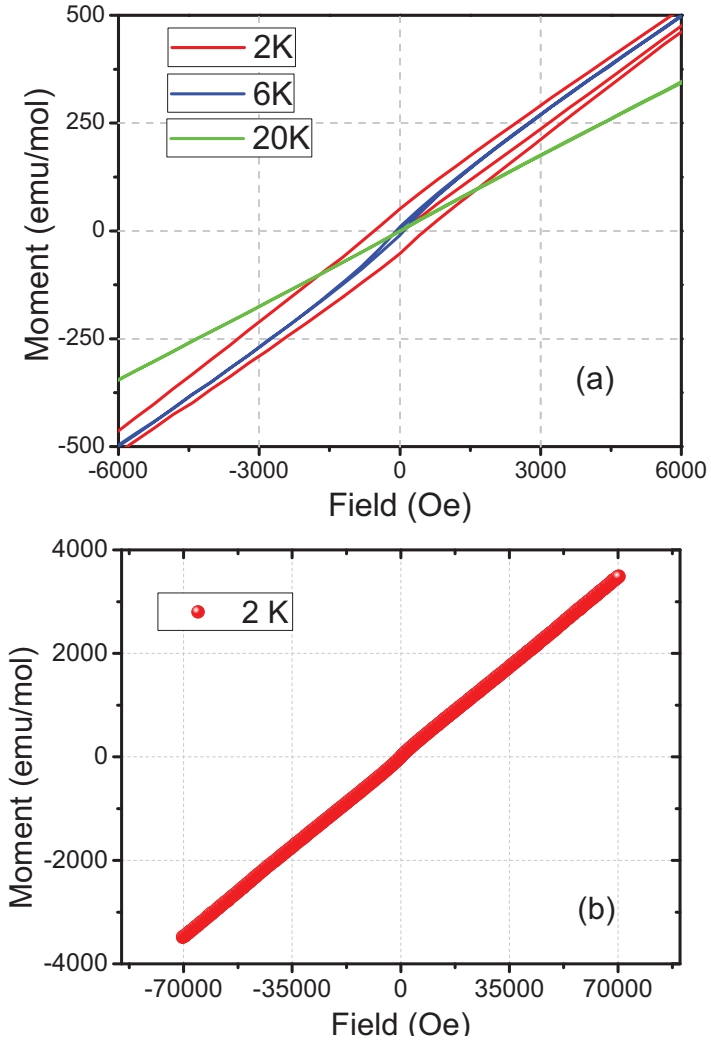

Figure 5-3-4 (a) Field-dependence of the magnetization $M(H)$ of $Na_3Co(CO_3)_2Cl$ at 2 K (red line), 6 K (blue line) and 20 K (green line). **(b)** $M(H)$ at 2 K with H up to 7 T.

More insight into the magnetic phase of the frozen state of $Na_3Co(CO_3)_2Cl$ was obtained by measuring the field dependent magnetization $M(H)$. The measurements were performed within the field range -7 T ≤ H ≤ 7 T at 2, 6 and 20 K after the sample

was zero-field-cooled. All the curves have been measured first from 0 to 7 T, then from 7 T to -7 T, and finally from -7 T to 7 T. The low-field part of $M(H)$ curves are shown in **Figure 5-3-4 (a)**. The full $M(H)$ profile at 2 K is shown in **Figure 5-3-4 (b)**.

As shown in **Figure 5-3-4 (a)**, the $M(H)$ curve for 2 K (< T_g) exhibits a clear hysteresis loop, whose coercivity decreases with increasing temperature. At 6 K there still a little coercivity left. At 20 K the $M(H)$ curve becomes linear. Lack of ferromagnetic long-range order, the hysteresis behavior at 2 K originates from the competition between the external magnetic field and the peculiar local anisotropy, which is expectable for spin glass systems below the freezing temperature. In **Figure 5-3-4 (b)**, the magnetization was measured up to 7 Tesla at 2 K. No saturation can be obtained within the range of applied field. For a spin glass below freezing temperature, there are randomly-distributed energy barriers for rotating cluster moments away from their anisotropy-pinned frozen orientation. The external field has to overcome these energy barriers before the various clusters can align with respect to the field direction and reach the saturation of the spins [42]. Here the nonattainment of spin saturation, as well as the hysteretic magnetization at 2 K, is consistent with a spin-glass-like behavior in $Na_3Co(CO_3)_2Cl$.

Below the spin-glass freezing temperature T_g, the spin dynamics of a spin-glass system should be characterized by a non-equilibrium, highly irreversible, metastable frozen state rather than a conventional long-range magnetic order. As one of the most intriguing properties in spin glasses, non-equilibrium spin dynamics of spin-glass phase has been often studied by an age-dependence of the magnetic response, namely the so-called memory effects [170-174]. When the spin glass is cooled from a high temperature above T_g to a low temperature below T_g, the initial state is not thermodynamically stable and will relax to a more stable state with less susceptible equilibrium. This approach to more stable states depends strongly on the thermal history of the system within the spin-glass phase, which can be represented by the memory effect of magnetization. In a typical memory effect protocol, the sample is zero-field-cooled from room temperature (well above T_g) to the base temperature (2 K in this case), and then a small DC field h is applied and the reference ZFC magnetization is measured from the base temperature to room temperature. After switching off the DC field h, the sample is ZFC again from room temperature to a waiting temperature T_w ($T_w < T_g$), where the sample is kept for a waiting time t_w. After this waiting time t_w, the sample cooling is subsequently

resumed down to the base temperature and then ZFC magnetization is measured again with DC field h from the base temperature to room temperature. During the isothermal holding time t_w, the magnetization relaxes to a lower value due to the rearrangement of the spin orientations towards the more equilibrium state. The approach of the spin configuration to the equilibration at the holding temperature corresponds to the aging process of the spin-glass system. If the system is cooled further, new aging process starts (rejuvenation effect). But the previous aging process is "remembered" by the spin glass and retieved when the system is reheated. This phenomenon is known as memory effect.

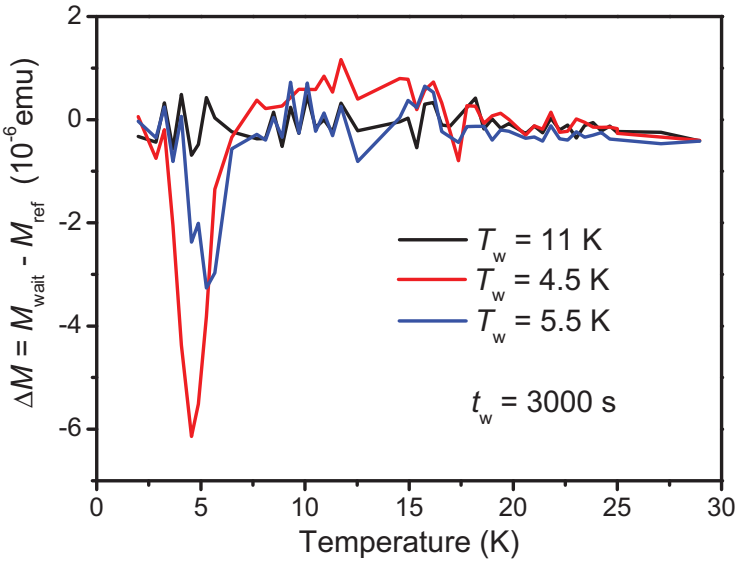

Figure 5-3-5 Memory effect observed in the ZFC magnetization measurements of $Na_3Co(CO_3)_2Cl$. The magnetization difference ΔM is plotted corresponding to three waiting temperatures, T_w = 11 K (black), 4.5 K (red) and 5.5 K (blue).

The memory effect was observed in $Na_3Co(CO_3)_2Cl$. Before measuring the memory effect of $Na_3Co(CO_3)_2Cl$, the SQUID magnetometer was digaussed and a zero field in sample position was achieved using the ultralow field option on SQUID. The lowest temperature which could be reached in my measurements was 2 K. It was hard to observe a full memory effect since the temperature interval between the base temperature and the spin-glass-like transition temperature T_g (~ 4.5 K) was rather

small. So two waiting temperatures, 4.5 K and 5.5 K, were chosen to leave enough temperature interval on the low-temperature side of T_w. Following the aforementioned experimental procedures, the reference ZFC magnetization and the waiting curves with waiting temperatures 4.5 K and 5.5 K were collected with a DC field h = 100 Oe. The memory effect at these two waiting temperatures were evidenced by the difference curves between the reference and the waiting magnetization data, as shown by the red (T_w = 4.5 K) and blue (T_w = 5.5 K) lines in **Figure 5-3-5**. Another waiting curve was taken at T_w = 11 K for comparison, as shown by the black line in **Figure 5-3-5**. The waiting time in three waiting procedures is 3000 s.

As shown in **Figure 5-3-5**, the difference curves for T_w = 4.5 K (red line) and T_w = 5.5 K (blue line) exhibit a dip at ~ 4.6 K and ~ 5.3 K, respectively. Taking into account the 0.25 K temperature step in the measurements, these two dips represent a clear memory phenomenon, which is due to the spontaneous arrangement of the magnetic moment configuration towards the more stable and less susceptible equilibrium when the system is kept unperturbed at constant temperature T_w. Observing memory phenomenon at T_w = 5.5 K may suggest that the spin freezing process already starts above T_g = 4.5 K, which is also consistent with the small hysteresis loop detected in the field dependence of magnetization at 6 K (see **Figure 5-3-4 (a)**). But at 11 K there is definitely no memory effect observed because the difference curve for T_w = 11 K is basically flat. The major spin-glass freezing process should happen around T_g = 4.5 K, which is determined by AC susceptibility measurements (given in next section), since in **Figure 5-3-5** the memory effect at ~ 4.5 K is more prominent (bigger dip) than that at ~ 5.5 K. Therefore the spin-glass phase of $Na_3Co(CO_3)_2Cl$ is more evidenced by the investigation of spin dynamics spanning the spin freezing temperature T_g in light of the memory effect, which was observed by retrieving the semi-equilibrated state due to the waiting procedure at constant temperature around the spin-glass freezing temperature.

5.3.2 AC Susceptibility

Spin glass behavior is usually studied by the AC susceptibility and the spin-glass temperature can be accurately determined by the frequency dependence of real or imaginary components [42, 174]. AC susceptibility technique is espetially important for spin glasses, since the driving field h_{ac} can be sufficiently small (about a few

Oersteds) and the magnetic susceptibility χ is measured by taking the derivative $\partial M/\partial h$ at angular frequency ω varying over a rather large frequency range. The dynamics of spin glasses can accordingly be studied over a large time scale.

The AC susceptibility measurement of $Na_3Co(CO_3)_2Cl$ was performed with an AC amplitude of $\mu_0 h_{ac}$ = 10 Oe at the frequencies $25 \le f \le 10^4$ Hz after ZFC from room temperature. The temperature dependence of the real component of the AC susceptibility χ' at different frequencies is plotted in **Figure 5-3-6**. The inflection point in DC magnetization at $T_b \approx 17$ K appears to be a peak in AC susceptibilities for all frequencies, and its peak position is frequency-independent, indicating this peak is not due to a spin-glass transition. The broad peak at around 4 K displays clear frequency dispersion. The temperature T_m at the maximum of this broad peak shifts to higher values as the frequency increases. The spin-glass-like transition is then evidenced by fitting the frequency dependence of the peak temperature to a critical power law [42, 174, 175],

$$\tau = \tau^* \left(\frac{T_m}{T_g} - 1 \right)^{-zv}, \tag{5.3.3}$$

where $\tau = (2\pi f)^{-1}$, τ^* is the relaxation time of individual particle moment, T_g is the static glassy transition temperature and zv is dynamic critical exponent. The best fit in terms of Eq. (5.3.3) is shown in the inset of **Figure 5-3-6**, yielding T_g = 4.5(4) K, $\tau^* = 10^{-10.7(5)}$ s and zv = 8.4(6). For the sake of clarity, the inset of **Figure 5-3-6** is plotted in the style of $\log(\tau)$ *vs*. $\log(T_m/T_g\text{-}1)$. The value of zv holds good in the range between 4 and 12 found in the spin glass materials [42, 175]. The value of relaxation time $\tau^* = 10^{-10.7(5)}$ s locates also in the characteristic range, 10^{-8}-10^{-12} s, usually derived for canonical spin glass [42, 175].

Another important factor used for quantitatively characterizing a magnetic glassy transition is the frequency shift K, which gives the relative variation of the peak temperature T_m with the angular frequency ω and often offers a good criterion for distinguishing a canonical spin glass from a superparamagnet. The frequency shift K is defined as $(\Delta T_m/T_m)$ per decade ω as follows [42, 174]

$$K = \frac{1}{T_m} \frac{\Delta T_m}{\Delta \log \omega}. \tag{5.3.4}$$

Using Eq. (5.3.4), the frequency shift K of $Na_3Co(CO_3)_2Cl$ is estimated to be about 0.04, much smaller than the values for superparamagnets and close to those observed in

spin glasses [42].

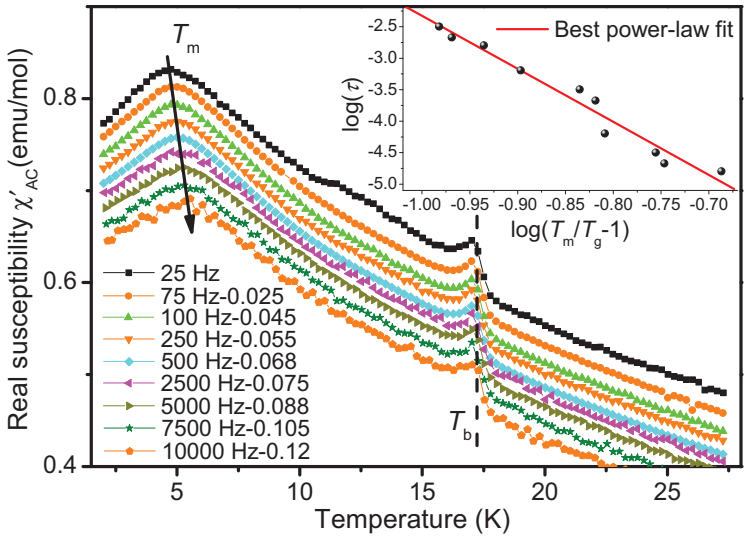

Figure 5-3-6 Temperature dependence of the real AC susceptibility component χ' of $Na_3Co(CO_3)_2Cl$ with an AC amplitude h_{ac} = 10 Oe at frequencies 25 ≤ f ≤ 10000 Hz. The y-axis corresponds to the data for 25 Hz. In order to see the frequency dependence clearly, the data of other frequencies are shifted. Inset: frequency dependence of the freezing temperature T_m with the best power-law fit (red line).

Another way of presenting the AC susceptibility data is to illustrate the relaxation-time distribution using the so-called Cole-Cole or Argand representation, where the AC susceptibility data can be plotted in the complex plane as χ' versus χ'' [42, 174, 176, 177]. In the Cole-Cole model the complex AC susceptibility, $\chi = \chi' - i\chi''$, is expressed as [177, 178]

$$\chi(\omega) = \chi_S + \frac{\chi_0 - \chi_S}{1 + (i\omega\tau_c)^{1-\alpha}}, \tag{5.3.5}$$

where χ_0 and χ_s are the isothermal (low frequency) and adiabatic (high frequency) susceptibilities, τ_c is the characteristic relaxation time and α reflects the polydispersivity of the system. In spin glass systems one expects values of α near to 1. Decomposing Eq. (5.3.5) into its real and imaginary parts, one has [179, 180]

$$\chi'(\omega) = \chi_S + \frac{\chi_0 - \chi_S}{2}\left(1 - \frac{\sinh[(1-\alpha)\ln(\omega\tau_c)]}{\cosh[(1-\alpha)\ln(\omega\tau_c)] + \cos[(1/2)(1-\alpha)\pi]}\right), \quad (5.3.6)$$

$$\chi''(\omega) = \frac{\chi_0 - \chi_S}{2}\left(\frac{\sin[(1/2)(1-\alpha)\pi]}{\cosh[(1-\alpha)\ln(\omega\tau_c)] + \cos[(1/2)(1-\alpha)\pi]}\right), \quad (5.3.7)$$

where $\omega = 2\pi f$. Then the Cole-Cole plot, namely the imaginary part χ'' as a function of the real part χ', can be expressed in the following form [178, 181],

$$\chi''(\chi') = -\frac{\chi_0 - \chi_S}{2\tan[(1-\alpha)\pi/2]} + \left\{(\chi' - \chi_S)(\chi_0 - \chi') + \frac{(\chi_0 - \chi_S)^2}{4\tan^2[(1-\alpha)\pi/2]}\right\}^{1/2}. \quad (5.3.8)$$

For a monodisperse ensemble of spin clusters with exactly one relaxation time, the Cole-Cole plot displays a semicircle with the center on the χ' axis. But for spin glass systems, this semicircle is flattened to an arc shape due to the large distribution of relaxation times.

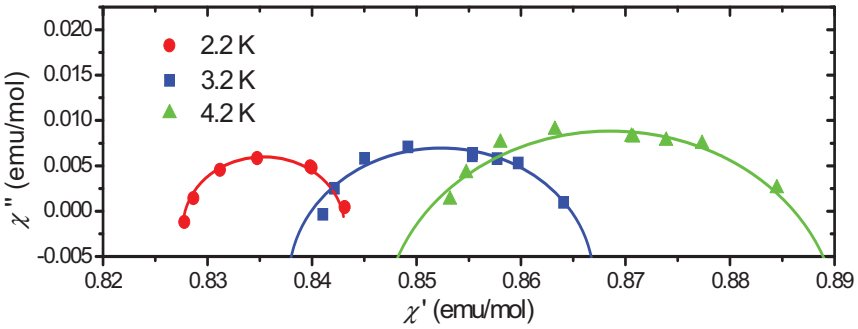

Figure 5-3-7 Cole-Cole plots of susceptibility χ'' *vs.* χ' for $Na_3Co(CO_3)_2Cl$ at 2.2 K (red circles), 3.2 K (blue squares) and 4.2 K (green triangles). The solid lines are the corresponding best fits with Eq. (5.3.8).

As shown in **Figure 5-3-7**, the Cole-Cole plots at 2.2 K, 3.2 K and 4.2 K are all flattened semicircles. As the temperature increases from 2.2 K to 4.2 K, namely approaches to the freezing temperature T_g, the Cole-Cole plot shifts upward and becomes more flattened, which is due to the strong polydispersivity and infinitely broad distribution of the relaxation times as T approaches T_g [42, 174]. The flattened-shape semicircles of the Cole-Cole plots indicate that $Na_3Co(CO_3)_2Cl$ is a spin-glass-like system rather than a superparamagnet.

As a summary of Section 5.3, the static and dynamic magnetic properties of $Na_3Co(CO_3)_2Cl$ have been extensively investigated by means of DC and AC susceptibility measurements. Two kinks were found in the low-field susceptibility measurements at ~ 17 K and ~ 4 K respectively. The former one exhibits no frequency dependence in the AC susceptibility measurements and no field dependence in DC magnetization measurements, and thus is temporarily attributed to an onset temperature for a long-range collective magnetic behavior. As to the later one, various methods were employed to discover its nature. In DC magnetization measurements, the field dependence of this peak follows the AT line, consistent with a spin-glass-like freezing. Clear hysteresis loop can be seen in the field dependence of magnetization at 2 K. Memory effect was observed around 4 K. In AC susceptibility measurements, the hump at ~ 4 K exhibits clear frequency dependence, which can be fitted with a critical power law. The obtained fitting parameters are consistent with the corresponding values of canonical spin-glass systems. The spin-glass-like transition temperature of $Na_3Co(CO_3)_2Cl$ is then determined to be T_g = 4.5(4) K. The value of frequency shift and the flattened-shape semicircles of the Cole-Cole plots indicate that the spin freezing at T_g is of spin-glass-like origin rather than a superparamagnetic blocking. Therefore $Na_3Co(CO_3)_2Cl$ is suggested to experience a spin-glass-like freezing process at T_g = 4.5(4) K by the static and dynamic magnetic characterizations.

5.4 Specific Heat of $Na_3Co(CO_3)_2Cl$

The specific heat of $Na_3Co(CO_3)_2Cl$ has been measured using a Quantum Design Physical Property Measurement System (PPMS) equipped with a liquid helium cryostat and a dilution cryostat. Relaxation method was applied to extract the heat capacity values [85, 86]. Unable to synthesize a crystal by now, $Na_3Co(CO_3)_2Cl$ powder was compressed with a load of 10 kbar pressure and a piece of compressed plate of 0.2 mm thickness and 1 mg mass was used for heat capacity measurements.

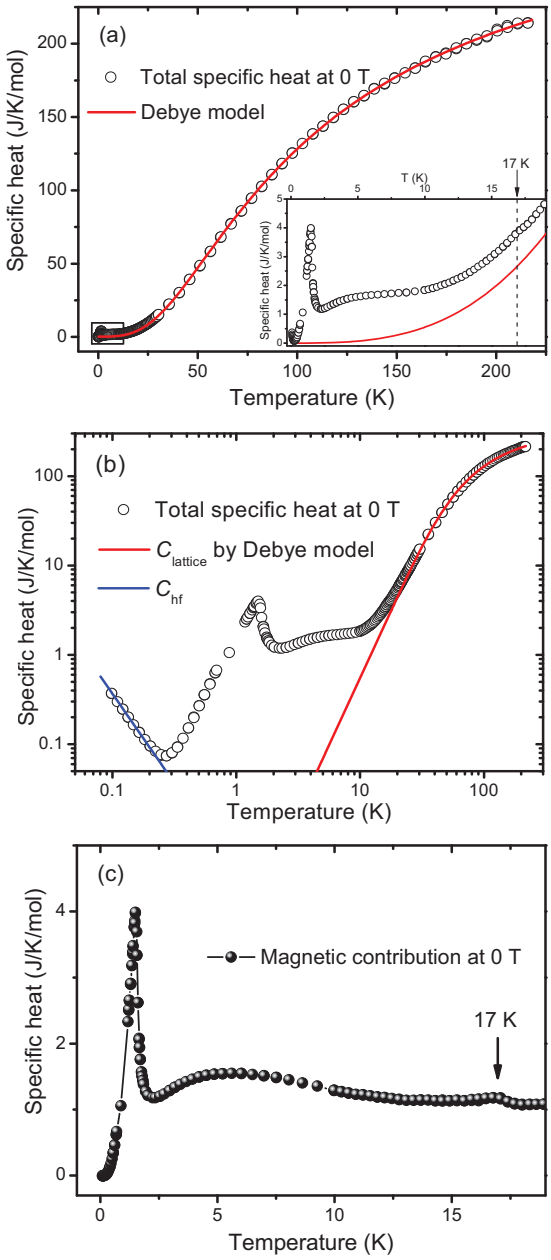

Figure 5-4-1 Temperature dependence of the specific heat of $Na_3Co(CO_3)_2Cl$ under zero external magnetic field with the best fit of a simple Debye model (red line) in linear-linear scale **(a)** and log-log scale **(b)**. Inset of **(a)**: the low temperature part (90 mK to 19 K) of the specific heat. Blue line in **(b)**: fit with the hyperfine interaction. **(c)** The low temperature part (90 mK to 19 K) of the magnetic specific heat at 0 T.

Figure 5-4-1 shows the temperature dependence of the specific heat of $Na_3Co(CO_3)_2Cl$ measured in zero external field within the temperature range 90 mK to 220 K in linear-linear scale **(a)** and log-log scale **(b)**. Without a non-magnetic reference material, it is difficult to determine the lattice specific heat precisely. However a simple Debye model may describe the lattice specific heat C_{lattice} nicely as shown by the red line in **Figure 5-4-1**, which is expressed in the conventional form [87],

$$C_{\text{Debye}} = 9sR\left(\frac{T}{\Theta_D}\right)^3 \int_0^{\Theta_D/T} \frac{x^4 e^x dx}{\left(e^x - 1\right)^2}, \tag{5.4.1}$$

where s is the number of atoms per formula unit, R is the ideal gas constant, and Θ_D is the Debye temperature. The best fit with the Debye model yields a Debye temperature of Θ_D = 380 ± 20 K.

As seen in the log-log plot in **Figure 5-4-1 (b)**, the specific heat of $Na_3Co(CO_3)_2Cl$ shows a clear upturn below 0.25 K. This upturn can be attributed to the high-temperature tail of the theoretical hyperfine contribution due to the nonzero magnetic moments of ^{59}Co nucleus. The hyperfine interaction gives rise to a Schottky specific heat anomaly with the high temperature tail given by [182]

$$C_{\text{hf}} = R\frac{I(I+1)}{3}\left(\frac{g_{\text{n}}\mu_{\text{N}}H_{\text{hf}}}{k_{\text{B}}T}\right)^2, \tag{5.4.2}$$

where I = 7/2 is the nuclear spin of ^{59}Co with 100% natural abundance, g_{n} is the nuclear g factor, μ_{N} is the nuclear magneton and H_{hf} is the effective hyperfine field. The fit using Eq. (5.4.2) was performed to the specific heat data below 0.25 K, where the hyperfine contribution became overwhelming as compared to the lattice and electronic spin contributions. The best fit is shown as the blue line in **Figure 5-4-1 (b)** and yields an effective hyperfine field in $Na_3Co(CO_3)_2Cl$, H_{hf} = 250(10) kOe.

In order to see the low-temperature anomalies clearly, the total and magnetic specific heat below 19 K is plotted in the inset of **Figure 5-4-1 (a)** and **Figure 5-4-1 (c)**, respectively. The magnetic specific heat is obtained by subtracting both the lattice contribution C_{lattice} and the hyperfine contribution C_{hf} from the total specific heat. The most striking features in this region are the hump at ~ 5 K and the sharp lambda-shape peak at 1.5 K. The hump at ~ 5 K should be due to the spin-glass-like transition at T_{g} = 4.5(4) K, since spin-glass systems normally exhibit a broad

maximum in magnetic specific heat with the peak temperature $T_{max} \approx 1.3\ T_g$ [42]. For canonical spin glasses, the broad maximum above T_g decreases slowly with increasing temperature and shifts towards higher temperature with increasing external field [42]. The total and magnetic specific heat of $Na_3Co(CO_3)_2Cl$ under various external magnetic fields is shown in **Figure 5-4-2 (a)** and **(b)**, respectively. The hump at ~ 5 K shifts to higher temperature and smears out as external magnetic field increases, which is consistent with the behavior of canonical spin glasses.

The sharp peak at 1.5 K in **Figure 5-4-1 (c)** is attributed to a long-range magnetic phase transition. The Néel temperature of $Na_3Co(CO_3)_2Cl$ is then determined to be 1.5 K. Accordingly the frustration parameter $f = |\Theta_{CW}|/T_N \approx 22.5$ [37], can be determined and attributes $Na_3Co(CO_3)_2Cl$ to the family of highly-frustrated magnets. Unfortunately, it is not applicable to carry out a precise fit to both the sharp peak at 1.5 K and the broad hump at ~ 5 K. First they are too close to be fitted separately. Second the hump at ~ 5 K associates to the spin-glass-like freezing of Co^{2+} spins so that a Schottky-type magnetic specific heat model is inappropriate since a probability distribution of energy splitting rather than several well-defined energy gaps, should be considered for spin-glass systems [136, 183, 184].

As shown in the inset of **Figure 5-4-1 (a)** and more clearly in **Figure 5-4-1 (c)**, the specific heat of $Na_3Co(CO_3)_2Cl$ exhibits a very small hump at ~ 17 K, whose position coincides with the inflection temperature observed in DC and AC susceptibility measurements. Again this small hump in specific heat is temporarily attributed to the onset of a long-range collective magnetic behavior in $Na_3Co(CO_3)_2Cl$.

The magnetic entropy at the spin-glass freezing temperature has been used to evaluate the frozen-in magnetic degrees of freedom [42]. The magnetic entropy S_m, as a function of temperature is shown in **Figure 5-4-3**, which can be expressed by the following thermodynamic relationship,

$$S_m(T) = \int_0^T \frac{C_m(T')}{T'} dT' , \qquad (5.4.3)$$

where $C_m(T')$ is the magnetic specific heat and obtained by subtracting the lattice specific heat $C_{lattice}$ and the hyperfine specific heat C_{hf} from the total specific heat. At the spin-glass-like transition temperature T_g = 4.5 K, the magnetic entropy is ~ 3.3 J mol^{-1} K^{-1}. Considering the total magnetic entropy $R\ln(4)$ = 11.5 J mol^{-1} K^{-1} expected for an S = 3/2 system, ~ 70% of the magnetic degrees of freedom are already frozen

above T_g. Only ~ 30% of the expected magnetic entropy is recovered at the freezing temperature, in agreement with the values for other canonical spin glasses [42].

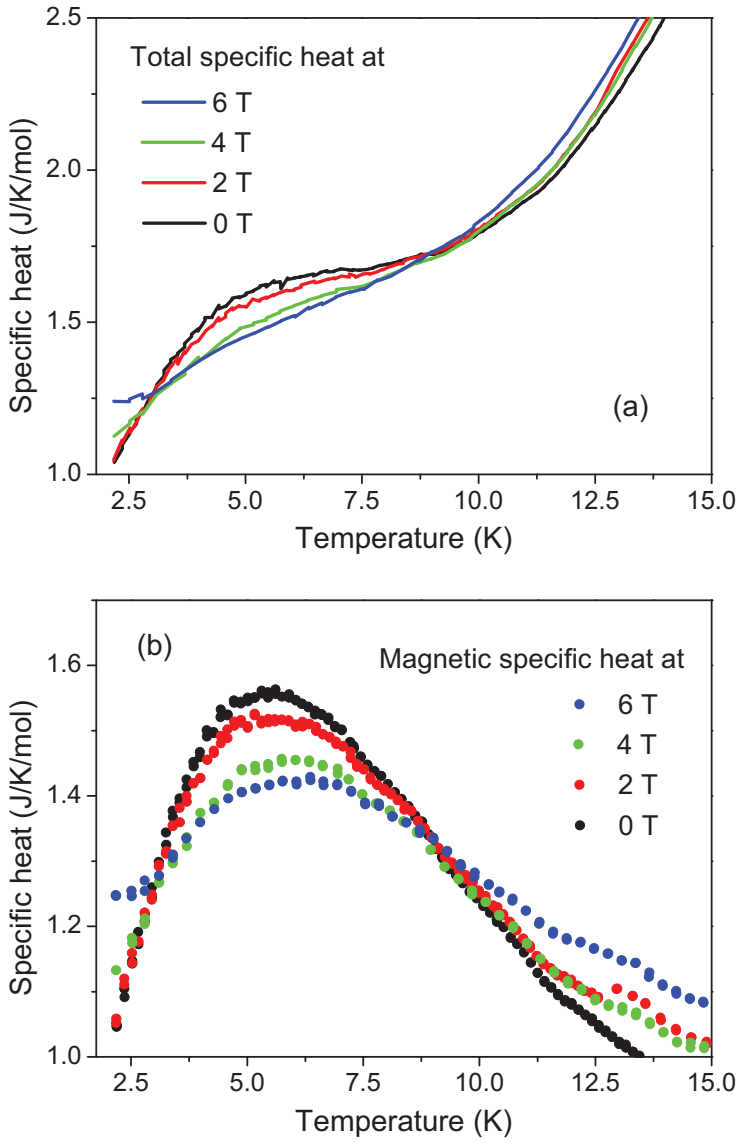

Figure 5-4-2 Temperature dependence of the total **(a)** and magnetic **(b)** specific heat of $Na_3Co(CO_3)_2Cl$ under external fields of 0, 2, 4 and 6 Tesla.

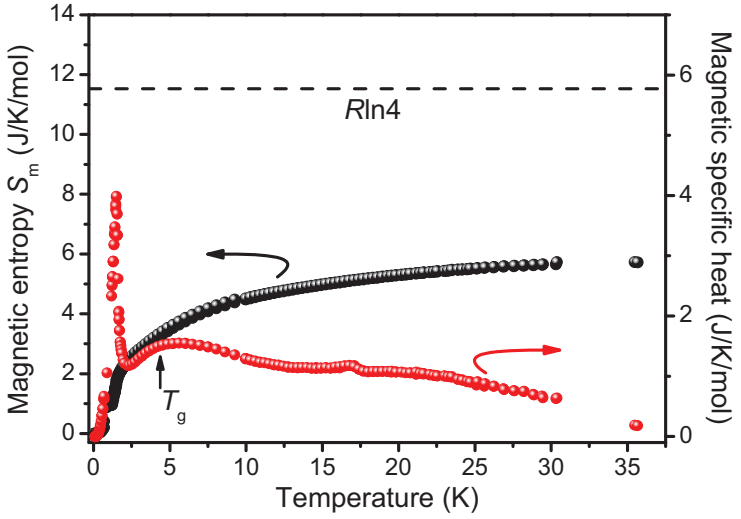

Figure 5-4-3 Magnetic entropy (black spheres) for Co^{2+} cations estimated by integrating C_m/T from 0.07 K to 35.5 K, along with the magnetic specific heat C_m (red spheres) at 0 T. Value of $R\ln(4)$ is indicated by the dashed line. T_g = 4.5 K is the spin-glass-like transition temperature.

As a summary of this section, the specific heat studies on $Na_3Co(CO_3)_2Cl$ give the following results: (i) Likely, there is a long-range magnetic phase transition at 1.5 K; (ii) The nuclear hyperfine contribution to the specific heat was observed owing to the relatively large nuclear magnetic moment of ^{59}Co in a appropriate hyperfine field; (iii) The possible onset of long-range spin collective behavior gives rise to a small hump at ~ 17 K; (iv) The broad maximum at ~ 5 K is associated with the spin-glass-like freezing process; (v) Only 30% of the total magnetic entropy has been recovered at the spin-glass-like freezing temperature T_g = 4.5 K, in agreement with the values obtained in canonical spin glasses.

5.5 Neutron Powder Diffraction of $Na_3Co(CO_3)_2Cl$

In order to determine the crystal structure more precisely and detect possible defect structures, we performed neutron powder diffraction (NPD) measurements on $Na_3Co(CO_3)_2Cl$. Neutron powder diffraction data for the refinement of the crystal

structure were collected on the high-resolution diffractometer SPODI [185] at FRM II research reactor (Garching, Germany). A Ge (551) monochromator was used to produce a monochromatic neutron beam of wavelength 1.5483(7) Å. The $Na_3Co(CO_3)_2Cl$ sample in powder form was filled in a thin-wall vanadium container and then mounted in top-loading closed-cycle refrigerator. Collection of neutron powder diffraction data was performed at various temperatures of 3.7, 6, 12, 14, 16, 30, 50, 100, 150, 200, 250, and 300 K. The Fullprof package [117] was used for the Rietveld refinement [162] of the crystal structure of $Na_3Co(CO_3)_2Cl$. The experimental NPD patterns (black circles) for 3.7 K and 30 K are shown in **Figure 5-5-1 (a)** and **(b)**, respectively, together with the Bragg positions (green short lines), the calculated patterns (red lines) and the differences (blue lines) between the experimental and calculated patterns. The difference profile obtained by subtracting the experimental pattern for 3.7 K from the one for 30 K is plotted as the black line shown in **Figure 5-5-1 (c)**.

As shown in **Figure 5-5-1 (a)** and **(b)**, the calculated patterns are in good agreement with the experimental ones. From the difference (black line in **Figure 5-5-1 (c)**) of the experimental data for 3.7 K and 30 K, there is no sign for any long-range or short-range magnetic order existing between these two temperatures. The absence of long-range magnetic order above 3.7 K is expected since the spins freeze randomly when crossing the spin-glass transition temperature T_g = 4.5 K [42, 150]. And the inflection temperature T_b = 17 K is thus confirmed not to be the onset of long-range magnetic order. The present NPD experiment could not be performed below 1.5 K, where a long-range magnetic phase transition is indicated in specific heat data. The long-range magnetic order of $Na_3Co(CO_3)_2Cl$ at 1.5 K will be discussed in Section 5.6. The NPD measurements show no indication of short-range spin order either, because the short-range spin correlations might be too weak to be separated from the background (see Section 5.6). Note that as shown in **Figure 5-5-1 (a)** and **(b)**, the background increases at low angles, just where magnetic scattering could be visible due to the form factor behavior. Showing no trace for magnetic scattering, the analysis of neutron powder diffraction data was focused on the determination of the average crystal structure of $Na_3Co(CO_3)_2Cl$.

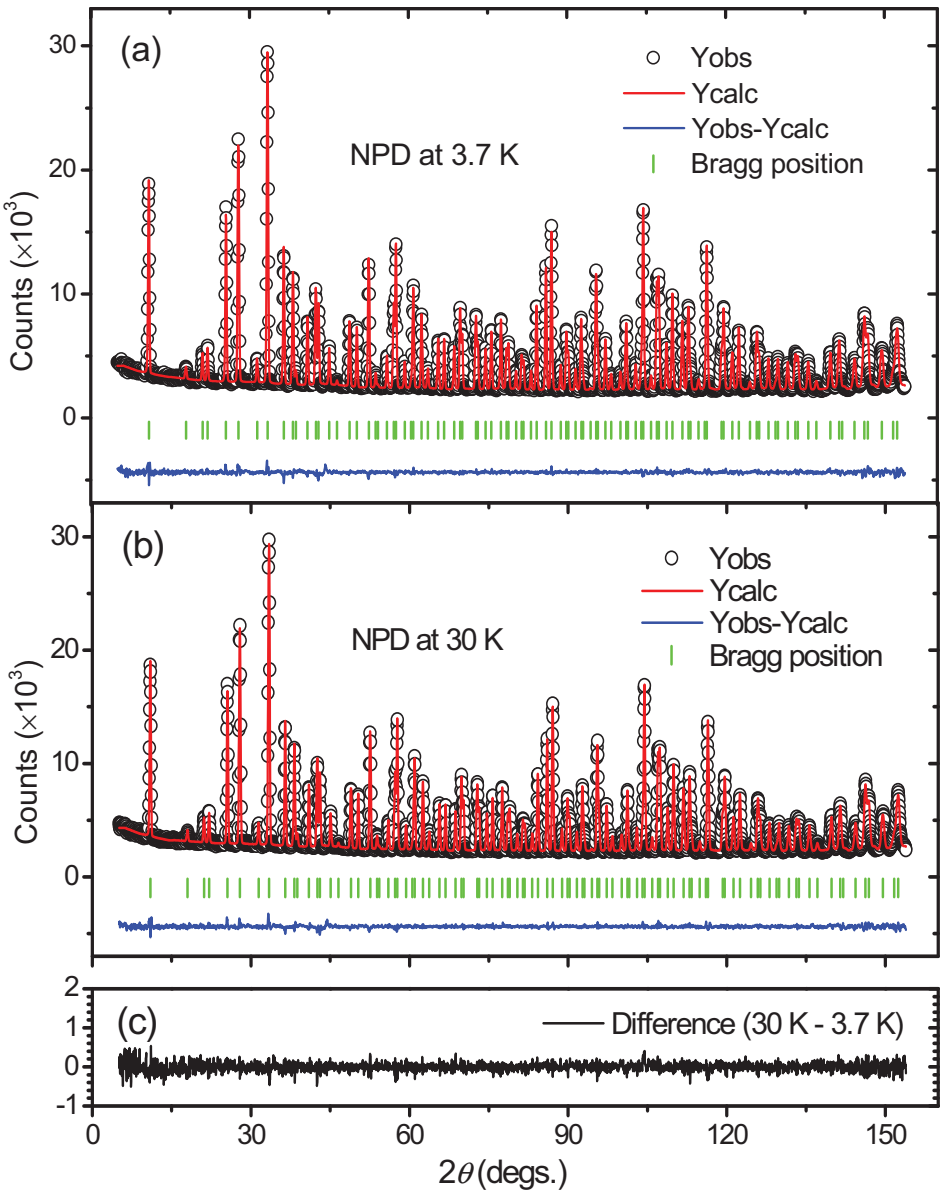

Figure 5-5-1 Experimental (Yobs), calculated (Ycalc) and difference (Yobs-Ycalc) neutron powder diffraction (NPD) patterns obtained at 3.7 K **(a)** and 30 K **(b)** with the Rietveld refinement. The green short lines indicate the positions of the Bragg reflections. **(c)** Difference pattern between the data for 3.7 and 30 K.

In the Rietveld refinement of crystal structure, the best agreement between the NPD data and the structural model has been found when Co has been modeled occupying (16*c*: $.\bar{3}.$) (0, 0, 0) site, C occupying (32*e*: .3.) (*x*+0.25, -*x*, *x*+0.25), Cl occupying (16*d*: $.\bar{3}.$) (0.25, 0.25, 0.5), O occupying (96*g*: 1) (*x*, *y*, *z*) and Na occupying (48*f*: 2..) (0.125, *y*, 0.125). Considering the experimental accuracy, the occupancies of all atoms are set as 1, because the change of occupation numbers is less than 10% if they are refined. Though Co sublattice displays a fully ordered pyrochlore, displacement on Na sites is obvious in the sense that the *y* position slightly deviates from -0.125 as expected for the ordered phase. The Co and C atoms are refined with isotropic model. Use of anisotropic atomic displacement parameters (ADP) on Na, O and Cl sites results in a significant improvement of the residuals of the refinement, especially at higher temperatures. The best fits to NPD patterns for 3.7 K, 30 K and 300 K are obtained with structure parameters and the reliability factors listed in **Table 5-5-1**, where the corresponding parameters for XRPD at 300 K (see Section 5.2) are also given for comparison. Due to symmetry constraints, the anisotropic atomic displacement parameters for Na, O and Cl sites were modeled as: Na (u_{11}, u_{22}, u_{33}, $u_{12} = u_{23} = 0$, u_{13}), O (u_{11}, u_{22}, u_{33}, u_{12}, u_{23}, u_{13}), and Cl ($u_{11} = u_{22} = u_{33}$, $u_{12} = -u_{23}$, $u_{12} = -u_{13}$). The refined isotropic and anisotropic atomic displacement factors for the NPD measurements at all 12 temperatures are listed in **Table 5-5-2 (a), (b)**. **Figure 5-5-2 (a)-(c)** illustrate the crystal structure in *a*-*b*, *b*-*c* and *a*-*c* planes with thermal-motion probability ellipsoids, which are derived from anisotropic temperature factor parameters. In **Figure 5-5-3**, the refined isotropic and anisotropic atomic displacement factors are plotted as a function of temperature.

The anisotropic temperature factors can indicate static disorder, an essential ingredient for the spin glass behavior in addition to magnetic frustration. At the lowest temperature the sequence of mean atomic displacement factors follows $u_{eq}(Na) \geq u_{eq}(Cl) \geq u_{eq}(C) \geq u_{eq}(Co)$, whilst the weight of constituents in $Na_3Co(CO_3)_2Cl$ (usually inversely proportional to the mean amplitude of thermal vibrations) reads as $m_{Na} < m_C < m_{Cl} < m_{Co}$, which might indicate some static atomic disorder on chlorine sites.

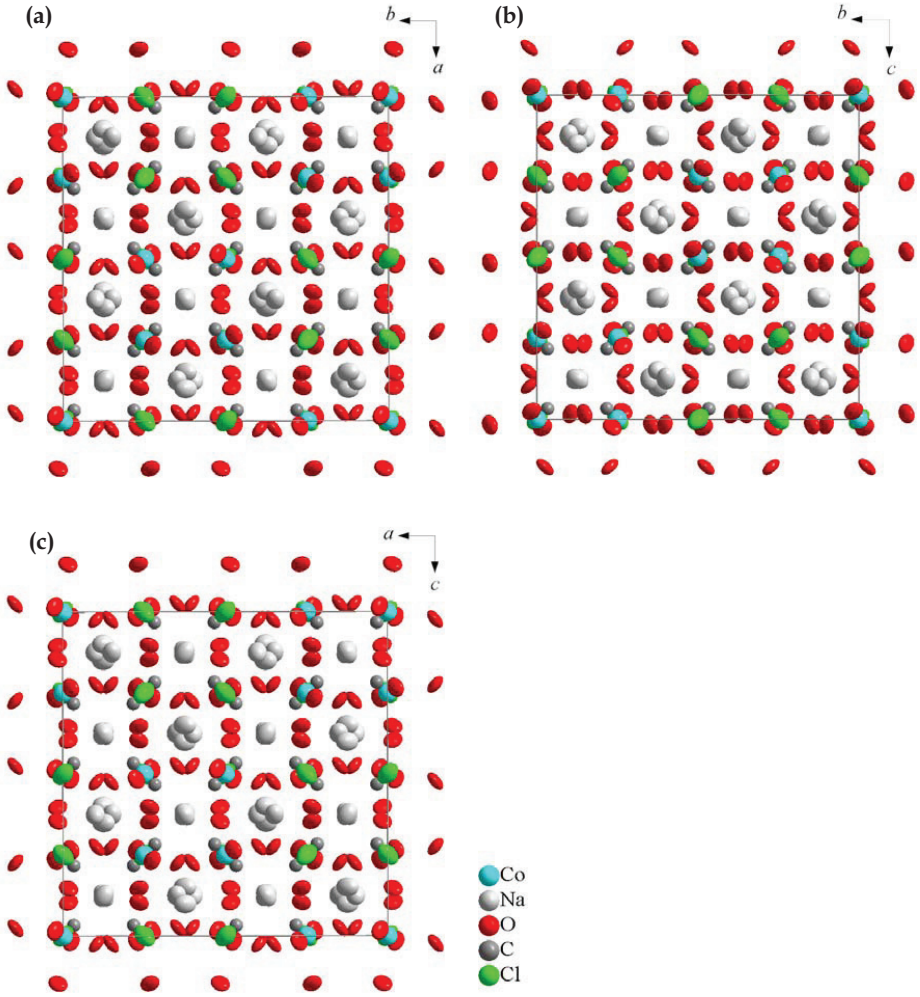

Figure 5-5-2 Crystal structure in *a*-*b*, *b*-*c* and *a*-*c* planes with thermal-motion probability ellipsoids, according to the obtained anisotropic atomic displacement parameters.

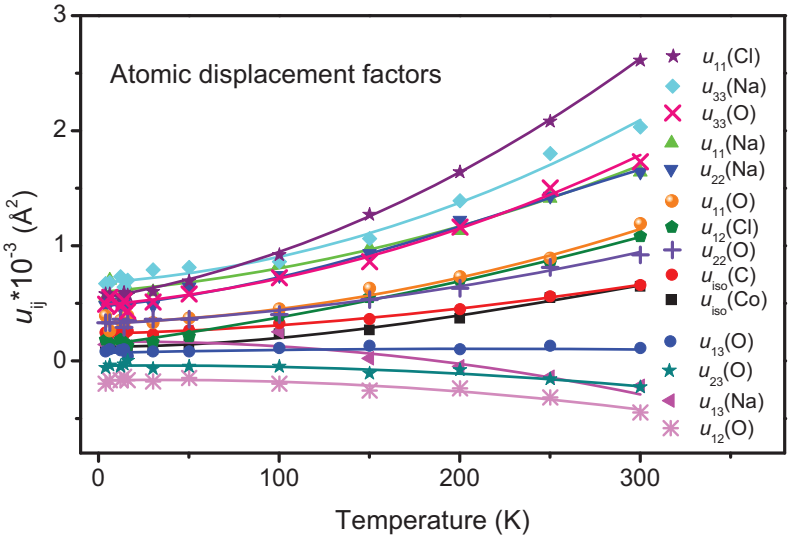

Figure 5-5-3 Temperature dependence of the refined isotropic and anisotropic atomic displacement factors of $Na_3Co(CO_3)_2Cl$. Lines are just guides to the eye.

In **Figure 5-5-4** the temperature dependence of the volume of the unit cell is plotted and it is modeled following the Grüneisen approximation for the zero pressure state, where the effects of thermal expansion are considered to be equivalent to elastic strain [186]. The temperature dependence of the volume of unit cell can be expressed as $V(T) = \gamma U(T)/K_0 + V_0$, where γ is Grüneisen parameter, K_0 is the bulk modulus and V_0 is the hypothetical cell volume at 0 K. The internal energy $U(T)$ is given under the Debye approximation by

$$U(T) = 9Nk_BT\left(\frac{T}{\theta_D}\right)^3 \int_0^{\theta_D/T} \frac{x^3}{e^x - 1} dx, \qquad (5.5.1)$$

where N is the number of atoms per unit cell, k_B is the Boltzmann constant and θ_D is the Debye temperature. The best fit to the data yields $\gamma/K_0 = (1.88 \pm 0.03) \times 10^{-9}$ Pa^{-1}, $\theta_D = 394.6 \pm 3.5$ K, $V_0 = 2737.99 \pm 0.02$ Å^3.

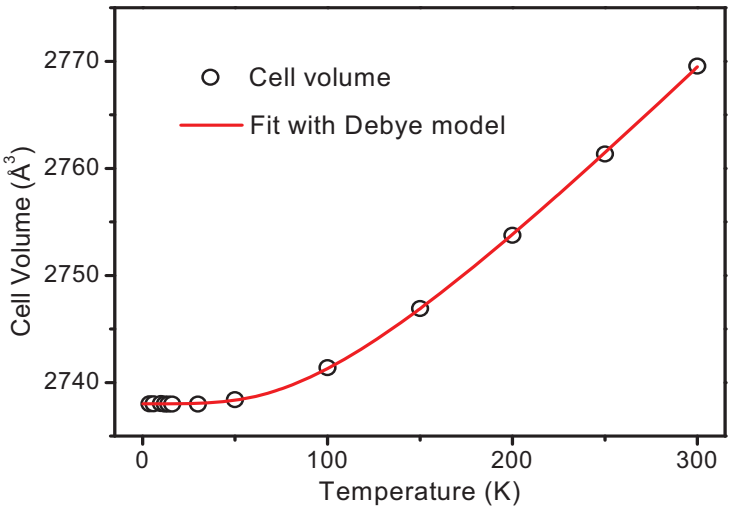

Figure 5-5-4 Temperature dependence of the unit cell volume of $Na_3Co(CO_3)_2Cl$. The red line is the best fit with the Debye model as described in the text.

As shown in **Figure 5-5-4**, no discontinuity can be seen in the temperature dependence of cell volume, indicative of no crystallographic phase transition over the investigated temperature range within the resolution of the present NPD experiments.

The positional displacement on Na sites can be interpreted with the local crystal environment of Na atoms. Each Na atom is surrounded by four oxygen atoms and two chlorine atoms. In **Figure 5-5-5**, the displacement of Na atomic position obtained from the refinement is shown as the orange sphere, while the Na position in ordered phase is shown as the gray sphere. The Na atom is "dragged" from the ordered-phase position towards the chlorine atoms. This is reasonable since chlorine anions possess more electron affinity than oxygen anions and therefore Na cations are attracted more by the chlorine anions, resulting in a positional displacement on Na sites. How this displacement influence the magnetism of $Na_3Co(CO_3)_2Cl$ is not clear. This displacement appears to be an average effect as discovered by the present NPD investigation. It could introduce fluctuations to the bond distances and serve as another important ingredient (i.e., disorder) of the spin-glass-like transition in $Na_3Co(CO_3)_2Cl$, in addition to the spin frustration. But the determination of the average crystal structure presented in this section cannot provide evidence for such disorder, which has to be identified by means of local probing methods, such as

extended x-ray-absorption fine structure (EXAFS), nuclear magnetic resonance (NMR), and neutron pair distribution function (NPDF) analysis.

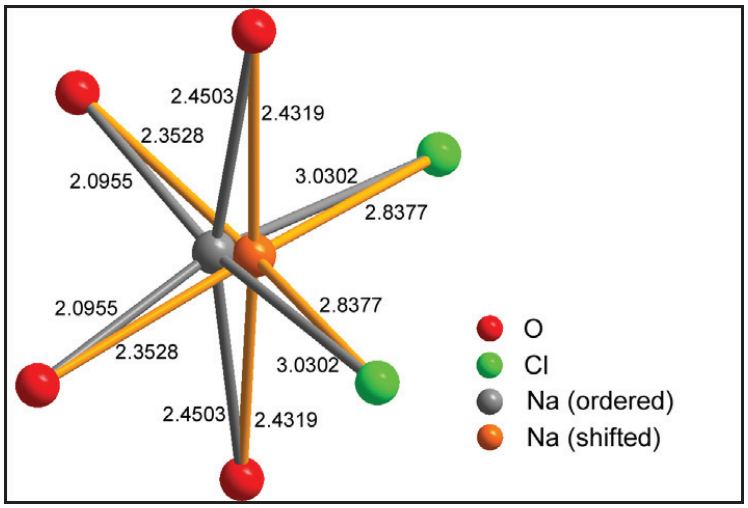

Figure 5-5-5 Local crystal environment of Na atom. Red spheres: O atoms; Green spheres: Cl atoms; Orange sphere: shifted Na position obtained from the refinement; Gray sphere: Na position in the ordered phase. The atomic distances are given in unit of Å.

As a summary to this section, the average crystallographic structure of $Na_3Co(CO_3)_2Cl$ has been determined. No evidence for long-range magnetic order can be seen in the neutron powder diffraction measurements from room temperature down to 3.7 K, consistent with the spin-glass-like transition at T_g = 4.5 K. Excellent refinements to the data have been obtained without introducing any magnetic contribution. Though Co sublattice displays a fully ordered phase, positional displacement from the ordered phase has been detected on Na sites, which could possibly lead to fluctuations in bond distances and trigger the spin-glass-like behavior in this system. But this possible disorder in bond distances requires hard proof from local probing experiments. Possible static atomic disorder could also exist on chlorine site. However, no clear evidence for atomic disorders in $Na_3Co(CO_3)_2Cl$ has been observed within the experimental resolution of the present NPD measurements. No change in the crystal structure has been found below and above 17 K. This suggests that the anomaly at 17 K in magnetic susceptibility and heat

capacity measurements might not be due to additional effects such as orbital order. But more experiments are needed to confirm this.

Table 5-5-1 Lattice parameters and reliability factors as determined by Rietveld refinements of the neutron powder diffraction (NPD) data at 3.7, 30 and 300 K, and the X-ray powder diffraction (XRPD) data at 300 K (see Section 5.2). The error bars are statistical errors given by the Fullprof program. The bound coherent scattering length for the elements in $Na_3Co(CO_3)_2Cl$ are: b_{Na} = 3.63 fm, b_{Co} = 2.49 fm, b_C = 6.646 fm, b_O = 5.803 fm, b_{Cl} = 9.577 fm [187].

		NPD			XRPD
		3.7 K	30 K	300 K	300 K
$a=b=c$ (Å)		13.9898(1)	13.9898(3)	14.0433(1)	14.0435(8)
$\alpha=\beta=\gamma$ (Å)		90	90	90	90
V (Å^3)		2738.011(21)	2738.011(22)	2769.551(29)	2769.705(26)
Na	y/b	-0.1510(5)	-0.1510(3)	-0.1502(2)	-0.1502(7)
O	x/a	-0.0243(6)	-0.0243(7)	-0.0230(9)	-0.0223(3)
	y/b	0.6469(8)	0.6469(3)	0.6469(9)	0.6459(1)
	z/c	0.5165(3)	0.5165(8)	0.5158(1)	0.5165(4)
C	x/a	0.0326(5)	0.0326(5)	0.0327(7)	0.0328(9)
Reliability factors (%):					
R_{wp}		6.75	6.87	7.09	10.6
R_p		7.06	7.29	8.32	14.1
R_B		1.77	1.81	1.90	5.51
χ^2		0.871	0.893	0.665	2.84

Table 5-5-2 (a) Isotropic atomic displacement factors u_{iso}×10^{-3} Å^2 for Co and C atoms, and the anisotropic ones u_{ij}×10^{-3} Å^2 for Na, O, and Cl atoms in $Na_3Co(CO_3)_2Cl$ at 3.7, 6, 12, 14, 16, and 30 K.

T (K)	3.7	6	12	14	16	30
u_{iso}(Co)	0.138(25)	0.111(25)	0.191(25)	0.114(25)	0.091(24)	0.097(24)
u_{iso}(C)	0.245(8)	0.240(8)	0.240(8)	0.229(8)	0.258(8)	0.227(8)
u_{11}(Na)	0.55(8)	0.70(8)	0.55(8)	0.61(8)	0.62(8)	0.60(8)
u_{22}(Na)	0.48(7)	0.51(7)	0.47(7)	0.50(7)	0.47(7)	0.48(7)
u_{33}(Na)	0.67(7)	0.68(7)	0.73(7)	0.64(7)	0.70(7)	0.79(7)
u_{13}(Na)	0.14(6)	0.19(6)	0.19(6)	0.13(6)	0.12(6)	0.17(6)
u_{11}(Cl)	0.58(2)	0.58(2)	0.55(2)	0.59(2)	0.57(2)	0.60(2)
u_{12}(Cl)	0.18(3)	0.15(3)	0.18(2)	0.16(3)	0.13(2)	0.16(3)
u_{11}(O)	0.39(4)	0.26(4)	0.35(4)	0.33(4)	0.39(4)	0.33(4)
u_{22}(O)	0.33(3)	0.33(3)	0.36(3)	0.29(3)	0.35(3)	0.36(3)
u_{33}(O)	0.49(4)	0.55(4)	0.47(4)	0.52(4)	0.43(4)	0.51(4)
u_{12}(O)	-0.20(2)	-0.17(2)	-0.17(2)	-0.14(2)	-0.17(2)	-0.18(2)
u_{13}(O)	0.08(2)	0.10(2)	0.09(2)	0.10(2)	0.04(2)	0.08(2)
u_{23}(O)	-0.06(2)	-0.04(2)	-0.05(2)	-0.03(2)	0.00(2)	-0.07(2)

Table 5-5-2 (b) Isotropic atomic displacement factors $u_{iso}\times10^{-3}$ Å^2 for Co and C atoms, and the anisotropic ones $u_{ij}\times10^{-3}$ Å^2 for Na, O, and Cl atoms in $Na_3Co(CO_3)_2Cl$ at 50, 100, 150, 200, 250, and 300 K.

T (K)	50	100	150	200	250	300
u_{iso}(Co)	0.149(25)	0.236(27)	0.270(28)	0.370(31)	0.550(34)	0.648(36)
u_{iso}(C)	0.264(8)	0.326(8)	0.361(8)	0.448(9)	0.558(9)	0.657(10)
u_{11}(Na)	0.66(8)	0.84(9)	0.98(9)	1.13(10)	1.41(11)	1.64(11)
u_{22}(Na)	0.64(7)	0.74(8)	0.93(8)	1.22(9)	1.43(10)	1.64(11)
u_{33}(Na)	0.81(7)	0.86(7)	1.06(8)	1.39(8)	1.80(9)	2.03(10)
u_{13}(Na)	0.25(7)	0.25(7)	0.02(7)	-0.05(8)	-0.14(8)	-0.22(9)
u_{11}(Cl)	0.69(2)	0.92(2)	1.27(3)	1.64(3)	2.08(3)	2.61(4)
u_{12}(Cl)	0.21(3)	0.39(3)	0.55(3)	0.71(4)	0.86(4)	1.11(5)
u_{11}(O)	0.37(4)	0.45(4)	0.63(4)	0.73(5)	0.89(5)	1.19(6)
u_{22}(O)	0.36(3)	0.40(3)	0.53(3)	0.63(4)	0.81(4)	0.92(4)
u_{33}(O)	0.58(4)	0.72(4)	0.86(4)	1.16(5)	1.50(5)	1.73(6)
u_{12}(O)	-0.15(3)	-0.20(3)	-0.26(3)	-0.24(3)	-0.32(3)	-0.45(3)
u_{13}(O)	0.08(2)	0.11(3)	0.13(3)	0.10(3)	0.13(3)	0.11(3)
u_{23}(O)	-0.05(2)	-0.05(3)	-0.11(3)	-0.08(3)	-0.16(3)	-0.23(3)

5.6 Polarized Neutron Scattering of $Na_3Co(CO_3)_2Cl$

As discussed in Sections 5.3 and 5.4, clear collective magnetic behavior has been observed in $Na_3Co(CO_3)_2Cl$. At low temperatures the spins should become antiferromagnetically correlated. Therefore spin correlations are normally expected from such spin systems, appearing as a modulation of the differential scattering cross section in a neutron scattering experiment. But the NPD measurements showed no indication of short-range spin correlations, because the spin correlations may be too weak to be separated from the background. In the heat capacity measurements, a long-range mangetic phase transition has been detected at 1.5 K. The lowest temperature reached in the NPD measurements was 3.7 K. Thus no long-range magnetic order was observed in NPD data presented in Section 5.5. In order to detect the short-range spin correlations and the long-range magnetic order in $Na_3Co(CO_3)_2Cl$, diffuse neutron scattering with polarization analysis was performed at DNS, FRM II.

5.6.1 Experimental Details

The polarized neutron scattering measurements were carried out on the neutron spectrometer DNS [95] at FRM II, equipped with a ^{4}He closed cycle cryostat and a dilution-insert cryostat, allowing a temperature range between 60 mK and 300 K. Approximately 5 g of sample was used for the polarized neutron scattering measurements. When using the ^{4}He closed cycle cryostat and the dilution-insert cryostat, the sample was sealed in an aluminum holder and a copper holder, respectively. During the mounting procedure, the sample and the holder were kept in a helium atmosphere. The energy of the incident neutron beam was 3.6 meV (corresponding to a wavelength of 4.74 Å). The structure factor was determined within the scattering vector range of $0.4 < Q < 2.2$ Å^{-1}. Within the quasistatic approximation, the nuclear coherent, spin-incoherent and magentic scattering cross sections were separated simultaneously with the *xyz*-polarization method in the spin-flip (SF) and non-spin-flip (NSF) channels [73]. The background subtraction, flipping ratio correction and data normalization were carried out using similar methods as discussed in Section 3.5.

5.6.2 Experimental Results and Discussion

Figure 5-6-1 shows the nuclear coherent (black circles), spin-incoherent (green circles) and magnetic (red circles) components of the total scattering from $Na_3Co(CO_3)_2Cl$ at 3.3 K by means of *xyz*-polarization analysis on DNS. The spin-incoherent scattering intensity is nearly constant, suggesting a successful separation of the different scattering contributions. Obviously, the magnetic contribution is very weak as compared to the nuclear and spin-incoherent scattering, and could hardly be seen without polarization analysis. The gaps in the spin-incoherent and magnetic components are due to the inperfect separations caused by the strong Bragg peaks at those positions.

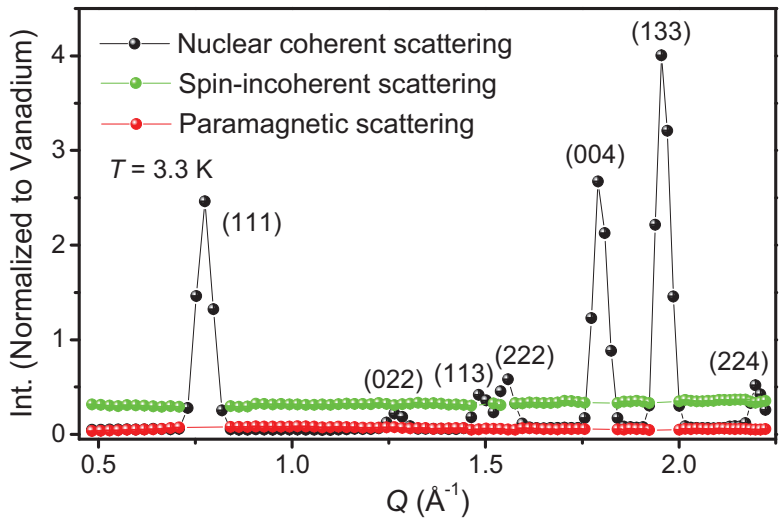

Figure 5-6-1 Nuclear coherent (black circles), spin-incoherent (green circles) and magnetic (red circles) contributions to the total diffuse neutron scattering from $Na_3Co(CO_3)_2Cl$ at 3.3 K separated by *xyz*-polarization analysis on DNS.

Figure 5-6-2 shows the differential magnetic cross section, $d\sigma_{mag}/d\Omega$, extracted from the total scattering cross section at 0.05, 3.3, 10, 30, 200, and 300 K. There is no trace of long-range magnetic order from 300 K to 3.3 K, consistent with the neutron powder diffraction measurements. At 50 mK, long-range magnetic order is evidenced by clear magnetic Bragg peaks superposed on the magnetic diffuse scattering, confirming that the sharp peak at 1.5 K in specific heat can be attributed to

a magnetic phase transition into a long-range ordered antiferromagnetic structure. In **Figure 5-6-2**, the differential magnetic cross sections are plotted in absolute unit which were determined by calibration against the spin-incoherent scattering of a known mass of vanadium standard. The scattering cross section at 300 K agrees well with the 73%-scaled pure paramagnetic form factor of Co^{2+} (S = 3/2) ion. Without energy analysis option, the magnetic scattering data taken on DNS are actually integrated within the energy-transfer window of DNS. The overall energy scale of the magnetic exchange in this system extends to about 3 meV (see Section 5.7), which is basically covered by the energy window (3.6 meV) of DNS. The loss of the magnetic scattering intensity is attributed to the limitation of the energy window of DNS.

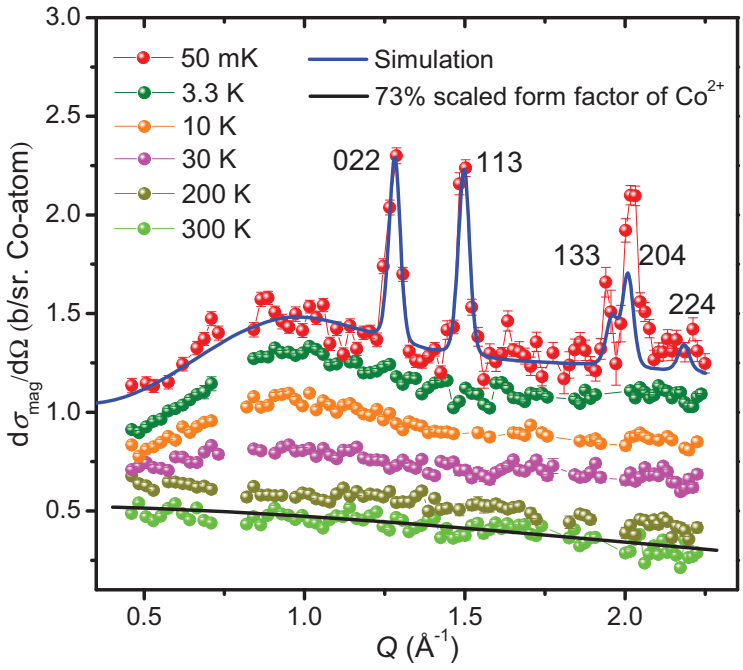

Figure 5-6-2 Temperature evaluation of the differential magnetic cross section. The *x*- and *y*- axis correspond to the data of 200 and 300 K. The data at other temperatures are displaced vertically by 0.2 b sr^{-1} per Co atom for clarity. The black line indicates the 73%-scaled paramagnetic form factor of Co^{2+} ion (S = 3/2). The blue line is the best fit to the magnetic scattering at 50 mK based on the all-in-all-out spin configuration (see text below).

The total differential magnetic cross section obtained at each temperature is determined by integration over the investigated range of scattering vector magnitude Q, shown as the black squares in **Figure 5-6-3**. The total differential magnetic cross section of pure paramagnetic Co^{2+} ions is given, ignoring the Debye-Waller term, by Eq. (3.5.4). Thus the total magnetic cross section of spin-only paramagnetic Co^{2+} ions within the investigated Q range can be determined as 4.69 b sr^{-1} per Co atom.

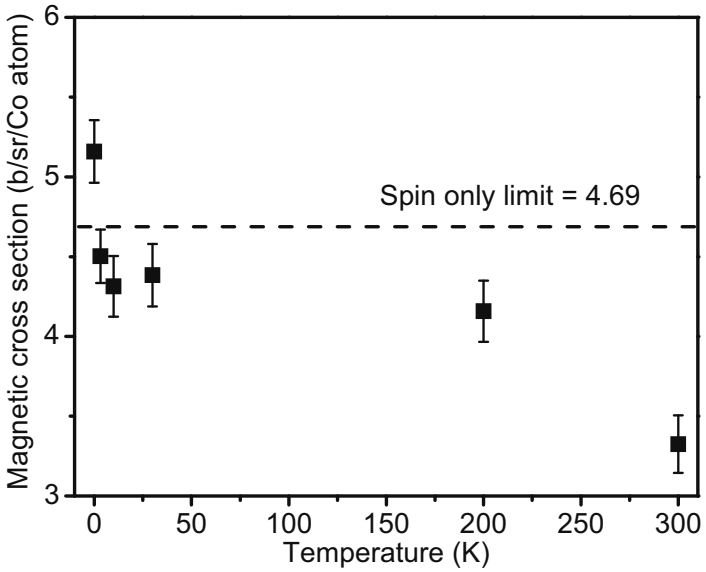

Figure 5-6-3 Temperature dependence of the total magnetic scattering cross section integrated over the Q range $0.4 < Q < 2.2$ $Å^{-1}$. The dashed line marks the spin-only limit for paramagnetic Co^{2+} ($S = 3/2$) ions.

As shown in **Figure 5-6-3**, the magnetic cross section at 300 K covers ~ 73% of the spin-only limit for paramagnetic Co^{2+} ions in high spin state ($S = 3/2$), while the magnetic cross sections at 3.3 K covers ~ 95% of the spin-only limit. The increase of measured magnetic cross section upon cooling can be attributed to the contribution from unquenched orbital moment of Co^{2+} ions. The magnetic cross section at 50 mK exceeds the spin-only cross section for Co^{2+} ions, confirming the contribution from orbital moment. The effective magnetic moment obtained at 50 mK is then determined as 4.2 μ_B per Co, much lower than the effective moment obtained by means of magnetic susceptibility measurements (see Section 5.3). The use of powder

sample with a dilution insert could be a reason for this. Though helium exchange gas and a copper holder were used in the DNS measurements, I found the thermal equilibrium had not been achieved during the experimental time. The sample was kept at 50 mK for 3 days and the magnetic Bragg peaks were seen to evolve gradually with observing time. The spectrum for 50 mK shown in **Figure 5-6-2** is derived from the last 12-hour measurement, possessing the most prominent magnetic Bragg peaks. So the effective moment determined from the magnetic cross section at 50 mK should be less than the one calculated from high-temperature susceptibility measurements.

The effect of the magnetic short-range order will be discussed first, which can be seen as a modulation of the differential scattering cross section in **Figure 5-6-2**. The strong reduction of the magnetic cross section below $Q \approx 0.9$ Å^{-1} indicates the existence of a strong antiferromagnetic component in the spin correlations, in agreement with the aforementioned susceptibility measurements of $Na_3Co(CO_3)_2Cl$, which show dominating antiferromagnetic coupling between Co^{2+} ions.

The data collected at 3.3 K (below the spin-glass-like transition temperature and above the long-range magnetic ordering temperature) was used for the analysis of the short-range spin correlations, as shown by the red circles in **Figure 5-6-4**. The differential magnetic scattering cross section of $Na_3Co(CO_3)_2Cl$ can be calculated with the formula given by I. A. Blech and B. L. Averbach for the differential scattering cross section of spin pairs, which, already in powder average, can be written as [99]

$$\frac{\mathrm{d}\sigma_{\mathrm{mag}}}{\mathrm{d}\Omega} = \frac{2}{3}S(S+1)\left(\frac{\gamma e^2}{mc^2}\right)^2 F^2(Q) + \left(\frac{\gamma e^2}{mc^2}\right)^2 F^2(Q) \times \sum_{n=1}^{N} c_n \left[a_n \frac{\sin Qr_n}{Qr_n} + b_n \left(\frac{\sin Qr_n}{Q^3 r_n^3} - \frac{\cos Qr_n}{Q^2 r_n^2} \right) \right], \tag{5.6.1}$$

where $\gamma e^2/mc^2$ and $F(Q)$ have been introduced in Eq. (3.5.4), and it is assumed that an arbitrary reference Co^{2+} ion is correlated to N surrounding Co^{2+} shells with occupation number c_n and shell radius r_n. a_n and b_n are related to the probability of finding spin pairs with parallel components and expressed as follows [99],

$$\begin{aligned} a_n &= \left\langle \boldsymbol{S}_0^{y} \cdot \boldsymbol{S}_n^{y} \right\rangle_n \\ b_n &= 2\left\langle \boldsymbol{S}_0^{x} \cdot \boldsymbol{S}_n^{x} \right\rangle_n - \left\langle \boldsymbol{S}_0^{y} \cdot \boldsymbol{S}_n^{y} \right\rangle_n \end{aligned} . \tag{5.6.2}$$

Here, $\left\langle \boldsymbol{S}_0^{\boldsymbol{\alpha}} \cdot \boldsymbol{S}_n^{\boldsymbol{\alpha}} \right\rangle_n$ is the average correlation of the $\boldsymbol{\alpha}$-direction component of the nth shell to the corresponding component of the origin spin. Denote $A_n = \left\langle \boldsymbol{S}_0^{\boldsymbol{x}} \cdot \boldsymbol{S}_n^{\boldsymbol{x}} \right\rangle_n$ and $B_n = \left\langle \boldsymbol{S}_0^{\boldsymbol{y}} \cdot \boldsymbol{S}_n^{\boldsymbol{y}} \right\rangle_n$. Then Eq. (5.6.1) becomes

$$\frac{d\sigma_{\text{mag}}}{d\Omega} = \left(\frac{\gamma e^2}{mc^2} \right)^2 F^2(Q) \left\{ \frac{2}{3} S(S+1) + \sum_{n=1}^{N} c_n \left[B_n \frac{\sin Qr_n}{Qr_n} + (2A_n - B_n) \left(\frac{\sin Qr_n}{Q^3 r_n^3} - \frac{\cos Qr_n}{Q^2 r_n^2} \right) \right] \right\}. \quad (5.6.3)$$

Due to the glassy nature of this system at 3.3 K, an analytical simulation of the spin correlations has been carried out by attempting a least-square fit with Eq. (5.6.3) to the magnetic differential scattering cross section obtained at 3.3 K. The best fit was achieved with two Co^{2+} shells, namely c_n = 6, 12 for n = 1, 2, shown as the blue line in **Figure 5-6-4**.

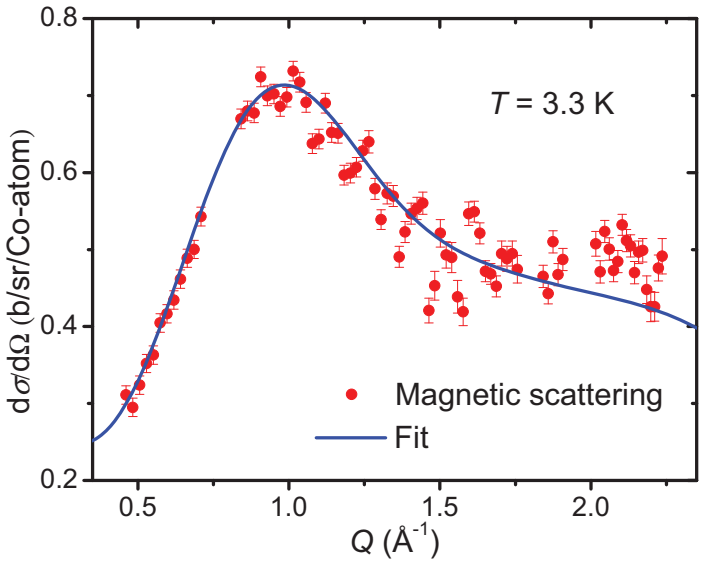

Figure 5-6-4 Differential magnetic scattering cross section at 3.3 K in absolute units (red circles) with the best fit (blue line) in terms of Eq. (5.6.4) among the nearest neighbors.

If the higher-order shells (n > 2) were included, the corresponding A_n and B_n were so small that the correlations between the origin and the n > 2 shells can be neglected. This agrees with the estimation of the correlation length using the peak at $Q \approx 1.0$ Å^{-1},

whose FWHM is $\Delta Q \approx 1.0$ Å^{-1} and approximately corresponds to the next-nearest-neighbor distance. The best fit yields A_1 = -0.14(3), B_1 = -0.05(1), A_2 = 0.04(2), B_2 = 0.01(1). The values of A_1 and B_1 are negative, indicating the nearest-neighbor Co^{2+} ions are antiferromagnetically coupled. Weak ferromagnetic coupling is found among the next nearest neighbors (A_2, $B_2 > 0$). A_2 and B_2 are quite small as compared with A_1 and B_1, indicative of dominating nearest-neighboring correlations.

As to the long-range magnetic order of $Na_3Co(CO_3)_2Cl$ at 50 mK, two clear magnetic Bragg peaks have been observed at 1.27 and 1.50 Å^{-1}, as superpositions of the 2 2 0 and 1 1 3 nuclear Bragg peaks, respectively. This suggests an antiferromagnetic ordered structure with propagation vector q_0 = (0, 0, 0). Two further magnetic peaks are observed at 1.93 and 2.03 Å^{-1}, which could correspond to the magnetic 1 3 3 and 2 0 4 reflections. But we are not confident on these two reflections due to the strong affection of the 1 3 3 nuclear reflection. Symmetry analysis based on representation theory indicates that the magnetic representation for magnetic Co^{2+} on 16c site is decomposed into three one-dimensional irreducible models (Γ_1, Γ_3 and Γ_5) and one three-dimensional irreducible model (Γ_8). Four possible magnetic structures corresponding to four different magnetic representations are displayed in **Figure 5-6-5**, together with the corresponding top views. The representation Γ_3, Γ_5 and Γ_8 can be ruled out directly because all these three models yield considerable intensity for the magnetic 1 1 1 reflection, while the 1 1 1 reflection does not exist as indicated in our DNS data taking into account the relative intensity of the nuclear and the magnetic reflections. The representation Γ_1 with all-in-all-out spin configuration leads to zero intensity for the 1 1 1 magnetic reflection. Therefore the fitting to the magnetic reflections has been carried out based on a all-in-all-out spin configuration, where the spins in one tetrahedron direct either towards or opposite the center of the tetrahedron. The fitting result is plotted in **Figure 5-6-2** as the blue line. The two prominent reflections 2 2 0 and 1 1 3 have been well fitted. Additional magnetic reflection 2 2 4 presents at Q = 2.18 Å^{-1} in the simulation, which is hard to be identified in DNS data due to its weak intensity. Given the fact that the calculated diffraction pattern based on all-in-all-out magnetic structural model fits well with our experimental data, we can safely conclude that the long-range magnetic order of $Na_3Co(CO_3)_2Cl$ is characterized by an all-in-all-out type spin configuration.

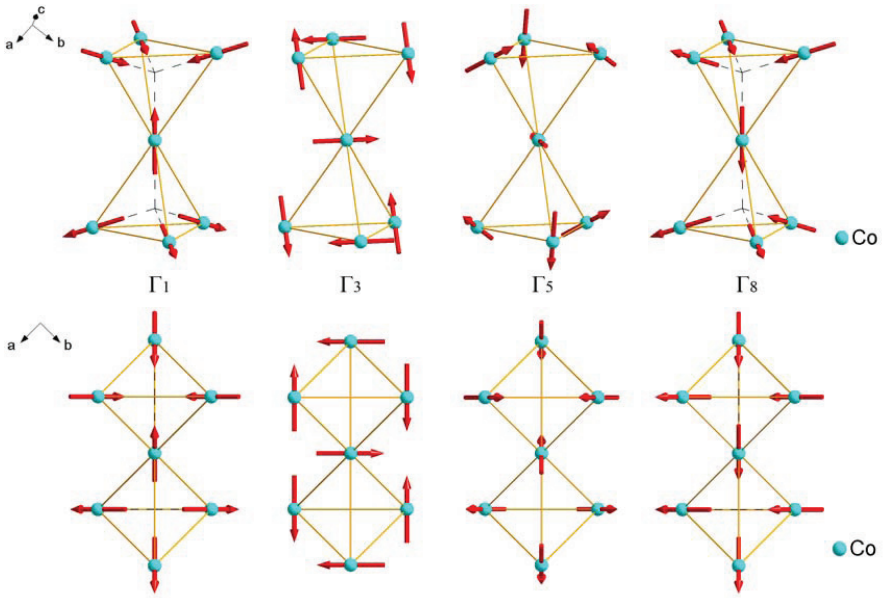

Figure 5-6-5 Schematic representation of a fragment of four possible ordered arrangements of Co spins in the low-temperature pyrochlore phase. Γ_1: All-in-all-out spin configuration. Γ_3: Non-collinear spin configuration with Co spins confined in *ab* plane and pointed to [±1 ±1 0] directions. Γ_5: Non-collinear spin configuration with Co spins pointed parallel to [±1/2 ±1/2 ±1] directions. Γ_8: Spin ice structure with two-in-two-out spin configuration. Bottom panels: top views of Γ_1, Γ_3, Γ_5 and Γ_8.

Figure 5-6-6 shows the pyrochlore lattice of Co^{2+} ions with the all-in-all-out spin arrangements. Note that the emergence of similar non-collinear antiferromagnetic ground state has been reported in some pyrochlore magnets [188-191]. As shown in **Figure 5-6-2**, there is still significant magnetic diffuse scattering at 50 mK in addition to the magnetic reflections. One explanation could be that $Na_3Co(CO_3)_2Cl$ enters a partially-ordered ground state within the experimental time window owing to its extremely slow magnetic relaxation. But temperature inhomogeneity could also lead to the magnetic diffuse scattering observed at 50 mK, because the DNS measurements were performed on a large quantity of powder samples. A precise determination of the magnetic ground state of $Na_3Co(CO_3)_2Cl$ will be interesting and requires more neutron scattering study on single crystals below 1.5 K in the future.

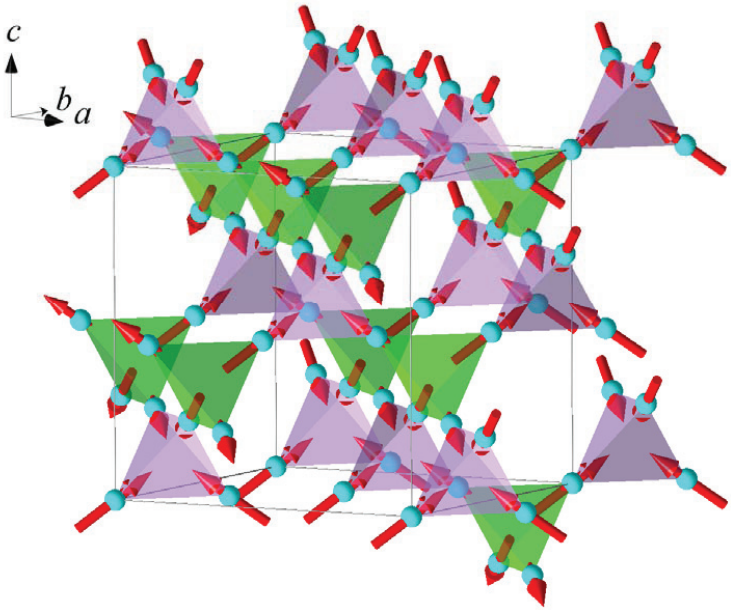

Figure 5-6-6 Pyrochlore lattice of Co^{2+} ions (cyan spheres) with the all-in-all-out spin arrangements. The all-in and all-out spin tetrahedra are highlighted as purple and green, respectively.

It is an interesting phenomenon that $Na_3Co(CO_3)_2Cl$ enters an ordered (or partially ordered) magnetic phase upon cooling from its spin-glass-like freezing temperature of 4.5 K. This scenario may be understood as a result of the intriguing phenomenon known as "order by disorder" [192] and has been observed from some other pyrochlore antiferromagnets [193-195]. Henley has shown that the frustrated face-centered-cubic antiferromagnets prefer to order into collinear structures at finite temerpatures [196]. Hence pyrochlore magnet tends to choose an ordered collinear structure because the entropy favors the ground state with the greatest density of low-energy excitations. Based on the meanfield theory, no long-range order should exist for the pyrochlore lattice with only nearest-neighbor antiferromagnetic interactions. But in some cases, additional degeneracy-lifting perturbations, e.g., further neighbor interactions, can also introduce long-range ordered ground states in pyrochlore magnets [194, 197-199]. Thus the weak ferromagnetic coupling between the next-nearest neighbors as indicated in the fit of diffuse magnetic neutron scattering may play an important role for the system to order (or patially order)

below 1.5 K. Also, a low-*T* structural distortion could lead to a magnetic phase transition. A strong Ising-like anisotropy in connection with magneto-elastic coupling could give rise to such structural distortion. It should be mentioned here that the 2 2 0 and 1 1 3 magnetic reflections indicated in **Figure 5-6-2** have also been observed in pyrochlore antiferromagnets $R_2Ru_2O_7$ (R = Y, Nd) [195].

As a summary to this section, the short-range magnetic order is clearly evidenced by the spin correlations found in the diffuse neutron scattering with polarization analysis. The analysis of the spin correlations indicates that the spin structure of this system is characterized by dominating antiferromagnetic coupling among the nearest neighbors with ferromagnetic next-nearest-neighbor interactions. The ferromagnetic coupling between the next-nearest neighbors is weak, which may be a mechanism for the long-range magnetic order below 1.5 K. Consisdent with the heat capacity measurements, the system enters a long-range magnetic order (or partial order) below 1.5 K. Magnetic Bragg peaks observed at 50 mK indicate that the long-range magnetic order of $Na_3Co(CO_3)_2Cl$ is of an all-in-all-out spin configuration.

5.7 Inelastic Neutron Scattering of $Na_3Co(CO_3)_2Cl$

Spin dynamics of spin glass materials, especially the dynamics of spin-freezing process, has been considerably studied by inelastic neutron scattering (INS) technique [200-205]. Inelastic neutron scattering provides a rather unique probe of collective spin excitations, since INS has the capability to probe spatial correlations of magnetic moments as well as their dynamical properties. A wide spectral distribution of relaxation times was revealed in the INS measurements on conventional metallic spin glasses such as CuMn [200]. For $T >> T_g$ one expects time-dependenct strong magnetic fluctuations in spin glass system, where inelastic neutron scattering is suitable for the investigation of spin dynamics because the energy broadening of the scattered neutrons is a direct measure of the spin relaxation rates [206]. Inelastic neutron scattering has also been utilized to search for possible spin waves in the frozen state of spin glasses. No evidence for spin-wave excitations has been found in the conventional metallic spin glasses by now [42, 150]. In $Eu_xSr_{1-x}S$ for x = 0.51, where the system exhibits a crossover from ferromagnetic to spin glass behavior, some broad spin-wave profiles were observed and attributed to the

random-field effect due to the coupling of ferromagnetic and spin-glass order parameters by Maletta et al. [207].

Though clear spin-glass-like behavior in $Na_3Co(CO_3)_2Cl$ has already been observed in aforementioned characterizations like magnetic susceptibility and specific heat, a complete study still requires the exploration of spin dynamics as a function of both energy and momentum transfer over the reciprocal space. In this section, the result of the inelastic neutron scattering investigation of $Na_3Co(CO_3)_2Cl$ over a wide temperature range from 3.5 K to 300 K is presented to shed more light on the spin dynamics of this system.

5.7.1 Experimental Details

The inelastic neutron scattering measurements were performed on the same $Na_3Co(CO_3)_2Cl$ powder sample as used in the polarized neutron scattering in Section 5.6. The INS spectra were recorded using the multi-chopper high-resolution time-of-flight spectrometer TOFTOF [208] at FRM II in Garching, Germany. TOFTOF covers scattering angles ranging from -15˚ to 140˚. The incident wavelength was 4.2 Å, allowing an investigated Q range from 0.2 to 3.0 $Å^{-1}$. The chopper rotation frequency was set to 14 000 rpm, resulting in an instrumental resolution of about 130 μeV full width at half maximum (FWHM) at zero energy transfer. A detail introduction to TOFTOF will be given in **Appendix C**. About 5 g of $Na_3Co(CO_3)_2Cl$ powder was sealed in a hollow-cylinder aluminum sample holder under helium atmosphere. Data were collected at temperatures of 3.5, 15, 50, and 300 K using a closed cycle cryostat. The instrumental resolution function of the spectrometer was determined by the measurement at 250 K on a vanadium standard, as shown in **Figure 5-7-1**. The background was determined by a measurement from an empty sample holder at 3.5 K. The raw data were treated by subtracting the scattering from the empty sample can and normalizing to the vanadium scan.

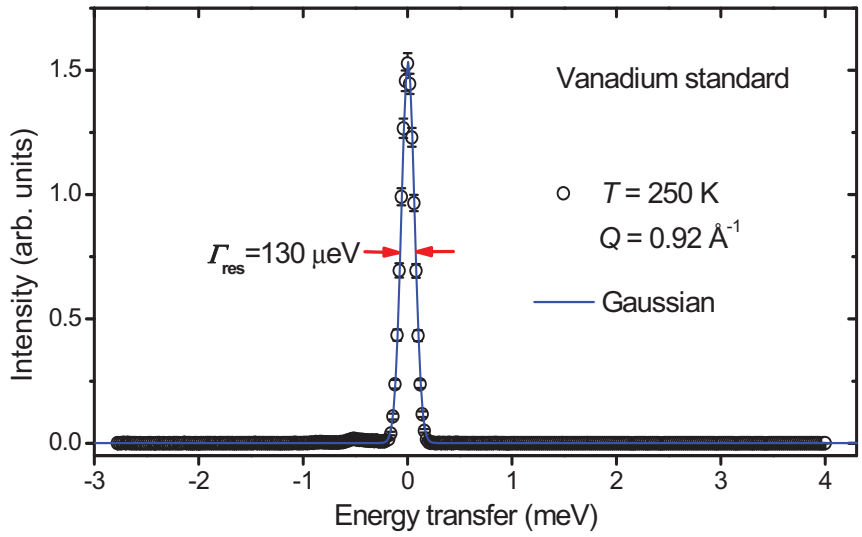

Figure 5-7-1 $I(E)$ at Q = 0.92 Å^{-1} measured from the vanadium standard at 250 K with incident wavelength 4.2 Å.

5.7.2 Experimental Results and Discussion

Figure 5-7-2 shows the contour plots of the INS spectra of sample scan **(a)**-**(d)** measured at 3.5, 15, 50, and 300 K, and the empty can **(e)** measured at 3.5 K. The spectrum of the empty can has not been subtracted in the INS spectra in **Figure 5-7-2 (a)**-**(d)**. All data shown in **Figure 5-7-2** have been normalized to vanadium standard. The high scattering intensities at zero energy transfer are the elastic scattering contributions. The negative and the positive energy transfers correspond to the loss and the gain of neutron energy in the scattering events, respectively. As shown in **Figure 5-7-2** and **Figure 5-7-3**, the measurements on the sample and the empty can suffer from the background from the detectors, which appears as the two peaks at energy transfer E ~ -0.5 meV and ~ -0.8 meV. The spectrum of empty can is taken as the background, which is difficult to be subtracted properly from the sample scans. **Figure 5-7-3 (a)** and **(b)** show the $I(E)$ spectra at constant Q = 0.92 Å^{-1} for the sample scan and the empty can scan, respectively. After the background subtraction, the resultant INS spectrum of the sample is shown in **Figure 5-7-6 (d)**.

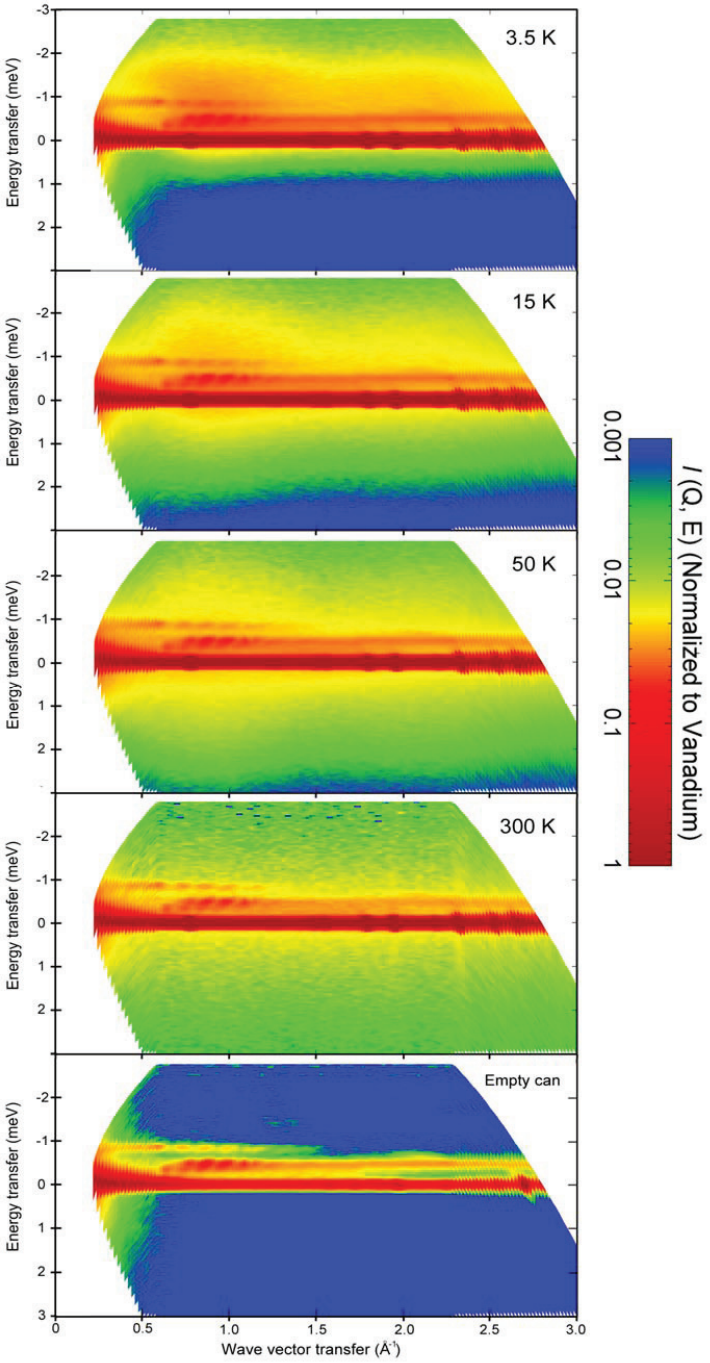

Figure 5-7-2 INS spectra of the sample scans at 3.5 **(a)**, 15 **(b)**, 50 **(c)** and 300 K **(d)**, and the empty-can scan at 3.5 K **(e)**.

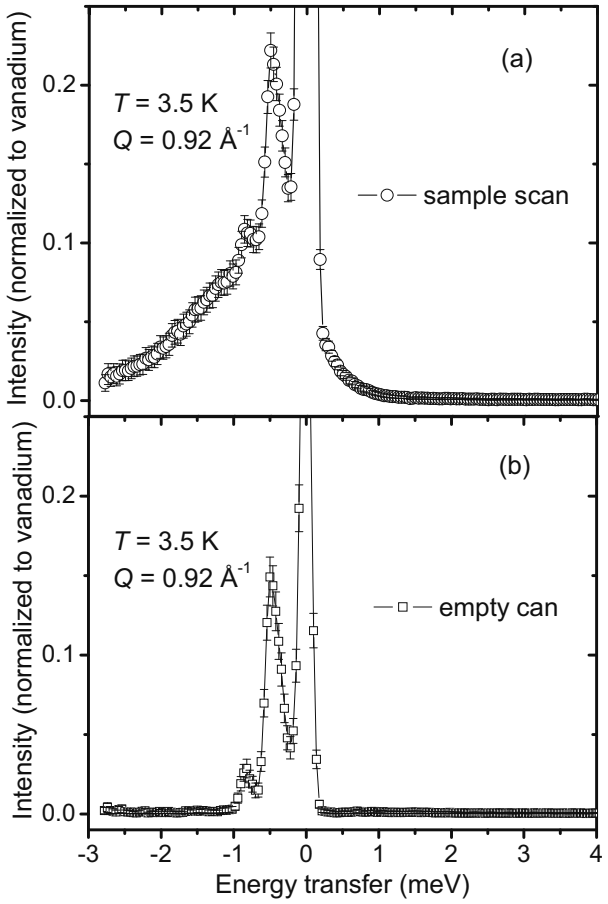

Figure 5-7-3 INS spectra of the sample scan **(a)** and empty can **(b)** scan at Q = 0.92 Å^{-1}.

Figure 5-7-4 shows a contour plot of the dynamic structure factor $S(Q, \omega)$ of $Na_3Co(CO_3)_2Cl$. The red riff at around zero energy transfer consists of elastic incoherent scattering component and nuclear Bragg reflections. As indicated by the white arrows in **Figure 5-7-4**, the first seven nuclear Bragg peaks correspond to reflections (111) at 0.78 Å^{-1}, (022) at 1.27 Å^{-1}, (113) at 1.49 Å^{-1}, (222) at 1.55 Å^{-1}, (004) at 1.80 Å^{-1}, (133) at 1.96 Å^{-1}, and (224) at 2.20 Å^{-1}, consistent with the neutron powder diffraction of $Na_3Co(CO_3)_2Cl$.

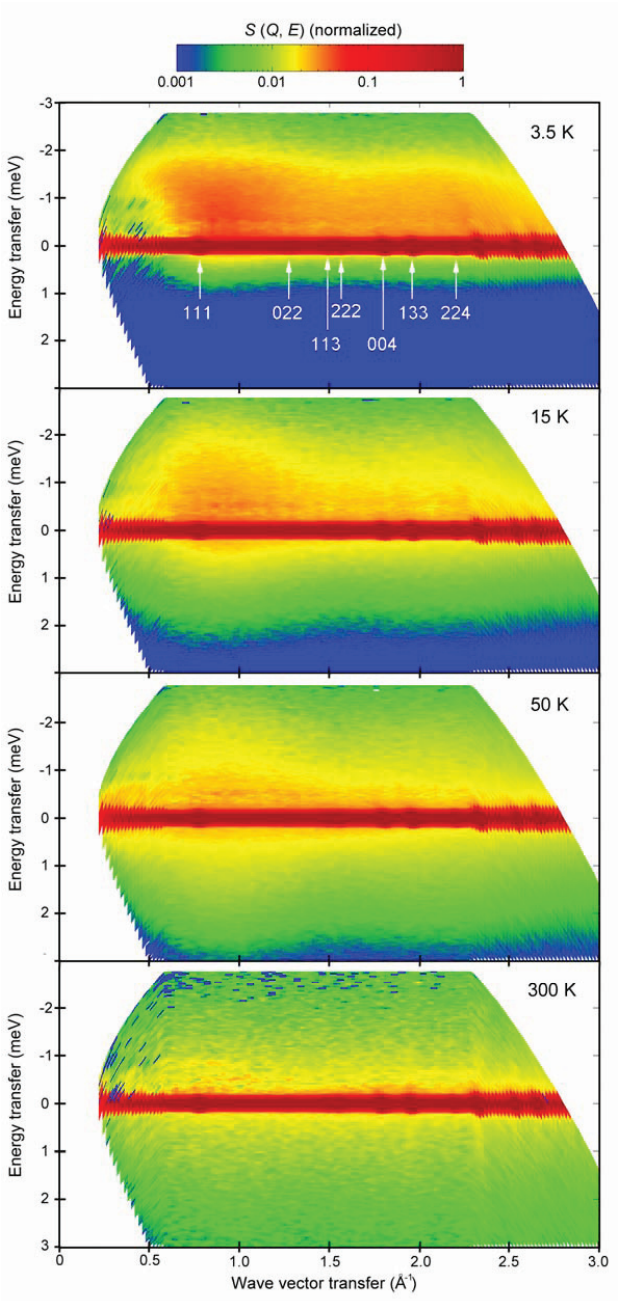

Figure 5-7-4 Contour plot of the dynamic structure factor $S(Q, \omega)$ of $Na_3Co(CO_3)_2Cl$ at 3.5, 15, 50, and 300 K. Magnetic intensity in logarithmic scale is coded with colors from blue to red to indicate increasing intensities.

Besides the central elastic scattering components in **Figure 5-7-4**, additional magnetic scattering is shown as the colors from green via yellow to red above the blue background, indicating of increasing intensities. The magnetic intensity extends over an energy-transfer range up to about 3 meV and reflects the overall energy scale of the magnetic exchange, which is in reasonable agreement with the Curie-Weiss temperature of 33.8 K as determined in the susceptibility measurements. At low temperature T = 3.5 K, magnetic scattering intensity is dominated by the neutron energy-loss process. The Q-dependence of magnetic scattering indicates a modulation around the magnetic form factor. A spin-wave-like profile centering around 0.9 Å^{-1}, which is rather broad but still visible by comparing the difference of the low-Q regions in plots for 3.5 K and 15 K. At 300 K (well above $-\Theta_{CW}$ = 33.8 K), quasielastic magnetic scattering for a purely paramagnetic state is expected.

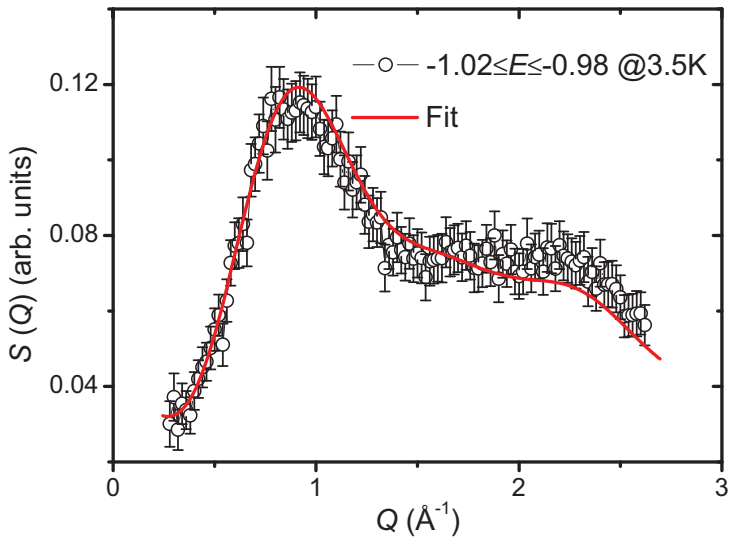

Figure 5-7-5 Q dependence of the magnetic scattering integrated within the energy transfer range -1.02 ≤ E ≤ -0.98 in TOFTOF data for 3.5 K, together with the best fit (red line) using Eq. 5.6.4.

The magnetic nature of the scattering intensity at non-zero energy transfer is evidenced by studying the Q-dependence of dynamic structure factor $S(Q, \omega)$ at constant ω. **Figure 5-7-5** shows a cut of $S(Q, \omega)$ after summing over the energy

transfer range -1.02 ≤ E ≤ -0.98 meV in the data for 3.5 K. The modulating Q-dependence of magnetic scattering is indicative of short-range spin correlations. As already discussed in Section 5.6, the Q dependence of magnetic scattering is fitted in terms of Eq. 5.6.4 with A_1 = -0.09(1), B_1 = -0.07(1), A_2 = 0.01(1), B_2 = 0.02(1), namely dominating antiferromagnetic spin correlations among the nearest neighbors and weak ferromagnetic spin correlations among the next nearest neighbors. The fitting result is plotted in **Figure 5-7-5** by the red line. Hence it is confirmed that the scattering intensity at non-zero energy transfer observed in TOFTOF data can be attributed to the magnetic contribution.

Hereafter, I examine the line-shape and temperature dependence of the magnetic component by considering the following general expression for the dynamic structure factor $S(Q, \omega, T)$, which is proportional to the imaginary part of the generalized susceptibility [209]

$$S(Q,\omega,T) = \hbar\omega\left(1-\exp(-\hbar\omega / k_{\mathrm{B}}T)\right)^{-1}\chi''(Q,\omega,T)\,. \tag{5.7.1}$$

$(1-\exp(-\hbar\omega/k_{\mathrm{B}}T))^{-1}$ is the detailed balance factor representing the difference in the scattering function on the neutron energy gain and loss side due to the thermal population. $\chi''(Q, \omega, T)$ is taken as a Lorentzian-shaped quasielastic line with width Γ at sufficiently high temperature [209],

$$\chi''(Q,\omega,T) = \chi_0(Q,T)\frac{\Gamma(Q,T)}{\omega^2+\Gamma^2(Q,T)}\,. \tag{5.7.2}$$

At high enough temperature, the dynamic structure factor is well described by a single quasielastic Lorentzian. Upon cooling collective magnetic excitations give rise to inelastic signals due to the increasing magnetic correlations. The low-T inelastic signals can be fitted with a damped harmonic oscillator (DHO) model multiplied by the detailed balance factor [209-211]

$$S(Q,\omega) = \frac{A_{\mathrm{DHO}}\omega\Gamma_{\mathrm{DHO}}}{\left(\omega^2-\omega_{\mathrm{DHO}}^2\right)^2+\left(\omega\Gamma_{\mathrm{DHO}}\right)^2}\frac{1}{1-e^{-\hbar\omega/k_{\mathrm{B}}T}}\,, \tag{5.7.3}$$

which corresponds to a double Lorentzian with oscilattor strength A_{DHO}, eigen-frequency ω_{DHO} and linewidth Γ_{DHO}.

In inelastic scattering measurements the experimental magnetic scattering represents the convolution between the resolution function $R(Q, \omega)$ of the instrument

and the pure magnetic signals of the sample. Thus the following relation should be used to fit the experimental structural factor

$$S_{\exp}(Q,\omega) = S(Q,\omega) \otimes R(Q,\omega)\,, \tag{5.7.4}$$

where $R(Q, \omega)$ has been determined by the vanadium scan. The energy resolution as determined by the vanadium scan is only about 0.13 meV, which is at least five times smaller than the typical FWHM of the quasielastic components and inelastic components in the present measurements. Therefore, the instrumental resolution function was neglected in the following fitting precedure of the data.

Figure 5-7-6 shows the cuts of $S(Q, \omega)$ for constant Q = 0.92 Å^{-1} at the investigated temperatures. The central elastic peak is fitted with a single Gaussian function (blue dashed line), whose width corresponds to the energy resolution of TOFTOF. The quasielastic component is fitted with a single Lorentzian function given by Eq. (5.7.2), multiplying a detailed balance factor. The inelastic component is fitted with two Lorentzian functions as described by Eq. (5.7.3), which are centered at $\pm\omega_d$ and multiplied by the detailed balance factor.

The quasielastic and inelastic components are shown by the green dashed lines in **Figure 5-7-6**. The red lines in **Figure 5-7-6** represent the sum of quasielastic and inelastic components. At 300 K, the quasielastic intensity can be described by a single Lorentzian. No inelastic component is observed. Upon cooling the system to 50 K, which is above the Curie-Weiss temperature but below the deviation temperature from Curie-Weiss law, a single Lorentzian cannot represent the data well. Additional inelastic components have to be involved to yield a good fit as shown in **Figure 5-7-6**. It can be seen that at 50 K the quasielastic component still dominates the INS spectrum and only weak inelastic component is need to account for the broad-hump-like feature at around ±2 meV. As the temperature decreases to 15 K, the inelastic component increases significantly and becomes dominant. The linewidth of the quasielastic component decreases upon decreasing temperatures (see **Figure 5-7-7**) and spectral weight of quasielastic component is transferred to the inelastic component of the collective magnetic excitations. At temperature T = 3.5 K < T_g, the quasielastic line shrinks into the elastic line within the instrumental resolution. The shrinking quasielastic component indicates a remarkable slowing down of the spin fluctuations.

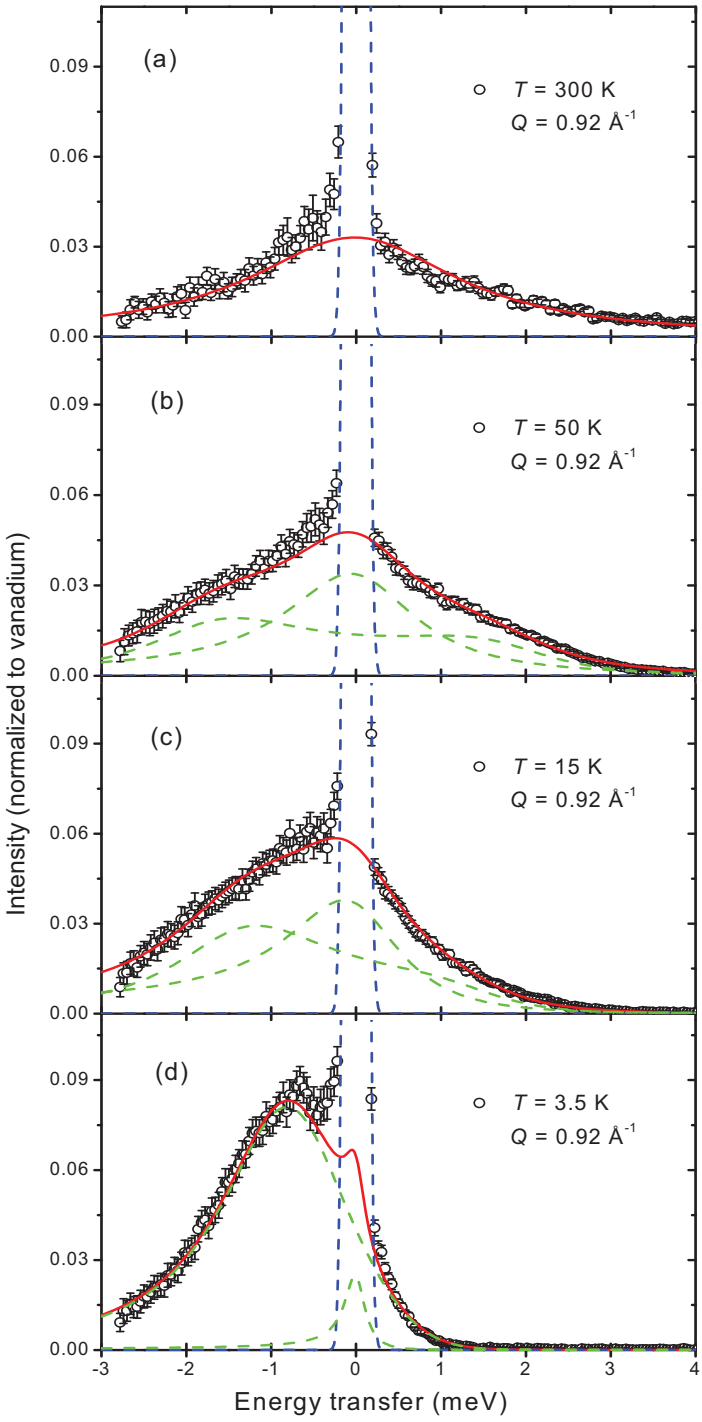

Figure 5-7-6 Dynamic structure factor $S(Q, \omega)$ of $Na_3Co(CO_3)_2Cl$ for constant wave vector transfer Q = 0.92 Å^{-1} at various temperatures.

The fitting results are summarized in **Figure 5-7-7**, where Γ_{quasi} and Γ_{in} represent the linewidth of quasielastic and inelastic components, and ω_d is the excitation energy. The quasielastic scattering contribution is considered to have vanished and the magnetic scattering becomes purely inelastic with an excitation energy of about 1.3 meV at Q = 0.92 Å^{-1} at 3.5 K.

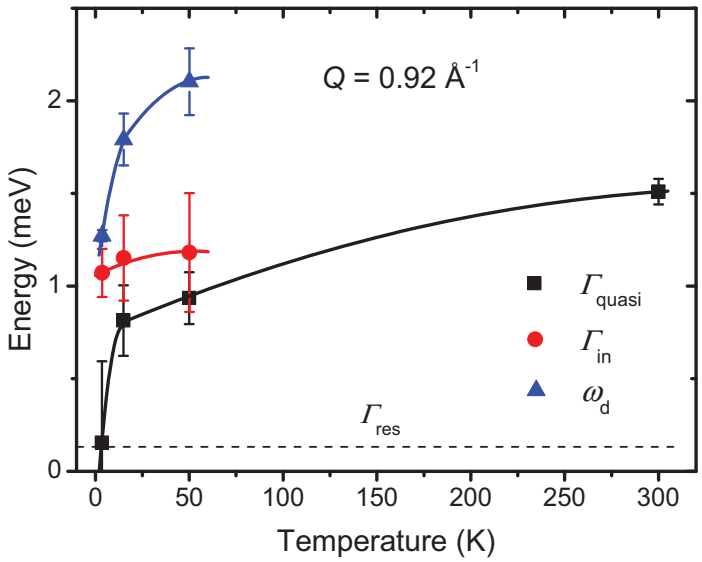

Figure 5-7-7 Temperature dependence of the linewidth and excitation energy of $Na_3Co(CO_3)_2Cl$ at Q = 0.92 Å^{-1}. The black squares represent the quasielastic linewidth Γ_{quasi}. The red circles and the blue triangles show the linewidth Γ_{in} and the excitation energy ω_d of the inelastic components. The dashed line marks the instrumental energy resolution Γ_{res}. Black, red, and blue lines are guides to the eye.

As seen in the INS spectrum for T = 3.5 K, a magnon-like dispersion seemingly emanates from the elastic line, although the inelastic feature is rather broad. The excitation energies for various Q at 3.5 K were investigated and the corresponding quasielastic and inelastic components (green lines) were plotted in **Figure 5-7-8**. The red lines in **Figure 5-7-8** is the sum of quasielastic and inelastic components. The data in the range of -0.7 < E < 0 meV were excluded from the fitting consideration due to the high back ground in this energy region, resulting in the deviations between the data and the fitting results. The linewidth of the quasielastic components are comparable to the instrumental resolution.

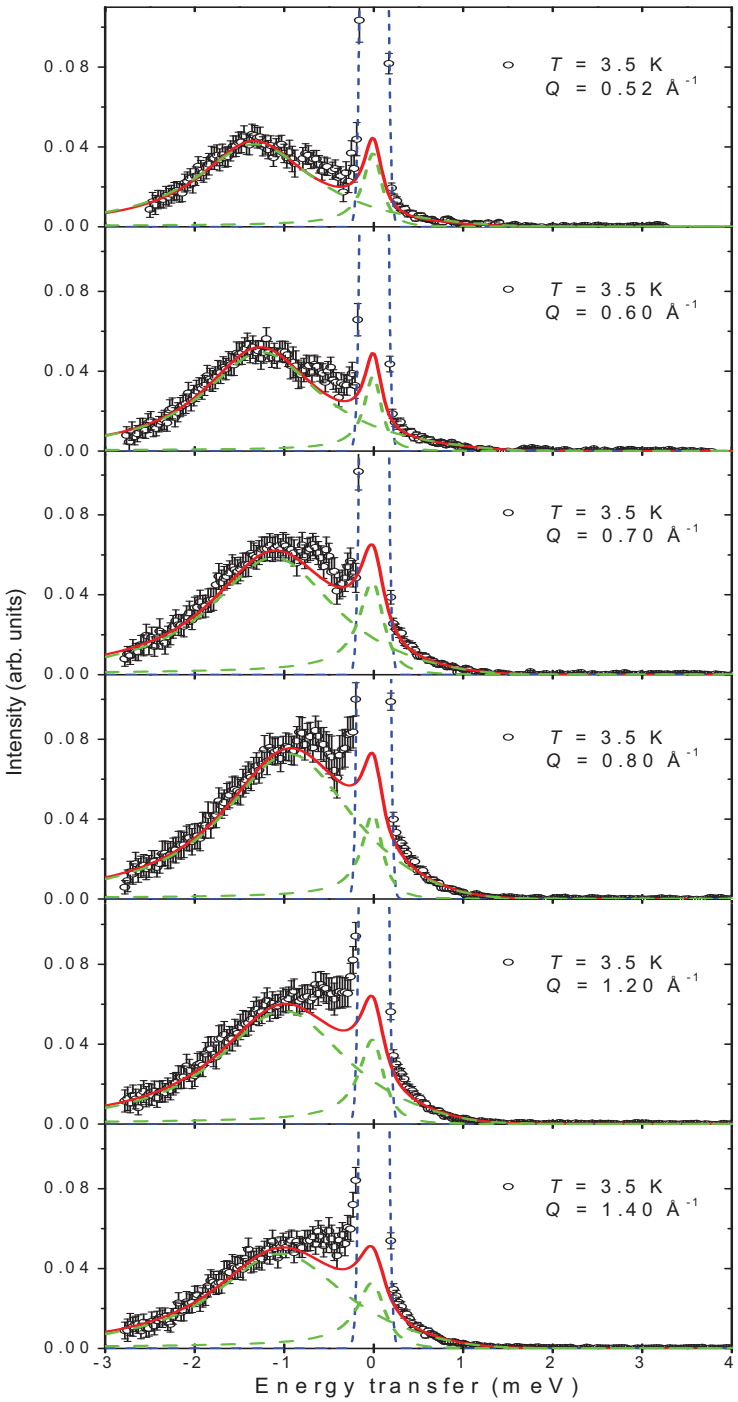

Figure 5-7-8 INS spectra for 3.5 K at various Q, along with the fit to the inelastic (red line) and the elastic (blue dashed line) components.

In **Figure 5-7-8**, the excitation energy of the inelastic component exhibits a Q dependence. Similar to the fits as shown in **Figure 5-7-6**, the INS spectra for 3.5 K at various Q are fitted with one Gaussian function to account for the elastic scattering, one Lorentzian function given by Eq. (5.7.2) for the quasielastic scattering, and a damped harmonic oscillator model given by Eq. (5.7.3) for the inelastic scattering. The linewidth (Γ_{in}), position (ω_d), and intensity (I_{in}) of the inelastic component are plotted in **Figure 5-7-9** as a function of Q.

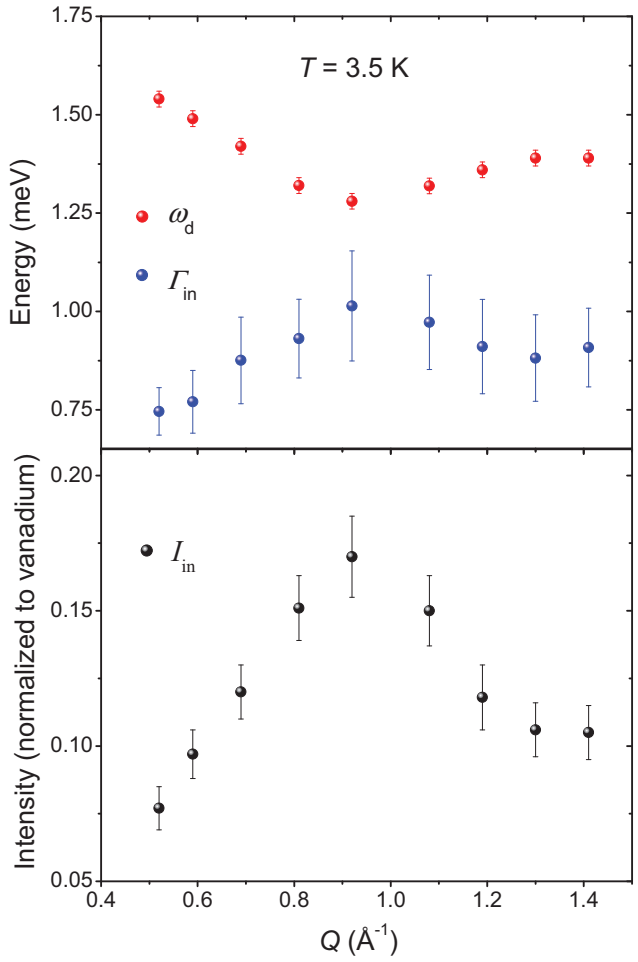

Figure 5-7-9 Q dependence of the linewidth (Γ_{in}), position (ω_d), and intensity (I_{in}) of the inelastic components obtained by the fit to the INS spectrum for 3.5 K.

As shown in **Figure 5-7-9**, the excitation energy of the inelastic component is about 1.54 meV at Q = 0.52 Å^{-1}. As Q increases, the excitation shifts to lower energy and reaches a minimum at around Q = 0.9 Å^{-1}. If Q increases further from 0.9 Å^{-1}, the excitation shifts to higher energy. Basically the Q dependence of the excitation energy follows a spin-wave-like behavior. But besides this qualitative explanation to the Q dependence of the excitation energy, a reliable quantitative determination of the spin-wave excitation is difficult using the present data, because the measured magnetic response is rather broad and strongly affected by the multiple scattering from the aluminum sample can.

As a summary of this section, the inelastic neutron scattering spectra of $Na_3Co(CO_3)_2Cl$ have been measured on TOFTOF at various temperatures. The overall energy transfer range of the magnetic scattering intensity is in reasonable agreement with the Curie-Weiss temperature, reflecting the strengh of the dominating magnetic exchange interactions. Above 3.5 K, no long-range magnetic order was detected as expected. But the system shows clear collective magnetic excitations below 15 K. The most intriguing result is that a spin-wave-like dispersion was observed at 3.5 K (below T_g = 4.5 K), which indicates that the glassy freezing temperature T_g does not correspond to a complete spin-glass freezing as expected in traditional metallic spin glasses [42, 150, 207]. But it should be noticed that the spin-wave-like zone center in **Figure 5-7-9** locates around Q = 0.9 Å^{-1}, inconsistent with the positions of the magnetic reflections observed in DNS measurements. The spin-wave-like dispersion indicated by the INS spectrum at 3.5 K is rather broad and not applicable for a reliable quantitative analysis, but may still serve as a first evaluation prior to the future neutron scattering measurements on this system at lower temperatures. Further inelastic neutron scattering measurements below 1.5 K are needed to fully understand the magnetic excitations of $Na_3Co(CO_3)_2Cl$.

5.8 Summary

In this chapter, a new spin-frustrated pyrochlore antiferromagnet $Na_3Co(CO_3)_2Cl$ is investigated in detail, which exhibits complicated magnetic behavior. The major results in this chapter is summarized as following:

1. The average crystal structure of $Na_3Co(CO_3)_2Cl$ has been determined by means of X-ray powder diffraction and neutron powder diffraction. $Na_3Co(CO_3)_2Cl$ crystallizes in cubic structure with space group $F\,d\,\bar{3}$ (#203). No structural phase transition has been found from 3.7 K to 300 K.
2. DC and AC susceptibility measurements display two anomalies at ~ 4 K and ~ 17 K. The former one is confirmed to be a spin-glass-like transition temperature by investigating its field-dependence and frequency-dependence. The Co^{2+} ions are in high spin state S = 3/2. The nearest-neighbor Co^{2+} spins are antiferromagnetically coupled, leading to strong geometrical spin frustration in this pyrochlore magnet. The Curie-Weiss temperature and the effective exchange constant are determined as -33.8 K and 0.26 meV, respectively.
3. The specific heat of $Na_3Co(CO_3)_2Cl$ shows a hump at ~ 5 K, consistent with the spin-glass-like transition at 4.5 K. A sharp peak in specific heat is observed at 1.5 K, which is due to the long-range magnetic phase transition.
4. No long-range magnetic order has been seen in the neutron powder diffraction measurements down to 3.7 K, consistent with the spin-glass-like transition at 4.5 K. No change in the crystal structure has been detected at 3.7 K and 30 K within the resolution of the presented neutron powder diffraction measurements, indicating that the inflection point at 17 K may not associate with additional effects such as an orbital order. Though Co sublattice displays a fully ordered pyrochlore lattice, positional displacement has been detected on Na sites. Possible static atomic disorder could exist on chlorine site. Local probing techniques will be needed to identify the possible disorder existing in this system.
5. Polarized neutron scattering investigations show that significant spin correlations build up below 30 K ($\approx -\Theta_{CW}$). The analysis of spin correlations indicates that the spin structure of this system is characterized by short-range spin correlations with dominating antiferromagnetic nearest-neighbor interaction and weak ferromagnetic next-nearest-neighbor interaction. Magnetic Bragg peaks observed at 50 mK indicate that $Na_3Co(CO_3)_2Cl$ enters a long-range magnetic order (or partial order) with an all-in-all-out spin configuration, consistent with the specific heat measurements.
6. Inelastic neutron scattering reveals also clear spin correlations at low temperatures. Quasielastic scattering dominates the INS spectra above 50 K. The fast decrease of quasielastic scattering from 15 K to 3.5 K accompanys with a

development of inelastic component. Collective magnetic excitations have been observed at 3.5 K, which indicates that the freezing temperature T = 4.5 K doesn't correspond to a complete spin-glass freezing as expected in traditional metallic spin glasses.

Now the magnetism of $Na_3Co(CO_3)_2Cl$ can be explained as follows. At high temeratures (T > 200 K), the spins are basically paramagnetic. As the temperature decreases below 200 K, deviation from the Curie-Weiss law occurs. Spin correlations start to develop around $-\Theta_{CW} \approx 30$ K (or a little higher than 30 K). At 17 K, some kind of long-range collective magnetic behavior happens, which exhibits a rather sharp feature in magnetic susceptibility and a small hump in specific heat. But the whole system does not display any long-range magnetic order detectable by neutron scattering methods. It seems that the spins are partially ordered at 17 K. As the temperature decreases further, the spin fluctuations slow down quickly. The spins experience a spin-glass-like freezing into the directions selected by local anisotropy at about (or a little higher than) 4.5 K, but this spin freezing is not complete in the sense that the spins may still be fluctuating with respect to the frozen directions. If the temperature keeps decreasing below the spin-glass-like freezing temperature, either an order-by-disorder mechanism driven by the thermal and/or quantum fluctuations or structual distortion due to magneto-crystalline coupling and strong Ising-like anisotropy, triggers a long-range magnetic order (or partial order) of this spin system.

It is an intriguing phenomenon that $Na_3Co(CO_3)_2Cl$ experiences a magnetic partial order at 17 K, a spin-glass-like transition at 4.5 K, and finally a long-range magnetic order (or partial order) at 1.5 K. The origin of the magnetic partial order at 17 K is not clear. But a recent theoretical investigation of classical pyrochlore antiferromagnet by Chern et al. [197] may shed light on this magnetic partial order. Their Monte Carlo simulations suggest a new, partially ordered phase with collinear spins at finite temperatures in classical Heisenberg pyrochlore antiferromagnet with a weak ferromagnetic next-nearest-neighbor interaction. In this intermediate partially-ordered phase, the spins display collinear order within a thin {100} layer but no order across different layers [197], which is similar with the magnetic behaviors of $Na_3Co(CO_3)_2Cl$ observed at 17 K. A tentative explanation is given here that the system enters some kind of intermediate partially-ordered magnetic phase at 17 K. The nature of the spin-glass-like transition at 4.5 K is also unclear. The present NPD

measurements show that $Na_3Co(CO_3)_2Cl$ is chemically ordered within the experimental resolution, but static atomic disorder could possibly exist on the chlorine sites. Also the subtle randomness of atomic bonds could be a source of disorder, serving as an ingredient of the spin-glass-like behavior in addition to the spin frustration. The determination of the existence of any atomic disorder in $Na_3Co(CO_3)_2Cl$ requires local probing methods, such as extended x-ray-absorption fine structure, nuclear magnetic resonance, and neutron pair distribution function analysis. The spin-glass-like behavior of $Na_3Co(CO_3)_2Cl$ at 4.5 K is different from those of typical spin glass systems in the sense that spins remain fluctuating below T_g, instead of being frozen up. This spin dynamics may have played an important role for $Na_3Co(CO_3)_2Cl$ in entering a long-range magnetic order (or partial order) at 1.5 K. For pyrochlore antiferromagnets with only nearest-neighbor interactions, there is a very high degree of frustration and no long-range magnetic order is predicted. But long-range order may occur if a finite next-nearest-neighbor exchange interaction is considered [194, 197-199]. For $Na_3Co(CO_3)_2Cl$, the weak ferromagnetic next-nearest-neighbor exchange interactions partially lifts the vast degeneracy of the nearest-neighbor model and result in a magnetically ordered ground state. A mean-field approach to the magnetic ordering in pyrochlore antiferromagnets with ferromagnetic next-nearest-neighbor interactions predicted a ground state with incommensurate magnetic order [198], while a later Monte Carlo simulation on such spin system suggested that the spins tend to order in a finite long-range order characterized by the commensurate spin order and remain largely fluctuating even in the ordered state [199]. A long-range magnetically ordered state of $Na_3Co(CO_3)_2Cl$ has been clearly indicated in our specific heat and polarized neutron scattering measurements. But our experiments cannot identify whether the spins order completely in the ground state. A representation analysis of the magnetic reflections obtained at 50 mK suggest that $Na_3Co(CO_3)_2Cl$ exhibits a commensurate magnetic order with an all-in-all-out type spin arrangement. A full characterization of this long-range magnetic order requires samples with larger crystal sizes and more neutron scattering experiments below 1.5 K. The ordered state in zero and applied fields is also interesting to be studied by means of neutron scattering and muon spin-relaxation experiments.

In conclusion, the crystal structure and the magnetism of spin-frustrated pyrochlore antiferromagnet $Na_3Co(CO_3)_2Cl$ has been investigated in this chapter. The

average crystal structure of $Na_3Co(CO_3)_2Cl$ has been determined and refined. The DC and AC magnetic susceptibility measurements provide strong evidences for a spin-glass-like transition at T_g = 4.5 K. An intermediate partially-ordered phase and a long-range magnetic order (or partial order) have been observed at 17 K and 1.5 K, respectively, qualitatively consistent with the theoretical predictions for pyrochlore antiferromagnets with weak ferromagnetic next-nearest-neighbor interactions. As a new model system of pyrochlore magnets, $Na_3Co(CO_3)_2Cl$ certainly deserves more experimental and theoretical investigations to understand the particular intermediate partially-ordered state and the long-range ordering state, as well as the nature of the spin-glass-like phase transition.

CHAPTER 6:

Conclusions

In this thesis，geometrical spin frustration has been extensively studied in both molecular-based spin cluster and infinite pyrochlore lattice. Topology of the crystal structures proves to be essential to form the exotic magnetic properties in these materials. Short-range magnetic order exists generally in these materials below their Curie-Weiss temperatures, as evidenced by the spin correlations measured using diffuse neutron scattering with polarization analysis method. The observed short-range spin correlations remain rather localized. In spin-frustrated molecular magnet $\{Mo_{72}Fe_{30}\}$, spin correlations are confined in individual molecules and no long-range magnetic order has been observed even down to 60 mK, due to the relatively large intermolecular distances. The simulation based on a frustrated three-sublattice spin model can successfully reproduce the short-range spin correlations in $\{Mo_{72}Fe_{30}\}$. In case of magnetic pyrochlore $Na_3Co(CO_3)_2Cl$, the spin structure is characterized by the dominating antiferromagnetic coupling between nearest neighbors and the weak ferromagnetic next-nearest-neighbor interactions. A long-range magnetic order is achieved at 1.5 K in $Na_3Co(CO_3)_2Cl$, which might be due to the existence of further-neighbor interactions. Therefore the interplay between spin frustration and lattice constraints leads to different magnetic behaviors in different systems.

Besides experimental characterizations, simulations of short-range spin correlations have been carried out to approach the magnetic ground state of $\{Mo_{72}Fe_{30}\}$. The spin correlations of the frustrated three-sublattice spin model are calculated by numerical average of the spin correlations over all the molecules, i.e., all possible versions of the three-sublattice spin model. The simulation results are in reasonable agreement with the spin correlations measured by polarized neutron scattering at 1.5 K. Therefore the three-sublattice model proves to be a good approach to the magnetic ground state of $\{Mo_{72}Fe_{30}\}$.

The magnetic excitations have been studied by means of both heat capacity and inelastic neutron scattering measurements. The low-temperature heat capacity method proves to be quite efficient in the determination of the low-lying magnetic excitations in molecular magnets, whose low-lying energy spectra can be described by discrete rotational bands with well defined energy gaps. The validity of the quantum rotational band model for $\{Mo_{72}Fe_{30}\}$ and the three-spin model for $\{As_6V_{15}\}$ has been checked by comparing the energy gaps obtained in heat capacity

measurements with the theoretical predictions and the existing inelastic neutron scattering results. However, it's not straightforward to explain the anomaly around the spin-glass-like freezing temperature in the heat capacity data of $Na_3Co(CO_3)_2Cl$, because a continuous distribution of energy gaps, instead of discrete energy levels, accounts for this anomaly. The temperature-dependent spin dynamics of $Na_3Co(CO_3)_2Cl$ was then investigated by means of inelastic neutron scattering, which reveals propagating modes below its spin-glass-like freezing temperature, showing the spins of $Na_3Co(CO_3)_2Cl$ remains fluctuating below T_g.

DC and AC susceptibility measurements are especially direct and valuable to determine the spin-glass-like transition in $Na_3Co(CO_3)_2Cl$. They offer the opportunities to characterize collective magnetic behaviors within certain timescales in addition to those of neutron scattering measurements.

The average crystal structure of $Na_3Co(CO_3)_2Cl$ has been investigated in detail using X-ray powder diffraction and neutron powder diffraction measurements. The determination of the crystal structure is mandatory prior to the analysis of magnetism. Possible positional disorder has been suggested, which could be essential for the formation of the spin-glass-like behavior of $Na_3Co(CO_3)_2Cl$, in addition to the strong spin frustration.

The research on the magnetic ground states of two molecular magnets, $\{Mo_{72}Fe_{30}\}$ and $\{As_6V_{15}\}$, expends the knowledge on these molecular magnets and may benefit the study on similar molecular-based spin clusters. Having achieved a good understanding to the magnetic properties of these materials, future work on these materials will be to interlink such spin clusters in layered 3D or 2D networks, which would be a milestone for realizing quantum computation in molecular-based magnetic systems.

As to the magnetic pyrochlore $Na_3Co(CO_3)_2Cl$, its complicated magnetic behavior has not yet been understood completely. More experiments are needed to study the long-range magnetic order below 1.5 K and the origin of the inflection point at 17 K. Though no applications are immediately evident for this material, it is worthy of more research to explain the remaining mystery in its magnetism. Magnetic pyrochlores always surprise the condensed matter physicists with exotic magnetic behavior and the interesting physics behind.

Appendices

A. Abbreviations

2D	two dimensional
3D	three dimensional
ACMS	AC/DC Magnetometry System
ADP	Atomic displacement parameter
AT line	Almeida-Thouless line
BASIS	neutron backscattering spectrometer at ORNL
DNS	diffuse neutron scattering instrument at FRM II
EPR	electron paramagnetic resonance
ESR	electron spin resonance
FC	field cooled
FCC	face-centered cubic
FRM II	Forschungsneutronenquelle Heinz Maier-Leibnitz
FWHM	full width at half maximum
ILL	Institut Laue-Langevin
INS	inelastic neutron scattering
JCNS	Jülich Center for Neutron Science
LHe	liquid helium
MPMS	Magnetic Property Measurement System
NMR	nuclear magnetic resonance
NPD	neutron powder diffraction
NPDF	neutron pair distribution function
NSF	non spin flip
NSHB	nonresonant spectral hole-burning
ORNL	Oak Ridge National Laboratory
POM	polyoxometalate
PPMS	Physical Property Measurement System
QRB	quantum rotational band
SF	spin flip
SMM	single-molecule magnet
SNS	spallation neutron source
SPODI	structure powder diffractometer at FRM II
SQUID	superconducting quantum interference device
TOF	time-of-flight
TOFTOF	time-of-flight spectrometer at FRM II
ULF	ultra low field
XAFS	X-ray absorption fine structure
XRPD	X-ray powder diffraction
ZFC	zero-field cooled

B. Example of the PCR File for Rietveld Refinement by Fullprof

```
COMM Na3Co(CO3)2Cl
! Current global Chi2 (Bragg contrib.) =     0.8706
! Files => DAT-file: NaCo_1,  PCR-file: NaCo_1
!Job Npr Nph Nba Nex Nsc Nor Dum Iwg Ilo Ias Res Ste Nre Cry Uni Cor Opt Aut
   1   0   1  53   2   0   0   0   1   0   1   0   1   0   0   0   0   0   0
!
!Ipr Ppl Ioc Mat Pcr Ls1 Ls2 Ls3 NLI Prf Ins Rpa Sym Hkl Fou Sho Ana
   0   0   1   0   1   0   4   0   0   3  10  -2   0   0   0   1   0
!
!lambda1  Lambda2  Ratio  Bkpos   Wdt    Cthm    muR   AsyLim   Rpolarz ->Patt# 1
 1.548286 1.548286 0.0000 10.000 20.0000 0.0000 0.2160 160.00    0.0000
!
!NCY  Eps  R_at  R_an  R_pr  R_gl  Thmin    Step    Thmax    PSD  Sent0
  50  0.02 0.98  0.98  0.98  0.98  0.9500 0.050016 153.9000 0.000 0.000
!
!2Theta/TOF/E(Kev)    Background  for Pattern#  1
        6.150      4217.686         0.000
        8.900      3789.785         0.000
       11.900      3510.444         0.000
       14.700      3309.947         0.000
       15.500      3291.139         0.000
       19.800      3068.535         0.000
       23.000      2966.908         0.000
       23.750      2951.271         0.000
       26.600      2877.879         0.000
       30.700      2900.558         0.000
       34.250      2761.814         0.000
       37.200      2698.408         0.000
       41.450      2645.822         0.000
       43.750      2742.831         0.000
       47.350      2632.780         0.000
       50.800      2433.398         0.000
       51.150      2437.282         0.000
       54.850      2436.359         0.000
       56.800      2375.534         0.000
       61.950      2428.906         0.000
       64.450      2394.211         0.000
       66.100      2306.693         0.000
       68.000      2299.038         0.000
       71.050      2339.670         0.000
       73.700      2302.182         0.000
```

```
        76.700      2347.278         0.000
        79.550      2333.353         0.000
        83.800      2247.333         0.000
        85.000      2219.176         0.000
        88.050      2251.674         0.000
        92.100      2252.666         0.000
        93.900      2260.809         0.000
        96.700      2272.877         0.000
        98.950      2269.698         0.000
       101.900      2308.531         0.000
       105.450      2245.314         0.000
       109.350      2330.947         0.000
       110.650      2273.973         0.000
       114.300      2273.904         0.000
       117.400      2351.795         0.000
       118.050      2266.241         0.000
       123.250      2386.778         0.000
       123.300      2301.707         0.000
       127.250      2372.658         0.000
       130.700      2296.507         0.000
       132.400      2338.142         0.000
       136.600      2273.309         0.000
       138.100      2315.909         0.000
       142.500      2513.495         0.000
       143.000      2315.436         0.000
       147.950      2636.560         0.000
       148.600      2438.570         0.000
       153.650      2614.786         0.000
!
! Excluded regions (LowT  HighT) for Pattern#  1
         0.00         6.10
       153.95       180.00
!
!
      28    !Number of refined parameters
!
!  Zero     Code     SyCos     Code    SySin     Code  Lambda     Code MORE ->Patt# 1
  0.00216  21.0    0.00000     0.0   0.00000     0.0 0.000000     0.00    0
!-------------------------------------------------------------------------------
!  Data for PHASE number:   1  ==> Current R_Bragg for Pattern#  1:     1.77
!-------------------------------------------------------------------------------
Na3Co(CO3)2Cl
!Nat Dis Ang Prl Pr2 Pr3 Jbt Irf Isy Str Furth        ATZ     Nvk Npr More
   5    0    0 0.0 0.0 1.0    0    0    0    0    0         232.345    0    5    0
```

```
!
F d -3                    <--Space group symbol
!Atom    Typ        X          Y          Z      Biso        Occ      In Fin N_t Spc
/Codes
!    beta11    beta22    beta33    beta12    beta13    beta23  /Codes
Co      Co       0.00000   0.00000   0.00000   0.13776   0.16667   0    0    0     0
                   0.00      0.00      0.00    100.50      0.00
Na      Na       0.12500  -0.15105   0.12500   0.00000   0.50000   0    0    2     0
                   0.00    111.00      0.00      0.00      0.00
       0.00055   0.00048   0.00067   0.00000   0.00014   0.00000
        121.00    131.00    141.00      0.00    151.00      0.00
O       O       -0.02436   0.64698   0.51653   0.00000   1.00000   0    0    2     0
                  161.00    171.00    181.00      0.00      0.00
       0.00039   0.00033   0.00049  -0.00020   0.00008  -0.00006
        191.00    201.00    211.00    221.00    231.00    241.00
C       C        0.03265   0.21735   0.03265   0.24469   0.33333   0    0    0     0
                  251.00   -251.00    251.00    260.50      0.00
Cl      Cl       0.25000   0.25000   0.50000   0.00000   0.16667   0    0    2     0
                   0.00      0.00      0.00      0.00      0.00
       0.00058   0.00058   0.00058   0.00018  -0.00018  -0.00018
        271.00    271.00    271.00    281.00   -281.00   -281.00
!-------> Profile Parameters for Pattern #  1
!  Scale        Shape1       Bov       Str1       Str2       Str3   Strain-Model
 0.93684E-01   0.11782   0.00000   0.00000   0.00000   0.00000        0
    11.00000    41.000     0.000     0.000     0.000     0.000
!    U         V          W          X          Y        GauSiz    LorSiz Size-Model
 0.030543  -0.032174   0.102065   0.000000   0.000000   0.000000   0.000000     0
   91.000     81.000     71.000      0.000      0.000      0.000      0.000
!      a          b          c         alpha       beta        gamma       #Cell Info
  13.989807  13.989807  13.989807  90.000000  90.000000  90.000000
   31.00000   31.00000   31.00000    0.00000    0.00000    0.00000
!  Pref1     Pref2       Asy1       Asy2       Asy3       Asy4
  0.00000   0.00000   0.08150   0.01917   0.00000   0.00000
     0.00      0.00     51.00     61.00      0.00      0.00
!  2Th1/TOF1     2Th2/TOF2  Pattern # 1
       6.100       153.900        1
```

C. Methods and Instruments

1. Diffuse neutron scattering spectrometer (DNS) [95, 212]

The JCNS diffuse neutron scattering spectrometer (DNS) at FRM II is a versatile diffuse cold neutron scattering time-of-flight spectrometer with polarization analysis. DNS allows an unambiguous separation of nuclear coherent, spin incoherent and magnetic scattering contributions over a large range of scattering vector Q and energy transfer E. DNS has a compact design with only 80 cm distance from the sample position to the surrounding detectors, leading to modest energy resolution and relatively large neutron intensity.

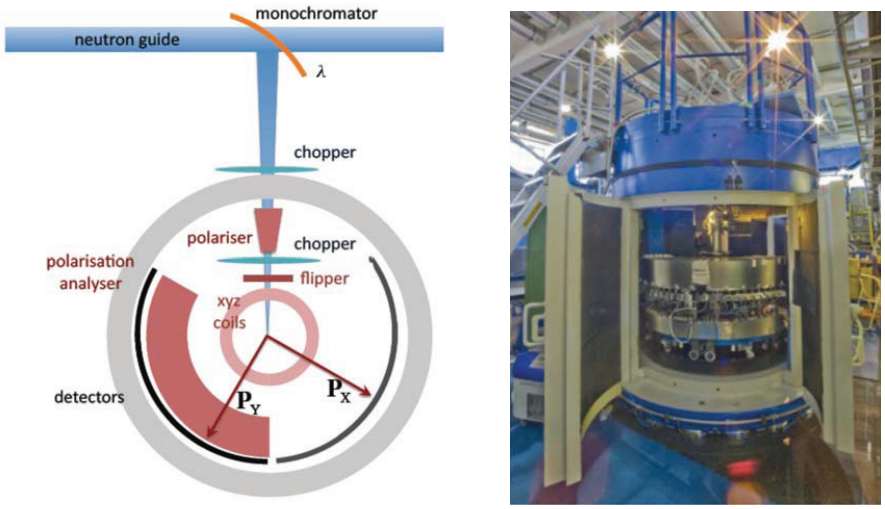

Figure C-1-1 Schematic view of DNS. [Pictures taken from W. Schweika, *Polarized Neutron Scattering and Polarization Analysis* in "*Neutron Scattering: Lectures of the JCNS Laboratory Course*", Th. Brückel et al. (eds.), (Forschungszentrum Jülich GmbH, Jülich 2010)]

A schematic representation of DNS is given in **Figure C-1-1**. The incident neutron wavelength λ ($2.4 < \lambda < 6$ Å) is selected by a horizontally and vertically adjustable PG(002) double focusing monochromator. In order to perform time-of-flight spectroscopy a double-chopper system is installed between the monochromator and

the sample position. A polarizer using m=3 Schärpf bender-type focusing supermirrors is placed between the two choppers to generate polarized neutrons. A polarizing supermirror is commonly composed of one type of magnetic layers with aligned magnetization and non-magnetic layers with varying thickness. Neutrons with spins either parallel or antiparallel to the layer magnetization have different reflectivities in the supermirror regime: spins parallel to the layer magnetization have high reflectivity, while the antiparallel ones are transmitted or absorbed.

Before being scattered by the sample, the polarized neutron beam has to be manipulated by the guide field to maintain the polarization direction. The guide field should be small enough not to influence the sample magnetization, but large enough to overcome the surrounding magnetic fields from the earth and other sources.

The reversal of neutron polarization on DNS is realized by a π-flipper right after the chopper system. The π-flippers are used to reverse the polarization and to detect whether the sample causes spin-flip scattering. The homogeneous field of a long rectangular coil is often used for this purpose. As shown in **Figure C-1-2**, the coils generate a homogeneous field $\boldsymbol{H}_{\text{coil}}$ perpendicular to the spin orientation and to the travel direction of the polarized neutron beam. The neutrons feel sudden changes of the field when enter and exit the coil. Inside the coil, the neutrons start to precess around the flipping field $\boldsymbol{H}_{\text{coil}}$. The polarization of the neutrons can be reversed by an angle of π through adjusting the current of the coil with respect to the geometry of the coil and the time of flight that neutrons spend inside the coil.

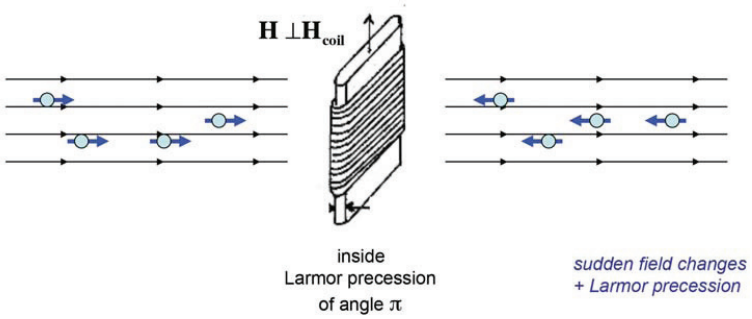

Figure C-1-2 Principle of a neutron π-flipper. [Picture taken from W. Schweika, *Polarized Neutron Scattering and Polarization Analysis* in "*Neutron Scattering: Lectures of the JCNS Laboratory Course*", Th. Brückel et al. (eds.), (Forschungszentrum Jülich GmbH, Jülich 2010)]

The sample position is surrounded by a set-up of three orthogonal Helmholtz coils, i.e., *XYZ*-coils. *XYZ*-coils generate the desired neutron polarizations, which are necessary for the polarization analysis. The field strength is large enough to enable an adiabatic rotation of the spin orientation, but small enough not to affect the sample magnetization. The *z*-coil is used to compensate the guide field at the sample position. After the scattering process and on the way to analyzers, the neutrons, which are brought into *x*- or *y*- direction in the scattering process, are reoriented by the *xyz*-coils back to the *z* direction. For the polarization analysis at *z* direction, no spin reorientation is needed to be done by the *xyz*-coils.

Multi-detector arrays are used to record the scattered neutrons. Analyzers are placed between the sample and the detectors to detect a specific polarization direction of the scattered neutrons. For non-polarized neutrons, 128 units of position sensitive ^{3}He detector tubes are available to cover scattering angles of $0 \leq 2\theta \leq 135°$ in the horizontal plane. For polarized neutrons, 24 units of ^{3}He detector tubes equipped with $m = 3$ supermirror polarization analyzers cover scattering angles of $0 \leq 2\theta \leq 120°$. The maximum momentum transfer Q_{max} that can be reached is 2.30 Å^{-1} for polarization analysis with an incoming wavelength of 4.74 Å.

DNS is ideal for the studies on complex spin correlations in highly frustrated magnets and strongly correlated electrons, as well as the structures of soft condensed matters such as the nanoscale confined polymers and proteins, via polarization analysis. The single-particle excitations, magnons and phonons can be investigated by single-crystal or powder time-of-flight spectroscopy. Uniaxial-, longitudinal- and vector- polarization analysis are practicable, ensuring wide applications of DNS in both hard and soft condensed matters.

Powder and polycrystalline samples have been used for the DNS measurements in this thesis. Three types of cryostats have been equipped, including close-cycle cryostat (T_{min} ~ 3 K), orange cryostat (T_{min} ~ 1.2 K) and dilution insert (T_{min} ~ 20 mK). Cylinder aluminum sample holders were used for measurements with close-cycle cryostat. Hollow cylinder copper holders were used with orange cryostat and dilution insert. It should be mentioned that Al holders are better for orange cryostat actually. The sample mounting procedures were done in helium atmosphere. **Figure C-1-3** shows the pictures of typical Al and Cu sample holders for DNS. The diameters of the sample holders could vary according to the sample properties, because the scattering probability should be kept below 10% to minimize the

multiple scattering events. The tail below the Cu holder in **Figure C-1-3** is a tube to let helium gas flow through, which will be cut off and sealed after the air in the sample holder is driven out. A design of Cu holder for measurements with dilution insert is shown in **Figure C-1-4**.

Figure C-1-3 Typical Al (left, diameter: 4 mm) and Cu (right, diameter: 9 mm) sample holders used for powder sample measurements on DNS.

Besides the sample measurements, the empty sample can and a black body standard (Cadmium) are measured to account for the background. The measured intensities are normalized to the monitor counts. The scattering intensities of the sample are determined by subtraction of the signals from the empty can and the black body. If a cryostat is used in sample measurements, the background measurements are carried out with the cryostat.

There is no incident beam polarizer or analyzer before the detector can work at 100% efficiency. A small amount of impurity neutrons with wrong polarization directions always manage to arrive at the detectors. This effect is characterized by the so-called "flipping ratio", which must be corrected for every detector by means of the scattering from an ideal isotropic incoherent scatterer, a NiCr alloy. The flipping ratio R is defined as $I_\uparrow/I_\downarrow$, where $I_\uparrow$ and $I_\downarrow$ are the background-corrected intensities with non-spin-flip and spin-flip scattering from NiCr alloy, respectively. The corresponding polarization is expressed as [213]

$$P_{NiCr} = \frac{I_\uparrow - I_\downarrow}{I_\uparrow + I_\downarrow} = \frac{I_\uparrow / I_\downarrow - 1}{I_\uparrow / I_\downarrow + 1} = \frac{R-1}{R+1} \qquad \text{(C.1.1)}$$

Insert: top view side view

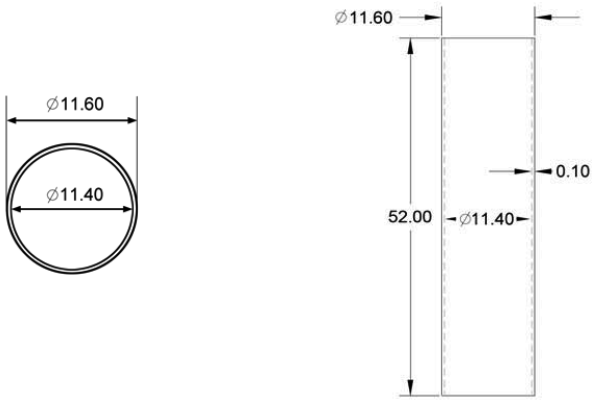

Lid: bottom view side view

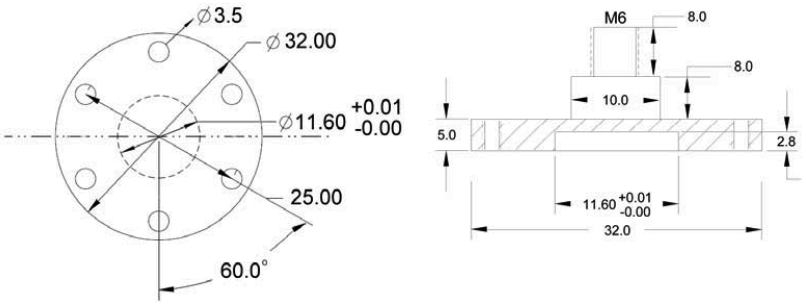

Can: top view side view

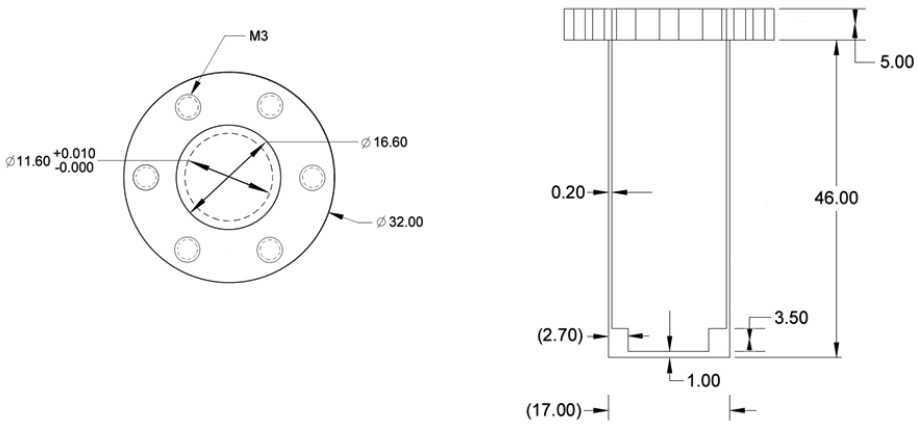

Figure C-1-4 Design of the Cu holder for DNS with dilution insert. The unit of the values is mm.

The background-corrected intensities with non-spin-flip and spin-flip for the sample are $I_{\uparrow\uparrow}$ and $I_{\uparrow\downarrow}$, respectively. The non-spin-flip and spin-flip scattering intensities of the sample after the correction of finite flipping ratio are denoted as $I_{\uparrow\uparrow}^{corr}$ and $I_{\uparrow\downarrow}^{corr}$. The background-corrected spin-flip and non-spin-flip scattering intensities of the NiCr alloy and the sample are plotted in **Figure C-1-5**, where the scattering intensity is shown as a function of the polarization [213].

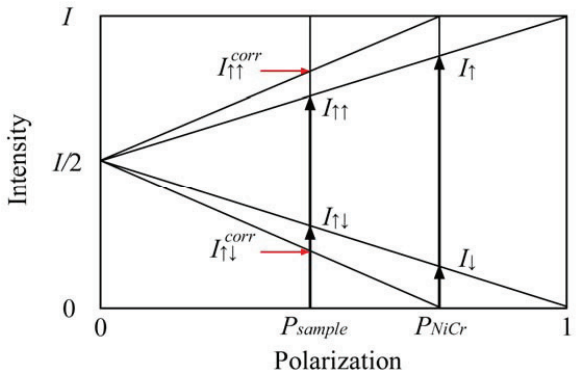

Figure C-1-5 Illustration of the non-spin-flip and spin-flip intensities $I_{\uparrow}$ and $I_{\downarrow}$ of the NiCr alloy, and the non-spin-flip and spin-flip intensities $I_{\uparrow\uparrow}$ and $I_{\uparrow\downarrow}$ of the sample, and the corresponding flipping-ratio-corrected intensities of the sample $I_{\uparrow\uparrow}^{corr}$ and $I_{\uparrow\downarrow}^{corr}$. All the intensities have been corrected for the background. [Picture re-designed from O. Schärpf, *The Spin of the Neutron as a Measuring Probe* (Institute Laue-Langevin, 1996)]

The correction of finite flipping ratio can then be done using simple rules of elementary geometry of proportionality [213].

$$I_{\uparrow\uparrow}^{corr} + I_{\uparrow\downarrow}^{corr} = I_{\uparrow\uparrow} + I_{\uparrow\downarrow} = I \tag{C.1.2}$$

$$\frac{I_{\uparrow\uparrow}^{corr} - I_{\uparrow\downarrow}^{corr}}{I} = \frac{I_{\uparrow\uparrow} - I_{\uparrow\downarrow}}{I_{\uparrow} - I_{\downarrow}} \tag{C.1.3}$$

$$I_{\uparrow\uparrow}^{corr} - I_{\uparrow\downarrow}^{corr} = \frac{I_{\uparrow\uparrow} - I_{\uparrow\downarrow}}{I_{\uparrow} - I_{\downarrow}} \cdot I = \left(I_{\uparrow\uparrow} - I_{\uparrow\downarrow}\right)\frac{I_{\uparrow} + I_{\downarrow}}{I_{\uparrow} - I_{\downarrow}} = \left(I_{\uparrow\uparrow} - I_{\uparrow\downarrow}\right)\frac{R+1}{R-1} \tag{C.1.4}$$

$$I_{\uparrow\uparrow}^{corr} = I_{\uparrow\uparrow} + \frac{1}{R-1}\left(I_{\uparrow\uparrow} - I_{\uparrow\downarrow}\right) \tag{C.1.5}$$

$$I_{\uparrow\downarrow}^{corr} = I_{\uparrow\downarrow} - \frac{1}{R-1}\left(I_{\uparrow\uparrow} - I_{\uparrow\downarrow}\right) \tag{C.1.6}$$

In the polarization analysis of DNS, the flipping ratio correction should be done in the three polarization directions *x*, *y*, *z* for every detector. In order to account for the effect of the measuring set-up for every detector, we define the polarization product $P_n = P_{polarizer}P_{analyzer}F_{flipper}$ for the n^{th} detector, where $P_{polarizer}$ is the polarization efficiency of the polarizer, $P_{analyzer}$ is the polarization efficiency of the analyzer and $F_{flipper}$ is the flipper efficiency. The flipping ratio R_n for the n^{th} detector can be determined as

$$R_n = \frac{I_n^{\uparrow}}{I_n^{\downarrow}}, \tag{C.1.7}$$

by measuring the non-spin-flip and spin-flip scattering intensities of a NiCr alloy. Accordingly, the polarization product P_n for each detector can be given by

$$P_n = \frac{R_n - 1}{R_n + 1}. \tag{C.1.8}$$

Replacing *R* in Eqs. (C.1.5) and (C.1.6) by R_n in Eq. (C.1.7), the correction for finite flipping ratio of the measured data from the sample can be done by using Eqs. (C.1.5) and (C.1.6). The measurement of NiCr alloy is performed with the same detector-bank positions as those used in the sample measurements, because the flipping ratio is not isotropic.

In order to determine the absolute scattering cross section of the sample, the measured intensities must be normalized to the scattering of a standard scatterer whose cross section and scattering behavior is well known [213]. In the DNS measurements, the measured scattering of the sample is normalized to the incoherent scattering of a known-mass vanadium standard, since vanadium is a nearly ideal incoherent scatterer with an incoherent scattering cross section of 5.08 barn and a coherent scattering cross section of only 0.0184 barn. Because the incoherent scattering is isotropic angularly, the measurement of vanadium standard can be taken at one or two detector-bank positions, which could save some beamtime.

Another important use of vanadium measurements is to correct the variation in the detector efficiency and the analyzer transmission.

Without the use of time-of-flight energy analysis, the measured scattering data are actually integrated over the entire energy range of DNS. On the energy-loss side, the energy range is limited by the incident neutron energy [213]. For example, most of the DNS experiments in this thesis used an incident wavelength of 4.74 Å, corresponding to the incident energy of 3.64 meV. Therefore 3.64 meV is the upper limit of the detectable energy range on the energy-loss side of DNS. On the energy-gain side, the limiting factors are the energy dependence of the transmission function $T(\omega)$ of the supermirror analyzers and the temperature factor from detailed balance behavior $B(\omega)$ [213]. The experimental magnetic scattering cross section is then given by [213-215]

$$\sigma_{mag}^{exp} = \int d\Omega \int_{-\infty}^{\omega_{\max}=E_i/\hbar} d\omega T\left(\lambda(\omega)\right)\left(\frac{d^2\sigma}{d\Omega d\omega}\right)_{mag}. \qquad \text{(C.1.9)}$$

$T(\lambda)$ is the wavelength dependent transmission function of the supermirror analyzers, and $\left(\frac{d^2\sigma}{d\Omega d\omega}\right)_{mag}$ is the double differential magnetic scattering cross section, which is proportional to $F^2(\mathbf{Q})\Gamma(\mathbf{Q},\omega)k'/k$. $\Gamma(\mathbf{Q},\omega)$ is the magnetization-magnetization correlation function between unit cells i and j,

$$\Gamma(\boldsymbol{Q},\omega) = \int dt \exp[-i\omega t] \sum_{ij} \exp\left[i\boldsymbol{Q}\cdot\left(\boldsymbol{R}_i - \boldsymbol{R}_j\right)\right]\left\langle \boldsymbol{S}_i(t)\cdot\boldsymbol{S}_j(0)\right\rangle. \qquad \text{(C.1.10)}$$

$\Gamma(Q, \omega)$ is related to the relaxation function $R(Q, \omega)$ via the detailed balance behavior $B(\omega)$ as

$$\Gamma(Q,\omega) = \frac{\hbar\omega}{1-e^{-\hbar\omega/k_B T}} R(Q,\omega). \qquad \text{(C.1.11)}$$

Due to the fixed angular position of each detector and the large angular region covered by all the detectors, the experimental scattering cross section can be expressed approximately as [215]

$$\sigma_{mag}^{exp} \sim \overline{f^2} \sum_{Q} \int_{-\infty}^{\omega_{\max}} d\omega \frac{k'(\omega)}{k} T\left(\lambda(\omega)\right) B(\omega) R(Q,\omega). \qquad \text{(C.1.12)}$$

The incident neutron energy $\hbar\omega_i$ of DNS limits the measured cross section to the

contributions from energies $E < \hbar\omega_i$. Considering the magnetic excitations of $\{Mo_{72}Fe_{30}\}$ and $Na_3Co(CO_3)_2Cl$ are both low-lying (< 3 meV) (see Chapters 3 and 5), the energy integration of DNS is applicable for these two systems. The *XYZ*-difference method used on DNS has been discussed in Chapter 2.

2. Neutron Backscattering Spectrometer (BASIS) [216]

The JCNS neutron backscattering silicon spectrometer BASIS at the spallation neutron source SNS, Oak Ridge National Laboratory, USA, is a near-backscattering, crystal-analyzer spectrometer designed to provide extremely high energy resolution. The research on BASIS spans many scientific disciplines, from dynamics of water in organic and inorganic systems to ionic liquids to electronic and nuclear spin magnetism [217].

Neutron backscattering spectroscopy is developed to investigate atomic or molecular motions on long time scales with energy resolutions of the order of μeV. The mean idea of neutron backscattering spectroscopy is to use Bragg angles of near 90° with moderate collimation for beam monochromatization and analysis in order to achieve very high energy resolution [218]. The Bragg equation is given by

$$\lambda = 2d\sin\theta . \tag{C.2.1}$$

Differentiate Eq. (C.2.1) and then we have

$$\frac{\Delta\lambda}{\lambda} = \frac{\Delta d}{d} + \cot\theta \cdot \Delta\theta , \tag{C.2.2}$$

where $\Delta\lambda/\lambda$ represents the relative width of the wavelength band for an ideally collimated beam, d is the lattice spacing and $\Delta d/d$ is due to lattice strains, primary and secondary extinction, $\Delta\theta$ is the angular divergence of the beam. The backscattering geometry in reciprocal space is illustrated in **Figure C-2-1**. τ is the corresponding reciprocal lattice vector and expressed as $2\pi/d$. Accordingly we have

$$\frac{\Delta\tau}{\tau} = \frac{\Delta d}{d} . \tag{C.2.3}$$

After being scattered by the sample, the beam becomes divergent. Define Δk as the difference between the modulus of the longest and shortest wave vector k_{max} and k_{min}. Based on the geometrical relation in **Figure C-2-1**, Δk is determined as [218]

$$\Delta k = k_{\max} - k_{\min} = k_0 \left[\frac{1}{\cos(\Delta\theta/2 + \varepsilon)} - 1 + \frac{\Delta\tau}{\tau} \right]. \quad \text{(C.2.4)}$$

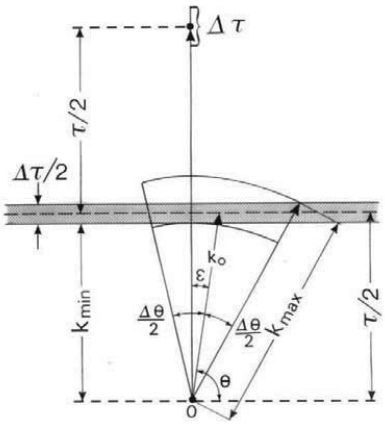

Figure C-2-1 Backscattering geometry in reciprocal space at $\theta \approx 90°$. [Picture taken from the review at http://www.ill.eu/sites/BS-review/HOME.html]

Since $\theta \approx 90°$ and $(\Delta\theta/2+\varepsilon)$ is very small, Eq. (C.2.4) can be expanded to the first order and comes to

$$\frac{\Delta k}{k_0} \approx \frac{1}{2}\left(\frac{\Delta\theta}{2} + \varepsilon \right)^2 + \frac{\Delta\tau}{\tau}. \quad \text{(C.2.5)}$$

For the case of near backscattering $\varepsilon < \Delta\theta/2$, $\Delta\lambda/\lambda$ is given by

$$\frac{\Delta\lambda}{\lambda} = \frac{\Delta k}{k} = \frac{1}{2}\left(\frac{\Delta\theta}{2} + \varepsilon \right)^2 + \frac{\Delta\tau}{\tau}. \quad \text{(C.2.6)}$$

A schematic view of BASIS is shown in **Figure C-2-2** [219]. The necessary timing resolution is achieved from a design of the long initial guide of 84 m. As a TOF-backscattering spectrometer, bandwidth choppers are employed on BASIS to acquire the desired wavelength bands. The scattered neutrons from the sample are analyzed for energy and wavevector transfer by an array of silicon crystals in near backscattering geometry (θ = 88°). The Si (111) crystal analyzers reflect the neutrons with a very narrow energy distribution, resulting in an extremely high energy resolution of 2.2 μeV at the elastic peak and a Q-range from 0.1 to 2.0 Å^{-1}. The filters

in front of the detectors remove the higher order Bragg reflections from the analyzer crystals. Upon using Si (311) analyzers, the energy resolution at elastic peak is 10 μeV and the Q-range can be extended to $0.6 < Q < 3.8$ Å^{-1} [220].

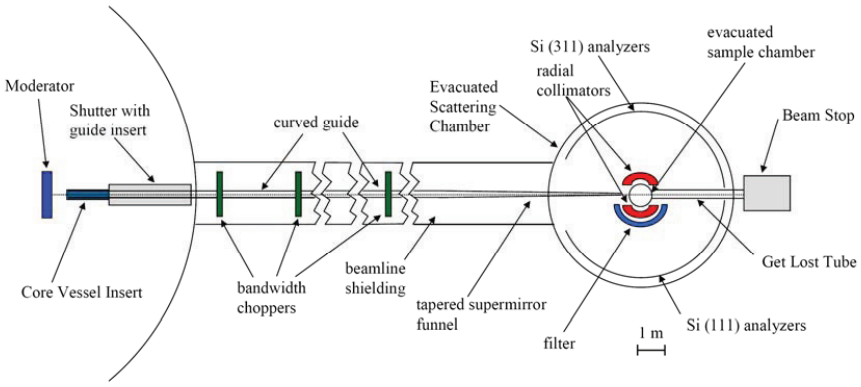

Figure C-2-2 Schematic view of BASIS. [Picture taken from K. W. Herwig, *The Silicon Backscattering Spectrometer at SNS*, presentation in "*Workshop on Cold Neutron Chopper Spectrometer*", Nist, 2001.]

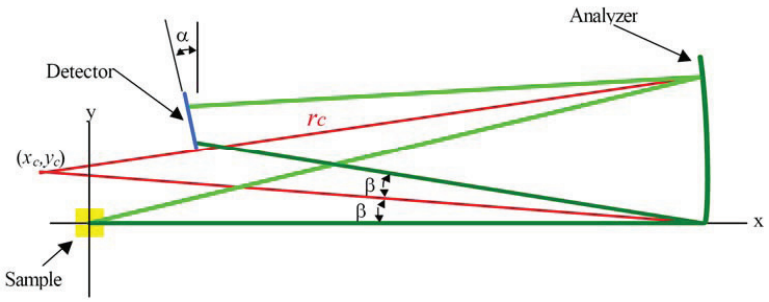

Figure C-2-3 Schematic view of the sample/analyzer/detector geometry on BASIS. [Picture taken from K. W. Herwig, *The Resolution Function of the High Resolution Backscattering Spectrometer at the Spallation Neutron Source*, Oak Ridge National Laboratory, 2000]

As shown in **Figure C-2-3**, the analyzer crystals are bent spherically and operated out of direct backscattering and can be rotated around the point (x_c, y_c) in the vertical dimension. The Bragg angle is given by 90°-β. Two of the flight paths from the sample to the detector are highlighted in green. The detector is tilted by an angle of a

to minimize the variations in the total flight path distances. Therefore, several parameters should be optimized, including the position of the detector, the detector tilt angle α, the radius r_c and the center (x_c, y_c) of the rotation for the analyzers.

In case of the inelastic scattering using the Si(111) analyzers operating at 60 Hz (source frequency), the accessible energy resolution and the dynamic range are given in **Figure C-2-4**. The elastic resolution is as low as 2.2 μeV. The accessible inelastic range lies between -1.5 meV and +18 meV. The solid colored bands indicate the bandwidths that can be achieved.

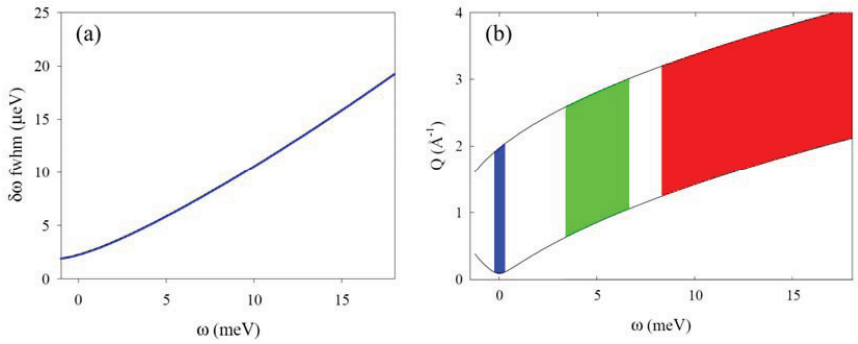

Figure C-2-4 (a) Inelastic resolution of BASIS using Si(111) analyzers. **(b)** Dynamic range of BASIS using Si(111) analyzers. [Pictures taken from K. W. Herwig, *The Silicon Backscattering Spectrometer at SNS*, presentation in "*Workshop on Cold Neutron Chopper Spectrometer*", Nist, 2001.]

3. Time-of-Flight Spectrometer TOFTOF [208, 221, 222]

The TOFTOF spectrometer is a multi-disc chopper time-of-flight (TOF) spectrometer for cold neutrons at the research neutron source Heinz Maier-Leibnitz (FRM II). Direct TOF method is used on TOFTOF to select the incident neutron energy and determine the scattered neutron energy. A schematic presentation of TOFTOF is shown in **Figure C-3-1**.

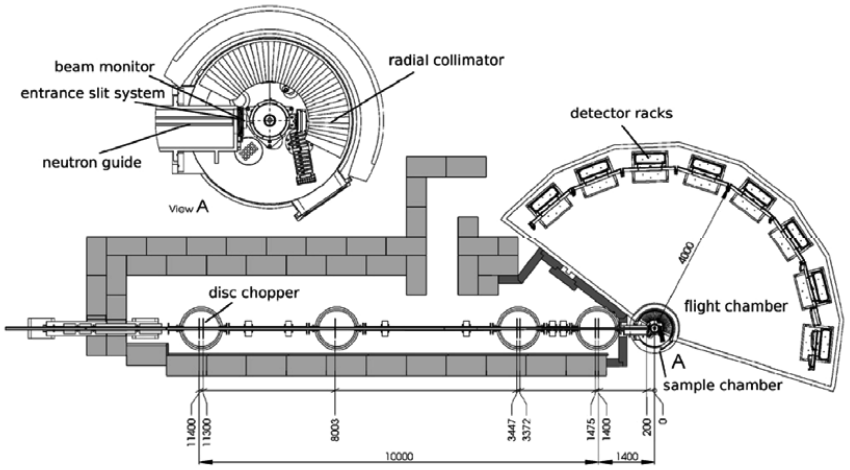

Figure C-3-1 Schematic view of TOFTOF spectrometer. View A is a layout of the sample chamber. [Picture taken from T. Unruh, J. Neuhaus and W. Petry, *Nuclear Instruments and Methods in Physics Research* A **580** (2007) 1414]

The outgoing neutrons from the moderator pass through an *S*-shaped curved neutron guide. The monochromatic neutron pulses are then achieved by seven high speed chopper discs in the primary spectrometer. The scattered neutrons are detected by the detectors, which are adjusted tangentially to the intersection lines of the Debye-Scherrer cones with the surface of a virtual sphere with a radius of 4 m around the center of the sample. The time-of-flight of the scattered neutrons from the sample to the detectors is measured and used for calculation of the neutron scattering spectra.

The TOF technique is useful as a low energy vibrational spectroscopic probe of the materials. The main idea of TOF method is to measure the time-of-flight of the

scattered neutrons from the sample to the detectors and thus determine their energy, as shown in **Figure C-3-2**. The incident neutron energy is selected by the rotation frequency of the Fermi chopper. Assume the distance between the chopper to the sample is R_i, the distance between the sample and the detector is R_f, and the incoming and outgoing neutron velocity is v_i and v_f, respectively. Then the neutron time-of-flight from the chopper to the detector is

$$\tau = \frac{R_i}{v_i} + \frac{R_f}{v_f}. \tag{C.3.1}$$

The scattered neutron energy can be calculated as

$$E_f = \frac{1}{2} m_n v_f^2 . \tag{C.3.2}$$

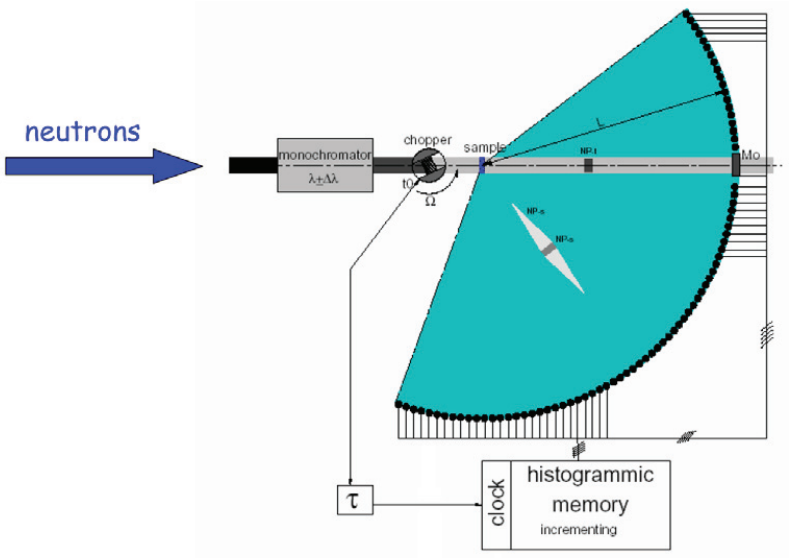

Figure C-3-2 Illustration of TOF method. [Picture taken from Michael Monkenbusch, *time-of-flight spectrometers*, presentation]

By covering a large solid angle with detectors, one can measure the complete Q – ω space simultaneously using TOF method. But the consequence of the decoupling of energy and scattering angle is, one has to use neutron pulses with a short burst time (< 20 μs) and has to wait until all neutrons in one pulse arrive at the detector before

starting the next pulse. This is illustrated in **Figure C-3-3**.

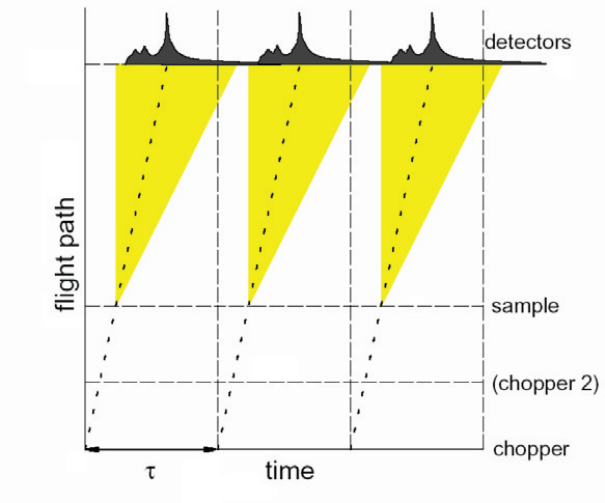

Figure C-3-3 Path-time diagram of TOF method. [Picture taken from Michael Monkenbusch, *time-of-flight spectrometers*, presentation]

After passing through the choppers and the monitor, the neutrons arrive at the sample and about 10% of them are scattered. The scattered neutrons enter the flight chamber and travel to the detectors. The flight chamber is filled with argon to avoid unwanted scattering by air molecules. The ^{3}He detectors of TOFTOF are installed on eight racks, as shown in **Figure C-3-1**. The flight path between the sample and the detector is 4 m. The scattering angle 2θ ranges from 7.5 to 140°. The detectors are well shielded from each other and from the environmental neutrons. The numbers of neutrons detected by the detectors are saved in time-of-flight bins in the raw data files.

The energy resolution of TOFTOF can be changed continuously in a wide range from 5 μeV to 5 meV by variation of the chopper rotation frequency, according to the specific needs of the experiments. The energy resolution of TOFTOF can be well calculated in the form of the instrumental line width ΔE (FWHM) [208]. **Figure C-3-4** shows the ΔE of the elastic line as a function of the incident neutron wavelength λ_i, at several chopper frequencies.

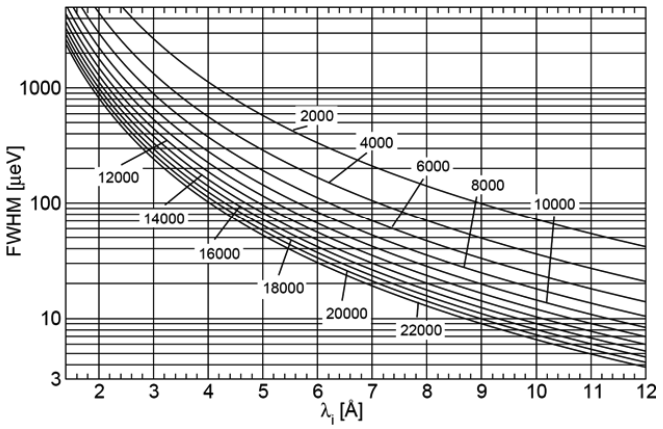

Figure C-3-4 Energy resolution of TOFTOF spectrometer at several chopper frequencies (in rpm). [Picture taken from T. Unruh, J. Neuhaus and W. Petry, *Nuclear Instruments and Methods in Physics Research* A **580** (2007) 1414]

As shown in **Figure C-3-5**, the accessible dynamic range of TOFTOF changes with the incident wavelength also, which should be considered prior to the measurements. An appropriate chopper frequency could be decided after estimating the energy resolution and the dynamic range needed for the experiments.

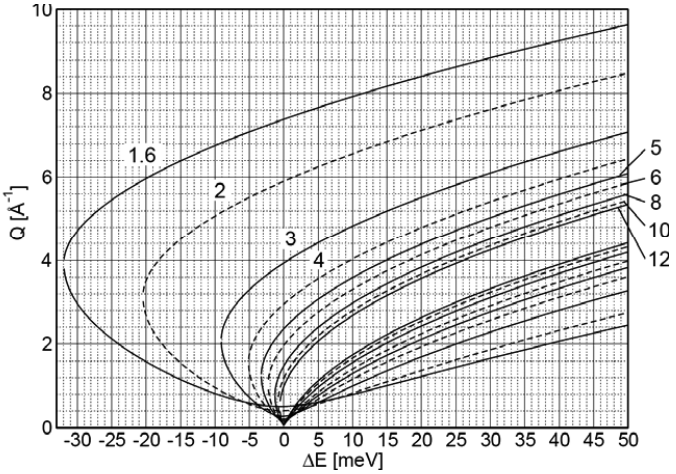

Figure C-3-5 Accessible dynamic range of the TOFTOF spectrometer for various incident neutron wavelengths in Å. [Picture taken from T. Unruh, J. Neuhaus and W. Petry, *Nuclear Instruments and Methods in Physics Research* A **580** (2007) 1414]

The TOFTOF spectrometer offers a continuous wide spectrum of incident neutrons with relatively high intensity of 10^{10} n/(cm^{2}s) at the sample position. The accessible dynamic range and the energy resolution of TOFTOF can be changed conveniently by varying the chopper frequencies from 1000 to 22,000 rpm. The extremely low background ensures a good signal to background ratio of TOFTOF. Therefore the TOFTOF spectrometer is a good choice for a wide range of investigations ranging from phonon density of states to low energetic magnetic excitations and from molecular diffusion and reorientations to internal vibrations of proteins [12].

4. Structure Powder Diffractometer (SPODI) [185, 223, 224]

The structure powder diffractometer SPODI at FRM II is dedicated for the crystallographic/magnetic structure determination with high *Q*-resolution using thermal neutrons. A picture and a schematic drawing of SPODI are shown in **Figure C-4-1 (a)** and **(b)**. Several monochromator take-off angles between 90° and 155° can be employed. Different wavelengths can be achieved at a standard monochromator take-off angle of 155°, including λ = 1.549 Å (Ge(551), as used in Chapter 5), 2.537 Å (Ge(331)), and 1.111 Å (Ge(771)).

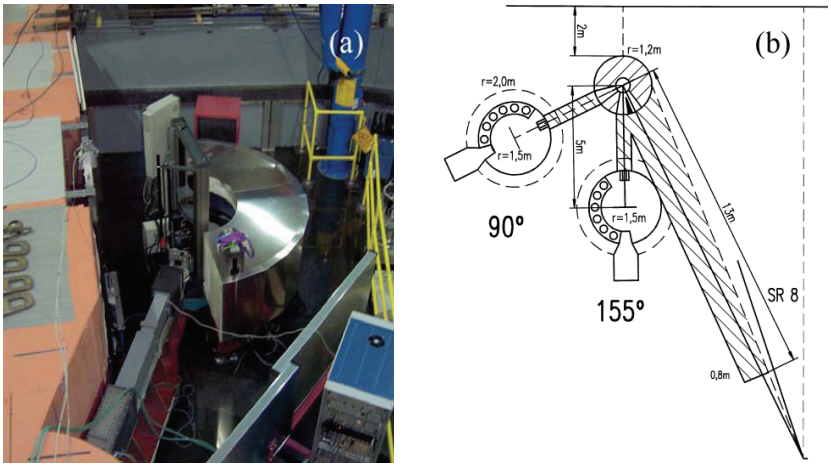

Figure C-4-1 Picture **(a)** and schematic drawing **(b)** of SPODI. [Picture taken from R. Gilles et al., *Physica* B **276-278** (2000) 87]

The detector system consists of 80 collimators and 80 ^{3}He detector tubes, covering a scattering angle of 160°. The detectors are position sensitive in vertical direction, allowing a large portion of Debye-Scherrer cone to be measured in two dimensions. The reference measurements on standard samples are taken to make efficiency correction and scattering angle correction for the collimator/detector pairs. The neutron counts as a function of detector height and scattering angle for each detector are included in the detector calibration. The measured two-dimensional data are integrated along the Debye-Scherrer rings to achieve the high-resolution diffraction patterns. The signal to noise ratio is improved by evacuating the beam path and well shielding from the environmental neutrons.

SPODI provides versatile sample environment devices, including the cold head cryostat (3.5-300 K), the "displex" cryostat (5-300 K), the high-temperature vacuum furnace (300-2100 K), high-pressure cell (up to 10 Gpa), and vertical magnet (7.5 Tesla). SPODI has become one of the top-ranking powder diffractometers in the world owning to its excellent performances.

5. Magnetic Property Measurement System (MPMS) [225]

The Quantum Design MPMS sample magnetometer utilizes Superconducting Quantum Interference Device (SQUID) technology, combined with patented enhancements. MPMS measures the DC magnetization and the AC susceptibility of the materials with superior measurement sensitivity at large temperature and magnetic field ranges. The static magnetic property characterizations presented in this thesis have been performed on MPMS.

The modular MPMS design consists of a SQUID detection system, a precision temperature control unit, a sophisticated computer operating system, and a high-field superconducting magnet. A picture of MPMS is shown in **Figure C-5-1**. The temperature range is $1.9 < T < 400$ K (the highest temperature is 800 K if an oven is installed). The magnetic field range is $-7.0 < H < +7.0$ Tesla. The controlling software, MPMS MultiVu, provides full automation and an easy, friendly user interface.

Figure C-5-1 Picture of Quantum Design MPMS.

The SQUID sensing loops of the SQUID detection system are configured as a highly balanced second-derivative coil set. The main idea of SQUID magnetometer is to separate two superconductors by thin insulating layers to form two parallel Josephson Junctions [226]. A schematic view of SQUID is shown in **Figure C-5-2**. If a constant biasing current is maintained in SQUID, the measured voltage is a periodic function of the change of the magnetic flux in the sensing loop. The period of the voltage variation corresponds to one flux quantum,

$$\Phi_0 = \frac{2\pi\hbar}{2e} = 2.0678\times10^{-15} \quad \text{tesla}\cdot\text{m}^2, \tag{C.5.1}$$

where $\hbar$ is the reduced Plank constant and e is the elementary charge. The magnetic flux change in the sensing loop is then characterized by the counts of oscillations, which could be measured with great accuracy. Therefore SQUID becomes a standard method to detect incredibly small magnetic fields. The sample magnetic moment can be determined down to the order of 10^{-8} emu.

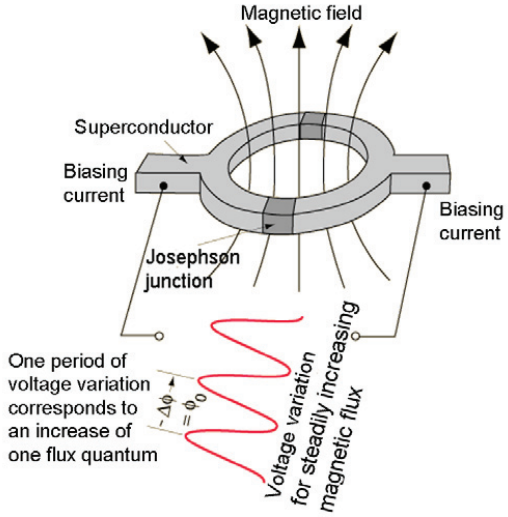

Figure C-5-2 Schematic view of SQUID. [Picture taken from an online introduction to SQUID at http://hyperphysics.phy-astr.gsu.edu/hbase/solids/squid.html#c3]

In this thesis, the samples for MPMS measurements are sealed in a gelatin capsule. A certain amount of cotton is put in the capsule to press the sample and avoid the shake of the sample. The capsule is then put in a drinking straw (lightweight homogeneous plastic tube). After adjusting the position of the capsule for an easier sample centering, the drinking straw is sealed with two spacers and connected to the sample rod. A mounted sample ready for measurements is shown in **Figure C-5-3**.

Figure C-5-3 Mounted sample ready for SQUID measurements.

Before all the measurements, the Ultra Low Field (ULF) option is used to provide fully automated remanent field profiling and nulling. The ULF option is necessary for performing precise zero-field-cooled measurements. The background signal from the drinking straw and the capsule with cotton should be measured. The sample signal is obtained by subtracting the background from the raw data.

6. Physical Property Measurement System (PPMS) [227]

The Quantum Design PPMS is designed to measure a variety of physical properties of materials, such as heat capacity, magnetometry, electro- and thermal-transport properties. **Figure C-6-1** shows a picture of PPMS. The two options, heat capacity and AC magnetometry system (ACMS), of PPMS used in this thesis will be discussed in this section.

Figure C-6-1 Picture of Quantum Design PPMS, which is running heat capacity measurement equipped with a dilution insert.

6.1 Heat capacity on Quantum Design PPMS

The heat capacity measurement system on PPMS performs fully automated relaxation heat capacity measurements. The heat capacity is measured under a high vacuum. The data analysis is done by means of a two-tau model, where accurate simulations are performed to the heat flow between the micro-calorimeter platform and the sample (tau2) and the heat flow between the platform and puck stage (tau1).

The heat capacity can be measured as a function of temperature and magnetic field. Using the standard ^{3}He cryostat, the temperature range of heat capacity is 1.9 – 400 K. In order to reach temperatures below 1.9 K, a ^{3}He-^{4}He dilution insert option is available, which allows the heat capacity to be measured from 50 mK to 4 K. The maximum field available is 9 Tesla. The resolution is 10 nJ/K at 2 K.

The mass of the samples for heat capacity measurements in this thesis is $1 < m < 5$ mg. The samples have a flat-plate shape with a smooth surface. The sample is mounted on the micro-calorimeter platform using a sample-mounting station, which is connected to a vacuum pump in order to prevent any damage to the puck. Apiezon N grease is used to increase the thermal conductivity between the micro-calorimeter platform and the sample. The background heat capacity of the micro-calorimeter and the Apiezon N grease is measured in an addendum run prior to the sample measurements and subtracted from the raw data of the sample measurements to acquire the absolute heat capacity of the sample. A picture of the sample mounting-station and the puck with the sample mounted is shown in **Figure C-6-2**.

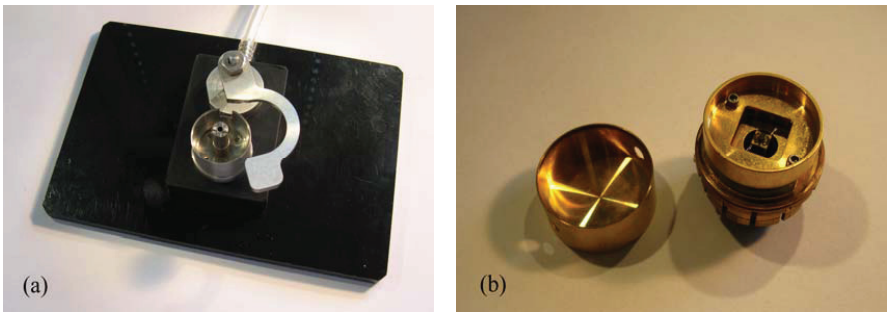

Figure C-6-2 (a) Sample-mounting station and **(b)** heat capacity puck with sample mounted and the radiation-shielding cap.

At the bottom of the sample chamber, there is a 12-pin connector wired to the system electronics. This connector allows convenient access to flexible applications of PPMS. The puck with sample is inserted into the sample chamber using an inserting tool and plugged to this connector. **Figure C-6-3** shows a schematic view of plugging the puck into the connector at the bottom of the sample chamber. As to the control of measurements, the PPMS MultiVu provides powerful software support, which automatically acquires, analyzes, and displays data.

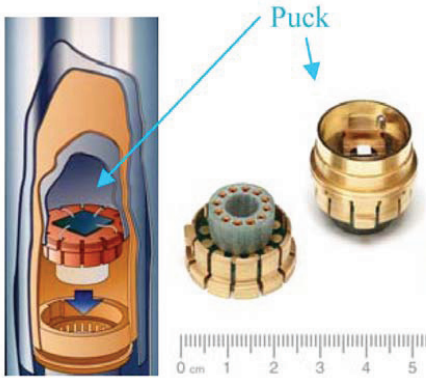

Figure C-6-3 Schematic view of plugging the puck into the connector at the bottom of the sample chamber of PPMS. [Picture taken from the user manual of PPMS, Quantum Design, Inc., USA]

6.2 ACMS on Quantum Design PPMS

The AC susceptibility of materials can be measured in conjunction with the automated temperature and field control capability of PPMS. The temperature range of ACMS is 1.9 < T < 350 K. The frequency and field amplitude ranges are 10 Hz < f < 10 kHz and 2 mOe < h < 15 Oe, respectively. The sensitivity of ACMS is 2×10^{-8} emu at 10 kHz. The phase-locked technology is used to measure AC susceptibility in ACMS option. ACMS improves the signal-to-noise ratio by using high-speed digital filter.

The sample used for ACMS in this thesis is in powder form. The sample is mounted in a drinking straw following the same way as described in **Appendix C. 5**. The AC susceptibility measurements can be carried out conveniently using the PPMS MultiVu software.

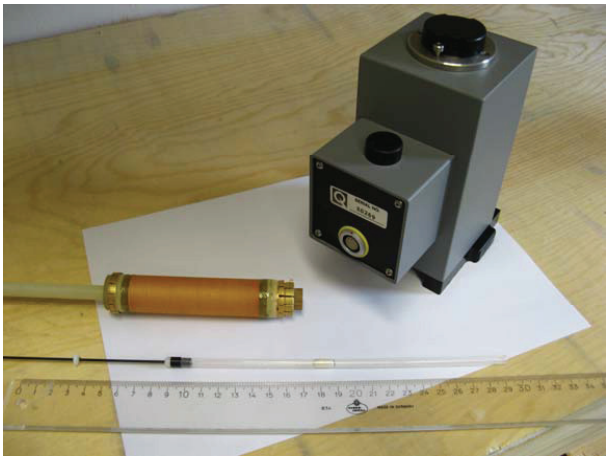

Figure C-6-4 Pictured are the servo-motor, coil set, sample rod, and the drinking straw with the capsule containing sample, for ACMS measurements on PPMS.

Bibliography

[1] O. Kahn, *Molecular Magnetism* (VCH Publishers Inc., New York, 1993).

[2] D. Gatteschi, R. Sessoli and J. Villain, *Molecular Nanomagnets* (Oxford University Press, Oxford, 2006).

[3] J. Mroziński, *Coordination Chemistry Reviews* **249** (2005) 2534.

[4] W. Linert and M. Verdaguer, *Molecular Magnets*, Special Edition of Monatshefte für Chemie/Chemical Monthly (Springer-Verlag, Wien, 2003), Vol. 134, No. 2.

[5] S. J. Blundell and F. L. Pratt, *J. Phys.: Condens. Matter* **16** (2004) R771.

[6] M. Tamura et al., *Chem. Phys. Lett.* **186** (1991) 401.

[7] A. Caneschi et al., *J. Am. Chem. Soc.* **113** (1991) 5873.

[8] R. Sessoli et al., *Nature* **365** (1993) 141.

[9] T. Lis, *Acta Crystallogr. Sect.* B **36** (1980) 2042.

[10] R. Sessoli and D. Gatteschi, *Angew. Chem. Int. Ed.* **42** (2003) 268.

[11] Y. Pontillon et al., *J. Am. Chem. Soc.* **121** (1999) 5342.

[12] C. Sangregorio et al., *Phys. Rev. Lett.* **78** (1997) 4645.

[13] G. Aromi et al., *Polyhedron* **17** (1998) 3005.

[14] W. Wernsdorfer et al., *Nature* **416** (2002) 406.

[15] J. R. Friedman et al., *Phys. Rev. Lett.* **76** (1996) 3830.

[16] L. Thomas et al., *Nature* **383** (1996) 145.

[17] W. Wernsdorfer and R. Sessoli, *Science* **284** (1999) 133.

[18] C. Schlegel et al., *Phys. Rev. Lett.* **101** (2008) 147203.

[19] M. Cavallini et al., *Phys. Chem. Chem. Phys.* **10** (2008) 784.

[20] L. Krusin-Elbaum et al., *Nature* **410** (2001) 444.

[21] A. R. Rocha et al., *Nat. Mater.* **4** (2005) 335.

[22] E. M. Chudnovsky and J. Tejada, *Macroscopic Quantum Tunneling of the Magnetic Moment* (Cambridge University Press, Cambridge, 1998).

[23] P. Kögerler, B. Tsukerblat and A. Müller, *Dalton Trans.* **39** (2010) 21.

[24] A. Müller et al., *Chem. Rev.* **98** (1998) 239.

[25] A. Müller and S. Roy, *Coord. Chem. Rev.* **245** (2003) 153.

[26] J. Villain et al., *Euro. Phys. Lett.* **27** (1994) 159.

[27] R. Sessoli, *Europhys. News* **34** (2003) 41.

[28] J. Stolze and D. Suter, *Quantum Computing* (Wiley-VCH, Weinheim, 2004).

[29] W. Wernsdorfer et al., *Phys. Rev.* B **72** (2005) 060409.

[30] E. Del barco et al., *Phys. Rev. Lett.* **93** (2004) 157202.

[31] S. Hill et al., *Science* **302** (2003) 1015.

[32] S. Bertaina et al., *Nature* (London) **453** (2008) 203.

[33] H. P. Andres, S. Decurtins and H. U. Güdel, *Neutron scattering of molecular magnets* in "*Frontiers of Neutron Scattering*", A. Furrer (ed.), (World Scientific, Singapore, 2000).

[34] R. Pellaux et al., *Inorg. Chem*. **36** (1997) 2301.

[35] G. Antorrena et al., *J. Magn. Magn. Mater.* **196** (1999) 581.

[36] I. Mirebeau et al., *Phys. Rev. Lett.* **83** (1999) 628.

[37] A. P. Ramirez, *Annual Review of Materials Science* **24** (1994) 453.

[38] H. T. Diep and H. Giacomini, *Frustration – Exactly Solved Frustrated Models* in "*Frustrated Spin Systems*", H. T. Diep (ed.), (World Scientific, Singapore, 2004).

[39] G. Toulouse, *Commun. Phys.* **2** (1977) 115.

[40] T. A. Kaplan, *Physical Review* **116** (1959) 888.

[41] J. Villain, *Journal of Physics* C: *Solid State Physics* **10** (1977) 4793.

[42] I. A. Mydosh, *Spin Glasses*: *An Experimental Introduction* (Taylor & Francis, London, 1993).

[43] G. H. Wannier, *Phys. Rev.* **79** (1950) 357.

[44] K. Kano and S. Naya, *Progress of Theoretical Physics* **10** (1953) 158.

[45] I. Syozi, *Progress of Theoretical Physics* **6** (1951) 306.

[46] C. Broholm et al., *Phys. Rev. Lett.* **65** (1990) 3173.

[47] W. Schweika, M. Valldor and P. Lemmens, *Phys. Rev. Lett.* **98** (2007) 067201.

[48] R. Moessner and A. P. Ramirez, *Physics Today* **59** (2006) 24.

[49] O. Kahn, *Chemical Physics Letters* **265** (1997) 109.

[50] M. Luban, *J. Magn. Magn. Mater.* **272-276** (2004) e635.

[51] A. J. Blake et al., *J. Chem. Soc. –Dalton Trans.* **4** (1997) 485.

[52] A. Honecker and M. E. Zhitomirsky, *J. Phys. Conf. ser.* **145** (2009) 012082.

[53] R. Schmidt, J. Richter and J. Schnack, *J. Magn. Magn. Mater.* **295** (2005) 164.

[54] A. Müller et al., *Angew. Chem. Int. Ed. Engl.* **38** (1999) 3238.

[55] A. Müller et al., *Chem. Phys. Chem.* **2** (2001) 517.

[56] J. Schnack, *Dalton Trans*., **39** (2010) 4677.

[57] J. Schnack and R. Schnalle, *Polyhedron* **28** (2009) 1620.

[58] C. L. Henley, *Phys. Rev. Lett.* **62** (1989) 2056.

[59] E. Berg, E. Altman and A. Auerbach, *Phys. Rev. Lett.* **90** (2003) 147204.

[60] I. Rousochatzakis, A. M. Läuchli and F. Mila, *Phys. Rev.* B **77** (2008) 094420.

[61] C. Schröder et al., *Phys. Rev. Lett.* **94** (2005) 017205.

[62] J. Schnack et al., *Eur. Phys. J.* B **24** (2001) 475.

[63] P. Böni and A. Furrer, *Introduction to Neutron Scattering* in "*Frontiers of Neutron Scattering*", A. Furrer (ed.), (World Scientific, Singapore, 2000).

[64] Th. Brückel, *A Neutron Primer: Elastic Scattering and the Properties of the Neutron* in "*Neutron Scattering: Lectures of the JCNS Laboratory Course*", Th. Brückel et al. (eds.), (Forschungszentrum Jülich GmbH, Jülich 2008).

[65] C. G. Shull, *Reviews of Modern Physics* **67** (1995) 753.

[66] G. Shirane, *Reviews of Modern Physics* **46** (1974) 437.

[67] A. Ioffe, *Neutron Sourses* in "*Neutron Scattering: Lectures of the JCNS Laboratory Course*", Th. Brückel et al. (eds.), (Forschungszentrum Jülich GmbH, Jülich 2008).

[68] D. Richter, *Scattering Techniques: Neutron Diffraction* in "*Magnetism Goes Nano: Lectures of the 36th Spring School of the Institute of Solid State Research*", S. Blügel, Th. Brückel, C. M. Schneider (eds.), (Forschungszentrum Jülich GmbH, Jülich 2005).

[69] O. Halpern and M. R. Johnson, *Phys. Rev.* **55** (1939) 898.

[70] S. V. Maleyev, *Zh. Eksperim. I Teor. Fiz.* **33** (1958) 129; S. V. Maleyev, *Zh. Eksperim. I Teor. Fiz.* **40** (1961) 1224.

[71] M. Blume, *Phys. Rev.* **130** (1963) 1670; *Phys. Rev.* **133** (1964) A1366.

[72] R. M. Moon, T. Riste and W. C. Koehler, *Phys. Rev.* **181** (1969) 920.

[73] O. Schärpf and H. Capellmann, *Phys. Stat. Sol.* (a) **135** (1993) 359.

[74] Th. Brückel, PhD Thesis, *Magnetische Fehlordnung in Dem Mischgranatsystem* $(Fe_xCr_{1-x})_2Ca_3(GeO_4)_3$, Eberhard-Karls-Universität zu Tübingen, 1988.

[75] W. Schweika, *Polarized Neutron Scattering and Polarization Analysis* in "*Neutron Scattering: Lectures of the JCNS Laboratory Course*", Th. Brückel et al. (eds.), (Forschungszentrum Jülich GmbH, Jülich 2010).

[76] T. Chatterji, *Neutron Scattering from Magnetic Materials* T. Chatterji (ed.) (Amsterdam: Elsevier, 2006).

[77] C. Schäffer et al., *Angew. Chem., Int. Ed.* **48** (2009) 149.

[78] C. Schröder et al., *Phys. Rev.* B **77** (2008) 224409.

[79] J. Schnack, M. Luban and R. Modler, *Europhys. Lett.* **56** (2001) 863.

[80] M. Axenovich and M. Luban, *Phys. Rev.* B **63** (2001) 100407.

[81] V. O. Garlea et al, *Phys. Rev.* B **73** (2006) 024414.

[82] J. Lago et al., *Phys. Rev.* B **76** (2007) 064432.

[83] W. L. Jolly, *The synthesis and Characterization of Inorganic Compounds* (Prentice Hall, Englewood Cliffs,1970).

[84] C. Kittel, *Introduction to Solid State Physics*, 7th edition (Wiley and Sons inc., USA, 1996).

[85] Y. Kraftmakher, *Phys. Rep.* **356** (2002) 1.

[86] J. S. Hwang, K. J. Lin and C. Tien, *Rev. Sci. Instrum.* **68** (1997) 94.

[87] A. Tari, *The specific heat of matter at low temperatures* (Imperial College Press, 2003).

[88] T. H. K. Barron and J. A. Morrison, *Canad. J. Phys.* **35** (1957) 799.

[89] M. Affronte, J. C. Lasjaunias and A. Cornia, *Eur. Phys. J.* B **15** (2000) 633.

[90] Z. Zhou et al., *Appl. Phys. Lett.* **89** (2006) 031924.

[91] S. Burgess and I. W. Shepherd, *Chem. Phys. Lett.* **50** (1977) 112.

[92] M. Foret et al., *Phys. Rev. Lett.* **77** (1996) 31.

[93] T. E. Mason et al., *Physica* (Amsterdam) **385-386B** (2006) 955.

[94] E. Mamontov et al., *Neutron News* **19** (2008) 22.

[95] W. Schweika and P. Böni, *Physica* B **297** (2001) 155.

[96] M. C. Bellissent-Funel, J. Teixeira and L. Bosio, *J. Chem. Phys.* **87** (1987) 2231.

[97] P. J. Brown, *Magnetic form factors* in "*International Tables for Crystallography*", A. J. C. Wilson (ed.), (Dordrecht: Kluwer Academic, 1995), Vol. C, pp. 391.

[98] G. L. Squires, *Introduction to the Theory of Thermal Neutron Scattering* (Cambridge University Press, Cambridge, 1978).

[99] I. A. Blech and B. L. Averbach, *Physics* **1** (1964) 31.

[100] M. Hasegawa and H. Shiba, *J. Phys. Soc. Japan* **73** (2004) 2543.

[101] S. Hill et al., *Phys. Rev. Lett.* **90** (2003) 217204.

[102] D. Gatteschi et al., *Science* **265** (1994) 1054.

[103] A. Müller and J. Döring, *Angew. Chem., Int. Ed. Engl.* **27** (1988) 1721.

[104] I. Chiorescu et al., *Phys. Rev. Lett.* **84** (2000) 3454.

[105] H. D. De Raedt et al., *Phys. Rev.* B **70** (2004) 064401.

[106] G. Chaboussant et al., *Europhys. Lett.* **66** (2004) 423.

[107] A. Tarantul, B. Tsukerblat and A. Müller, *Inorg. Chem.* **46** (2007) 161.

[108] B. Tsukerblat, A. Tarantul and A. Müller, *J. Chem. Phys.* **125** (2006) 054714.

[109] V. V. Dobrovitski, M. I. Katsnelson and B. N. Harmon, *Phys. Rev. Lett.* **84** (2000) 3548.

[110] A.–L. Barra et al., *J. Am. Chem. Soc.* **114** (1992) 8509.

[111] I. Chiorescu et al., *J. Magn. Magn. Mater.* **221** (2000) 103.

[112] G. Chaboussant et al., *Europhys. Lett.* **59** (2002) 291.

[113] N. P. Konstantinids and D. Coffey, *Phys. Rev.* B **66** (2000) 174426.

[114] D. Gatteschi et al., *Mol. Eng.* **3** (1993) 157.

[115] T. Sakon et al., *Phys.* B **346-347** (2004) 206.

[116] D. Gatteschi et al., *Coord. Chem. Rev.* **250** (2006) 1514.

[117] G. Chaboussant et al., *Phys. Stat. Sol. (c)* **1** (2004) 3399.

[118] V. V Platonov et al., *Physics of the Solid state* **44** (2002) 2104.

[119] B. Tsukerblat, A. Tarantul and A. Müller, *Phys. Lett.* A **353** (2006) 48.

[120] P. W. Anderson, *Mater. Res. Bull.* **8** (1973) 153.

[121] A. P. Ramirez, *Nature* **421** (2003) 483.

[122] A. Yoshimori, *J. Phys. Soc. Jpn.* **14** (1959) 807.

[123] J. Villain, *Phys. Chem. Solids* **11** (1959) 303.

[124] J. Villain, *J. Phys.* C **10** (1977) 1717.

[125] K. H. Fischer and J. A. Hertz, *Spin Glasses* (Cambridge: Cambridge University Press, 1991).

[126] J. R. Wedagedera, *Exact Solution for Some Mean Field Spin Glass Models* (VDM Verlag, Dr. Müller, 2010).

[127] D. Chowdhury, *Spin Glasses and Other Frustrated Systems* (World Scientific, Singapore, 1986).

[128] R. Böhmer, *Current Option in Solid State & Materials Science* **3** (1998) 278.

[129] M. D. Ediger, *Annu. Rep. Phys. Chem.* **51** (2000) 99.

[130] C. A. M. Mulder, A. J. Van Duyneveldt and J. A. Mydosh, *Phys. Rev.* B **23** (1981) 1384.

[131] V. Cannella and J. A. Mydosh, *Phys. Rev.* B **6** (1972) 4220.

[132] B. D. Gaulin et al., *Phys. Rev. Lett.* **69** (1992) 3244.

[133] J. N. Reimers et al., *Phys. Rev.* B **43** (1991) 3387.

[134] J. E. Greedan et al., *Phys. Rev.* B **43** (1991) 5682.

[135] M. J. P. Gingras et al., *Phys. Rev. Lett.* **78** (1997) 947.

[136] N. P. Raju, E. Gmelin, and R. K. Kremer, *Phys. Rev.* B **46** (1992) 5405.

[137] J. S. Gardner, M. J. P. Gingras and J. E. Greedan, *Rev. Mod. Phys.* **82** (2010) 53.

[138] P. W. Anderson, *Phys. Rev.* **102** (1956) 1008.

[139] J. Villian, *Z. Phys.* B **33** (1978) 31.

[140] J. S. Gardner et al., *Phys. Rev. Lett.* **83** (1999) 211.

[141] B. Canals and C. Lacroix, *Phys. Rev. Lett.* **80** (1998) 2933.

[142] J. S. Gardner et al., *Phys. Rev. Lett.* **82** (1999) 1012.

[143] Y. Machida et al., *Phys. Rev. Lett.* **98** (2007) 057203.

[144] A. P. Ramirez et al. *Nature* (London) **399** (1999) 333.

[145] S. T. Bramwell and M. J. P. Gingras, *Science* **294** (2001) 1495.

[146] C. Castelnovo, R. Moessner and S. L. Sondhi, *Nature* **451** (2008) 42.

[147] D. J. P. Morris et al., *Science* **326** (2009) 411.

[148] T. Fennell et al., *Science* **326** (2009) 415.

[149] L. D. C. Jaubert and P. C. W. Holdsworth, *Nature Physics* **5** (2009) 258.

[150] K. Binder and A. P. Young, *Rev. Mod. Phys.* **58** (1986) 801.

[151] M. J. P. Gingras et al., *J. Appl. Phys.* **79** (1996) 6170.

[152] E. F. Shender et al., *Phys. Rev. Lett.* **70** (1993) 3812.

[153] J. R. L. de Almeida, *J. Phys.*: *Condens. Matter* **11** (1999) L223.

[154] S. Sachdev, *Phys. Rev.* B **45** (1992) 12377.

[155] Th. Brückel et al., *Z. Phys.* B – *Cond. Mat.* **97** (1995) 391.

[156] Th. Brückel et al., *Phys. Lett.* A **162** (1992) 357.

[157] J. E. Greedan et al., *Solid State Commun.* **59** (1986) 895.

[158] J. N. Reimers, J. E. Greedan and M. Sato, *J. Solid State Chem.* **72** (1988) 390.

[159] C. H. Booth et al., *Phys. Rev.* B **62** (2000) R755.

[160] A. Keren and J. S. Gardner, *Phys. Rev. Lett.* **87** (2001) 177201.

[161] J. E. Greedan et al., *Phys. Rev.* B **79** (2009) 014427.

[162] R. A. Young, *The Rietveld Method* (Oxford University Press, United States, 1993).

[163] B. M. Bartlett, *J. Am. Chem. Soc.* **127** (2005) 8985.

[164] D. Mehandjiev and E. Nikolova, *Thermochimica Acta* **23** (1978) 117.

[165] M. Kurmoo, *Philos. Trans. R. Soc. London* Ser. A **357** (1999) 3041.

[166] J. De Almeida and D. Thouless, *J. Phys.* A **11** (1978) 983.

[167] D. N. H. Nam et al., *Phys. Rev.* B **59** (1999) 4189.

[168] A. P. Young and H. G. Katzgraber, *Phys. Rev. Lett.* **93** (2004) 207203.

[169] E. A. Velásquez et al., arXiv:1011.3388v1 (unpublished).

[170] R. Mathieu et al., *Phys. Rev.* B **63** (2001) 094201.

[171] K. Jonason et al., *Phys. Rev. Lett.* **81** (1998) 3243.

[172] P. E. Jönsson et al., *Phys. Rev.* B **70** (2004) 174402.

[173] T. Jonsson et al., *Phys. Rev.* B **59** (1998) 8770.

[174] S. Bedanta and W. Kleemann, *J. Phys.* D*: Appl. Phys.* **42** (2009) 013001.

[175] P. C. Hohenberg and B. I. Halpcrin, Rev. Mod. Phys. **49** (1977) 435.

[176] K. S. Cole and R. H. Cole, *J. Chem. Phys.* **9** (1941) 341.

[177] A. K. Jonscher, *Dielectric Relaxation in Solids* (Chelsea Dielectrics Press, London, 1983).

[178] O. Petracic et al., *Phase Transitions* **76** (2003) 367.

[179] C. Dekker et al., *Phys. Rev.* B **40** (1989) 11243.

[180] K. Ravindran et al., *Phys. Rev.* B **40** (1989) 9431.

[181] M. Hagiwara, *J. Magn. Magn. Mater.* **177-181** (1998) 89.

[182] R. G. Scurlock and W. N. R. Stevens, *Proc. Phys. Soc.* **86** (1965) 331.

[183] M. W. Klein and R. Brout, *Phys. Rev.* **132** (1963) 2412.

[184] M. W. Klein, *Phys. Rev.* **136** (1964) A1156.

[185] M. Hoelzel et al., *Neutron News* 18 (2007) 23.

[186] D. C. Wallace, *Thermodynamics of Crystals* (Dover, New York, 1998).

[187] A.-J. Dianoux and G. Lander (eds.), *Neutron Data Booklet* (Institut Laue-Langevin, 2003).

[188] G. Ferey et al., *Rev. Chim. Miner.* **23** (1986) 474.

[189] H. Shinaoka, T. Miyake and S. Ishibashi, *arXiv*: 1111.6347.

[190] K. Tomiyasu et al., *arXiv*: 1110.6605.

[191] X. Wan et al., *Phys. Rev.* B **83** (2011) 205101.

[192] J. Villain et al., *J. Phys.* (Paris) **41** (1980) 1263.

[193] M. J. Harris et al., *Phys. Rev. Lett.* **73** (1994) 189.

[194] N. P. Raju et al., *Phys. Rev.* B **59** (1999) 14489.

[195] M. Ito et al., *J. Phys. Soc. Jpn*. **69** (2000) 888.

[196] C. L. Henley, *J. Appl. Phys.* **61** (1987) 3962.

[197] G.-W. Chern, R. Moessner, and O. Tchernyshyov, *Phys. Rev.* B **78** (2008) 144418.

[198] J. N. Reimeirs, A. J. Berlinsky, and A.-C. Shi, *Phys. Rev.* B **43** (1991) 865.

[199] D. Tsuneishi, M. Ioki, and H. Kawamura, *J. Phys.: Condens. Matter* **19** (2007) 145273.

[200] A. P. Murani, *J. Phys.* (Paris) **39** (1978) C6-1517.

[201] A. P. Murani, *J. Appl. Phys.* **49** (1978) 1604.

[202] A. P. Murani, *Phys. Rev. Lett.* **41** (1978) 1406.

[203] A. P. Murani and A. Heidemann, *Phys. Rev. Lett.* **41** (1978) 1402.

[204] A. P. Murani and J. L. Tholence, *Solid State Commun.* **22** (1977) 25.

[205] K. Motoya et al., *Phys. Rev.* B **44** (1991) 183.

[206] H. Scheuer, M. Loewenhaupt and W. Just, *J. Mag. Mag. Mat.* **4** (1977) 77.

[207] H. Maletta et al., *J. Appl. Phys.* **52** (1981) 1735.

[208] T. Unruh, J. Neuhaus, and W. Petry, *Nucl. Instrum. Methods* A **580** (2007) 1414.

[209] A. Krimmel et al., *Phys. Rev.* B **79** (2009)134406.

[210] B. Fåk and B. Dorner, *Physica* B **234-236** (1997) 1107.

[211] G. Shirane, S. M. Shapiro, and J. M. Tranquada, *Neutron Scattering with a Triple-Axis Spectrometer* (Cambridge University Press, Cambridge, 2002).

[212] DNS website, http://www.jcns.info/jcns_dns.

[213] O. Schärpf, *The Spin of the Neutron as a Measuring Probe* (Institute Laue-Langevin, 1996).

[214] Th. Brückel et al., *Europhys. Lett.* **4** (1987) 1189.

[215] Th. Brückel et al., *Solid State Communications* **70** (1989) 53.

[216] BASIS website, http://www.sns.gov/instruments/SNS/BASIS/.

[217] B. Frick et al., *Z. Phys. Chem.* **224** (2010) 33.

[218] Neutron backscattering review, http://www.ill.eu/sites/BS-review/HOME.html

[219] K. W. Herwig, *The Silicon Backscattering Spectrometer at SNS*, presentation in "*Workshop on Cold Neutron Chopper Spectrometer*", Nist, 2001.

[220] K. W. Herwig, *Conceptual analysis for the backscattering spectrometer at the*

Spallation Neutron Source (Oak Ridge National Laboratory, 1999).

[221] TOFTOF website, http://www.frm2.tum.de/en/science/spectrometry/toftof.

[222] J. Voigt, *Magnetic and Lattice Excitations: Inelastic Neutron Scattering* in "*Neutron Scattering: Lectures of the JCNS Laboratory Course*", Th. Brückel et al. (eds.), (Forschungszentrum Jülich GmbH, Jülich 2010).

[223] SPODI website, http://www.frm2.tum.de/en/science/diffraction/spodi.

[224] R. Gilles et al., *Physica* B **276-278** (2000) 87.

[225] Quantum Design MPMS website, http://www.qdusa.com/products/mpms.

[226] SQUID on-line introduction, http://hyperphysics.phy-astr.gsu.edu/hbase/solids/squid.html#c3.

[227] Quantum Design PPMS website, http://www.qdusa.com/products/ppms.

Personal Bibliography

Journal Articles

[1] **Zhendong Fu**, Paul Kögerler, Ulrich Rücker, Yixi Su, Ranjan Mittal, and Thomas Brückel, "An approach to the magnetic ground state of the molecular magnet $\{Mo_{72}Fe_{30}\}$", ***New Journal of Physics*** **12**, 083044 (2010).

[2] **Zhendong Fu**, Yishen Cui, Siyuan Zhang, Jing Chen, Dapeng Yu, Lu Niu, Jianzhong Jiang, and Shu-Lin Zhang, "Study on the quantum confinement effect on ultraviolet photoluminescence of crystalline ZnO nano-particles with nearly uniform size", ***Applied Physics Letters*** **90**, 263113 (2007).

[3] Lianyi Chen, **Zhendong Fu**, et al., "New class of plastic bulk metallic glass", ***Physical Review Letters*** **100**, 075501 (2008).

[4] Lianyi Chen, **Zhendong Fu**, et al., "Ultrahigh strength binary Ni-Nb bulk glassy alloy composite with good ductility", ***Journal of Alloys and Compounds*** **443**, 105 (2007).

[5] Jing Chen and **Zhendong Fu**, "α-PbO_2-type nanophase of TiO_2 from coesite-bearing eclogite in Dabie Mountains, China - Comment", ***American Mineralogist*** **91**, 1699 (2006).

[6] Shulin Zhang, Yanbin Zhang, **Zhendong Fu**, et al., "Study of the size effect on the optical mode frequencies of ZnO nano-particles with nearly uniform size", ***Applied Physics Letters*** **89**, 243108 (2006), also selected by ***Virtual Journal of Nanoscale Science & Technology*** **14** (2006).

[7] Shulin Zhang, Yanbin Zhang, Wei Liu, **Zhendong Fu**, et al., "Lack of dependence of the Raman frequency of optical vibrational modes on excitation wavelength in polar nano semiconductors", ***Applied Physics Letters*** **89**, 063112 (2006).

[8] M. Y. Ge, J. F. Liu, H. P. Wu, C. W. Yao, Y. W. Zeng, **Zhendong Fu**, S. L. Zhang, and J. Z. Jiang, "Synthesis of Germanium Nanowires", ***J. Phys. Chem. C*** **111**, 11157 (2007).

[9] **Zhendong Fu**, Subhankar Bedanta, Yanzhen Zheng, Anatoliy Senyshyn, Yinguo Xiao, Yixi Su, Wouter Borghols, Paul Kögerler, Ulrich Rücker, and Thomas Brückel, "Spin-glass-like magnetic behavior in the geometrically frustrated compound $Na_3Co(CO_3)_2Cl$", to be submitted.

[10] **Zhendong Fu**, Paul Kögerler, Ulrich Rücker, and Thomas Brückel, "Magnetic excitations of molecular magnet $\{As_6V_{15}\}$: a heat capacity study", to be submitted.

[11] **Zhendong Fu**, Yanzhen Zheng, Giovanna Giulia Simeoni, Paul Kögerler, Ulrich Rücker, and Thomas Brückel, "Magnetic excitations of spin-frustrated pyrochlore antiferromagnet $Na_3Co(CO_3)_2Cl$", to be submitted.

Conference Talks

[1] **Zhendong Fu** (presenter), Paul Kögerler, Ulrich Rücker, Yixi Su, Ranjan Mittal, and Thomas Brückel, "Magnetic excitations and spin correlations in the spherical Keplerate molecular magnet $\{Mo_{72}Fe_{30}\}$", *Deutsche Physikalische Gesellschaft (DPG) 2009 Spring Meeting*, Dresden, March 2009.

[2] **Zhendong Fu** (presenter), Paul Kögerler, Ulrich Rücker, Yixi Su, Ranjan Mittal, and Thomas Brückel, "The magnetic ground state of the molecular magnet $\{Mo_{72}Fe_{30}\}$ studied by polarized neutron scattering", *International Conference on Polarized Neutrons and Synchrotron X-rays for Magnetism (PNSXM)*, Bonn, August 2009.

Poster Presentations

[1] **Zhendong Fu**, Paul Kögerler, Ulrich Rücker, Yixi Su, Ranjan Mittal, and Thomas Brückel, "Magnetic ground state of the frustrated molecular magnet $\{Mo_{72}Fe_{30}\}$", *International Conference on Magnetism (ICM)* 2009, Karlsruhe, July 2009.

[2] **Zhendong Fu**, Paul Kögerler, Ulrich Rücker, Yixi Su, Ranjan Mittal, and Thomas Brückel, "Magnetic ground state of the frustrated molecular magnet $\{Mo_{72}Fe_{30}\}$", *German Conference for Research with Synchrotron Radiation, Neutrons and Ion Beams at Large Facilities (SNI)* 2010, Berlin, February 2010.

1. **Soft Matter**
   From Synthetic to Biological Materials
   Lecture manuscripts of the 39th IFF Spring School March 3 – 14, 2008
   Jülich, Germany
   edited by J.K.G. Dhont, G. Gompper, G. Nägele, D. Richter, R.G. Winkler (2008),
   c. 1000 pages
   ISBN: 978-3-89336-517-3

2. **Structural analysis of diblock copolymer nanotemplates using grazing incidence scattering**
   by D. Korolkov (2008), III, 167 pages
   ISBN: 978-3-89336-522-7

3. **Thermal Nonequilibrium**
   Thermal forces in fluid mixtures
   Lecture Notes of the 8th International Meeting on Thermodiffusion,
   9 – 13 June 2008, Bonn, Germany
   edited by S. Wiegand, W. Köhler (2008), 300 pages
   ISBN: 978-3-89336-523-4

4. **Synthesis of CMR manganites and ordering phenomena in complex transition metal oxides**
   by H. Li (2008), IV, 176 pages
   ISBN: 978-3-89336-527-2

5. **Neutron Scattering**
   Lectures of the JCNS Laboratory Course held at the Forschungszentrum Jülich and the research reactor FRM II of TU Munich
   edited by R. Zorn, Th. Brückel, D. Richter (2008), ca. 500 pages
   ISBN: 978-3-89336-532-6

6. **Ultrafast Magnetization Dynamics**
   by S. Woodford (2008), 130 pages
   ISBN: 978-3-89336-536-4

7. **Role of Surface Roughness inTribology: from Atomic to Macroscopic Scale**
   by C. Yang (2008), VII, 166 pages
   ISBN: 978-3-89336-537-1

8. **Strahl- und Spindynamik von Hadronenstrahlen in Mittelenergie-Ringbeschleunigern**
   von A. Lehrach (2008), II, 171 Seiten
   ISBN: 978-3-89336-548-7

9. **Phase Behaviour of Proteins and Colloid-Polymer Mixtures**
   by C. Gögelein (2008), II, 147 pages
   ISBN: 978-3-89336-555-5

10. **Spintronics – From GMR to Quantum Information**
    Lecture Notes of the 40th IFF Spring School March 9 – 20, 2009
    Jülich, Germany
    edited by St. Blügel, D. Bürgler, M. Morgenstern, C. M. Schneider,
    R. Waser (2009), c. 1000 pages
    ISBN: 978-3-89336-559-3

11. **ANKE / PAX Workshop on SPIN Physics**
    JINR, Dubna, Russia / June 22. – 26, 2009
    Org. Committee: A. Kacharava, V. Komarov, A. Kulikov, P. Lenisa, R. Rathmann,
    H. Ströher (2009), CD-ROM
    ISBN: 978-3-89336-586-9

12. **Entwicklung einer Nanotechnologie-Plattform für die Herstellung Crossbar-basierter Speicherarchitekturen**
    von M. Meier (2009), 135 Seiten
    ISBN: 978-3-89336-598-2

13. **Electronic Oxides –**
    Correlation Phenomena, Exotic Phases and Novel Functionalities
    Lecture Notes of the 41st IFF Spring School March 8 – 19, 2010
    Jülich, Germany
    edited by St. Blügel, T. Brückel, R. Waser, C.M. Schneider (2010), ca. 1000 pages
    ISBN: 978-3-89336-609-5

14. **4th Georgian-German School and Workshop in Basic Science**
    Tbilisi, Georgia / May 3 – 7, 2010
    Org. Committee: E. Abrosimova, R. Botchorishvili, A. Kacharava, M. Nioradze,
    A. Prangishvili, H. Ströher (2010); CD-ROM
    ISBN: 978-3-89336-629-3

15. **Neutron Scattering**
    Lectures of the JCNS Laboratory Course held at Forschungszentrum Jülich and the research reactor FRM II of TU Munich
    edited by Th. Brückel, G. Heger, D. Richter, G. Roth and R. Zorn (2010),
    ca 350 pages
    ISBN: 978-3-89336-635-4

16. **Ab *initio* investigations of magnetic properties of ultrathin transition-metal films on *4d* substrates**
    by A. Al-Zubi (2010), II, 143 pages
    ISBN: 978-3-89336-641-5

17. **Investigation of a metal-organic interface realization and understanding of a molecular switch**
    by O. Neucheva (2010), 134 pages
    ISBN: 978-3-89336-650-7

18. **Reine Spinströme in lateralen Spinventilen, *in situ* Erzeugung und Nachweis**
von J. Mennig (2010), V, 95 Seiten
ISBN: 978-3-89336-684-2

19. **Nanoimprint Lithographie als Methode zur chemischen Oberflächen-strukturierung für Anwendungen in der Bioelektronik**
von S. Gilles (2010), II, 169 Seiten
ISBN: 978-3-89336-686-6

20. **Macromolecular Systems in Soft- and Living-Matter**
Lecture Notes of the 42nd IFF Spring School 2011 February 14 – 25, 2011 Jülich, Germany
edited by J. K.G. Dhont, G. Gompper, P. R.Lang, D. Richter, M. Ripoll, D. Willbold, R. Zorn (2011), ca. 1000 pages
ISBN: 978-3-89336-688-0

21. **The spin structure of magnetic nanoparticles and in magnetic nanostructures**
by S. Disch (2011), V, 342 pages
ISBN: 978-3-89336-704-7

22. **Element-selective and time-resolved magnetic investigations in the extreme ultraviolet range**
by P. Grychtol (2011), xii, 144 pages
ISBN: 978-3-89336-706-1

23. **Spin-Transfer Torque Induced Dynamics of Magnetic Vortices in Nanopillars**
by V. Sluka (2011), 121 pages
ISBN: 978-3-89336-717-7

24. **Adsorption von Phthalocyaninen auf Edelmetalloberflächen**
von I. Kröger (2011), vi, 206 Seiten
ISBN: 978-3-89336-720-7

25. **Time-Resolved Single Molecule FRET Studies on Folding/Unfolding Transitions and on Functional Conformational Changes of Phospho-glycerate Kinase**
by T. Rosenkranz (2011), III, 139 pages
ISBN: 978-3-89336-721-4

26. **NMR solution structures of the MIoK1 cyclic nucleotide-gated ion channel binding domain**
by S. Schünke (2011), VI, (getr. pag.)
ISBN: 978-3-89336-722-1

27. **Neutron Scattering**
    Lectures of the JCNS Laboratory Course held at Forschungszentrum Jülich and the research reactor FRM II of TU Munich
    edited by Th. Brückel, G. Heger, D. Richter, G. Roth and R. Zorn (2011), ca 350 pages
    ISBN: 978-3-89336-725-2

28. **Neutron Scattering**
    Experiment Manuals of the JCNS Laborator Course held at Forschungszentrum Jülich and the research reactorFRM II of TU Munich
    edited by Th. Brückel, G. Heger, D. Richter, G. Roth and R. Zorn (2011), ca. 180 pages
    ISBN: 978-3-89336-726-9

29. **Silicon nanowire transistor arrays for biomolecular detection**
    by X.T.Vu (2011), vii, 174 pages
    ISBN: 978-3-89336-739-9

30. **Interactions between parallel carbon nanotube quantum dots**
    by K. Goß (2011), viii, 139 pages
    ISBN: 978-3-89336-740-5

31. **Effect of spin-orbit scattering on transport properties of low-dimensional dilute alloys**
    by S. Heers (2011), viii, 216 pages
    ISBN: 978-3-89336-747-4

32. **Charged colloids and proteins: Structure, diffusion, and rheology**
    by M. Heinen (2011), xii, 186 pages
    ISBN: 978-3-89336-751-1

33. **Scattering Methods for Condensed Matter Research: Towards Novel Applications at Future Sources**
    Lecture Notes of the 43rd IFF Spring School 2012
    March 5 – 16, 2012 Jülich, Germany
    edited by M. Angst, T. Brückel, D. Richter, R. Zorn ca. 1000 pages
    ISBN: 978-3-89336-759-7

34. **Single-Site Green Function of the Dirac Equation for Full-Potential Electron Scattering**
    by P. Kordt (2012), 138 pages
    ISBN: 978-3-89336-760-3

35. **Time Resolved Single Molecule Fluorescence Spectroscopy on Surface Tethered and Freely Diffusing Proteins**
    by D. Atta (2012), iv, 126 pages
    ISBN: 978-3-89336-763-4

36. **Fabrication and Utilization of Mechanically Controllable Break Junction for Bioelectronics**
by D. Xiang (2012), 129 pages
ISBN: 978-3-89336-769-6

37. **Contact Mechanics and Friction of Elastic Solids on Hard and Rough Substrates**
by B. Lorenz (2012), iv, 121 pages
ISBN: 978-3-89336-779-5

38. **Ab initio Calculations of Spin-Wave Excitation Spectra from Time-Dependent Density-Functional Theory**
by M. Niesert (2012), 146 pages
ISBN: 978-3-89336-786-3

39. **Neutron Scattering**
Lectures of the JCNS Laboratory Course held at Forschungszentrum Jülich and the research reactor FRM II of TU Munich
edited by Th. Brückel, G. Heger, D. Richter, G. Roth and R. Zorn (2012), ca 350 pages
ISBN: 978-3-89336-789-4

40. **Neutron Scattering**
Experiment Manuals of the JCNS Laborator Course held at Forschungszentrum Jülich and the research reactorFRM II of TU Munich
edited by Th. Brückel, G. Heger, D. Richter, G. Roth and R. Zorn (2012), ca. 175 pages
ISBN: 978-3-89336-790-0

41. **Influence of a shear flow on colloidal depletion interaction**
by C. July (2012), xviii, 105 pages
ISBN: 978-3-89336-791-7

42. **NMR studies on the isolated C39 peptidase-like domain of ABC transporter Haemolysin B from *E. coli*: Investigation of the solution structure and the binding interface with HlyA**
by J. Lecher (2012), 126 pages
ISBN: 978-3-89336-793-1

43. **Spin Correlations and Excitations in Spin-frustrated Molecular and Molecule-based Magnets**
by Z. Fu (2012), 208 pages
ISBN: 978-3-89336-797-9

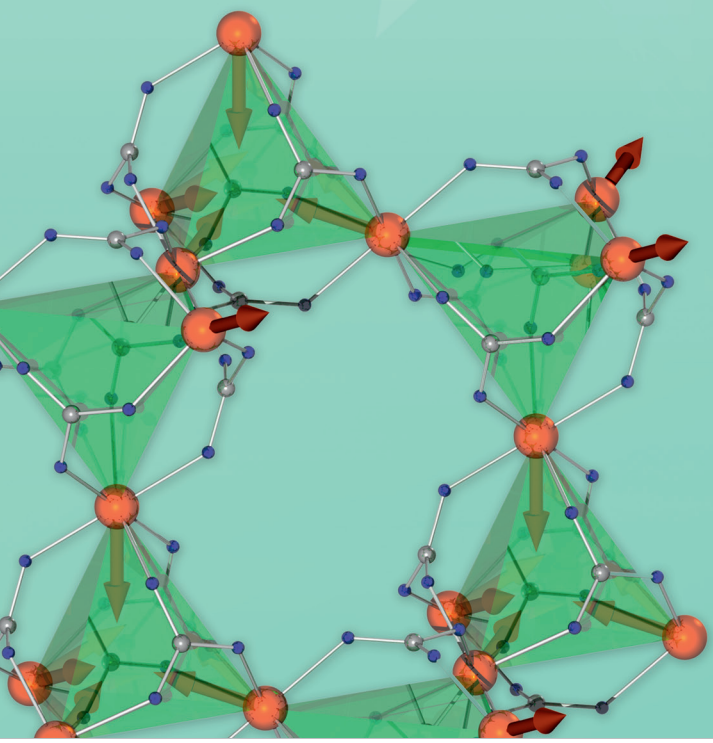

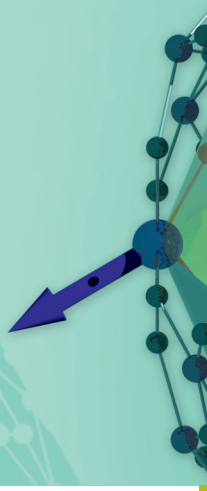

Schlüsseltechnologien / Key Technologies
Band / Volume 43
ISBN 978-3-89336-797-9

JÜLICH
FORSCHUNGSZENTRUM